University of Nottingham
UK | CHINA | MALAYSIA

Doctor of Philosophy

Model Updating Frameworks for the Estimation of Lateral Soil-Pile Interaction Parameters

---

Andreas Ioakim
Master of Engineering (MEng)
Master of Science (MSc)

This thesis is submitted to the University of Nottingham for the degree of Doctor of Philosophy in the Department of Civil Engineering

January 2025

Head of Department:
Mohamed Elmaghrbi

Supervisor:
Luke J. Prendergast

Abstract

Resilient infrastructure systems, particularly in safety-critical applications such as offshore wind turbines (OWTs), demand advanced monitoring frameworks that can accommodate complex dynamics and inherent uncertainties. Structural Health Monitoring (SHM) is central to this goal, ensuring the operational integrity of OWT foundations while supporting safety, efficiency, and sustainability. This thesis advances the field of SHM by integrating physics-based modelling with data-driven techniques, combining the reliability of numerical simulations and the adaptability of data-oriented methods. This hybrid approach overcomes the limitations of purely data-driven methods, which can produce accurate but physically inconsistent predictions, and purely physics-based models, which can be computationally expensive and sensitive to parameter uncertainties.

Focusing on soil-pile interaction (SPI), this work addresses key challenges in estimating critical system parameters that influence the dynamic response and structural integrity of pile foundations. The thesis develops and evaluates deterministic and stochastic model updating frameworks, each designed to handle varying data availability and changing environmental or operational conditions. The deterministic framework employs frequency-response functions (FRFs) using input-output data, while the stochastic frameworks utilise output-only data and Modal Assurance Criterion (MAC)-based updating. These frameworks are validated using numerical simulations, with field tests conducted in selected scenarios.

Throughout the thesis, numerous challenges are systematically addressed. These include achieving both physical interpretability and computational feasibility, maintaining accuracy under measurement uncertainties, ensuring robustness against varying operational conditions, and promoting scalability to real-world OWT systems. Addressing these challenges requires careful selection of an appropriate modelling approach, including model reduction strategies to balance accuracy and efficiency. The choice of parameters to be estimated, objective function formulation for robust performance, and selection or development of suitable optimisation algorithms are also critical factors. Additionally, the frameworks are designed to be applicable under operational conditions, where environmental and loading un-

certainties must be accounted for.

This thesis demonstrates that hybrid SHM frameworks, integrating data-driven and physics-based methods, enhance the predictive accuracy and reliability of OWT foundation monitoring. The findings emphasise the role of vibration data in model updating for estimating operating parameters while reducing uncertainty. These frameworks offer a structured approach to quantifying uncertain parameters and assessing the condition of pile foundations under dynamic uncertainties. By bridging theoretical insights with practical frameworks, this research contributes to the advancement of SHM for pile foundations.

Acknowledgments

First and foremost, I would like to express my heartfelt gratitude to my supervisor, Dr. Luke Prendergast, for his immense support and guidance throughout my PhD journey. His continuous encouragement and insightful advice during our weekly meetings were of paramount importance and played a vital role in my progress and development.

I extend my deepest gratitude to Dr. Szymon Greś. His expertise in vibration-based Structural Health Monitoring and system identification was instrumental in expanding my knowledge. I am particularly grateful for the way he generously shared his work, supported me in my research, and provided emotional encouragement. His guidance was crucial in inspiring my fascination with this intriguing yet challenging field.

I am also deeply thankful to Prof. Eleni Chatzi. Despite her demanding schedule, she always responded positively to my requests for collaboration and provided unwavering support. Her guidance and willingness to meet and offer her insights were invaluable. Moreover, her passion and dedication to the field were truly inspiring.

I would also like to thank Dr. Michael Döhler for his valuable contributions. I am grateful for his meaningful input, and his support throughout the process.

My gratitude extends to the University of Nottingham, particularly the Faculty of Engineering and the Nottingham Centre for Geomechanics, for their moral and financial support. Their funding and assistance allowed me to conduct and present my work at various conferences over the years. Additionally, I would like to acknowledge the High-Performance Computing Facility at the University of Nottingham for providing the computational resources necessary for my research.

Last but certainly not least, I would like to express my heartfelt gratitude to my friends, my girlfriend Shaikha, and my family: my father Vakis, my mother Elena, and my brother Kyriakos. Your unwavering support and belief in me have been a constant source of strength and motivation throughout this fulfilling yet challenging journey. I could not have reached this point without you.

Declaration

I declare that this thesis was composed by myself and that the results contained herein have not been submitted for any other degree. I confirm that the work presented is entirely my own, except where it forms part of jointly-authored publications. In such cases, my contributions and the names of the other authors have been acknowledged and detailed. I further confirm that appropriate credit has been given wherever reference is made to the work of others.

A two-stage method to estimate the embedded length of foundation piles using FRF-based model updating, *Mechanical Systems and Signal Processing*

Andreas Ioakim: I confirm that I, as the lead author, was solely responsible for the design and development of the model updating framework building upon a method previously developed by Wu et al. (2018). I conducted the implementation of the analysis, as well as the collection and analysis of the data. The initial draft of the paper was composed by me, and I integrated subsequent revisions by Dr. Luke Prendergast into the manuscript.

Luke J. Prendergast: Supervised the research and actively supported the development of the framework and its implementation. He was a co-author of the previously developed method upon which this framework was built (Wu et al., 2018) and the lead author of a study applying that method to experimental data (Prendergast et al., 2019). He was closely involved in the research, offering meaningful suggestions and provided detailed feedback on the manuscript.

An indirect data-driven model-updating framework to estimate soil-pile interaction parameters using output-only data, *Engineering Structures*

Andreas Ioakim: I confirm that I, as the lead author, was solely responsible for designing and developing the model updating framework, which estimates soil-pile

interaction parameters. This framework builds upon the model updating approach introduced by Greś et al. (2021b) and Greś et al. (2021d). I conducted the implementation of the numerical analysis, as well as the collection and analysis of the data. Additionally, I analysed the experimental data and carried out the experimental validation. The initial draft of the paper was composed by me, and I integrated subsequent revisions from my co-authors into the manuscript.

Szymon Greś: Supported the development of the framework and its implementation. He was the lead author of two studies that formed the foundation of the current framework (Greś et al., 2021b; Greś et al., 2021d) and provided already developed MATLAB functions from these works. He assisted in writing the section "Methodology" in the original paper and provided feedback on the manuscript.

Michael Döhler: Co-author of (Greś et al., 2021b; Greś et al., 2021d). He was actively involved in the research, providing meaningful suggestions throughout the work, offering constructive critique, and contributing valuable feedback on the manuscript.

Luke J. Prendergast: Supervised the research, actively supported the interpretation of the results, and provided the field data. He was closely involved in the research, offering meaningful suggestions throughout the process, providing constructive critique, and contributing detailed feedback on the manuscript.

Eleni Chatzi: Supervised and actively supported the research work, providing meaningful suggestions throughout the process. She offered constructive critique, contributed valuable insights, and provided detailed feedback on the manuscript.

Monitoring pile scour using model-updating with deterministic and stochastic methods

Andreas Ioakim: I confirm that I, as the lead author, was solely responsible for the design and development of three model updating frameworks. I adapted the FRF-based and CMA-ES frameworks from previously developed methods (Ioakim & Prendergast, 2024; Ioakim et al., 2025) for scour estimation, while I independently designed and developed the DE-based framework and all of its functionalities. I conducted the implementation of the analysis, as well as the collection and analysis of the data. The initial draft of the manuscript was composed by me, and I integrated subsequent revisions from Drs. Szymon Greś and Luke Prendergast into the manuscript.

Szymon Greś: He was actively involved in the research, providing meaningful

suggestions throughout the work, offering constructive critique, and contributing valuable feedback on the manuscript.

Luke J. Prendergast: He supervised and actively supported the research, providing meaningful suggestions throughout the work, offering constructive critique, and contributing valuable feedback on the manuscript.

Contents

List of Figures

List of Algorithms

List of Tables

List of Notations

Latin symbols

Symbol	Units	Chapter	Description
$\mathbf{A}, \mathbf{B}, \mathbf{C}, \mathbf{D}$	-	2, 4, 5, B	System matrices in state-space representation
D	m	2–5	Width (diameter) of the pile
D_r	-	2, 3	Relative density of sand
D_s	m	5	Scour depth
E	$\mathrm{N\,m^{-2}}$	2–A	Young's modulus of the pile material
$E_{py,0}$	$\mathrm{N\,m^{-2}}$	2	Initial stiffness of soil derived from $p-y$ relationships
e_k	-	3	Convergence tolerance for stiffness ratio
e_m	-	3	Convergence tolerance for mass ratio
$E_S \mid E_S(z)$	$\mathrm{N\,m^{-2}}$	2–5	Small-strain Young's modulus of the sand at depth z
$f_i \mid f_n$	Hz	2–5	Identified frequency of the i-th or n-th mode
$f_i^{\min}, f_i^{\max}$	Hz	2, 4	Confidence bounds for the i-th natural frequency
f_{1j}, f_{2j}	Hz	2	Closest frequencies to the left/right of the j-th eigenfrequency f_j
F_{model}	$\mathrm{m\,s^{-2}\,N^{-1}}$	3, 5	Amplitude at the model FRF peak
f_{model}	Hz	3, 5	Frequency at the model FRF peak
F_{target}	$\mathrm{m\,s^{-2}\,N^{-1}}$	3, 5	Amplitude at the target FRF peak
f_{target}	Hz	3, 5	Frequency at the target FRF peak
$F(\theta) \mid \mathcal{L}$	-	2, 4, 5	Objective function for optimization
$G_S \mid G_S(z)$	$\mathrm{N\,m^{-2}}$	2–5	Shear modulus of the soil at depth z
I	$\mathrm{m^4}$	2–A	Moment of inertia of the pile
k_i	$\mathrm{N\,m^{-1}}$	3–A	Stiffness of the i^{th} spring element
$K_S \mid K_S(z)$	$\mathrm{N\,m^{-3}}$	3–A	Subgrade reaction modulus at depth z

Continued on next page

List of Notations – continued from previous page

Symbol	Units	Chapter	Description
$\mathcal{K} \mid \mathcal{K}^{\theta}$	$\mathrm{N\,m^{-1}}$	2–B	Stiffness matrix of the system under θ
L_0	m	3–A	Pile length
L_1	m	3–A	Pile embedded length
L_a	m	3	Active length of the pile
$\mathcal{J}$	-	2, B	Jacobian matrix
$\mathcal{L}_{\mathrm{f}}$	-	5	Objective function term for frequency errors
$\mathcal{L}_{\mathrm{mac}}$	-	5	Objective function term for MAC errors
M_i	kg	3–5	Mass at the i^{th} spring element
M_{Pile}	kg	3, 4	Total mass of the pile
$\mathcal{M} \mid \mathcal{M}^{\theta}$	kg	2–B	Mass matrix of the system under parameter θ
n_{modes}	-	4, 5	Number of vibration modes considered
N_s	-	4–5	Number of springs in the discretized model (topmost spring)
p	-	2, 5	Number of block rows in the covariance matrix
Q	-	3, 4	Number of springs in the top quarter of the pile
$\mathbf{q}(t)$	m	3–A	Displacement vector at time t
$\dot{\mathbf{q}}(t)$	$\mathrm{m\,s^{-1}}$	3–B	Velocity vector at time t
$\ddot{\mathbf{q}}(t)$	$\mathrm{m\,s^{-2}}$	3–B	Acceleration vector at time t
q_c	$\mathrm{N\,m^{-2}}$	2, 3–5	Resistance to penetration from CPT
r_k	-	3	Residual term for stiffness in FRF-based method
r_m	-	3	Residual term for mass in FRF-based method
r_ω	-	3	Residual term for natural frequency in FRF-based method
t	s	2–A	Continuous time
t_0	m	2–A	Wall thickness of the pile
$\mathbf{u}_k$	N	2, B	Input vector at the k-th time step
$\mathbf{w}_k, \mathbf{v}_k$	$[\mathrm{m}, \mathrm{m\,s^{-1}}]$, $\mathrm{m\,s^{-2}}$	2, 5, B	Process noise and measurement noise vectors
w_k	-	3–5	Stiffness weighting factor scaling the soil stiffness profile
w_m	-	3–5	Mass weighting factor scaling the soil mass profile

Continued on next page

List of Notations – continued from previous page

Symbol	Units	Chapter	Description
$\mathbf{x}_k$	m	2, 5, B	State vector at the k-th time step in a state-space model
$\mathbf{y}_k$	$\mathrm{m\,s^{-2}}$	2, 5, B	Output vector at the k-th time step (accelerations)

Greek symbols

Symbol	Units	Chapter	Description
α_0, α_1	-	3, A	Rayleigh damping coefficients
γ	$\mathrm{kN\,m^{-3}}$	3, 4	Bulk unit weight of the soil
$\Delta^{\theta}_{f_i}$	-	2, 4	Normalized frequency difference for the i-th mode
$\Delta^{\theta}_{\mathrm{MAC}_i}$	-	2, 4	Normalized difference between identified and model-predicted mode shapes (MAC)
Δt	s	3–5	Sampling interval
θ	-	2–A	Parameter vector in optimization-based model updating
$\mathbf{\Lambda}$	$\mathrm{rad\,s^{-2}}$	2, B	Diagonal matrix of eigenvalues
λ_i	$\mathrm{rad\,s^{-2}}$	2–5, B	Continuous-time eigenvalue for the i-th mode
$\mathcal{N}(\mu, \Sigma)$	-	2, 4, 5, B	Normal distribution with mean μ and covariance Σ
ν_s	-	2–A	Soil Poisson's ratio
ξ_i	-	2–5	Damping ratio for the i-th mode
Σ_ϕ	-	2, 4, 5	Covariance matrix of mode shape estimates
$\mathbf{\Phi}$	-	2, 4, 5,B	Matrix of eigenvectors / mode shapes
$\phi_n \mid \phi_i$	-	2–5	Mode shape vector for the n-th or i-th mode
$\mathbf{\Omega}$	$\mathrm{rad\,s^{-1}}$	2, B	Diagonal matrix of natural circular frequencies
$\omega_n \mid \omega_i$	$\mathrm{rad\,s^{-1}}$	2, B	Natural circular frequency of mode n or i

Abbreviations

Symbol	Units	Chapter	Description
CMA-ES	-	2, 4–6	Covariance matrix adaptation evolution strategy
DE	-	2, 5, 6	Differential evolution strategy
FFT	-	2, 3, 5–A	Fast Fourier transform
FRF	-	2, 3, 5–A	Frequency Response Function
MAC(ϕ, ψ)	-	2, 4, 5	Modal Assurance Criterion (MAC) between mode shapes ϕ and ψ
OMA	-	2–6	Operational modal analysis
PSD	-	2, 4, 5	Power spectral density
SPI	-	2–A	Soil-pile interaction
SNR	-	3, 5	Signal-to-noise ratio
SSI	-	2–6	Stochastic subspace identification

Symbols and abbreviations that are used locally within specific chapters are defined and explained upon their first introduction to ensure clarity and consistency.

All algorithms in this thesis use zero-based indexing, where counting starts at zero and excludes the last element.

Chapter 1

Introduction

1.1 Background

1.1.1 Energy

Global climate change, rising energy demands, and the increasing costs of energy generation have become pressing concerns for governments and societies worldwide (Díaz & Soares, 2020; Osman et al., 2023). Over the past few decades, international agreements such as the Kyoto Protocol, the Paris Agreement, and the European 2030 climate and energy framework have sought to reduce greenhouse gas emissions, promote renewable energy adoption, and enhance energy efficiency (United Nations Framework Convention on Climate Change (UNFCCC), 1997, 2015). These initiatives highlight the urgency of transitioning away from fossil fuels, which remain the dominant energy source, contributing significantly to global emissions while posing environmental, economic, and geopolitical risks (Tott-Buswell et al., 2024).

Renewable energy sources, including wind and solar power, are central to achieving these ambitious climate goals due to their sustainability, availability, and declining operational costs (Ibata-Arens et al., 2018). By 2050, it is estimated that up to 90% of global energy could be derived from renewables, highlighting their pivotal role in decarbonising energy systems (Osman et al., 2023). However, the inherent variability of wind and solar resources, coupled with the harsh operating conditions in offshore and remote installations, present challenges for system reliability. Addressing these issues requires complementary measures such as energy storage, resilient infrastructure, and advanced modelling techniques to ensure long-term operational efficiency (Antoniadou et al., 2015; Zappa et al., 2019).

Offshore wind power plays a pivotal role in achieving renewable energy targets,

benefiting from stronger and more consistent wind flows compared to onshore sites, which result in higher capacity factors (Díaz & Soares, 2020). Recent advancements in turbine technology, coupled with the growing technological maturity and cost competitiveness of wind energy, have further accelerated its adoption (Ciang et al., 2008). The UK alone plans to design and install approximately 1200 offshore wind turbines (OWTs), each rated at 10 MW, over the coming years, requiring a capital expenditure of £30–45 billion (Byrne et al., 2019). These investments reflect the global momentum for offshore wind, with similar ambitions across Europe, the USA, China, and Taiwan (DeCastro et al., 2019).

While offshore wind offers significant advantages, such as higher and more consistent wind speeds, these benefits come with increased challenges and costs. Offshore wind turbine (OWT) units can cost two to three times more than onshore turbines, primarily due to the complexities of installation equipment, vessel mobilisation, and challenging environmental conditions (Wu et al., 2019).

Despite the higher costs, the resource potential is immense. For example, the North Sea could theoretically generate 120 GW of electricity—more than double the UK's demand, if only one-third of its shallower seabed areas were utilised (MacKay, 2016). However, with many shallow regions becoming saturated, the industry is moving into deeper waters that require more advanced foundation solutions and higher capital investment (Tott-Buswell et al., 2024). Foundations themselves can account for 15% of the unit's cost in shallower waters and up to 35% in deeper regions, emphasising the critical importance of selecting the most suitable foundation type based on water depth, soil characteristics, and turbine capacity (Kallehave et al., 2015; Tott-Buswell et al., 2024).

1.1.2 Infrastructure of offshore wind turbines

OWT foundations face unique challenges in inspection, maintenance, and repair, particularly in inaccessible marine environments (Ciang et al., 2008). These foundations must withstand dynamic wave loading, complex soil-structure interactions, and environmental risks such as fatigue, corrosion, and scour, all of which add significant complexity to their design and long-term performance. Structural health monitoring (SHM) has emerged as a critical tool to address these challenges, enabling the early detection of damage, optimising maintenance strategies, and ensuring the structural integrity of foundations under demanding conditions. By integrating advanced monitoring technologies with data analysis, SHM systems provide actionable insights into foundation performance, helping to mitigate risks that, if left unaddressed, could compromise the stability of turbines and sig-

nificantly increase life-cycle costs (Ciang et al., 2008; Kamariotis et al., 2023). As illustrated in Figures 1.1 and 1.2, the growing scale of wind installations underscores the critical importance of optimised design and monitoring systems for OWT foundations. SHM plays a pivotal role in ensuring the safe operation, structural reliability, and cost-effectiveness of foundations (Byrne et al., 2019; Kamariotis et al., 2023).

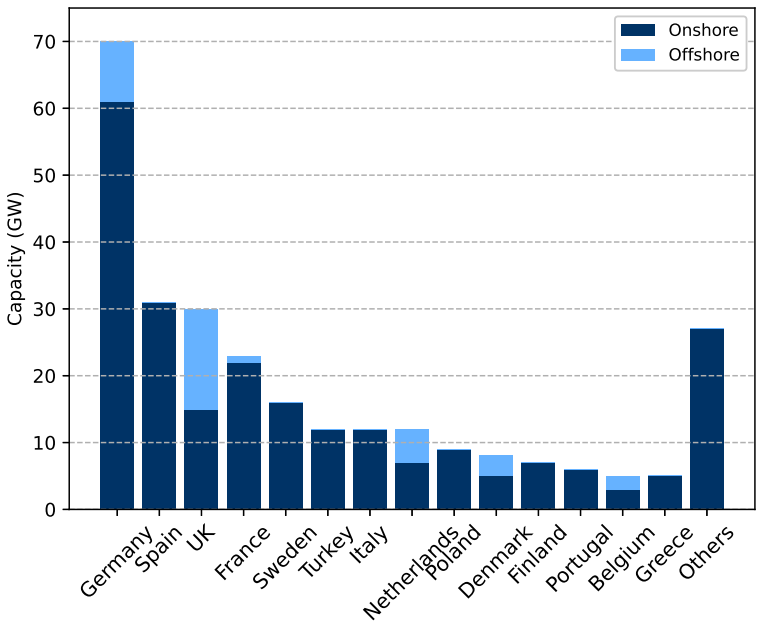

Figure 1.1: Total wind installations by country (Costanzo et al., 2023).

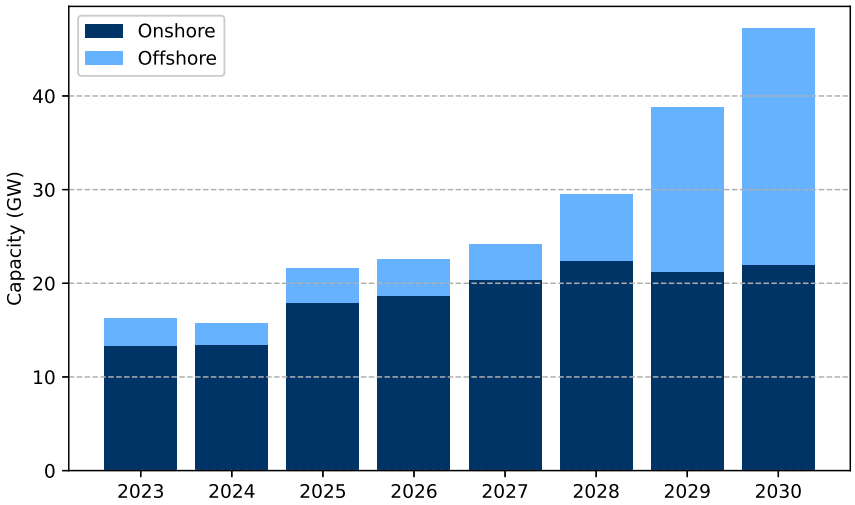

Figure 1.2: New wind installations in the EU by year (Costanzo et al., 2023).

Fixed foundations are widely used for installations up to 50 m depths, with

monopiles being the most dominant due to their simplicity and cost-effectiveness (Byrne & Houlsby, 2003; Tott-Buswell et al., 2024). As water depths exceed 50 m, floating structures like spar and semi-submersible platforms are gaining attention, though their adoption is still limited due to technical and economic challenges (Tott-Buswell et al., 2024). Figure 1.3 illustrates various foundation types, while Figure 1.4 highlights the dominance of monopiles, which account for 76% of installed foundations. Jackets (9%) and gravity bases (5%) cater to deeper waters or specific seabed conditions, while emerging floating foundations remain in early stages of development (Komusanac et al., 2021).

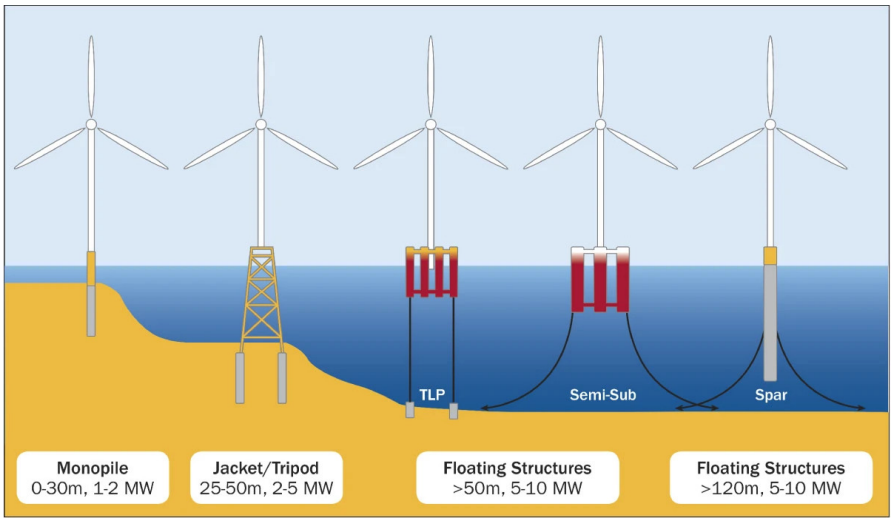

Figure 1.3: OWT foundation types (Bailey et al., 2014).

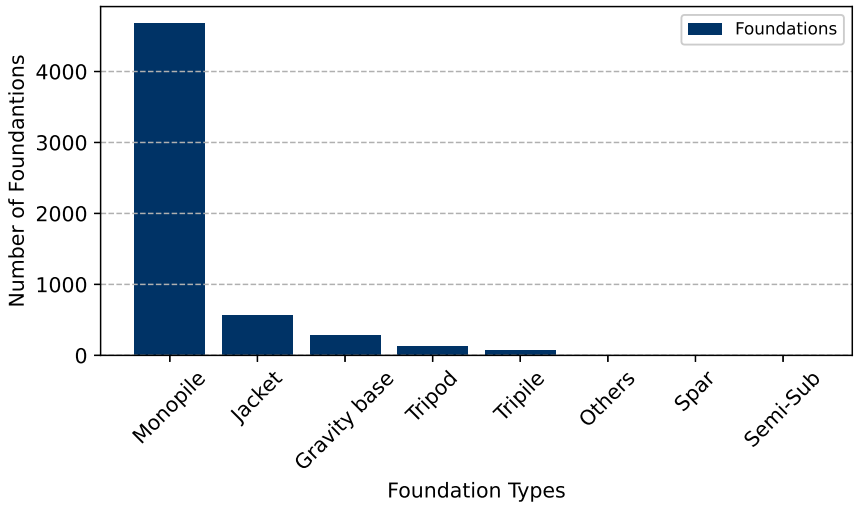

Figure 1.4: Distribution of OWT foundations (Komusanac et al., 2021).

The prevalence of monopile foundations underscores their critical role in offshore wind development, driven by their simplicity, ease of installation, and es-

tablished design methodologies. Typically consisting of large-diameter steel tubes, monopiles can measure up to 8–10 m in diameter, 30–50 m in length, and weigh up to 1000 t (Byrne et al., 2019). Two primary physics-based modelling methods are commonly used to simulate soil-pile systems: the direct continuum modelling method, which employs detailed 3D continuum models to capture site-specific soil conditions and complex interactions, and the indirect substructure approach, which simplifies the system by representing soil-pile interaction (SPI) through idealised models such as springs, dashpots, and masses.

While OWTs hold immense potential, challenges in foundation monitoring remain underexplored. The remote offshore environment, combined with dynamic loading conditions, subjects the soil-pile system to risks that traditional inspection methods cannot fully address. These limitations underscore the need for advanced, data-driven approaches to systematically evaluate structural integrity. In this context, SHM emerges as a vital technology, offering continuous, in-depth assessments that support proactive maintenance of foundations.

1.2 Structural health monitoring (SHM)

SHM is an interdisciplinary field aimed at ensuring the safety, reliability, and long-term performance of structural systems. It leverages data from real structures to monitor the condition of infrastructure over time. Integrating expertise from civil engineering, computer science, materials science, and other disciplines, SHM enables the monitoring of structures, addressing the limitations of traditional maintenance strategies that often rely on periodic visual inspections or manual testing.

SHM systems integrate structural data with computational tools to extract actionable insights, supporting decisions related to prognosis, maintenance, and repair. Recent advancements in sensor technology have made cost-effective deployment feasible, enabling the collection of large, heterogeneous datasets. When combined with advanced computational methods, these datasets serve as the foundation for transitioning from traditional inspections to automated, "cradle-to-grave" monitoring frameworks (Chatzi & Papadimitriou, 2016). Such frameworks are particularly valuable for dynamically sensitive structures like OWT foundations, which require continuous evaluation to optimise maintenance and ensure structural integrity.

1.2.1 Vibration-based SHM

Vibration-based SHM assesses the condition of a structure by analysing its dynamic behaviour through vibration response data. Sensors measuring quantities such as accelerations, velocities, or strains enable monitoring of structural performance under both operational and extreme loading conditions. This non-invasive approach offers two primary benefits: (i) the ability to monitor structures during normal operation without interruption, and (ii) reduced maintenance costs due to minimal interference with functionality. The methodology typically involves two steps: first, identifying modal properties (natural frequencies, damping ratios, and mode shapes) from measured vibration data to characterise the structural response; second, integrating data-driven methods with physics-based models to update uncertain parameters, such as soil stiffness, material properties, and geometry.

This hybrid approach combines the strengths of data-driven frameworks and physics-based models. It avoids the limitations of purely data-driven methods, which may yield accurate but physically inconsistent predictions, and purely physics-based models, which can be computationally intensive and sensitive to parameter uncertainties. By leveraging this methodology, vibration-based SHM enables the creation of a digital twin—a virtual representation of the structure that offers a comprehensive understanding of its dynamic behaviour. This integration facilitates accurate diagnosis of current conditions and prognostic insights into future performance (Cicirello, 2024; Greś, 2019).

Techniques like Operational Modal Analysis (OMA) enable the extraction of these modal properties without requiring controlled excitations, making them especially effective for large, flexible structures such as wind turbines (Döhler & Mevel, 2013; Ebrahimian et al., 2018; Greś et al., 2022b; Oliveira et al., 2021). By tracking how modal properties evolve over time, engineers can detect early signs of structural issues, including changes in soil stiffness, scouring, or damage accumulation.

1.2.2 Model updating in SHM

Although physics-based models are essential for simulating large-scale structures under various loads, they often incorporate simplifying assumptions and uncertain parameters, leading to discrepancies between predictions and real-world behaviour (Dhandole & Modak, 2010; Tedesco et al., 1999). Model updating addresses these limitations by calibrating parameterised models against measured dynamic data,

thereby improving the reliability of structural response predictions (Friswell & Mottershead, 1995; Mottershead & Friswell, 1993; Papadimitriou et al., 2000). The process can be approached through direct methods, which solve for parameters in a single step using modal relationships, or via iterative techniques that progressively minimise the mismatch between measured and simulated responses (Alkayem et al., 2018; Friswell & Mottershead, 1995; Sehgal & Kumar, 2016). By refining uncertain parameters and reducing prediction errors, model updating enhances the reliability of SHM, supports damage identification, and informs life-cycle management strategies.

Beyond refining structural simulations, model updating supports various practical applications. These include optimal sensor placement (Mehrjoo et al., 2022), fatigue damage estimation (Giagopoulos et al., 2019), assessments of complex or historic structures (Ferrari et al., 2019), and damage detection (An et al., 2019; Ou et al., 2017). By integrating operational data with numerical models, model updating enhances condition assessments, aids maintenance decisions, and improves overall lifecycle management.

A consideration during model updating is parameter compensation, where errors or uncertainties in one parameter are offset by adjustments in another. This phenomenon can lead to non-unique solutions or parameter correlation, especially when limited data or high model complexity is involved (Goulet et al., 2010). Recognising and addressing such compensation effects is essential for obtaining physically meaningful and robust parameter estimates.

1.3 Aims and objectives

The primary aim of this thesis is to advance the field of SHM by developing and evaluating model updating frameworks capable of accurately estimating critical SPI parameters, including embedded pile length and scour depth. This work addresses the need for robust, data-driven approaches that can enhance the reliability of numerical models and support the long-term monitoring, maintenance, and design of OWT foundations.

To achieve this aim, the following objectives are pursued:

O1: Develop an FRF-based approach: Develop and validate an FRF-based model updating framework for piles subjected to lateral impact loads, focusing on identifying the embedded length and soil parameters (Chapter 3).

O2: Design a stochastic output-only framework: Employ stochastic system identification and evolutionary optimisation to estimate the embedded

length of pile foundations using output-only vibration data, thereby omitting the need for measured input forces (Chapter 4).

O3: Compare deterministic and stochastic methods under varying conditions: Investigate and benchmark multiple model updating strategies for scour depth estimation, assessing trade-offs in accuracy, robustness, and computational cost under both impact and ambient excitation (Chapter 5).

O4: Validate and assess performance: Apply the proposed methods to numerical simulations and, where applicable, experimental data to evaluate convergence properties, quantify uncertainties, and demonstrate their effectiveness. Specifically, the FRF-based framework presented in Chapter 3 was validated through numerical simulations, while the stochastic output-only framework in Chapter 4 was validated both numerically and experimentally. A comparative assessment, including a newly developed stochastic approach for scour estimation in Chapter 5, was carried out using numerically generated data.

1.4 Challenges

Developing robust model updating frameworks for SPI presents a range of challenges, stemming from the inherent complexity of the problem and the limitations of both data-driven and physics-based approaches. This section outlines the key challenges addressed in this thesis.

Relying solely on data-driven methods can yield models that fit observed behaviour well but may lack physical interpretability. Conversely, physics-based models, while grounded in physical principles, require parameter assumptions that may not represent the actual SPI behaviour. Therefore, this work combines data-driven and physics-based approaches to develop hybrid frameworks that leverage the strengths of both methodologies. Iterative model updating methods are employed to ensure physically meaningful solutions that align with experimental data.

Selecting an appropriate SPI modelling method is critical for capturing the complex dynamic behaviour of pile foundations. Additionally, choosing a computationally efficient method is essential, as these frameworks require iteratively refining the parameters and solving the problem multiple times. To assess the model updating frameworks, a series of numerically generated target models is created, representing pseudo-experimental datasets. These target models include variations in geometrical, physical, and mechanical properties, such as pile diameters, embedded lengths, and soil stiffness profiles. Noise and uncertainties are

introduced into the models to simulate real-world conditions.

The dynamic response of SPI systems is influenced by key parameters such as embedded pile length, scour depth, soil mass, and stiffness profiles. This thesis investigates how these parameters affect the lateral response of the system. Modal parameters, including natural frequencies and mode shapes, are extracted from vibration data using frequency-domain peak picking for deterministic methods and time-domain stochastic subspace identification for stochastic frameworks.

An effective objective function is crucial for model updating. In the deterministic framework, peaks of the frequency response function (FRF) are used, while the stochastic framework incorporates natural frequencies and mode shapes. These objective functions are optimised to estimate parameters of interest with high accuracy and reliability.

Operational turbines often provide acceleration data but lack load information, necessitating the use of output-only methods. Stochastic frameworks are developed to address this challenge, enabling parameter estimation using vibration data alone. Additionally, UQ techniques are employed to quantify uncertainties in the vibration data, ensuring reliable and robust results.

To lower computational costs, numerical models are optimised using techniques such as compressed sparse row (CSR) matrices in deterministic frameworks and modal reduced-order models (ROMs) in stochastic approaches. High-performance computing (HPC) resources further accelerate the model updating process, enabling the analysis of complex models within practical timeframes.

The accuracy, robustness, and computational efficiency of the developed frameworks are systematically evaluated using both numerical simulations and field data when feasible. Comparative analyses highlight the advantages, limitations, and suitable applications of deterministic and stochastic methods, providing insights into their deployment for real-world monitoring of OWT foundations.

1.5 Thesis structure

This thesis is organised into six chapters, as outlined below:

- **Chapter 2: Literature review.** Reviews the state-of-the-art in SPI modelling, system identification, model updating methods, and uncertainty quantification, highlighting existing gaps and open questions that form the basis for this thesis.
- **Chapter 3: Deterministic model updating for SPI.** Proposes a two-

stage FRF-based iterative framework to estimate the embedded pile length and soil parameters for laterally impacted piles. The approach is tested against numerically simulated piles to demonstrate convergence and accuracy.

- **Chapter 4: Data-driven model updating using subspace identification and evolutionary optimisation.** Introduces a stochastic, output-only identification framework to estimate embedded pile length and soil parameters using measured vibration data. The method's effectiveness is validated first on numerical examples and subsequently on a full-scale field test.

- **Chapter 5: Comparative study of deterministic and stochastic frameworks for scour detection.** Evaluates three distinct methods, an FRF-based deterministic approach and two stochastic approaches for estimating scour depth in pile foundations. These frameworks are tested against numerically generated datasets under impact load and ambient noise conditions to compare accuracy, robustness, and computational costs.

- **Chapter 6: Conclusions and future work.** Summarises the findings from Chapters 3–5, outlines limitations, and suggests directions for future research, particularly in the context of real-world OWT foundation monitoring.

Chapter 2

Literature review

The literature review is organised into four interlinked parts that mirror the methodological flow of the frameworks developed in this thesis. Section 2.1 reviews physics-based models for dynamic soil-pile interaction, establishing the theoretical background for the modelling component of the model updating frameworks. Section 2.2 surveys deterministic and stochastic system identification methods for extracting modal properties from input-output and output-only measurements; these methods form the basis for the identification components of the frameworks. Section 2.3 reviews state-of-the-art deterministic and stochastic model updating strategies. Finally, Section 2.4 examines uncertainty quantification methods applied to both the model updating process and the estimated modal parameters. Together, these sections establish the foundation on which the model updating frameworks developed in this thesis are built.

2.1 Dynamic modelling of soil-pile interaction (SPI)

Monopiles supporting offshore wind turbines (OWTs) are dynamically sensitive structures subjected to various excitations with differing amplitudes and frequencies. These excitations include lateral loads from tidal forces, wave action, and wind, along with dynamic loads that occur during 'rotor stop' events or faults in the turbine or drivetrain (Prendergast et al., 2019; Zdravković et al., 2020). Consequently, the system is dynamically sensitive, with an increased likelihood of resonance.

Piles, particularly in offshore environments, are designed to resist dynamic lateral loads applied on the structure. Their lateral load resistance exhibits linear behaviour under small-strain conditions and transitions to non-linear behaviour un-

der larger loads. This resistance is typically characterised using load-displacement relationships (Li et al., 2022) as it can be viewed in Figure 2.1. The response of a pile foundation to dynamic loading is influenced by interactions among three interconnected systems: the structure, the foundation, and the surrounding soil. Soil-pile interaction (SPI) analysis evaluates the combined response of these systems to specified dynamic or ground motions, accounting for the linked interactions between the pile, structure, and soil (Stewart et al., 2012).

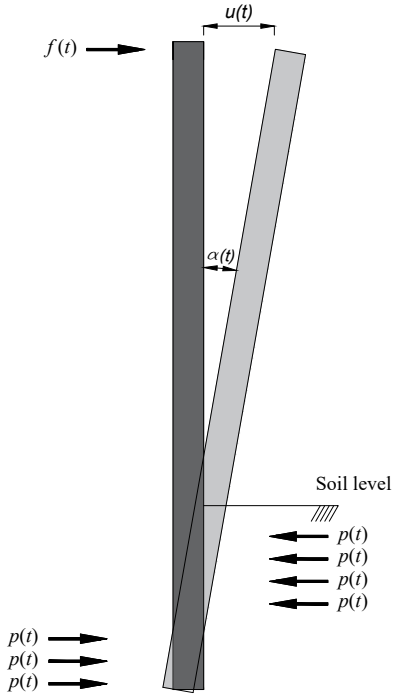

Figure 2.1: Laterally loaded SPI .

Modal analysis is fundamental to the design, monitoring, and maintenance of pile foundations. By identifying modal parameters such as natural frequencies and mode shapes, engineers can ensure that the operational frequency range avoids resonance with external loads, minimising the risk of amplified structural vibrations and preserving the stability of the entire system. Additionally, the modal properties can be used to monitor pile foundations over time, enabling the detection of changes in the system that may indicate structural issues.

In the context of structural health monitoring (SHM), modal analysis is used to evaluate the condition of a structure by analysing its dynamic response. Specifically, operational modal analysis (OMA) techniques enable the identification of modal properties based solely on a structure's natural dynamic response, making them particularly effective for monitoring large, flexible structures like wind

turbines and have been widely employed for a wide range of superstructure components (Abdallah et al., 2018; Avendano-Valencia et al., 2020; Döhler & Mevel, 2013; Greś et al., 2022b; Oliveira et al., 2018). By tracking changes in modal properties over time, potential issues such as scouring, soil stiffness degradation, or structural degradation can be identified early, enabling proactive maintenance interventions to ensure the structure's reliability and safety.

Furthermore, OMA provides deeper insights into how structures respond to operational and environmental loads, including harmonic excitations from rotor rotation and wave loading (Oliveira et al., 2021). Monitoring tools, such as those described in (Abdallah et al., 2018; Avendano-Valencia et al., 2020), have demonstrated the effectiveness of tracking modal properties throughout a structure's lifecycle, offering a robust framework for long-term performance assessment.

To assess the dynamic SPI for monopile-supported systems, comprehensive modelling of both the structure and the surrounding soil is essential. This modelling allows for the accurate calculation of modal parameters, including natural frequencies and mode shapes, which are crucial for monitoring and comparing the modelled behaviour to the actual response of the structure. Two primary physics-based modelling methods are commonly used to simulate the soil-pile system: the direct continuum modelling method and the indirect substructure approach.

The standard method for calculating the natural frequency and mode shapes of a structural system involves defining stiffness and mass matrices, followed by eigenanalysis. However, for integrated OWT-monopile systems, the variability and cyclic nature of environmental loads often require a time-domain analysis. This approach enables the assessment of the structure's dynamic response to fluctuating loads, such as those induced by wind and waves (Arany et al., 2017; Bhattacharya, 2019). Furthermore, the dynamic responses of the soil and pile are particularly sensitive to loading frequencies associated with rotor harmonics, specifically 1P and 3P, which correspond to the frequencies of full blade rotation and blade-passing events, respectively, in three-blade turbines as shown in Fig 2.2 (Tott-Buswell et al., 2024).

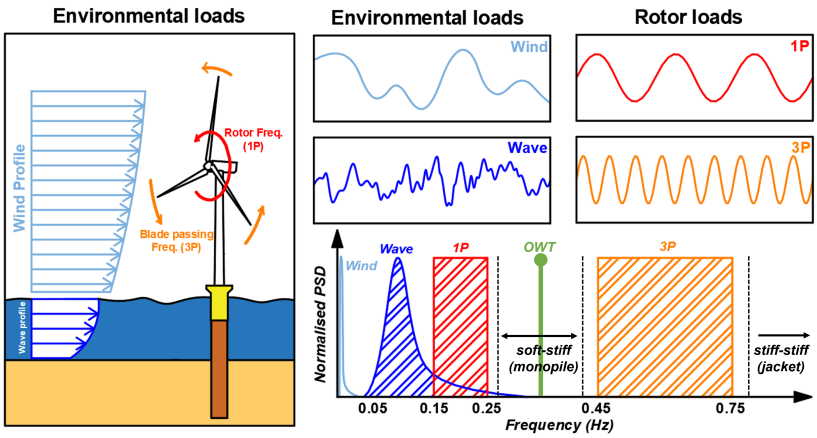

Figure 2.2: Excitation loads on OWTs and their power spectral density (PSD) (Tott-Buswell et al., 2024).

To effectively model and simulate the dynamic behaviour of SPI, it is essential to account for the complexities of the SPI problem. Detailed simulations are key to developing models that capture the complex nature of these interactions and enable the creation of digital twins capable of replicating the dynamic response of the structure. These digital twins are invaluable for monitoring the condition of the system over time, detecting changes in dynamic behaviour, and supporting maintenance strategies to ensure the reliability and safety of the structure.

2.1.1 Direct modelling

Numerical physics-based methods aim to approximate continuous (infinite-dimensional) problems with discrete (finite-dimensional) models, enabling their solution using finite computational resources. In direct analysis, the soil is often represented using a continuous model that incorporates both foundation and structural elements, with boundaries defined at the edges of the soil mesh and interface elements at the foundation-soil interface. Figure 2.3 illustrates a direct three-dimensional FE mesh, showcasing the discretisation of a domain into finite elements for numerical analysis.

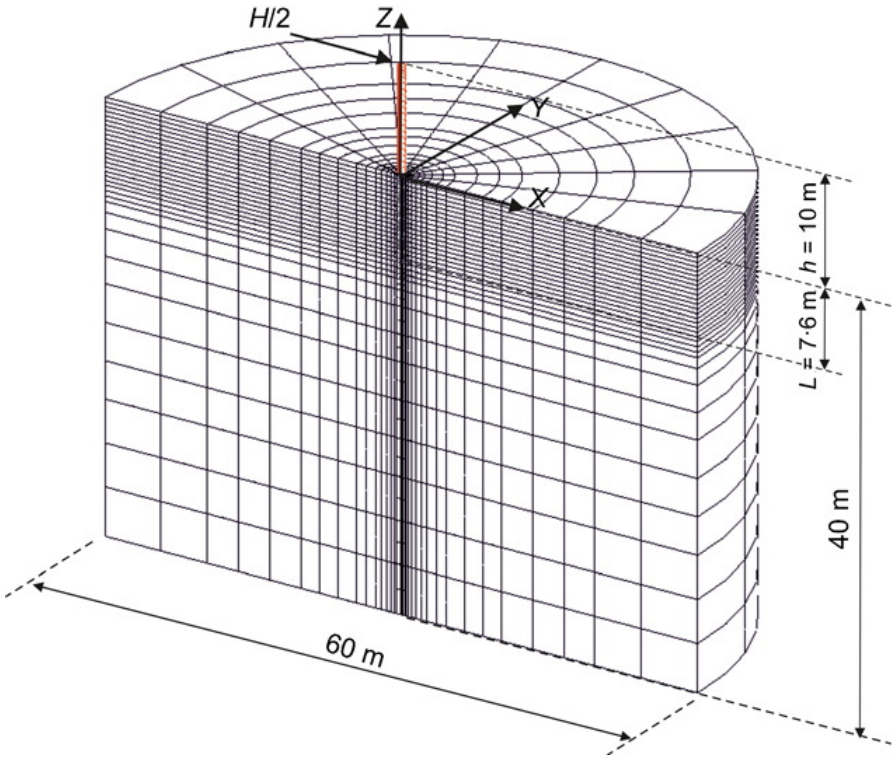

Figure 2.3: Example of three-dimensional FE mesh (Zdravković et al., 2020).

The direct method provides a detailed representation of SPI, effectively capturing the complexity of dynamic responses under variable loading. A critical component of this method is the evaluation of site response, particularly wave propagation through the soil. Wave propagation analyses are commonly performed using equivalent linear soil property representations within finite element (FE), finite difference (FD), or boundary element methods (Lysmer et al., 1999; Wolf, 1985). These techniques allow direct analysis to address a range of soil-structure interaction effects.

Direct solutions to the SPI problem are computationally intensive, particularly when dealing with complex geometries or pronounced soil and material nonlinearities. As a result, such analyses are sparingly used in industry and are typically reserved for scenarios involving highly nonlinear soil behaviour or unique geometric conditions, where detailed SPI simulations are essential to approximating real-world responses accurately (Stewart et al., 2012; Zdravković et al., 2020).

Several studies have investigated the behaviour of laterally loaded piles in clay, utilising both analytical or semi-analytical elastic methods (Basu et al., 2009; Poulos & Davis, 1980) and advanced numerical approaches based on FE modelling (Brown & Shie, 1990; Haiderali & Madabhushi, 2016; Jung et al., 2015; Yang & Jeremić, 2002; Zdravković et al., 2020). These works often simulate the response of clay using a total stress approach, applying failure criteria such as Tresca (Jung

et al., 2015) or von Mises (Brown & Shie, 1990; Yang & Jeremić, 2002). Common assumptions include treating the undrained shear strength (S_u) as uniform (Yang & Jeremić, 2002) or increasing with depth (Jung et al., 2015), while the Young's modulus is considered either constant (Brown & Shie, 1990), proportional to S_u (Jung et al., 2015), or dependent on the confining pressure (Yang & Jeremić, 2002).

The characterisation and modelling of sand behaviour present additional challenges due to the sensitivity of sand to confining pressure and void ratio, which significantly influence its volume change and maximum shear strength (Been & Jefferies, 1985; Bolton, 1986). For example Broms (1964) proposed a formulation for the modulus of subgrade reaction that accounts for the density of the sand, suggesting scaling factors of 0.75 and 0.5 for loose and dense sand, respectively. Similarly, Rosquoet et al. (2007) conducted experimental studies on the ultimate lateral soil resistance using centrifuge models under lateral cyclic loading and compared the results with Broms' theoretical predictions. As expected, Rosquoet reported an increase of 800 kN in ultimate lateral resistance as the relative density (D_r) increased from 53% to 86%, with values comparable to those predicted by Broms.

Consequently, when modelling the response of laterally loaded piles in sands, relatively simple constitutive models, such as Mohr–Coulomb models that predict constant strength and dilatancy, may require different parameter sets to account for variations in relative density (Achmus et al., 2009). This approach has yielded consistent results, as seen in studies by Abdel-Rahman and Achmus (2005), Achmus et al. (2009), and Stone et al. (2018). Such adjustments allow for a more accurate representation of sand behaviour in numerical models, improving the predictive capability of laterally loaded pile response simulations in various soil conditions.

Although direct methods use advanced modelling techniques and can capture the complex nature of the SPI problem, they are associated with high computational costs. Additionally, these methods require accurate characterisation of the problem, often involving a large number of soil parameters that need to be carefully accounted for. This complexity makes direct methods particularly challenging to use in scenarios where iterative model updating techniques are employed, as these approaches require iterative reanalysis and repeated comparisons with experimental data. Due to these limitations, this PhD focuses on indirect methods for SPI modelling, which offer a more computationally efficient alternative while still providing valuable insights into the dynamic response of soil-pile systems.

2.1.2 Indirect modelling

In the substructure approach, a widely adopted model for analysing SPI is the Beam-on-Winkler Foundation (BWF) model, commonly referred to as the Winkler model. This physics-based method represents the pile foundation within a one-dimensional framework, simulating the surrounding soil as a series of discrete, independent, and closely spaced springs, masses, and dashpots (Winkler, 1867). By reducing the SPI problem to a one-dimensional representation, the BWF model significantly simplifies computational requirements compared to complex three-dimensional continuum models, offering an efficient yet sufficiently accurate approach for many engineering applications.

In the BWF model, the pile is typically modeled using Timoshenko beam theory to account for lateral loading, while the surrounding soil is represented as distributed lateral springs along the pile's length. This configuration captures key SPI characteristics by assuming that the displacement of each pile node corresponds directly to the soil's reaction at that specific location, independent of the behaviour of adjacent nodes. This simplification provides a computationally efficient approach to analysing SPI while effectively representing the pile's lateral deformation under external forces (Winkler, 1867).

At the core of the Winkler model is the pressure-deflection relationship for each point along the foundation element, described by:

$$\mathbf{p}(x,t) = K_s \cdot \mathbf{w}(x,t) \tag{2.1}$$

where $\mathbf{p}(x,t)$ denotes the applied pressure ($\mathrm{N/m^2}$) at a given time t, $\mathbf{w}(x,t)$ represents the deflection (m) at that point and time, and K_S is the coefficient of subgreade reaction ($\mathrm{N/m^3}$). Equation (2.1) assumes a linear-elastic relationship, excluding energy dissipation and inertial effects.

For small-strain applications, a key component of the model is the representation of soil stiffness, derived from traditional *p-y* relationships. The initial (small-strain) spring stiffness, expressed as $k_0 = E_{py,0}\Delta L$, is calculated using *p-y* formulations. Here, $E_{py,0}$ represents the initial stiffness of the soil, typically calibrated using empirical data specific to soil types, such as API sand (Dührkop, 2009; Kallehave et al., 2012). This relationship is visually illustrated in Figure 2.4.

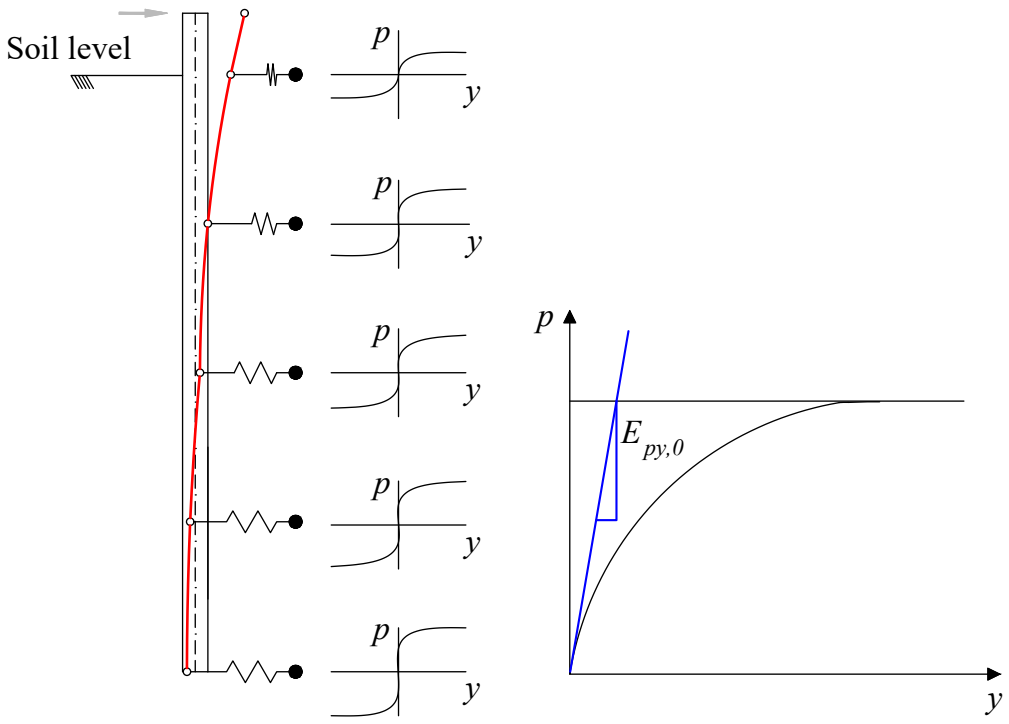

Figure 2.4: Derived $E_{py,0}$ from laterally loaded Winkler model based on p-y curves.

However, applying the Winkler model to dynamic scenarios introduces additional complexities, particularly due to the nonlinear and inelastic behaviour of soil at larger deformations. Accurately capturing soil behaviour under dynamic loading requires consideration of various dynamic parameters, including initial stiffness, load-displacement response curves, cyclic degradation, unload-reload stiffness, and radiation and hysteretic damping coefficients. This area has garnered significant interest, particularly in earthquake engineering, where beam-on-nonlinear Winkler foundation (BNWF) models have been developed to better address soil-structure response under large-strain dynamic conditions (Juirnarongrit & Ashford, 2006; Prendergast & Gavin, 2016).

Non-linear SPI models are essential for accurately simulating the response of pile foundations under dynamic and cyclic loading conditions, especially for large offshore structures such as wind turbines. In practical applications, non-linear models are employed to capture the intricate, cycle-dependent behaviour of soil, which includes complex phenomena such as cyclic degradation, stiffness variation, and energy dissipation.

The BNWF model builds on the traditional BWF approach but incorporates non-linear springs that can represent more realistic soil behaviour under dynamic loads. In BNWF models, the soil is idealised as a series of non-linear springs

distributed along the pile length, each defined by load-displacement curves known as p-y curves. These curves capture the non-linear relationship between lateral soil resistance p and lateral pile displacement y at various depths. It is worth noting that the p-y relationships can be adapted to reflect soil characteristics for different depths and soil types, enabling the BNWF model to handle layered soil profiles effectively.

Advanced non-linear SPI models also consider kinematic interaction effects, which describe the response of the SPI system to ground motion, especially relevant for seismic scenarios (Burd et al., 2020b). For example, Kampitsis et al. (2013) developed a dynamic BNWF model based on Timoshenko beam theory, incorporating features like geometrical non-linearity, rotary inertia, and shear deformation. Their model uses a series of p-y springs, including a non-linear p-y spring connected in series with an elastic spring-damper element (Kelvin–Voigt model), to simulate near-field soil plasticity and far-field confining stiffness effectively.

The effectiveness of non-linear SPI models has been evaluated through extensive comparisons with experimental data. For instance, Boulanger et al. (1999) validated a BNWF model using dynamic centrifuge model tests with soil layers of soft clay overlying sand. The dynamic p-y parameters were tuned based on site response measurements, confirming the model's capability in representing the soil-pile response under earthquake loading.

In summary, non-linear SPI models, particularly the BNWF model, are indispensable for accurately capturing the pile response under dynamic loads. By combining the foundation's flexibility with a realistic representation of soil non-linearity, these models offer a comprehensive approach to understanding SPI and have become a standard approach for assessing soil behaviour under complex loading regimes.

This PhD focuses on developing frameworks for model updating of BWF small-strain models. While the primary focus is on these simpler models, the model updating frameworks are designed to be adaptable for application to non-linear models such as those described above or the three-dimensional-FE models (FEMs), offering the potential to handle more detailed and complex simulations. However, the computational cost associated with such adaptations must be carefully considered.

The initial small-strain stiffness, commonly represented by the small-strain shear modulus (G_S), Young's modulus (E_S) or ($E_{py,0}$) when derived directly from p-y relationships is fundamental for modelling the lateral elastic response of SPI systems at low deformation levels. In static analyses, K_S plays a significant role

in both small-strain and large-strain applications. Accurately specifying this parameter can be challenging, as it depends on several factors, including the loading scheme, foundation geometry, and subgrade material properties. Its precise representation is therefore essential for achieving realistic simulations of SPI behaviour under dynamic conditions.

A range of subgrade reaction theories (Biot, 1937; Elachachi et al., 2004; Okeagu & Abdel-Sayed, 1984; Sadrekarimi & Akbarzad, 2009; Vesić, 1961) offer different approaches to estimating this initial stiffness, each rooted in distinct assumptions about soil properties, loading conditions, and foundation geometry.

Biot (1937) proposed an empirical equation to calculate the K_S by equating the maximum moments in an infinite beam resting on a three-dimensional elastic soil continuum. Bending-moment and deflection curves were presented and values for K_S were proposed that allow the BWF models to produce acceptable results, dependent on both the beam stiffness and the elasticity of the foundation.

$$K_S = \frac{0.95E_S}{D(1-\nu_S^2)}\left(\frac{D^4E_S}{(1-\nu_S^2)EI}\right)^{0.108} \tag{2.2}$$

where E_S is the small-strain Young's modulus of the soil, D is the width of the foundation, ν_S is the Poisson's ratio of the soil, and EI represents the flexural rigidity of the foundation.

Similarly, Vesić (1961) relates the subgrade reaction modulus to the soil's small-strain properties and pile dimensions. Vesic demonstrated that, for beams of infinite length resting on an elastic-isotropic half-space, using the K_S in analysis leads to overestimated bending moments and underestimated contact pressures and deflections. He proposed analytical procedures to address these discrepancies for beams of various lengths, providing a more accurate foundation for calculating SPI parameters.

$$K_S = \frac{0.65E_S}{D(1-\nu_S^2)}\left(\frac{E_SD^4}{EI}\right)^{1/12} \tag{2.3}$$

In alternative approaches, Meyerhof and Baikie (1963) (Okeagu & Abdel-Sayed, 1984; Sadrekarimi & Akbarzad, 2009) derived an equation for circular cross-sections, emphasising the relationship between soil stiffness and element width. Their study investigated the ultimate load of curved steel sheets bearing against dense sand backfill through scaled loading tests, which measured strains, soil pressures, and deflections. The stress-deformation and strength characteristics of the sand were evaluated using triaxial compression tests, from which representative values of the K_S were calculated. These coefficients closely aligned with

those deduced from the loading tests.

$$K_S = \frac{E_S}{D(1-\nu_S^2)} \tag{2.4}$$

To investigate the variability in the K_S for laterally loaded open-ended piles a similar analysis to that of Prendergast and Gavin (2016) is conducted. Three models are examined: Biot, Vesic, and Meyerhof & Baike (M&B). The analysis is conducted by varying D and E_S and choosing $\nu_S = 0.1$, $E = 200\,\text{GPa}$ and wall thickness ($t_0 = 0.1\,\text{m}$). The diameters considered range from $2\,\text{m}$ to $6\,\text{m}$, and the small-strain modulus is analysed for loose ($E_S = 50\,\text{MPa}$), medium dense ($E_S = 100\,\text{MPa}$), and dense sand ($E_S = 150\,\text{MPa}$) conditions.

The results, presented in Figure 2.5, reveal an overestimation of the K_S by M&B: The M&B model consistently overestimates K_S compared to Biot and Vesic. This is because M&B does not account for the wall thickness, which is included in the calculation of the moment of inertia (I) in both Biot and Vesic models. Additionally, M&B neglects the pile's material property E, which further reduces its accuracy. For example, for $E_S = 50\,\text{MPa}$ and $D = 2.0\,\text{m}$, M&B predicts $K_S = 25.3\,\text{MN/m}^3$, which is approximately 66% higher than Biot prediction of $K_S = 15.2\,\text{MN/m}^3$ and 118% higher than Vesic prediction of $K_S = 11.6\,\text{MN/m}^3$.

Nevertheless, these estimates will prove to have an important role in the subsequent analysis, serving as the initial estimates of the soil stiffness profile for the model updating methods discussed in Sections chapters 3 to 5.

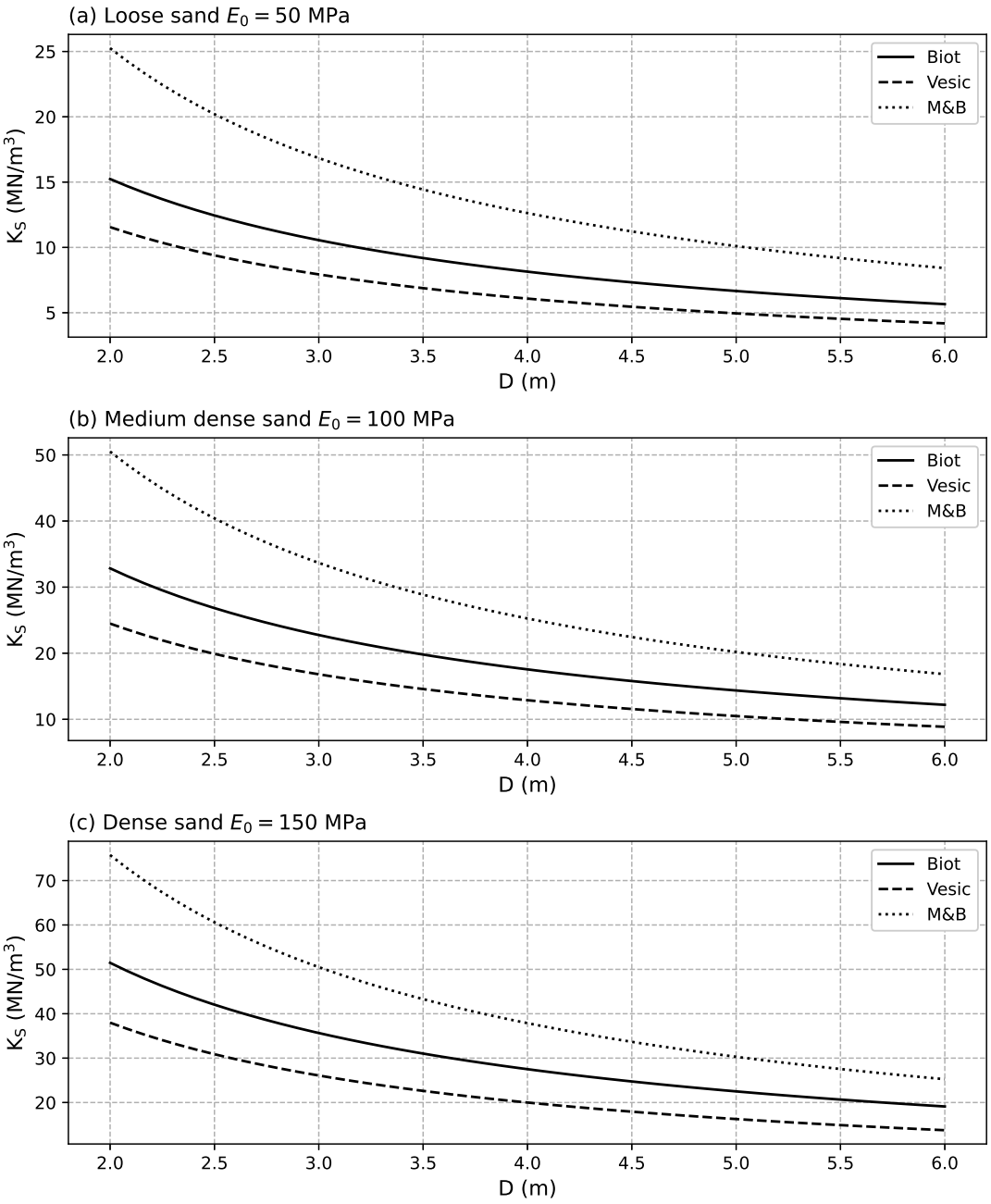

Figure 2.5: Variation of the K_S with pile diameter (D) for loose, medium dense, and dense sands using Biot, Vesic, and M&B models.

The E_S or G_S profile for a given site can be estimated using shear wave velocity measurements or data from site investigation tests such as the Cone Penetration Test (CPT) (Liu et al., 2021a; O'Neill & Murchison, 1983; Suryasentana & Lehane, 2016).

CPT data provide insights into soil stiffness and density, making them particularly useful for deriving parameters such as the E_S and G_S. In a CPT, a cone is pushed into the ground at a steady rate using a rig connected to a series of rods

equipped with an electronic measuring system. As the cone penetrates the soil, it records data on the soil's resistance to penetration (q_c), which can subsequently be used to estimate the (G_S).

Similarily, the Multichannel Analysis of Surface Waves (MASW) offers a non-invasive method to measure in situ shear wave velocity, which is directly indicative of small-strain stiffness (Donohue et al., 2004). This technique has been widely applied in geotechnical engineering, including quality control for ground improvement, due to its ability to generate detailed shear wave velocity profiles for assessing soil stiffness. MASW works by using surface waves, specifically Rayleigh waves, whose dispersion characteristics are analysed to infer stiffness profiles at various depths, enabling immediate field assessments. This method is particularly useful for evaluating soil properties in heterogeneous or disturbed conditions and serves as a practical alternative to intrusive tests, especially when direct access to deeper strata is limited.

In combination, MASW and CPT provide a comprehensive dataset for developing initial stiffness profiles essential for modelling SPI. While these methods are effective for estimating the G_S, their results are subject to geotechnical uncertainties due to spatial variability, particularly in deeper offshore locations where soil properties can vary significantly. Furthermore, the characteristics of the soil may evolve over time, making initial test results less accurate for long-term modelling. Parameter transformations, such as those involving the rigidity index (ratio of G_S to $\sigma'_v \tan\phi$), and the selection of subgrade reaction models further contribute to uncertainties, potentially influencing key predictions such as system natural frequencies (Reale et al., 2021). Therefore, while MASW and CPT are valuable as initial estimators, their outputs must be refined using data from operational SPI systems to account for in situ conditions and temporal changes, ensuring reliable and accurate modelling.

The natural frequencies and mode shapes of an SPI system depend on the global stiffness and mass matrices, which can be computed through time-domain or frequency-domain analyses (Tedesco et al., 1999). Frequency-domain analysis is computationally efficient for linear systems, as vibration modes are derived by solving the system's eigenvalue problem. The eigenvalue problem is expressed as:

$$(\mathcal{K} - \mathbf{\Lambda}\mathcal{M})\mathbf{\Phi} = \mathbf{0} \tag{2.5}$$

where $\mathcal{K}$ and $\mathcal{M}$ are the global stiffness and mass matrices, $\mathbf{\Lambda}$ is a diagonal matrix of eigenvalues, $\mathbf{\Phi}$ is the matrix of eigenvectors, and $\mathbf{0}$ is the zero vector. Vibrational modes are represented in the columns of $\mathbf{\Phi}$ as eigenvectors ϕ_n, and modal

frequencies are stored in $\mathbf{\Lambda}$ as eigenvalues ω_n^2. The derivation of Equation (2.5) from the undamped equation of motion is detailed in Section B.1.1.

While the stiffness matrix $\mathcal{K}$ is extensively studied in the literature, challenges persist in accurately defining the mass matrix $\mathcal{M}$ for soil-pile systems. These difficulties arise primarily from the complexity of quantifying the soil mass contributing to modal vibrations, which can lead to inaccuracies in analyses (Fitzgerald et al., 2019).

Furthermore, the application of small-strain stiffness models presents several challenges. The initial stiffness of the soil-pile system can change significantly after pile installation due to soil consolidation and disturbance, which modify the soil properties around the pile. Accurate parameter selection in these models is essential, as even minor deviations can influence predictions of dynamic response, impacting the estimation of modal properties—an important factor in SHM. By estimating suitable mass and stiffness matrices within small-strain models, it is possible to simulate small-strain vibrations, providing valuable insights into the actual state of the soil-pile system. When combined with model updating methods that align estimated modal responses with observed data, small-strain modelling becomes a powerful tool for identifying issues such as scour and soil degradation.

Model updating is a process that refines mass and stiffness matrices by matching numerical model responses with empirical data (Dezi et al., 2012; Prendergast et al., 2019; Wu et al., 2018) and which will be reviewed in Section 2.3. When applied in SHM, it facilitates the detection of structural damage by comparing a structure's frequency responses to baseline measurements (Domaneschi et al., 2013; OBrien & Malekjafarian, 2016). These methods are particularly useful for identifying geotechnical phenomena such as scour and gapping (Fitzgerald et al., 2019; Giordano et al., 2020). While numerical physics-based modelling provides valuable initial estimates of mass and stiffness matrices, the actual in situ behaviour of SPI systems can differ due to factors like soil degradation, structural wear, and changes in system dynamics over time (Darvishi-Alamouti et al., 2017; Ziegler et al., 2015). To address these effects, data from actual SPI systems must be integrated into model updating methods to refine the matrices and accurately extract parameters that reflect the real state of the system.

2.1.3 Embedded pile length

One property that is particularly important for SPI models is the accurate determination of foundation pile embedded length. This parameter is critical in SHM, where accurate modelling of geometrical properties is necessary for devel-

oping digital twins, which are consecutively used for damage detection and other monitoring applications. To address this need, numerous non-destructive methods have been developed in the literature to assist in determining pile length.

Early research primarily focused on applying stress-wave propagation techniques to timber piles. Holt et al. (1994) introduced a nondestructive testing method that utilised dispersive stress-wave propagation alongside specialised signal-processing techniques. By analysing bending waves generated through impact loading, their Short Kernel Method (SKM) enabled the estimation of pile length with an accuracy of approximately $\pm 10\%$. This approach demonstrated that guided waves could provide practical insights into both the pile embedment depth and its physical condition, laying the groundwork for further advancements in wave-based pile length estimation.

Subsequent theoretical research explored wave propagation in cylindrical piles embedded in soil. Hanifah (1999) derived a three-dimensional elasticity-based frequency equation for longitudinal guided waves in a cylindrical pile embedded in soil with varying stiffness and density. The study demonstrated that lower-order longitudinal modes, experience less attenuation and are therefore more easily induced, facilitating a straightforward interpretation of pile properties. These findings highlighted the potential of guided waves to capture subtle interactions between the pile and surrounding soil, shaping subsequent experimental and theoretical research in this area.

Building on these theoretical advancements, Chao (2002) expanded the guided wave approach to practical settings by integrating both laboratory and field tests. Using conventional impulse response tests and newly developed frequency-controlled tests on small-scale prototype piles, the research validated the applicability of three-dimensional guided wave theory to real-world conditions. By identifying bulk shear wave velocities and mode attributes, Chao's work demonstrated that guided wave interpretations could surpass traditional impulse response methods, enabling the detection of defects that would otherwise remain invisible to simpler time-domain analyses.

In parallel, further theoretical developments targeted various structural configurations and wave types. Wang (2004) investigated Rayleigh-Lamb waves in embedded plate-like structures, such as diaphragm walls, and flexural waves in solid cylindrical piles. The study established relationships between phase velocity, group velocity, and attenuation across a wide range of frequencies. These theoretical insights demonstrated that examining an extended frequency range could uncover smaller-scale defects and provide a more nuanced understanding of pile conditions, thereby enhancing the detection capabilities of wave-based methods.

Experimental testing came from Lynch Jr (2007), who developed two experimental methods to induce flexural waves in accessible portions of concrete piles. By comparing measured velocities and frequencies with theoretical values for flexural branches, the study validated guided wave propagation predictions for real piles under varying boundary conditions, ranging from traction-free to fully embedded states. Lynch's results highlighted the robustness of guided wave theory when properly implemented and interpreted, paving the way for more advanced, field-ready techniques.

More recently, Samu and Guddati (2019) proposed an advanced signal-processing and dispersion analysis technique to enhance estimation accuracy and practical applicability. By accounting for the inherent dispersion in wave propagation and reflections from the pile tip, EDAR provides a robust mapping from measured signals to embedded depth. This technique avoids the often unreliable time-domain peak-picking process for dispersive signals, instead delivering highly accurate depth estimates (within approximately 5% error) in controlled laboratory settings. However, initial field validations revealed that further refinements are required for broader applicability. In response, Samu and Guddati (2020) introduced a refined EDAR methodology. The study revealed that initial arrivals in field signals were dominated by transverse waves, while reflections were primarily governed by longitudinal waves due to differential attenuation in the soil. By carefully incorporating both wave types, the improved EDAR approach achieved accurate embedded depth estimation under field conditions. A typical configuration of the test and the experimental setup is shown in Figure 2.6

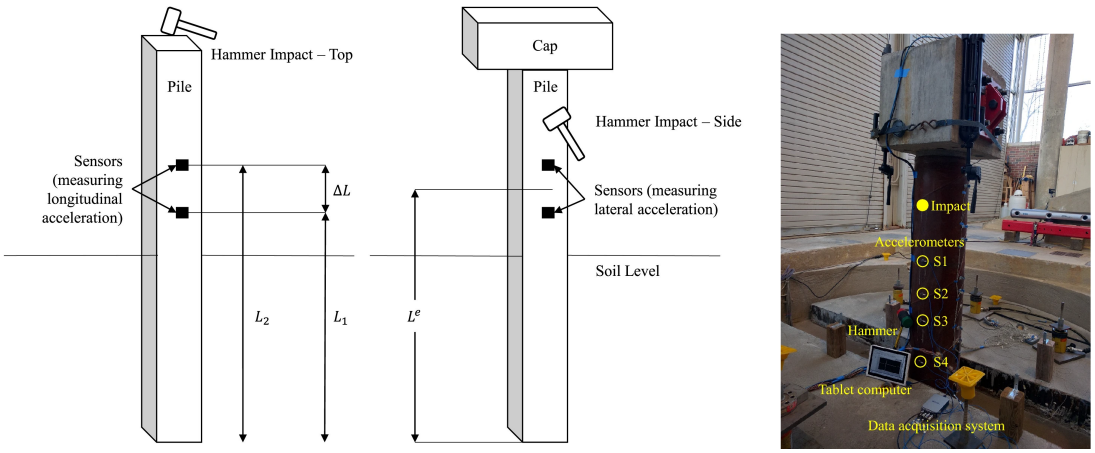

(a) (b)

Figure 2.6: (a): setup of pile for axial and lateral impact (Samu & Guddati, 2020), (b): experimental setup of concrete filled steel tube (Samu & Guddati, 2019)

Further advancements came from Cui et al. (2022), who integrated a three-dimensional guided wave model and a modified Ridders' root-searching algorithm

into the EDAR framework. By constructing a spectral element model of the cylindrical pile and analysing the phase difference of signals acquired from multiple sensors, Cui et al. achieved over 95% accuracy in pile length estimation. This approach utilised a broader frequency range and more sophisticated dispersion relationships, demonstrating that the integration of advanced modelling, numerical algorithms, and wave theory can significantly enhance reliability while minimising the need for multiple sensor configurations.

Wave-based methods for pile length estimation have advanced significantly, demonstrating high accuracy in controlled settings. By leveraging longitudinal and transverse wave interactions with advanced signal processing, they offer robust tools for assessing pile conditions. However, challenges such as unaddressed mobilised mass, the requirement for impact testing and the need for multiple receivers underscore the importance of developing hybrid frameworks that integrate operational data with numerical modelling approaches for improved SHM of SPI systems.

2.1.4 Pile scour

Scour is a complex erosional phenomenon involving the removal of seabed material caused by the action of flowing water. In the context of OWTs supported by monopile foundations, scour occurs when local flow accelerations and vortex formations around the pile induce localised sediment transport and removal (Briaud et al., 2005; Prendergast & Gavin, 2014). As seabed sediments erode, the effective embedment depth and lateral support provided by the surrounding soil are reduced. This loss of material and stiffness decreases the load capacity of the foundation, potentially compromising the stability and longevity of the OWT. With the increasing deployment of OWTs in marine environments globally, the need to understand, predict, and mitigate scour has grown substantially. A schematic representation of a vibration-based scour sensor is illustrated in Figure 2.7.

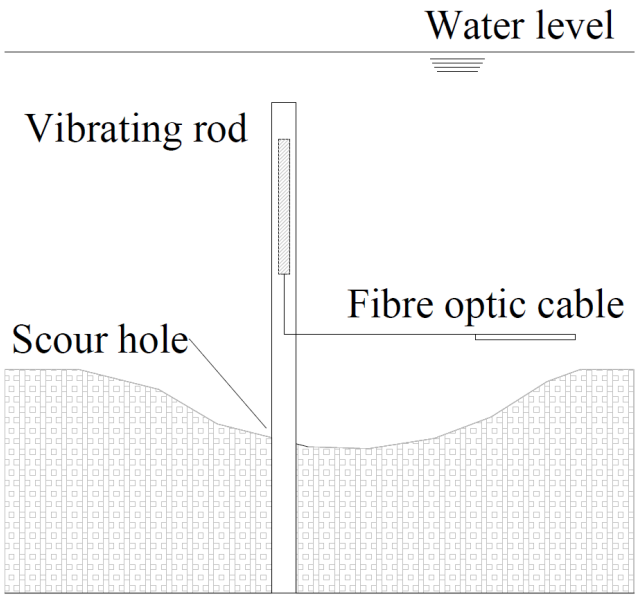

Figure 2.7: Schematic representation of scour sensor (Prendergast & Gavin, 2014)

Scour mechanisms in offshore environments are influenced by various factors, including currents, waves, tidal actions, and sediment properties. Unlike riverine conditions, where scour typically develops under relatively steady flow, marine scour is shaped by the more complex and variable hydrodynamic loading from combined waves and currents (Negro et al., 2014; Prendergast et al., 2018). While the presence of waves can sometimes reduce ultimate scour depths compared to current-only conditions (Sumer et al., 1992), the interaction remains highly site- and environment-dependent, introducing uncertainty in predicting scour depths. Furthermore, the backfilling and re-densification of eroded sediments under wave action can partially or fully restore the soil stiffness around the pile, adding another layer of complexity to scour characterisation (Prendergast et al., 2018; Sørensen & Ibsen, 2013).

A body of research has investigated the impacts of scour on marine structures, building on insights initially developed for bridges and other infrastructure (Foti & Sabia, 2011; Klinga & Alipour, 2015; Prendergast & Gavin, 2016; Prendergast et al., 2013). In the offshore wind sector, significant uncertainties remain regarding how scour affects soil properties such as stiffness, cyclic load response, lateral response, and long-term bearing capacity. Backfill material deposited into scour holes under wave action may exhibit altered stiffness characteristics, potentially restoring or even increasing stiffness relative to pre-scour conditions (Prendergast et al., 2018; Sørensen et al., 2010). Consequently, the precise nature of this soil-structure interaction remains an active area of research.

The complexities of scour prediction are compounded by site-specific condi-

tions, soil variability, and evolving seabed morphologies caused by seabed migration and seasonal changes (Matutano et al., 2013; Reale et al., 2021). Ongoing research has sought to reduce these uncertainties. For example, Li et al. (2020) and Chortis et al. (2020) examined how different scour hole geometries affect the lateral load-displacement behaviour and p–y curves for monopiles. Their findings highlight that not only the depth but also the shape and extent of the scour hole influence the effective stiffness and bearing capacity of the soil. Similarly, Wang et al. (2020) employed advanced numerical simulations to study scour effects on large-diameter monopiles, illustrating how nonlinearities in pile head displacements evolve with increasing scour depth.

Monopiles are highly sensitive to changes in boundary conditions that affect their embedded length and lateral support. As scour progresses, the free length of the pile above the supporting soil layer increases, reducing foundation stiffness and the natural frequencies of the OWT system. Studies by Prendergast et al. (2015) and Sørensen and Ibsen (2013) have demonstrated that scour can cause measurable decreases in the system's natural frequencies. This shift is particularly critical given the narrow operational frequency windows OWTs must maintain to avoid resonance with excitation frequencies from wind and waves (Figure 2.2). Changes in frequency due to scour are more pronounced in looser soils (Abhinav & Saha, 2017; Prendergast et al., 2015), making natural frequency shifts a key indicator in SHM frameworks. Furthermore, research has shown that higher vibration modes exhibit greater sensitivity to scour (Mayall et al., 2018; Prendergast et al., 2018), suggesting that a multi-modal assessment could enhance the detection of changes in foundation conditions.

Research has increasingly focused on leveraging changes in dynamic characteristics—such as shifts in natural frequencies and mode shapes—to detect and quantify scour-related damage. Building on principles initially developed in bridge engineering (Prendergast & Gavin, 2016; Prendergast et al., 2013), where vibration-based techniques have been used to detect scour by observing reductions in natural frequencies, similar methods are being adapted and validated for offshore monopile foundations. Mayall et al. (2018) emphasised the importance of understanding the interaction between scour depth, soil-foundation stiffness, and the dynamic response of OWTs. By developing an integrated framework that combines one-dimensional and three-dimensional FE modelling, experimental testing, and field monitoring, they demonstrated how scour alters the dynamic behaviour of turbine structures.

SHM strategies can benefit from coupling advanced numerical models with data-driven analysis to assess and monitor scour-induced frequency changes. Prob-

abilistic approaches, such as Monte Carlo simulations and spatially correlated soil profiles modeled using random field theory, provide a comprehensive understanding of the uncertainty inherent in scour predictions and the probable range of changes in natural frequencies and load-resisting capacities (Prendergast et al., 2018; Reale et al., 2021). Experimental and field data further help calibrate and validate these models, ensuring reliability. In practice, operators can use readily available vibration data from standard turbine instrumentation or dedicated monitoring systems to infer scour progression. A significant decrease in key natural frequencies or shifts in higher-mode frequencies beyond predefined thresholds can trigger maintenance interventions or adjustments in operational load management strategies.

As the offshore wind industry advances and turbine capacities increase, managing scour risk and its associated uncertainties becomes critical. There is a need for improved prediction methods and advanced SHM strategies that make use of OMA data to manage the challenges scour imposes on monopile foundations. These models use trusted physics-based modes coupled with operating vibrational data to estimate actual scour depth, rather than relying solely on natural frequency shifts to trigger interventions. By incorporating both natural frequencies and mode shapes, these models provide more reliable and robust predictions.

2.2 System identification

Identification of linear systems from the measured data forms an interdisciplinary research domain that integrates mathematical modelling, control systems, statistics, and signal processing. In structural engineering, these techniques—commonly referred to as modal identification—have gained significant attention for their ability to determine vibration modal properties such as natural frequencies, mode shapes and damping ratios, as well as to identify changes in structural vibration characteristics under extreme or operational conditions.

Advancements in data acquisition technologies, including low-cost sensors, fiber optic sensors, and wireless sensor networks, have significantly improved the monitoring of large and complex structural systems. Accurate vibration mode identification is essential for ensuring the safety and serviceability of structures subjected to dynamic loads such as wind, waves, and earthquakes. In the context of SPI, system identification is applied to vibration sensor data—such as accelerations, velocities, or strains—collected along the length of pile foundations. The primary objective is to extract modal parameters, including natural frequencies and mode shapes, through free vibration analysis. These identified modal proper-

ties serve as essential inputs for applications such as model updating and damage identification.

Vibration-based modal identification methods are generally categorised into two main approaches: frequency-domain methods and time-domain methods. While debates persist regarding their relative strengths and limitations, these approaches are theoretically equivalent (Pintelon & Schoukens, 2012). Therefore, the choice of identification method should be guided by practical considerations, including the expected structural characteristics (e.g., the density of closely spaced modes, the magnitude of damping ratios, or the presence of nonlinear behaviour), the specific objectives of the analysis (e.g., achieving a complete and accurate representation of the modal model or focusing on a subset of modes critical to the structure's performance), and the nature and quality of the available data (e.g., noise levels, sampling rates, or data completeness) (Aktan et al., 1997; Maia & Silva, 2001).

System identification methods can also be classified as either deterministic or stochastic. Deterministic methods require full set of inputs and outputs and assume noise-free data. In contrast, stochastic methods are particularly useful in cases where the structure is excited by unmeasurable or unknown forces, such as ambient vibrations, and only output measurements such as accelerations are available. These methods operate under the assumption that the input is a realisation of a stochastic process, often modelled as ambient noise. The choice between deterministic and stochastic methods depends on the nature of the excitation, the available data, and the specific requirements of the system under study (Peeters, 2000).

In this literature review, an overview of both frequency-domain and time-domain methods is provided, discussing their historical development, key techniques, and applications in structural engineering.

2.2.1 Frequency-domain methods

Frequency-domain methods have been widely used in structural engineering owing to their algorithmic straightforwardness and robustness. These approaches analyse the spectrum plots of structures subjected to known or unknown excitations (Ghanem & Shinozuka, 1995; Pintelon et al., 1994). The strengths of frequency-domain methods include their ability to perform partial modelling within limited frequency bands, effective noise reduction, simple merging of data from different experiments, and the elimination of the need for initial model estimates (Ghanem & Shinozuka, 1995; Pintelon et al., 1994).

Peak picking (PP)

One of the earliest and simplest frequency-domain methods is the peak picking method, which identifies natural frequencies as peaks in the amplitude of spectrum plots such as the frequency response function (FRF) or power spectral density (PSD) functions (Bendat & Piersol, 1993; Bishop & Gladwell, 1963). This method is widely used in civil engineering due to its simplicity of implementation and computational efficiency, as it primarily relies on the fast Fourier transform (FFT) (Felber, 1994). The core process involves locating eigenfrequencies by detecting peaks in the spectrum plot. The FRF matrix $\mathbf{H}(\omega) = \mathcal{F}(\mathbf{H}(t))$ is the Fourier transform of the impulse response function and it is described in Equation (2.6) by Peeters and Ventura (2003):

$$\mathbf{H}(j\omega) = \sum_{i=1}^{n_m} \frac{1}{j\omega - \lambda_i} \phi_i \mathbf{l}_i^T, \tag{2.6}$$

where ω is the circular frequency (rad/s), n_m is the number of modes, $\phi_i \in \mathbb{C}^l$ are the mode shapes, $\mathbf{l}_i^T \in \mathbb{C}^{n_i}$ are the modal participation vectors, l is the number of outputs, n_i is the number of inputs, and λ_i are the continuous-time eigenvalues. The eigenvalues λ_i are directly related to the eigenfrequencies ω_i and the damping ratios ξ_i in (2.7)

$$\lambda_i, \lambda_i^* = -\xi_i \omega_i \pm j\omega_i \sqrt{1 - \xi_i^2}. \tag{2.7}$$

When damping is small and eigenfrequencies are sufficiently distinct, the FRFs exhibit a local maximum around the eigenfrequency ω_i and can be approximated as (2.8)

$$\mathbf{H}(j\omega) \approx \frac{1}{\xi_i \omega_i} \phi_i \mathbf{l}_i^T, \tag{2.8}$$

from which the mode shapes and modal participation factors can be identified once the eigenfrequency and damping ratio are identified.

In the case where the structure is weakly damped with distinct natural frequencies and proportional damping, the half power bandwidth method can be employed to estimate the damping ratio in Equation (2.9) (Reynders, 2012):

$$\xi_j \approx \frac{f_{2j} - f_{1j}}{f_j}, \tag{2.9}$$

where f_{1j} and f_{2j} are the closest frequencies on the left and right to f_i.

To improve peak identification accuracy, several refinements have been proposed. Inspecting the coherence function between two channels can assist in selecting eigenfrequencies, as coherence approaches one at resonance frequencies due to a high signal-to-noise ratio (Bendat & Piersol, 1993). Similarly, analysing the phase angles of the cross spectra helps confirm the presence of real modes, where phase angles are expected to be either 0° or 180° at resonance. Felber (1994) implemented the peak picking method by computing an averaged normalised PSD from the diagonal elements of the spectrum matrix, offering a comprehensive view of the eigenfrequencies. This method also allows the identification of mode types, such as torsion or bending, by adding or subtracting signals from symmetric points of the structure. Furthermore, Felber's output-only approach demonstrated that selecting a suitable reference sensor enables efficient computation of spectra between all sensors and the reference directly from time-domain data, reducing computational effort.

Despite its advantages, the peak picking method relies on the assumptions of low damping and well-separated modes (Peeters, 2000). Nevertheless, it remains popular in civil engineering applications due to its ease of implementation and computational efficiency. The method has been successfully applied to a wide range of structures, including bridges and pile foundations (Ioakim & Prendergast, 2024; Prendergast et al., 2019).

Complex mode indicator function (CMIF)

To enhance modal identification beyond the capabilities of peak picking, the complex mode indicator function (CMIF) and frequency domain decomposition (FDD) methods were developed (Brincker et al., 2001b; Prevosto, 1982). Both techniques employ singular value decomposition (SVD) of spectral matrices, such as the FRF or PSD matrices in Equation (2.10), to overcome limitations of earlier methods, including the presence of multiple closely spaced modes (Reynders, 2012). Specifically, the CMIF method applies SVD to the FRF matrix at each spectral line (peak), with the resulting eigenvalues representing the squares of the singular values (Shih et al., 1988). Peaks in the CMIF correspond to the proximity of the frequency axis to an eigenvalue, indicating potential modal frequencies and providing a measure of the physical magnitude of each mode and its damped natural frequency (Shih et al., 1988). Similarly, the FDD method adapts CMIF principles by applying SVD directly to the PSD matrix, offering a computationally efficient approach to extract modal parameters in stochastic environments (Reynders, 2012) in Equation (2.10) by Peeters and Ventura (2003).

$$\mathbf{S}_y(j\omega) = U(j\omega)\Sigma(j\omega)U^T(j\omega), \tag{2.10}$$

where $U \in \mathbb{C}^{l\times l}$ represents a complex matrix whose columns are the singular vectors. The diagonal matrix $\Sigma \in \mathbb{R}^{l\times l}$ contains the real positive singular values arranged in descending order.

Building upon CMIF, the FDD method (Brincker et al., 2001a, 2001b) operates in an output-only context by utilising PSD functions instead of FRFs. By applying SVD to the PSD matrix, FDD effectively isolates closely spaced modes that are difficult to resolve with simpler methods. The singular values highlight significant modal contributions, with peaks corresponding to distinct modes. FDD was proved to identify harmonic components and provide a clear separation of the response spectra initially into single degree-of-freedom (SDOF) systems, even under noisy conditions (Brincker et al., 2001b). However, accurate association of singular value peaks with specific modal frequencies often requires user interaction, particularly in complex or noisy datasets (Döhler, 2011; Gattulli, 2016).

Recent advancements have enhanced FDD's robustness and accuracy in multi-dataset output-only modal analysis. Amador and Brincker (2021) introduced two new scaling approaches to merge mode shape components from different datasets. The first approach re-scales the PSDs before constructing a global PSD matrix, followed by FDD application. The second approach directly forms the global PSD matrix and subsequently re-scales mode shape components using reference singular vectors. These methods streamline the extraction of global mode shapes, increasing FDD's effectiveness in scenarios with multiple datasets and complex structural systems.

Prediction error methods (PEM) and maximum likelihood

Prediction error methods (PEM) and maximum likelihood approaches are iterative, optimisation-based techniques designed to minimise the discrepancy between predicted and measured system outputs (Åström & Bohlin, 1965; Åström & Eykhoff, 1971). PEM operates by employing a predictor filter to estimate outputs based on past inputs and outputs, minimising the prediction error and providing parameter estimates that are statistically consistent and efficient under appropriate conditions (Ljung, 1999). PEM is an adaptable framework that encompasses several special cases, including linear least squares regression, maximum likelihood identification, and Bayesian inference (Reynders, 2012). These methods leverage statistical and numerical optimisation tools, enabling robust system identification across diverse modelling contexts.

PEM and maximum likelihood methods are not restricted to frequency-domain systems. Recursive PEM algorithms enable real-time updates of parameter estimates, making them particularly suitable for identifying time-varying systems (Döhler, 2011). These methods are valued for their flexibility, theoretical robustness, and ability to deliver precise parameter estimates in dynamic environments. However, the iterative optimisation process involved in PEM and maximum likelihood methods can be computationally intensive, especially when applied to complex or large-scale systems. Their performance is highly dependent on the quality of the input data and the chosen model structure. Challenges such as ensuring convergence reliability and avoiding local minima require careful consideration during implementation (Guillaume et al., 1998).

The least-squares complex frequency-domain (LSCF) method offers a reliable approach to modal parameter estimation by fitting a transfer function model to measured FRFs using a least-squares criterion (Guillaume et al., 1998; Van der Auweraer et al., 2001). The method is effective in separating closely spaced modes and provides stable identification of system poles across varying system orders, visualised through stabilisation diagrams for distinguishing physical and spurious poles (Huang et al., 2017; Van der Auweraer et al., 2001). This stability makes LSCF well-suited for challenging estimation problems, including mistuned bladed rotor systems, where it has demonstrated high accuracy in identifying eigenvalues from both computational and experimental forced response data (Huang et al., 2017).

The PolyMAX algorithm, an extension of the LSCF method, enhances modal analysis by addressing challenges such as closely spaced modes and multiple-input systems (Guillaume et al., 2003; Peeters et al., 2004). By fitting a right matrix fraction description (RMFD) model to FRFs, PolyMAX produces fast-stabilising stabilisation diagrams and improves mode separation, making it particularly effective for structures with closely spaced natural frequencies (Peeters et al., 2004). This method has demonstrated advantages in stability and accuracy, particularly for high-order or highly damped systems with large modal overlap, enabling its application to complex estimation cases (Guillaume et al., 2003; Peeters et al., 2004).

PolyMAX can also be adapted for output-only modal analysis. For instance, Devriendt et al. (2010) generalised transmissibility measurements to a multivariable context, showing how combining measurements under varying loading conditions can provide accurate estimates of modal parameters. However, limitations remain, such as the potential underestimation of damping ratios (Döhler, 2011).

2.2.2 Time-domain methods

Time-domain methods are widely employed in experimental modal analysis, especially in scenarios where only output measurements are available, and input forces are unknown or impractical to measure. By operating directly on time-series data, these methods offer advantages such as eliminating spectral leakage biases, improving modal uncoupling, and providing superior spectral resolution (Gattulli, 2016; Peeters & De Roeck, 1999).

Ibrahim time domain (ITD)

The Ibrahim time domain (ITD) method (Ibrahim, Mikulcik, et al., 1976) identifies modal parameters by analysing free vibration response data. The method constructs matrices from response measurements at multiple time steps to extract the system's eigenvalues and mode shapes, assuming that all modes are adequately excited. In its original formulation, the ITD method requires that the number of sensors be at least half the system order to ensure all modes are captured in the response data. This constraint is particularly useful for systems with closely spaced natural frequencies and heavy damping, where some frequency-domain methods often struggle due to their reliance on SDOF approximations (Ibrahim, Mikulcik, et al., 1976). Despite its strengths, the ITD method has certain limitations. The requirement for a specific sensor-to-system order ratio can be restrictive for large and complex structures. Additionally, the method assumes that all modes are sufficiently excited and accurately captured, which may not hold true for modes that are weakly excited, heavily damped, or inadequately represented due to sensor placement. These factors can compromise the accuracy of modal parameter estimation, particularly in practical scenarios involving large or complex systems.

Random decrement (RD)

The random decrement (RD) technique, introduced by Cole (1968), is a widely used time-domain method for extracting free decay responses from random vibration data. It transforms complex system responses into signatures resembling free vibrations, enabling modal parameter estimation. Originally developed for SDOF systems, RD operates by averaging response segments that meet specific triggering conditions, effectively reducing noise and enhancing modal identifiability. This method simplifies the interpretation of random vibrations, even in challenging conditions such as combined buffet and flutter tests (Cole, 1968). However, potential biases and the need to satisfy underlying assumptions must be carefully addressed

to ensure reliable parameter estimation.

Eigensystem realisation algorithm (ERA)

The eigensystem realisation algorithm (ERA) (Juang & Pappa, 1985) is a widely used identification method in modal analysis, initially developed for impulse response data. ERA constructs a Hankel matrix from the system's impulse response data and applies SVD to extract the dominant dynamic modes. This process enables ERA to construct a balanced state-space model, minimising vibrational energy loss during modal reduction and ensuring accurate identification of modal parameters. Later, the algorithm was extended to include data correlations (ERA/DC), which uses correlations of response data instead of direct response values, significantly reducing noise-induced bias errors without requiring model overspecification (Juang et al., 1988).

To adapt ERA for output-only applications, the natural excitation technique (NExT) (James et al., 1995) was introduced. NExT treats cross-correlation functions between output measurements as equivalent to free decay responses, allowing ERA to extract modal parameters from ambient vibration data. This enables the identification of modal parameters under operating conditions, such as wind turbines, where damping characteristics vary significantly.

The combination of ERA and its extensions (NExT, ERA/DC) makes it a robust tool for modal analysis, applicable across a range of structural and environmental conditions. In the NExT/ERA framework, a reference signal is selected, and cross-correlation functions with other measurements are computed. These cross-correlation functions serve as the system's response estimates, which are then arranged into a Hankel matrix. Applying Singular SVD to this matrix extracts the system's dominant dynamic characteristics. Solving the resulting eigenproblem yields the natural frequencies and mode shapes of the structure (Döhler, 2011).

Recent advancements include an improved stabilisation-diagram technique that integrates Monte Carlo sampling, fuzzy C-means clustering, and sifting manipulations to eliminate spurious modes. This method enables the ERA to identify modal parameters automatically with higher accuracy and efficiency, making it suitable for real-time structural health monitoring (Feng et al., 2023).

Auto-regressive (AR)

Auto-regressive (AR) methods, including ARMA (auto-regressive moving average) and ARMAX (auto-regressive moving average with exogenous inputs) models, are

fundamental tools for identifying linear time-invariant (LTI) systems. These models describe the system's output as a function of past outputs, inputs, and noise terms, providing a straightforward framework for capturing structural dynamics (Gattulli, 2016; Peeters, 2000).

ARMAX models extend ARMA by incorporating input effects alongside noise, making them particularly suited for scenarios where both deterministic and stochastic dynamics interact. These models are expressed in Equation (2.11) by Döhler (2011):

$$\mathbf{y}_k = \sum_{i=1}^{p} \mathbf{A}_i \mathbf{y}_{k-i} + \sum_{i=0}^{q} \mathbf{B}_i \mathbf{e}_{k-i} + \sum_{i=0}^{s} \mathbf{C}_i \mathbf{u}_{k-i}, \tag{2.11}$$

where $\mathbf{y}_k$ is the system output, $\mathbf{u}_k$ the input, $\mathbf{e}_k$ the noise term, and $\mathbf{A}_i, \mathbf{B}_i, \mathbf{C}_i$ the model coefficients related to the outputs, the noise and the external inputs respectively. ARX models, a simplified subset of ARMAX, omit the moving average noise component, making them easier to estimate using linear least squares methods (Reynders, 2012). However, this simplicity comes at the cost of reduced accuracy in capturing unmeasured inputs or noisy data.

Methods such as Instrumental Variables (IV) which account for noise correlations by leveraging external instruments have been developed to address practical challenges in estimating AR parameters, such as model order selection and bias reduction (Söderström & Stoica, 1981).

Due to their computational efficiency and versatility in both time and frequency domains, ARX and ARMA models remain widely used for system identification across various applications. Recent literature demonstrates applications of AR methods in civil structural health monitoring. For example, a damage identification approach leverages continuously extracted time series of AR coefficients from strain data under moving train loads, using these coefficients as highly sensitive damage features (Anastasia et al., 2023). These advancements underscore the versatility of AR-based methods in integrating system identification with damage detection, under complex loading conditions.

Subspace identification

Subspace identification methods were formalised into a unified framework in the 1990s by Van Overschee and De Moor (1996) and Viberg (1995), building on foundational principles shared with realisation techniques (e.g., ERA) and IV methods. Compared to maximum likelihood approaches, subspace methods offer greater robustness and computational efficiency, making them well-suited for

system identification (Reynders, 2012). These methods excel in identifying LTI systems by directly extracting state-space models from input-output or output-only data. They apply numerical techniques such as QR decomposition and SVD to the response data, along with statistical properties like covariances and spectral estimates, to extract modal parameters (Van Overschee & De Moor, 1996).

The state-space representation provides a mathematical framework for these methods, described by:

$$\begin{aligned} \mathbf{x}_{k+1} &= \mathbf{A}\mathbf{x}_k + \mathbf{B}\mathbf{u}_k + \mathbf{w}_k, \\ \mathbf{y}_k &= \mathbf{C}\mathbf{x}_k + \mathbf{D}\mathbf{u}_k + \mathbf{v}_k \end{aligned} \tag{B.26}$$

where $\mathbf{x}_k \in \mathbb{R}^n$ is the state vector, $\mathbf{u}_k \in \mathbb{R}^m$ the input vector, $\mathbf{y}_k \in \mathbb{R}^r$ the output vector, and $\mathbf{w}_k$ and $\mathbf{v}_k$ represent process and measurement noise, respectively (Döhler, 2011). In deterministic cases where $\mathbf{u}_k$ are known and $\mathbf{w}_k$, $\mathbf{v}_k$ are equal to zero, subspace methods identify the system matrices $\mathbf{A}$ and $\mathbf{C}$ directly from data. In purely stochastic scenarios, where inputs are unknown, the algorithms rely on correlations within the measured output data. A representation of the different variations of the State-Space formulation can be viewed in Figure 2.8.

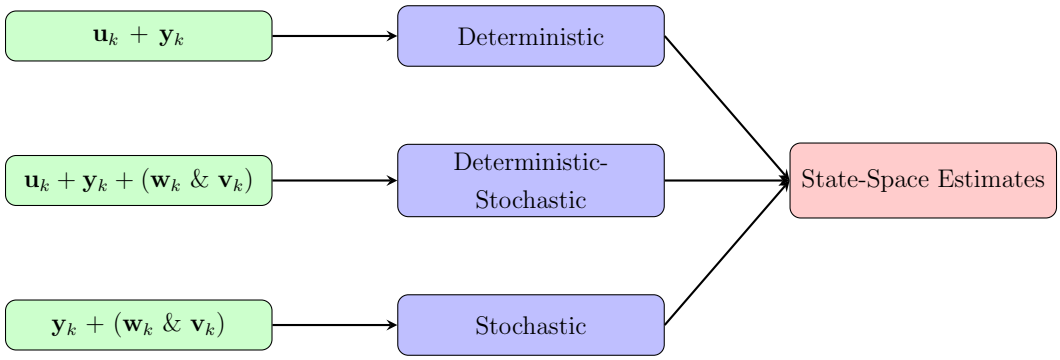

Figure 2.8: Representation of state-space variations

Many scenarios, such as OMA, involve unknown or poorly determined input loads, necessitating output-only subspace identification techniques where only the $\mathbf{y}_k$ is available and the input matrices $\mathbf{B}$ and $\mathbf{D}$ are assumed to be zero. In cases where partial input data $\mathbf{u}_k$ is observed, combined deterministic-stochastic subspace identification algorithms can be applied. For purely output-only scenarios, stochastic subspace identification (SSI) methods are widely used, with two main algorithms being: covariance-driven (SSI-COV) and data-driven (SSI-DATA).

Deterministic-stochastic subspace identification methods extend the applicability of subspace techniques to systems where both input data and noise are present. These algorithms balance robustness and efficiency, with extensions in-

corporating IV to address challenges such as biases introduced by colored noise (Verhaegen, 1993). Subspace algorithms such as the Past Input Multi-variable Output Error State Space (PI-MOESP) method (Verahegen & Dewilde, 1992; Verhaegen, 1993; Verhaegen & Dewilde, 1992) and Canonical Variate Analysis (CVA) project the input-output data into Hankel matrices to isolate observability matrices. Applying SVD to these Hankel matrices enables the extraction of dominant system modes while filtering out noise. PI-MOESP, in particlular, focuses on the deterministic subsystem by projecting data onto the row space of available inputs, ensuring robust identification even with uncorrelated stochastic outputs (Reynders, 2012). This characteristic makes it highly effective for systems with measurable inputs and noise. Studies, such as Bauer's survey (Bauer, 2005), have further analysed the statistical properties of subspace methods, providing insights into their asymptotic behaviour and identifying open research questions for improving accuracy and reliability.

In SSI-COV, the identification process begins with estimating covariance functions of the measured outputs. A block Hankel matrix is constructed from these covariances, and system matrices are extracted using SVD (Van Overschee & De Moor, 1996). SSI-COV is robust in handling noise and unmeasured inputs by modelling them as stochastic processes, making it particularly suitable for output-only modal analysis (Peeters, 2000). Under specific assumptions about statistical consistency and noise characteristics (Reynders, 2012, Assumptions 5.1–5.3), SSI-COV provides robust and asymptotic estimates, ensuring accurate identification of system dynamics (Döhler, 2011).

In SSI-DATA, raw time-series data is directly used to construct the block Hankel matrix, bypassing the intermediate step of covariance estimation. This approach projects the row space of future outputs onto the row space of past outputs, removing deterministic state-space dynamics while reducing the influence of uncorrelated noise (Van Overschee & De Moor, 1996) under specific assumptions(Reynders, 2012: Assumption 5.3). SSI-DATA is computationally more efficient than SSI-COV, particularly for large datasets, making it advantageous in practical engineering applications (Peeters & De Roeck, 1999). Advancements in SSI-DATA address challenges such as positive realness using techniques like Tikhonov regularisation, improving the robustness and accuracy of system matrix estimates (Goethals, 2005; Goethals et al., 2003).

Both SSI-COV and SSI-DATA methods rely on a state-space model of the

form:

$$\begin{aligned} \mathbf{x}_{k+1} &= \mathbf{A}\mathbf{x}_k + \mathbf{w}_k, \\ \mathbf{y}_k &= \mathbf{C}\mathbf{x}_k + \mathbf{v}_k \end{aligned} \tag{B.28}$$

where $\mathbf{x}_k$ is the state vector, $\mathbf{y}_k$ the output vector, and $\mathbf{w}_k$ and $\mathbf{v}_k$ represent process and measurement noise, respectively (Döhler, 2011). The goal is to estimate the system matrices $\mathbf{A}$ and $\mathbf{C}$, which characterise the dynamics of the observed system.

SSI-COV and SSI-Data, which operate in an output-only setting, are particularly well-suited for civil engineering applications where controlled excitations are often impractical (Peeters & De Roeck, 1999). Notably, SSI algorithms have been proven consistent under conditions of nonstationary noise and varying system dynamics (Benveniste & Mevel, 2007). Further developments, such as reference-based SSI methods (Peeters & De Roeck, 1999; Reynders, 2012), make use of overlapping reference sensors to improve computational efficiency and global mode shape estimation. A pseudocde for SSI-COV is shown in Algorithm 1.

Literature has focused on enhancing the robustness and accuracy of SSI methods. For instance, advancements in stabilisation diagram techniques have been proposed to automate the identification of true system modes and eliminate spurious ones (Brincker et al., 2000). SSI methods have been successfully applied in various engineering fields. In civil engineering, they are widely used for modal analysis and SHM (Greś et al., 2021d, 2022b; Reynders, 2021).

Greś et al. (2023) proposed a statistical methodology for model order selection in covariance-driven subspace identification. This method actively selects the dynamic signal subspace by statistically analysing the eigenvalue condition numbers of the output covariance Hankel matrix. By separating the signal subspace from the noise subspace using user-defined thresholds, the framework enhances robustness in identifying system dynamics. The methodology demonstrated improved damage detection on a medium-size wind turbine blade by increasing sensitivity to small damage and reducing false alarms. In another study, Greś et al. (2021c) addressed challenges in subspace identification caused by periodic inputs from rotating machinery, such as those present in wind turbines.

Subspace algorithms have been successfully applied to identify state-space models in systems ranging from industrial processes to complex civil engineering structures (Van Overschee & De Moor, 1996). Moreover, their ability to integrate frequency- and time-domain data provides flexibility for diverse identification problems. Despite these strengths, challenges remain, particularly SSI methods face challenges such as determining the optimal model order and ensuring

adequate sensor placement (Döhler, 2011). The accuracy of the identified models heavily depends on data quality, presence of noise and the appropriateness of the chosen parameters. Furthermore, SSI-COV may be computationally intensive due to covariance estimation, while SSI-DATA requires careful handling of data to prevent bias from noise and unmeasured inputs. Research now has turned to the UQ within the SSI frameworks which will be reviewed in Section 2.4.

Peeters and Ventura (2003) conducted a benchmark study to evaluate various system identification methods for extracting the dynamic properties of bridges. The Z24-Bridge, a three-span reinforced concrete bridge located in Switzerland, served as the case study. This structure was extensively monitored under various environmental conditions before being demolished, making it an ideal benchmark for modal analysis.

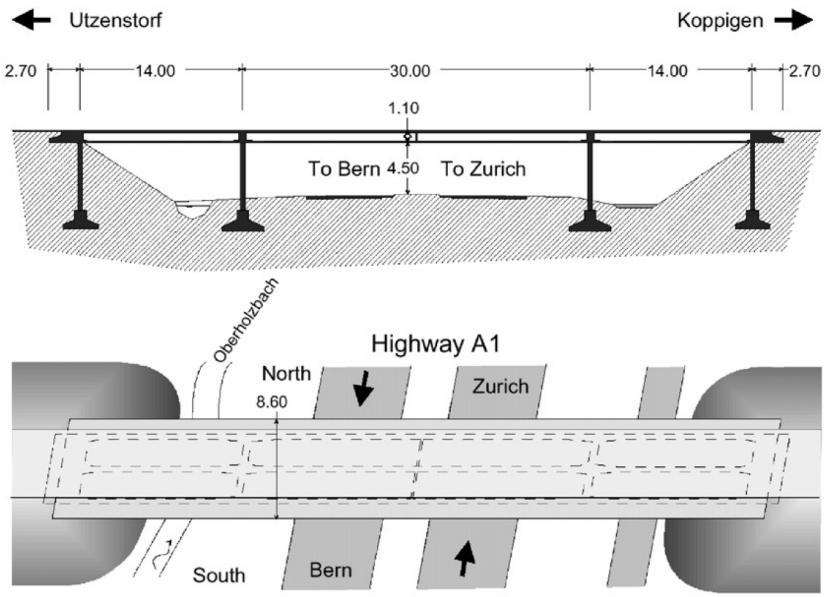

Figure 2.9: Longitudinal section and top view of the Z24-Bridge (Krämer et al., 1999).

The study engaged excitation techniques, including ambient, free, and forced vibrations. The study applied a diverse set of system identification methods ranging from traditional techniques like the Peak-Picking and Complex Mode Indicator Function to more advanced approaches such as SSI-COV and SSI-DATA. The study was conducted by six different research teams and aimed to assess the relative performance of the system identification methods in accurately identifying modal parameters such as natural frequencies, damping ratios, and mode shapes.

One key finding was the consistent reliability of subspace-based methods (SSI-COV and SSI-DATA) in accurately capturing dynamic properties across all excitation types. These methods were particularly robust in handling noisy data and

closely spaced modes. Additionally, stabilisation diagrams allowed distinction of physical modes from spurious modes effectively. Furthermore, the use of SVD enhanced the accuracy and computational efficiency of these methods, illustrating their suitability to large-scale civil engineering structures.

Simpler methods, like Peak-Picking and CMIF, were found to be more sensitive to noise and required significant manual intervention, particularly in scenarios involving ambient excitation. While these methods offered quick insights, their limitations became evident in scenarios requiring high precision or dealing with overlapping modes.

Another critical aspect of the study was the comparison of excitation techniques. Forced vibration tests, such as shaker and drop-weight impacts, provided clearer input-output relationships, enhancing the accuracy of traditional methods. However, ambient excitation data, often encountered in operational conditions, demonstrated the necessity of advanced techniques like SSI for reliable system identification without the need for controlled inputs.

The tables presented below illustrate the comparative results of eigenfrequencies, damping ratios, and MAC values extracted by various identification methods and research teams using shaker and ambient data. Tables 2.1 and 2.2 report the relative eigenfrequencies obtained from shaker and ambient data, highlighting the consistency and variability across different methods, including PP, CMIF, refined frequency domain polyreference (RFP), and subspace approaches. Similarly, Tables 2.3 and 2.4 detail the relative damping ratios, emphasising the sensitivity of methods like SUBSP 2 to certain modes and the stability of results for CMIF and PP approaches. Finally, Table 2.5 compares the MAC values between mode shapes derived from shaker and ambient data, providing insights into the accuracy of mode shape correlations across methods.

Table 2.1: Relative eigenfrequencies extracted by different identification methods and research teams from the shaker data.

Method	**Mode 1**	**Mode 2**	**Mode 3**	**Mode 4**	**Mode 5**
PP 3	1.000	1.000	1.000	1.000	1.008
CMIF 2	0.992	0.996	0.991	-	1.008
RFP 1	1.000	1.000	1.003	1.000	1.000
SUBSP 2	0.994	1.033	1.005	0.990	1.016
SUBSP 6	0.994	1.002	0.996	1.000	0.991

Table 2.2: Relative eigenfrequencies extracted by different identification methods and research teams from the ambient data.

Method	**Mode 1**	**Mode 2**	**Mode 3**	**Mode 4**	**Mode 5**
PP 1	1.000	1.000	1.000	1.000	0.984
CMIF 2	0.998	0.998	1.006	1.000	1.016
RFP 1	1.000	1.000	0.997	-	-
SUBSP 2	1.000	1.002	1.003	-	0.992
SUBSP 6	0.997	1.002	0.999	1.000	0.992

Table 2.3: Relative damping ratios extracted by different identification methods and research teams from the shaker data.

Method	**Mode 1**	**Mode 2**	**Mode 3**	**Mode 4**	**Mode 5**
PP 3	-	-	-	-	-
CMIF 2	1.004	1.355	1.881	-	1.637
RFP 1	0.877	0.273	0.428	0.672	0.896
SUBSP 2	1.228	4.94	0.673	1.052	1.218
SUBSP 6	1.208	1.000	1.159	1.140	0.887

Table 2.4: Relative damping ratios extracted by different identification methods and research teams from the ambient data.

Method	**Mode 1**	**Mode 2**	**Mode 3**	**Mode 4**	**Mode 5**
PP 1	-	-	-	-	-
CMIF 2	0.889	1.076	1.376	1.208	2.416
RFP 1	0.777	0.861	0.674	-	-
SUBSP 2	1.104	2.284	1.451	-	0.964
SUBSP 6	1.348	1.067	1.095	1.151	1.189

Table 2.5: MAC values between mode shapes extracted from shaker data and ambient data.

Method	**Mode 1**	**Mode 2**	**Mode 3**	**Mode 4**	**Mode 5**
RFP-PP 1	0.993	0.882	0.801	-	0.698
RFP 1	0.962	0.846	0.469	-	-
CMIF 2	0.983	0.964	0.891	-	-
SUBSP 6	1.000	1.000	0.956	0.837	0.948
SUBSP 7	1.000	1.000	0.912	0.886	0.880

Tables 2.1 and 2.2 indicate that most methods provide consistent eigenfrequency estimates across the shaker and ambient data, with minor deviations observed in SUBSP 2 and CMIF 2 for certain modes. Damping ratios, shown in Tables 2.3 and 2.4, exhibit greater variability across methods, particularly for SUBSP 2, which shows high sensitivity in a specific mode.

Finally, Table 2.5 presents the MAC values between mode shapes extracted from shaker and ambient data, with SUBSP methods achieving the highest correlation, indicating strong consistency across excitation sources. In contrast, RFP-based methods show lower MAC values, especially for higher modes, reflecting challenges in capturing mode shape consistency. Overall, the results suggest that subspace-based methods, particularly SUBSP 6 and 7, demonstrate robust performance in capturing modal properties across different excitation scenarios, while methods like CMIF exhibit variability in damping ratio estimation and mode shape consistency. These findings underscore the importance of selecting appropriate identification techniques based on the target properties and operational conditions.

Overall, the study highlighted the advantages of subspace-based methods for SHM and dynamic property identification in large-scale civil structures. It also underscored the importance of proper excitation and data processing techniques, particularly for methods that rely on ambient vibrations. The benchmark findings reinforced the need for robust identification frameworks in bridge monitoring and paved the way for adopting subspace methods in similar applications.

Algorithm 1 Covariance-Driven SSI for Modal Parameter Estimation (SSI-COV)

Require: Output data matrix $\mathbf{y} \in \mathbb{R}^{N \times r}$, block size p, block size q, maximum model order $n_{\max}$, sampling interval Δt

Ensure: Identified frequencies, damping ratios, and mode shapes $\{f_i,\, \xi_i,\, \phi_i\}_{i=0}^{n_{\max}}$

Step 1: Form Covariance Hankel Matrices. Use the measured output $\mathbf{y}$ to form a block covariance (Hankel) matrix $\mathbf{T}$.

Step 2: Perform SVD on T.

$$[U, S, V^T] \;=\; \mathrm{SVD}(\mathbf{T}), \quad U_1 \;=\; U[:,\, 0{:}n_{\max}].$$

Step 3: Construct Observability Matrix.

$$\mathbf{O} = U_1 \sqrt{S[0{:}n_{\max},\, 0{:}n_{\max}]}, \quad \mathbf{C} = \mathbf{O}[0{:}r,\, :].$$

Step 4: Partition O into Shifted Blocks.

$$\mathbf{G}_{\mathrm{up}} = \mathbf{O}[0{:}(pr),\, :], \quad \mathbf{G}_{\mathrm{dn}} = \mathbf{O}[r{:}(qr),\, :].$$

Step 5: Identify System Matrix A.

$$\mathbf{A} = \mathbf{G}_{\mathrm{up}}^{\dagger}\, \mathbf{G}_{\mathrm{dn}}.$$

Step 6: Compute Continuous-Time Poles and Modal Parameters.

$$\mathbf{A}\,\mathbf{v}_i = \lambda_i \mathbf{v}_i, \quad \nu_i = \frac{\ln(\lambda_i)}{\Delta t}, \quad f_i = \frac{\sqrt{\mathrm{Re}(\nu_i)^2 + \mathrm{Im}(\nu_i)^2}}{2\pi},$$

$$\xi_i = \frac{-\,\mathrm{Re}(\nu_i)}{\sqrt{\mathrm{Re}(\nu_i)^2 + \mathrm{Im}(\nu_i)^2}} \times 100\%, \quad \phi_i = \mathbf{C}\,\mathbf{v}_i.$$

Step 7: Return Modal Parameters. Return $\{f_i,\, \xi_i,\, \phi_i\}_{i=0}^{n_{\max}}$.

2.3 Model updating methods

Physics-based models such as those reviewed in 2.1 for SPI are essential for simulating complex systems that cannot be easily described analytically. In structural engineering, these models are used to analyse forces, displacements, and vibration responses under various loading conditions, including operational, wind and wave loads. However, the accuracy of these models is often limited by simplifying assumptions, unknown system properties (e.g., material or geometric characteristics), structural damage and uncertain boundary conditions can introduce

significant errors.

To address these issues, model updating methods also known as finite element model updating (FEMU), parameter estimation or parameter identification techniques—have been developed (Friswell & Mottershead, 1995; Mottershead & Friswell, 1993). These techniques aim to reconstruct or calibrate unknown system properties using observed system behaviour, thereby improving the predictive capability of the numerical models towards the actual expected behaviour. Essentially, model updating methods are designed to address discrepancies between the predicted behaviour of physics-based models and the observed behaviour of real systems by calibrating model parameters using data from vibration tests on actual structures. This process typically involves solving an inverse problem to adjust some or all system matrices, such as mass, stiffness, and damping (Dhandole & Modak, 2010). Once updated, these models can serve various purposes, including structural design support, SHM, and damage assessment. For instance, by incorporating experimentally derived natural frequencies and mode shapes, an updated numerical model can act as a baseline for detecting and evaluating structural changes over time. In this thesis, the focus is on updating physics-based models. These models are based in fundamental physical laws and provide a framework for predicting structural behaviour. Model updating is employed to refine these models, ensuring that the estimated parameters not only fit the observed data but also remain consistent with physical laws. This is particularly critical in scenarios such as SPI, where accurate representation of soil-structure interaction is necessary for assessing the stability and reliability of foundation systems.

The definition of model updating varies across the literature. Some authors define it as an optimisation process wherein the deviation between the predicted and measured structural behaviour is minimised (Schommer et al., 2017), while others emphasise the gradual adjustment of numerical model parameters to better match the actual structural response (Friswell & Mottershead, 1995; Mottershead & Friswell, 1993). In this thesis, the model updating framework is not considered merely as an optimisation procedure. Instead, it follows the definition proposed by Mottershead and Friswell (1993), which describes model updating as the process of modifying a numerical model to better reproduce the measured response of an actual structure.

Friswell and Mottershead (1995) classify model updating methods into two broad categories: (i) direct methods and (ii) iterative methods. Direct methods reviewed in Section 2.3 utilise the equations of motion and modal orthogonality properties to compute a closed-form solution (Sehgal & Kumar, 2016). While these methods are effective in reproducing measured data, they are highly sensi-

tive to noise and require accurate, spatially complete modal data, which is rarely available for large-scale structures. Additionally, updated mass and stiffness matrices generated through direct methods may not be Symmetric-Positive-Definite (SPD), potentially rendering the model physically meaningless (Alkayem et al., 2018; Sehgal & Kumar, 2016). These limitations often make direct methods unsuitable for large-scale systems. Iterative approaches, on the other hand, address these challenges by iteratively minimising an error function to update model parameters based on experimental results (Alkayem et al., 2018; Sehgal & Kumar, 2016).

In the context of uncertainty, iterative model updating methods can be broadly classified into deterministic and stochastic approaches. The deterministic approaches does not account for uncertainties associated with the inferred parameters. It calibrates a single model using a specific set of test data, yielding precise parameter values and a single model prediction with maximum fidelity for that dataset (Faes & Moens, 2020). These methods are systematic, benefiting from decades of development and relatively straightforward implementation (Mottershead & Friswell, 1993). However, they face challenges such as high computational costs during global optimisation of parameters, an inability to address uncertainties in test data or model assumptions, and reliance on a single-point solution that neglects alternative, equally plausible solutions. This reduces their robustness in scenarios requiring uncertainty quantification (Simoen & Lombaert, 2016).

In contrast, stochastic approaches address both modelling and output uncertainties. Unlike deterministic methods that treat model parameters as unknown-but-fixed constants, stochastic model updating requires the model parameters to be characterised by comprehensive descriptions, including constants, intervals, and precise or imprecise probabilities (Bi et al., 2023). These methods provide interval-based or probabilistic distributions for parameters, offering a comprehensive representation of uncertainty in model predictions. In stochastic model updating, maximum accuracy regarding a single test is not the only objective; instead, the focus is on guaranteeing the robustness of the model while acknowledging inevitable output uncertainty and reducing modelling uncertainty in the experimental process (Bi et al., 2023).

The classification of uncertainties into modelling and output uncertainties has been widely accepted (Simoen et al., 2015). Modelling uncertainty arises from the lack of knowledge, which is expected to be reduced by model updating. Output uncertainty derives from the inherent randomness of the system and cannot be reduced; however, an appropriate representation is still required by performing UQ. Recent advancements in stochastic model updating have explored methods

that combine stochastic system identification techniques with evolutionary optimisation algorithms to estimate model parameters under uncertainty. These approaches leverage output-only data to identify modal parameters and use optimisation algorithms to calibrate numerical models accordingly (Azam et al., 2015; Ebrahimian et al., 2018; Greś et al., 2021d; Ioakim et al., 2025). Such methods have shown promise in handling large-scale structures and complex systems where uncertainties play a significant role.

Direct methods

Direct model updating methods, established in the late 1970s, reconstruct system matrices in single step (Friswell & Mottershead, 1995). Early works, such as Baruch and Itzhack (1978), focused on correcting stiffness matrices under known mass assumptions. Later, Berman (1979) and Berman and Nagy (1983) introduced techniques to update mass and stiffness together, demonstrating applicability to large models with incomplete modal data. Variations of these approaches included updating of damping matrix (Friswell et al., 1998), ensuring structural connectivity (Kabe, 1985), and accommodating measurement errors (Beattie & Smith, 1992). Methods like the cross-model cross-mode (CMCM) (Hu et al., 2007) performed simultaneous mass-stiffness updates but still required complete modal data. More recently, Modak (2014) applied direct updating to vibro-acoustic FEMs.

Despite these contributions, direct methods face challenges with noise sensitivity, data completeness, and preserving physical interpretability (Alkayem et al., 2018; Modak, 2014). Consequently, this thesis emphasises on iterative deterministic and stochastic updating methods, which are better suited for uncertain, incomplete data and complex, large-scale structures.

2.3.1 Iterative methods

Due to the aforementioned disadvantages and challenges of direct methods, they don't tend to find application in large-scale structures in practice. Instead, iterative and indirect approaches have been developed to address these issues more effectively (Augustyn et al., 2020; Friswell & Mottershead, 1995).

Sensitivity-based methods

Sensitivity-based methods iteratively adjust mass and stiffness matrices to minimise discrepancies between measured and analytical results. Collins et al. (1974)

introduced an iterative approach employing Taylor series expansions to relate eigenvalues and modal displacements, achieving effective convergence on benchmark models. Chen and Garba (1980) proposed a matrix perturbation method for updating matrices without requiring explicit parameter relationships, and validated the method using data from the Viking Orbiter spacecraft. Kim et al. (1983) extended this approach with a nonlinear penalty function, improving convergence on a uniform cantilever beam.

Subsequent developments refined these techniques. Lin et al. (1995) advanced the inverse eigen-sensitivity method for faster convergence with incomplete data, while Nehete et al. (2015) introduced a coupled eigen-sensitivity method enhancing accuracy in vibro-acoustic contexts. Sensitivity-based strategies have also proven effective in practical scenarios—Sarvi et al. (2014) successfully detected damage in dome models, and Saidou et al. Saidou Sanda et al. (2018) applied a similar method for bridge damage detection under traffic-induced vibrations.

The sensitivity method is based on the linearisation of the generally nonlinear relationship between measurable outputs, such as natural frequencies, mode shapes, or displacement responses, and the selected model parameters (θ) (Mottershead et al., 2011). This method is developed from a Taylor series expansion truncated after the linear term:

$$\epsilon_z = z_m - \mathbf{z}(\theta) \approx r_i - \mathbf{G}_i(\theta - \theta_i), \tag{2.12}$$

where the residual, r_i, is defined at the i-th iteration as:

$$r_i = z_m - z_i, \tag{2.13}$$

such that the linearisation is carried out at $\theta = \theta_i$. The measured and analytically predicted outputs are denoted by z_m and $z_i = \mathbf{z}(\theta)$, respectively. These typically represent eigenfrequencies, mode shapes, or FRFs. The sensitivity matrix $\mathbf{G}_i$ is defined as:

$$\mathbf{G}_i = \left[\frac{\partial z_j}{\partial \theta_k}\right]_{\theta=\theta_i}, \tag{2.14}$$

where $j = 1, 2, \ldots, q$ denotes the output data points and $k = 1, 2, \ldots, p$ is the parameter index. The sensitivity matrix $\mathbf{G}_i$ is computed at the current value of the complete vector of parameters $\theta = \theta_i$. The error, ϵ_z, is assumed to be small for parameters θ in the proximity of θ_i.

At each iteration, Equation (2.14) is solved for:

$$\Delta\theta_i = \theta - \theta_i, \tag{2.15}$$

and the model is then updated to give:

$$\theta_{i+1} = \theta_i + \Delta\theta_i \tag{2.16}$$

This procedure continues until consecutive estimates θ_i and θ_{i+1} are sufficiently converged.

Hansen et al. (2017) investigated a sensitivity-based approach for detecting damage scenarios through numerical simulations and experimental validation. A simple beam model with predefined mass perturbations was used in the numerical study to evaluate the framework's accuracy. Modal parameters, including natural frequencies and mode shapes, were derived using FE modelling for both undamaged and damaged states. An experimental validation was conducted on a T-shaped steel structure shown in Figure 2.10 subjected to localised mass changes, with modal parameters extracted via OMA under random excitation conditions.

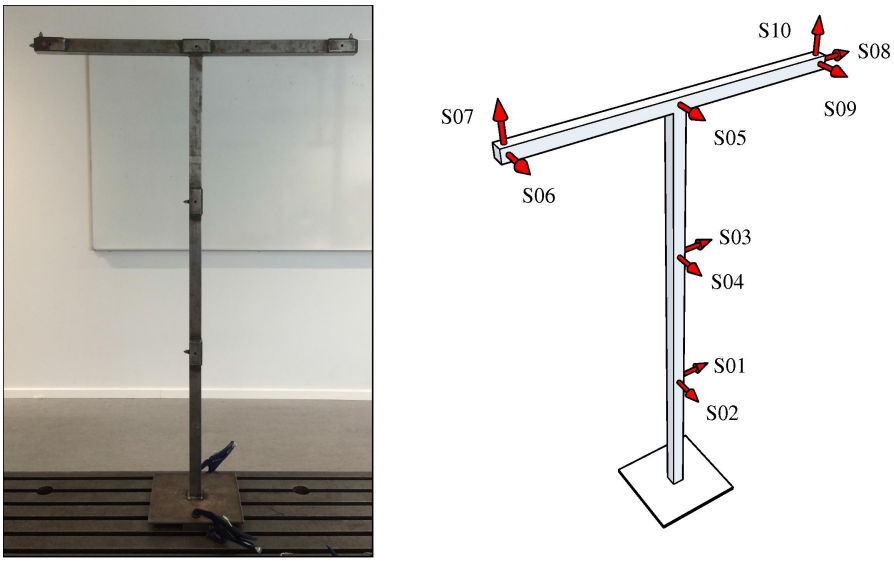

Figure 2.10: T-shaped structure with sensor locations and orientations, illustrating the physical test setup and sensor configuration (Hansen et al., 2017).

Response surface method (RSM)

The response surface method (RSM) provides an iterative approach to FEM updating by replacing computationally expensive FEMs with surrogate response surfaces, enabling efficient calculations without requiring FEM evaluations at every iteration. In RSM, updating parameters serve as inputs for constructing n-dimensional response surfaces, while model responses are treated as outputs.

These surrogate models minimise an error function to approximate the relationship between parameters and responses, ultimately yielding updated model parameters (Sehgal & Kumar, 2016).

Ren and Chen (2010) demonstrated the effectiveness of RSM in updating FEMs for civil engineering structures. Using a quadratic polynomial surrogate, they approximated the relationship between structural parameters and natural frequencies, significantly reducing computational costs while maintaining convergence. The method was validated on a simulated beam and a full-size precast box girder bridge, showcasing rapid convergence and efficiency. However, the accuracy of the approach was found to depend on the quality of the surrogate response surface. De Munck et al. (2008) applied RSM to calculate fuzzy envelope FRFs for structures with uncertain properties, achieving a reduction in computational costs by a factor of 50 compared to traditional methods. Their approach enabled scalable fuzzy analysis for large-scale models, such as the GARTEUR benchmark aircraft, but similarly highlighted the importance of accurately capturing nonlinear parameter interactions for reliable results.

Bayesian-based methods

Bayesian theory-based methods rely on Bayes' theorem, which incorporates a probability distribution to reflect the uncertainties in FEM parameters (Alkayem et al., 2018). These methods offer significant advantages over sensitivity-based approaches, including the ability to provide statistical confidence intervals, flexibility in parameter selection, and resistance to overfitting (Marwala, 2010). Sohn and Law (1997), introduced a Bayesian framework for damage detection in multistorey frame structures. They demonstrated success under conditions like low noise levels and limited DOFs but noted computational demands and non-uniqueness of solutions due to similar modal responses. The approach was later extended to experimental data from reinforced concrete bridge columns (Sohn & Law, 2000) and plate-type structures such as ship hulls (Kurata et al., 2012), validating its applicability but highlighting challenges such as modelling uncertainties and loading effects.

Lye et al. (2021) provided a tutorial on Bayesian model updating, focusing on its application in engineering contexts. The paper explored three advanced sampling techniques—Markov Chain Monte Carlo (MCMC), Transitional Markov Chain Monte Carlo (TMCMC), and Sequential Monte Carlo (SMC)—and their effectiveness in sampling from posterior distributions. These techniques were ap-

plied to case studies, ranging from a simple one-dimensional problem to an 18-dimensional parameter estimation challenge, to assess their computational performance and robustness.

The findings highlighted distinct trade-offs between the methods. TMCMC demonstrated superior robustness, consistently sampling from complex posteriors, including high-dimensional cases, but required longer computation times due to the need to generate samples for every transitional distribution. In contrast, MCMC and SMC offered faster computation but exhibited limitations in handling more challenging posterior distributions.

Kamariotis et al. (2023) proposed a Bayesian decision analysis framework to quantify the economic benefits of vibration-based SHM systems. By leveraging the Value of SHM (VoSHM) metric, the framework evaluates life-cycle cost savings compared to traditional inspection-based maintenance strategies. The approach integrates probabilistic models of deterioration with SHM outputs, incorporating environmental variability, such as temperature-dependent changes in material properties, to enhance prediction accuracy. Gradual and shock deterioration are modelled stochastically, with particle filtering used to update structural reliability and deterioration states in real time, enabling adaptive inspection and maintenance planning.

Numerical investigations validated the framework on a two-span bridge model subject to environmental variability and scour-induced deterioration. Continuous SHM proved effective in reducing costs and improving decision-making. Case studies demonstrated its versatility, showing benefits in scenarios of gradual, observed, and unobserved shock deterioration, as well as in near real-time diagnostics to avoid unnecessary closures after extreme events. While robust, the framework assumes uninterrupted SHM functionality and does not account for potential system failures or modelling errors, providing an upper limit to the economic benefits of SHM adoption.

Bayesian inference also plays a critical role in UQ, as elaborated by Simoen and Lombaert (2016), who emphasised its capability to address both modelling and output uncertainties.

Optimisation-based updating methods

As previously mentioned, physics-based models are numerical representations of physical phenomena. In this context, we consider the numerical models discussed in Chapter 2.1 that are able to represent SPI modelling. Simoen et al.

(2015) explained that these models describe the relationship between the input and output variables of a system, encapsulated by their model or transfer operator, $\mathbf{G_M}$. The transfer operator is defined using a finite set of numerical model parameters, θ_M, allowing the system's output response, $\mathbf{y}$, to be expressed generally as:

$$\mathbf{y} = \mathbf{G_M}(\mathbf{x}, \theta_M) \tag{2.17}$$

for any input vector $\mathbf{x}$. The outputs of these models include vibration data such as accelerations, displacements, or strains. It is often more practical to work with outputs that are independent of the input $\mathbf{x}$, such as FRFs or modal properties, since the input is frequently unknown and contains its own errors in real-world applications. To identify the modal properties, it is essential to apply the system identification methods reviewed in Section 2.2.

It is essential to note that as the parameter vector θ_M varies over a domain $\mathbf{D_M} \subseteq \mathbb{R}^{N_M}$, the transfer operator $\mathbf{G_M}(\theta_M)$ represents not a single model but rather a set or class of models denoted as $\mathbf{M}_M$. This means that each specific choice of θ_M corresponds to a unique model within this class, capturing different possible behaviours of the SPI system. In stochastic updating methods, this set of models embodies the uncertainties and variability in the model parameters, allowing us to represent and propagate uncertainty through the model. Conversely, in deterministic updating, the transfer operator $\mathbf{G_M}$ corresponds to a single model $\mathbf{M}$ which holds a specific θ_M, focusing on finding the best-fit parameters that minimise the discrepancy between the model predictions and observed data.

Selecting an appropriate set of model parameters θ_M is a critical and nontrivial task. The parameters must be capable of accurately representing the unknown physical properties of the actual system and should be sensitive to changes in the outputs of interest, such as modal properties or dynamic responses. For example, parameters like mobilised mass, soil stiffness, and the pile's length significantly influence the vibrational behaviour of the SPI system and therefore should be included.

By carefully selecting a finite set of significant parameters, we can create a robust model that is both accurate and efficient for iterative model updating. This updated model can then be used to monitor the soil-pile system (diagnosis) or to predict the behaviour of the soil-pile system under various conditions (prognosis).

Parameter estimation involves determining an optimal set of model parameters θ_M^* that minimises the misfit between experimental data, denoted as $\bar{\mathbf{d}}$, and the model predictions $\mathbf{y} = \mathbf{G_M}(\theta_M)$. This discrepancy is represented by the objective

F or cost function $\mathcal{L}$, making the parameter estimation problem equivalent to the following optimisation problem:

$$\theta_M^* = \arg\min_{\theta_M \in \mathbf{D_M}} F\left(\mathbf{G_M}(\theta_M), \bar{\mathbf{d}}\right) = \arg\min_{\theta_M \in \mathbf{D_M}} F(\theta_M) \tag{2.18}$$

Here, the latter equality acknowledges that for a given model class and a fixed set of experimental data $\bar{\mathbf{d}}$, the objective function F depends solely on the model parameters θ_M. The optimisation problem may include constraints based on the nature of the parameter estimation problem and any prior information about the model parameters. For instance, inequality constraints can be applied when it is known that parameters should lie within certain ranges, such as physical limits of material properties.

The objective function F is often formulated in terms of residuals, with the most commonly used indicators being the structural dynamic properties—natural frequencies and mode shapes. These properties are reliable indicators of a structure's behaviour, as any changes in the structure typically alter its stiffness (or flexibility), leading to shifts in its dynamic properties.

In the context of SPI, the vibration data $\bar{\mathbf{d}}$ might consist of measured accelerations along the pile obtained from field tests, laboratory experiments or operating structures, leading to identified natural frequencies or mode shapes. The model predictions $\mathbf{G_M}(\theta_M)$ compute these quantities based on the current parameter estimates. The objective function F aims to quantify the discrepancy between the identified and computed output. A common formulation of the objective function F is the sum of squared differences between the identified and predicted values:

$$F(\theta_M) = \sum_{i=1}^{N} \left(\mathbf{y}_i - \bar{\mathbf{d}}_i\right)^2 \tag{2.19}$$

where N is the number of measured data points, y_i are the model predictions, and $\bar{\mathbf{d}}_i$ are the corresponding experimental data.

The optimisation seeks the parameter values that minimise $F(\theta_M)$, effectively reducing the discrepancy between the model and the data. Constraints are essential to ensure that the solution is physically meaningful, for example, in this PhD thesis, the mobilised mass and stiffness, as well as the embedded length, need to be positive numbers. Additionally, the scour depth must be positive but also smaller than the embedded length of the pile.

By solving this optimisation problem, we obtain an updated set of model parameters θ_M^* that provide the best fit to the experimental data within the specified

constraints. This calibrated model enhances the accuracy of the predictions and can be used for diagnostic purposes, such as identifying changes in the system's properties over time, or for prognostic purposes, such as predicting the system's response to future loading conditions.

One of the earliest optimisation-based model updating methods was developed by Levin and Lieven (1998), who introduced two FEM updating approaches: one based on the Genetic Algorithm (GA) and the other on the Simulated Annealing (SA) algorithm. These methods were applied to model updating problems using measured data and various objective functions. However, their sensitivity to parameter selection and computational inefficiency limited their applicability to large-scale structures. Similarly, Marwala (2002) employed a GA to minimise discrepancies between measured and FEM-predicted data, demonstrating its ability to identify global minima but with the drawback of high computational cost.

Hao and Xia (2002) applied these approaches and combined GA with SA in a hybrid algorithm for damage detection in beam-type structures. Using static response displacements and natural frequencies from FEM software, the method was validated through case studies of damaged cantilever beams. This hybrid approach proved more computationally efficient than standard GAs and was effective under varying boundary conditions, even with incomplete or sparse data.

Another contribution was with the development of Particle Swarm Optimisation (PSO) by Kennedy and Eberhart (1995) which is widely used in SHM, more recently applied to SHM by Gui et al. (2017) for damage detection. Their study compared the performance of PSO, GA, and Grid Search (GS) algorithms in optimising the penalty parameters and Gaussian kernel function parameters of support vector machines (SVMs). Using a benchmark dataset with 17 damage scenarios, they demonstrated that all three optimisation-based SVM methods significantly improved sensitivity, accuracy, and effectiveness over conventional methods. Although the GA-based SVM achieved higher average accuracy than PSO, PSO was noted for its computational efficiency, particularly when dealing with larger datasets.

Optimisation algorithms

This section reviews two evolutionary optimisation algorithms employed in Chapters 4, 5 to solve the optimisation problem described in Section 2.3.1 by viewing the key concepts and the underlying philosophy of the algorithms. Detailed review of the optimisation algorithms is available by Igel et al. (2007) for the covariance matrix adaptation evolution strategy (CMA-ES) and by Das and Suganthan

(2010) for the differential evolution (DE). Key concepts and reference example pseudo-codes can be found in Algorithms 2–4 to aid basic understanding.

Covariance matrix adaptation evolution strategy (CMA-ES)

Igel et al. (2007) provide an in-depth exploration of the CMA-ES, a robust algorithm for solving complex optimisation problems. The algorithm generates candidate solutions using multivariate normal distributions and iteratively adapts its covariance matrix to enhance search efficiency. This dynamic adaptation allows the method to explore the search space effectively and converge to optimal solutions.

The algorithm employs a parent solution that is iteratively updated by generating λ new candidate solutions. The parent solution is replaced if a candidate outperforms it. To improve the search process, the step size σ_{cmaes} and covariance matrix C_{cmaes} are adjusted at each iteration. The step size adaptation depends on the success rate (p_{succ}) relative to a predefined target ($p_{\text{succ}}^{\text{target}}$), with adjustments ensuring stability through a damping parameter, d. The update rule for the step size is expressed as:

$$\sigma_{cmaes} = \sigma_{cmaes} \cdot \exp\left(\frac{1}{d} \cdot \frac{p_{\text{succ}} - p_{\text{succ}}^{\text{target}}}{1 - p_{\text{succ}}^{\text{target}}}\right).$$

The covariance matrix C_{cmaes} is iteratively updated to reflect the evolving search distribution. This process incorporates an evolution path, p_c, which stabilises the search by smoothing successive updates. To prevent over-scaling, updates to the evolution path are paused when the smoothed success rate exceeds a threshold (p_{thresh}). The covariance matrix is updated as a weighted combination of the previous matrix and the outer product of the evolution path, maintaining a balance between exploration and convergence.

This iterative adaptation of both σ_{cmaes} and C_{cmaes} underpins the CMA-ES's effectiveness in navigating complex search spaces and achieving high optimisation performance.

Algorithm 2 CMA-ES

Require: Stopping criterion, population size λ

Initialise generation count $g = 0$, parent solution $a^{(g)}_{\text{parent}}$

while the stopping criterion is not met **do**

$a^{(g+1)}_{\text{parent}} = a^{(g)}_{\text{parent}}$

for $k = 1, \ldots, \lambda$ **do**

$\mathbf{x}^{(g+1)}_k \sim \mathcal{N}(\mathbf{x}^{(g)}_{\text{parent}}, \sigma^{(g)2}_{cmaes} C^{(g)})$

end for

updateStepSize$(a^{(g+1)}_{\text{parent}}, \frac{\lambda^{(g+1)}_{\text{succ}}}{\lambda})$

if $f(\mathbf{x}^{(g+1)}_{1:\lambda}) \leq f(\mathbf{x}^{(g)}_{\text{parent}})$ **then**

$\mathbf{x}^{(g+1)}_{\text{parent}} = \mathbf{x}^{(g+1)}_{1:\lambda}$

updateCovariance$(a^{(g+1)}_{\text{parent}}, \frac{\mathbf{x}^{(g+1)}_{\text{parent}} - \mathbf{x}^{(g)}_{\text{parent}}}{\sigma^{(g)}_{cmaes,\text{parent}}})$

end if

Increment generation count: $g = g + 1$

end while

Algorithm 3 updateStepSize

procedure updateStepSize$(a = [\mathbf{x}, p_{\text{succ}}, \sigma_{cmaes}, p_c, C], p_{\text{succ}})$

$p_{\text{succ}} = (1 - c_p) p_{\text{succ}} + c_p p_{\text{succ}}$

$\sigma_{cmaes} = \sigma_{cmaes} \cdot \exp\left(\frac{1}{d} \cdot \frac{p_{\text{succ}} - p^{\text{target}}_{\text{succ}}}{1 - p^{\text{target}}_{\text{succ}}}\right)$

end procedure

CMA-ES has been effectively applied to parameter estimation problems in diverse domains, demonstrating its robustness and adaptability in model updating. For instance, Mao et al. (2022) used an auxiliary model-based CMA-ES (AM-CMA) algorithm to estimate parameters in Hammerstein nonlinear systems with colored noise, achieving high efficiency and accuracy. Additionally, Aghmasheh et al. (2017) employed CMA-ES in the identification of parameters for gray box models used in power transformer analysis. These applications highlight CMA-ES capacity to handle complex, nonlinear systems, offering robust solutions in scenarios where traditional methods fall short.

Differential evolution (DE)

Das and Suganthan (2010) provides a comprehensive review of the DE algorithm, a population-based optimisation method. This version of DE algorithm with binomial crossover operates in four main steps: initialisation, mutation, crossover, and selection.

The algorithm begins by defining its control parameters, which include the scale factor (F_{DE}), the crossover rate (Cr), the population size (NP), and the

initial generation count ($G = 0$). A population of NP individuals is randomly initialised within the search space, where each individual is represented as a vector in D-dimensional space.

In the mutation step, a donor vector is generated for each individual by combining three randomly selected vectors from the population. The donor vector is computed as:

$$\tilde{\mathbf{V}}_{i,G} = \mathbf{X}_{r1,G} + F \cdot (\mathbf{X}_{r2,G} - \mathbf{X}_{r3,G}),$$

where $r1$, $r2$, and $r3$ are distinct indices randomly chosen from the population such that $r1 \neq r2 \neq r3 \neq i$. This step introduces diversity and promotes exploration of the search space.

In the crossover step, a trial vector is created by combining elements of the donor vector and the target vector. This process is governed by the crossover rate (Cr) and is formalised as:

$$u_{j,i,G} = \begin{cases} v_{j,i,G}, & \text{if rand}(0,1) \leq Cr \text{ or } j = j_{\text{rand}}, \\ x_{j,i,G}, & \text{otherwise.} \end{cases}$$

This ensures that trial vectors retain variability while incorporating features from the original target vector.

The selection step compares the fitness of the trial vector with that of the target vector. If the trial vector performs better or equally, it replaces the target vector in the next generation:

$$\mathbf{X}_{i,G+1} = \begin{cases} \tilde{\mathbf{U}}_{i,G}, & \text{if } f(\tilde{\mathbf{U}}_{i,G}) \leq f(\mathbf{X}_{i,G}), \\ \mathbf{X}_{i,G}, & \text{otherwise.} \end{cases}$$

The algorithm iterates through these steps until a stopping criterion, such as a maximum number of generations or achieving a desired fitness level, is met. This iterative process allows DE to balance exploration and exploitation of the search space effectively.

Algorithm 4 Differential Evolution Algorithm with Binomial Crossover

Require: Scale factor F, crossover rate Cr, population size NP, stopping criterion

Initialise generation count $G = 0$

Randomly initialise a population $P_G = \{\mathbf{X}_{1,G}, \mathbf{X}_{2,G}, \ldots, \mathbf{X}_{NP,G}\}$, where

$$\mathbf{X}_{i,G} = [x_{1,i,G}, x_{2,i,G}, \ldots, x_{D,i,G}]$$

and each individual is uniformly distributed in the range $[\mathbf{X}_{\min}, \mathbf{X}_{\max}]$.

while the stopping criterion is not met **do**

for $i = 1, \ldots, NP$ **do**

Mutation Step: Generate a donor vector $\tilde{\mathbf{V}}_{i,G} = [v_{1,i,G}, \ldots, v_{D,i,G}]$ using:

$$\tilde{\mathbf{V}}_{i,G} = \mathbf{X}_{r1,G} + F \cdot (\mathbf{X}_{r2,G} - \mathbf{X}_{r3,G}),$$

where $r1, r2, r3$ are distinct random indices chosen from $\{1, \ldots, NP\}$ such that $r1 \neq r2 \neq r3 \neq i$.

Crossover Step: Generate a trial vector $\tilde{\mathbf{U}}_{i,G} = [u_{1,i,G}, \ldots, u_{D,i,G}]$:

$$u_{j,i,G} = \begin{cases} v_{j,i,G}, & \text{if rand}(0,1) \leq Cr \text{ or } j = j_{\text{rand}} \\ x_{j,i,G}, & \text{otherwise.} \end{cases}$$

Selection Step: Evaluate the trial vector $f(\tilde{\mathbf{U}}_{i,G})$:

if $f(\tilde{\mathbf{U}}_{i,G}) \leq f(\mathbf{X}_{i,G})$ **then**

$\mathbf{X}_{i,G+1} = \tilde{\mathbf{U}}_{i,G}$

else

$\mathbf{X}_{i,G+1} = \mathbf{X}_{i,G}$

end if

end for

Increment generation count: $G = G + 1$

end while

DE has proven effective in handling complex optimisation problems in structural health monitoring and model updating. For instance, Liu et al. (2021b) employed DE in a hybrid framework for localising low-velocity impacts on composite plate structures. By optimising multi-domain feature extraction and impact localisation, the approach demonstrated high accuracy and feasibility in challenging scenarios. Similarly, Liu and Mao (2017) applied DE to a nonprobabilistic UQ enhanced damage diagnosis method, addressing uncertainties in real-world SHM applications. The DE algorithm converted variable fluctuations into uncertainty

intervals for damage-sensitive features, successfully detecting and localising damages in numerical and laboratory-scale models. These studies underscore DE's robustness in optimising complex, high-dimensional problems in structural analysis and monitoring.

2.3.2 Frequency response function (FRF)-based model updating

FRFs effectively capture the dynamic properties of structures, ensuring that the physics-based model accurately reproduces the observed behaviour. By making use of FRFs directly, the model updating approach minimises the errors associated with modal fitting and eliminates the necessity for direct alignment between predicted and measured mode shapes (D'Ambrogio & Zobel, 1994; Ereiz et al., 2022; Friswell & Mottershead, 1995). This attribute is particularly beneficial for structures with densely distributed modes, where modal fitting can become error-prone (Shadan et al., 2016, 2018; Wu et al., 2020) as well as for structures that have only a limited number of sensors not adequate for building the mode shapes appropriately. Furthermore, one of the primary advantages of using FRF data over modal data is that it negates the need to extract modal parameters from measurements, which can introduce additional errors due to the modal identification process (Lee & Shin, 2002). FRF-based model updating has been applied across various approaches, including sensitivity, Bayesian, and optimisation-based model updating methods. In this section, we will review literature where it has been utilised within these three frameworks.

Extensive research has been conducted to develop and refine FRF-based model updating methods. Imregun et al. (1995) proposed a sensitivity-based approach using simulated experimental frequency data, initially applied to a free-free beam with known modelling inaccuracies. The study examined challenges such as the impact of noisy and incomplete data, coordinate mismatches, and numerical stability. The method was later extended to update proportional damping matrices using experimentally measured FRFs, addressing issues like convergence sensitivity and noise-induced instability.

Lin and Ewins (1990) incorporated experimental FRF datasets, enabling simultaneous updating of damping, mass, and stiffness matrices. The method was validated on the GARTEUR structure, demonstrating accuracy for both proportional and non-proportional damping systems, with potential for application in more complex structures (Lin & Zhu, 2006). Later, Lin and Zhu (2007) intro-

duced a method utilising FRFs under base excitation to update FEMs. This technique effectively identified mass and stiffness errors in multi-beam structures, maintaining accuracy even with measurement noise up to 3%.

Pradhan and Modak (2012) proposed an FRF-based method specifically targeting the damping matrix. By minimising the discrepancy between measured and model FRFs, this approach independently updates the damping matrix, thereby preventing the inadvertent transfer of mass and stiffness errors into the damping parameters. The method demonstrated robust performance in fixed-fixed beam structures under various data conditions, including complete, incomplete, and noisy datasets. Further advancements in sensitivity-based FRF model updating have been explored to enhance parameter selection and updating efficiency.

Fathi et al. (2020) introduced a Bayesian model updating framework utilising incomplete FRF data, specifically targeting the structural integrity monitoring of jacket platforms. Instead of traditional model reduction or data expansion methods, this framework increases the number of data points in the objective function by incorporating FRF data across different excitation frequencies. Experimental validation on a scaled 2D fixed platform revealed the method's effectiveness in damage detection and model updating. Additionally, simulations involving noisy data, FEM uncertainties, and incomplete measurements demonstrated the framework's resilience to uncertainties and noise levels.

In deterministic optimisation-based model updating methods more recently, Wu et al. (2018) introduced an iterative model updating approach that uses FRF data to estimate mobilised soil stiffness and mass profiles in beam-Winkler models. This method iteratively adjusted the soil mass and stiffness parameters to align the model's FRF with target data, successfully addressing uncertainties in soil-pile systems. Numerical simulations demonstrated the approach's reliability across diverse pile geometries, soil densities, and stiffness distributions. Although noise and inaccuracies in damping specification introduced errors, the method consistently converged toward unique and accurate solutions. However, the study noted potential challenges when extending the method to real piles due to uncertainties in geometrical and material properties and discrepancies between numerical reference models and real-world pile behaviour. Figure 2.11, demonstrates how the framework is able to converge to the target model FRF iteratively.

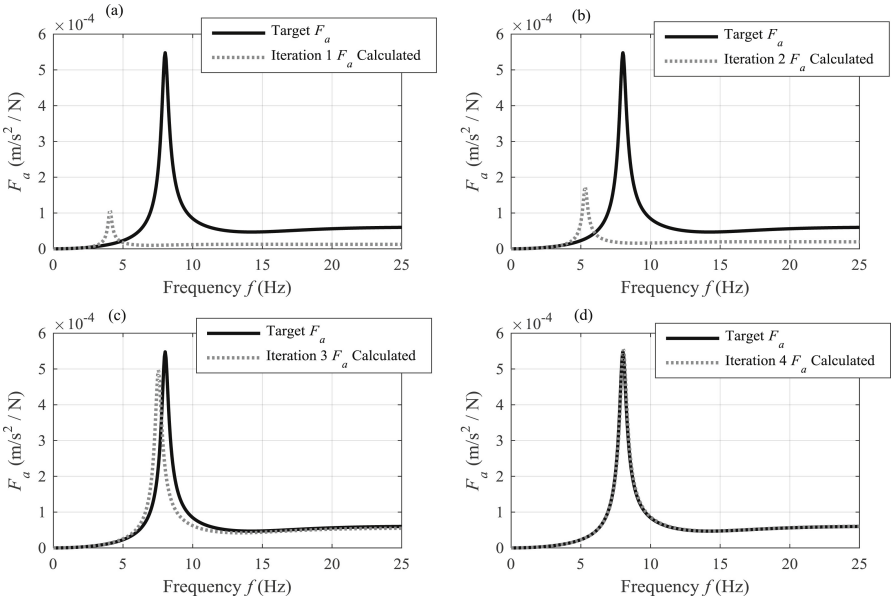

Figure 2.11: Comparison of numerical FRF and target FRF throughout the iterative convergence process (Wu et al., 2018).

Building upon Wu's approach, Prendergast et al. (2019) validated the FRF-based model updating method using experimental pile data. The study targeted laterally impacted piles with varying length-to-diameter (L/D) ratios and incorporated five subgrade reaction formulations to initialise soil stiffness parameters. Experimental results showed the method's robustness in estimating mobilised soil stiffness and mass across different initial conditions. However, variations in FRF peak heights due to experimental noise and impact intensity introduced inconsistencies in the results. The study also highlighted the influence of the active soil depth, noting that stiffness and mass contributions beyond 20% of the pile's embedded length had limited impact on the first vibration mode. Challenges such as signal processing errors and limitations in higher mode evaluations were identified, suggesting the need for longer time signals and refined experimental protocols.

Ioakim and Prendergast (2024) further advanced the FRF-based model updating methodology by developing a two-stage iterative approach to estimate the pile's embedded length, as well as the soil stiffness and mass profiles of the SPI system, detailed in Chapter 3.

These advancements underline the growing importance of FRF-based optimisation methods in tackling SPI challenges, offering robust tools for damage detection and dynamic parameter estimation in complex engineering systems. However, addressing limitations related to experimental noise, higher mode effects, and nonlinear SPI remains a critical area for future research.

2.3.3 Modal assurance criterion (MAC)-based model updating

The modal assurance criterion (MAC) serves as an important tool in model updating, offering a quantitative measure of the consistency between modal vectors derived from experimental data and those predicted by numerical models. The MAC emerged from the necessity to assess the quality of experimental modal vectors obtained from measured FRFs (Allemang, 2003).

Mathematically, the MAC between two modal vectors $\mathbf{v}(p)$ and $\mathbf{v}(q)$ is defined in Equation (2.20) (Peeters & De Roeck, 2001).

$$\mathrm{MAC}(p,q) = \frac{|\mathbf{v}(p)^T\mathbf{v}(q)|^2}{(\mathbf{v}(p)^T\mathbf{v}(p))(\mathbf{v}(q)^T\mathbf{v}(q))} \tag{2.20}$$

where $\mathbf{v}(p)^T$ denotes the conjugate transpose of the modal vector $\mathbf{v}(p)$. By definition, the MAC value ranges from 0 to 1, where 0 indicates no consistent correspondence and 1 signifies perfect linear correspondence between the modal vectors. This normalisation ensures that the MAC is bounded, facilitating straightforward interpretation of modal consistency. A graphical representation of a three DOF system can be viewed in Figure (2.12)

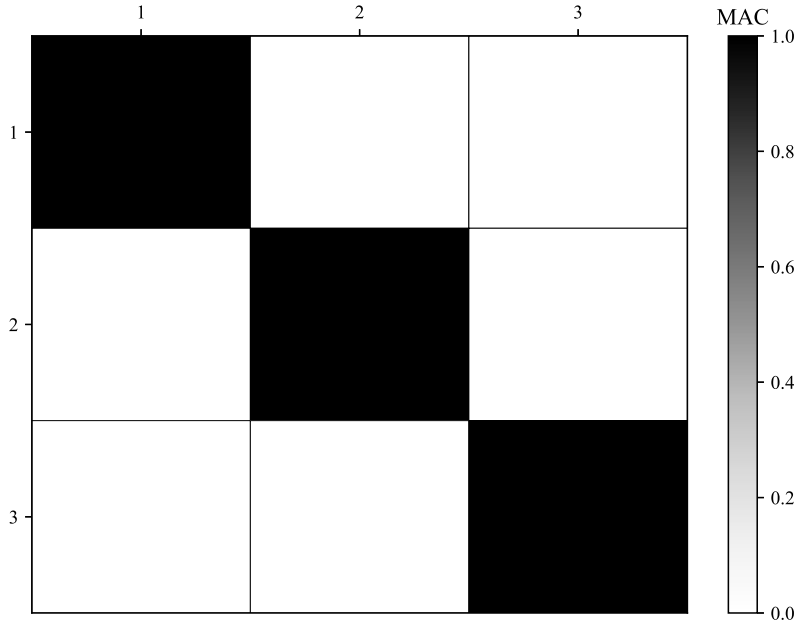

Figure 2.12: Graphical representation of a MAC for a 3 DOF system.

Unlike the orthogonality checks prevalent in the late 1970s, which combined

errors from analytical model development, model reduction, and modal vector estimation into a single indicator, the MAC provides a more isolated and reliable measure of modal consistency. The normalisation by the magnitudes of the modal vectors ensures that the MAC is a bounded scalar quantity between 0 and 1, avoiding the confusion associated with unbounded or non-normalised measures. Secondly, as a least squares-based measure, the MAC is particularly sensitive to significant discrepancies between modal vectors, effectively minimising large errors while remaining relatively insensitive to minor variations. This characteristic enhances the robustness of the model updating process by mitigating the impact of noise and estimation errors inherent in FRF measurements (Allemang, 2003).

In practical applications, researchers have combined natural frequencies and mode shapes using the MAC for damage detection. Zhao and Zhang (2012) utilised changes in natural frequencies and mode shapes for structural damage identification. They employed the MAC to analyse the sensitivity of mode shapes between different orders, selecting mode shapes with high sensitivities to damage to calculate a damage index that improved localisation and quantification accuracy. Numerical validation on a six-span planar truss beam demonstrated the method's effectiveness in detecting single and multiple damage locations and quantifying the extent of damage.

Radzieński et al. (2011) compared six modal-based damage detection methods, including the MAC, COMAC, and wavelet transformation (WT). While generalised FD and WT indicators successfully located damage in noisy environments, the MAC and others struggled. To address these limitations, they proposed a hybrid damage indicator combining changes in natural frequencies and a single mode shape, demonstrating its effectiveness for localising damage in beam-like structures. Capecchi et al. (2016) integrated natural frequencies, mode shapes, and modal curvature squares (MCS) for damage identification in a parabolic arch. By incorporating MCS into the objective function alongside frequency and displacement differences, they improved the convexity of the optimisation process and enhanced convergence. This approach effectively pre-localised damage and reduced the ill-conditioning of the inverse problem, demonstrating the utility of combining modal parameters for accurate damage detection in complex structural forms.

Maes et al. (2022) used the MAC and natural frequencies to construct an objective function for damage detection in a railway bridge in Leuven, Belgium. This study emphasised the importance of eliminating the influence of environmental variations on natural frequencies obtained from long-term monitoring campaigns. To achieve this, two black-box modelling techniques were explored without the

use of physics-based modelling: linear regression and robust principal component analysis (PCA). The MAC was used alongside natural frequencies to evaluate the alignment of modal vectors, ensuring an effective representation of structural dynamics in the objective function. The integration of MAC with frequencies allowed for improved sensitivity to structural changes, facilitating the identification of small modifications introduced during retrofitting or other structural alterations.

2.4 Uncertainty quantification (UQ)

As already mentioned model updating inherently involves solving inverse problems, where the objective is to determine the model parameters that produce a given output by inverting the standard forward relationship between these parameters and the system response. Optimisation-based parameter estimation aims to find the optimal parameter set that minimises discrepancies between computed and measured data. However, this inverse problem is frequently ill-posed and ill-conditioned, implying that small errors in measured data or modelling assumptions can lead to large uncertainties in the estimated parameters. Such sensitivity underscores the importance of uncertainty quantification (UQ) in the model updating process (Friswell & Mottershead, 1995; Simoen et al., 2015; Steenackers & Guillaume, 2006).

UQ provides a framework for evaluating how uncertainties in inputs (e.g., measurements, model assumptions, and environmental conditions) and outputs (e.g., measurement noise) propagate through the identification process and impact final estimates of model parameters, predicted responses, and reliability indices. Over the past decades, diverse UQ methodologies have been developed and are broadly categorised into probabilistic, non-probabilistic, and hybrid approaches. Probabilistic methods use statistical models to derive confidence bounds or probability distributions for parameter estimates (Simoen et al., 2015). Non-probabilistic methods employ frameworks like interval analysis, evidence theory, and fuzzy sets, which avoid strict assumptions about underlying probability distributions. Hybrid approaches combine elements of both, enabling the comprehensive treatment of complex and heterogeneous uncertainty sources (Simoen et al., 2015). These methods collectively enhance the robustness and reliability of structural model updating and damage assessment.

UQ of modal parameters

By looking at non-probabilistic methods in system identification, SSI approaches have laid the theoretical groundwork for understanding estimation uncertainties, showing that under suitable assumptions (e.g., zero-mean white noise disturbances, sufficiently rich inputs), parameter estimates converge in a statistical sense. Early foundational research provided asymptotic covariance expressions for the estimated state-space parameters (Bauer & Jansson, 2000; Chiuso & Picci, 2004; Peeters, 2000; Verhaegen, 1993; Viberg et al., 1997), demonstrating how the conditioning of inputs and system properties affects the accuracy of the identified model. While these studies focused on theoretical systems, the translation of uncertainty from state-space parameters to modal parameters was initially less developed. Addressing this gap, subsequent works introduced methods to propagate the uncertainties of the identified system matrices directly into modal parameters.

For instance, Pintelon et al. (2007) addressed a critical gap in OMA by proposing a methodology to calculate uncertainty bounds on estimated modal parameters, which were previously unavailable. Their approach was demonstrated through both simulations and real measurement examples, such as the OMA of a bridge. Reynders et al. (2008) developed a methodology to estimate variance errors from a single ambient vibration test using the first-order sensitivity of modal parameter estimates to perturbations in the measured output-only data. Additionally, they proposed a bias removal procedure employing a stabilisation diagram to enhance the accuracy of the modal parameters. Both studies demonstrated the effectiveness of these approaches through simulations and real measurement examples, highlighting the practicality of using first-order sensitivity methods for UQ in modal analysis.

For a broader discussion of variance computation in SSI algorithms, including both output-only and input/output methods, Mellinger et al. (2016) introduced new schemes for estimating the variances of frequencies, damping ratios, and mode shapes. Their methodology covers four subspace algorithms, considering the stochastic nature of input data in input/output methods. Monte Carlo simulations validated the accuracy of the proposed variance estimations, and the algorithms were applied to real-world vibration tests, such as the in-flight monitoring of aircraft, demonstrating their robustness and applicability in practical scenarios. More recently, Reynders (2021) presented a methodology for assessing the accuracy of system matrices identified using SSI methods, specifically focusing on the data-driven implementation.

Greś et al. (2022a) provided a comprehensive review and practical framework

for uncertainty propagation in subspace-based system identification methods. The study specifically addressed the estimation of covariance related to the state-space matrices B and D, which are associated with input measurements. Using explicit first-order perturbation-based schemes, they developed covariance expressions for the B and D matrices and applied them to quantify the uncertainty of the resulting parametric transfer function. Their proposed approach was validated through simulations of a mechanical system and laboratory experiments on a plate, offering valuable insights into uncertainty quantification for both output-only and input/output subspace methods.

In another study, Greś et al. (2022b) validated the statistical Delta method for UQ in the context of several input/output and output-only subspace identification algorithms. Their study focused on assessing the accuracy of Delta method-based approximations of uncertainty in modal parameters and modal indicators, using statistical distance measures to compare these approximations against results from Monte Carlo simulations. The research included experimental data from a wind turbine blade tested in a laboratory environment. The findings demonstrated that the Delta method provides a reliable characterisation of the distributions of modal parameter estimates, including eigenfrequencies, damping ratios, and MAC, based solely on data from a single dataset.

Recent research has extended UQ frameworks to the MAC and Modal Phase Collinearity (MPC), which are used for evaluating mode shape consistency and complexity, respectively (Greś et al., 2021a, 2021b). For the MAC, UQ addresses the challenges posed by its bounded nature between 0 and 1. When the MAC is close to 1, indicating nearly identical mode shapes, its distribution deviates from Gaussian, requiring a scaled and shifted the quadratic χ^2 approximation for accurate confidence intervals. This framework reduces the risk of misinterpreting spurious modes or missing subtle structural changes. Similarly, UQ for the MPC, designed to assess whether mode shapes are real or complex, provides a Gaussian approximation for its distribution when the corresponding mode shapes are complex. Validation through Monte Carlo simulations and experimental studies, such as those on the S101 Bridge and offshore structures, demonstrates the reliability of these UQ methods in monitoring structural health and identifying damage.

Greś et al. (2021d) proposed a series of refinements to traditional modal-based objective functions for structural model updating. Their work addressed uncertainties in both natural frequency and mode shape estimates. By integrating statistical uncertainties, they improved the robustness of the objective function used in optimisation tasks. Here, the work of Greś et al. (2021b) and Greś et al. (2021d) is reviewed, which is relevant to Chapters 4 and 5; the complete study

can be accessed in the original papers.

Originally, the parameter-based objective function depended on normalised differences between model-predicted and measured natural frequencies and MAC values. This standard approach was subsequently enriched by incorporating confidence intervals for the natural frequency estimates (Wahab & De Roeck, 1999).

The normalised difference between the estimated natural frequency $\hat{f}_i$ and the model's natural frequency f_i^θ, under a certain parameter θ, is defined in Equation (2.21).

$$\Delta_{f_i}^\theta = 1 - \frac{f_i^\theta}{\hat{f}_i}. \tag{2.21}$$

For mode shape comparisons, the MAC is employed to assess the consistency between the identified mode shape $\hat{\phi}_i$ (estimated from measurements that correspond to the true but unknown system parameter θ_*) and the physics-based model mode shape ψ_i^θ. When θ matches the true system parameter θ_*, the MAC value approaches unity as the data length $N \to \infty$, indicating highly consistent mode shape estimates. Deviations of the MAC value from unity signal discrepancies between measured and model-predicted mode shapes. This difference from unity can be expressed in Equation (2.22).

$$\Delta_{\mathrm{MAC}_i}^\theta = 1 - \mathrm{MAC}(\hat{\phi}_i, \psi_i^\theta). \tag{2.22}$$

The traditional objective function quantifies discrepancies between measured and model-generated modal parameters (natural frequencies and mode shapes). Combining the terms $\Delta_{f_i}^\theta$ and $\Delta_{\mathrm{MAC}_i}^\theta$, the overall objective function $F(\theta)$ was formulated to represent the total discrepancy between measured and numerical modal parameters across all modes:

$$F(\theta) = \sum_{i=1}^{m} \Delta_{f_i}^\theta + \sum_{i=1}^{m} \Delta_{\mathrm{MAC}_i}^\theta, \tag{2.23}$$

where m is the number of considered modes. This objective function maps the parameter space into a multidimensional objective space, providing a quantitative measure of how closely the model parameters match the measurements.

To further enhance this framework, the study developed an objective function that accounts for uncertainties in both natural frequencies and MAC estimates. By using a second-order Taylor expansion, the bounded and asymmetric distribution of MAC values was accurately modelled. This improved statistical integration of MAC into the optimisation process ensures that the objective function better rep-

resents the true discrepancies, while also acknowledging the inherent uncertainty in modal parameter estimation.

For SSI methods, the modal parameter estimates (natural frequencies and mode shapes) have been shown to be asymptotically Gaussian (Bauer et al., 1999; Mellinger et al., 2016). As stated in Equation (2.24):

$$\hat{f}_i \approx \mathcal{N}\left(f_{i,*}, \frac{1}{N}\sigma_{f_i}^2\right), \quad \text{and} \quad \begin{bmatrix}\Re(\hat{\phi}_i)\\ \Im(\hat{\phi}_i)\end{bmatrix} \approx \mathcal{N}\left(\begin{bmatrix}\Re(\phi_{i,*})\\ \Im(\phi_{i,*})\end{bmatrix}, \frac{1}{N}\Sigma_{\phi_i}\right), \tag{2.24}$$

where $\Re(\cdot)$ and $\Im(\cdot)$ denote the real and imaginary parts of a complex variable, $\mathcal{N}(\mu, \Sigma)$ denotes a Gaussian distribution with mean μ and covariance Σ, and $\sigma_{f_i}^2 \in \mathbb{R}$, $\Sigma_{\phi_i} \in \mathbb{R}^{2r\times 2r}$ are the asymptotic covariances of $\hat{f}_i$ and $\hat{\phi}_i$, respectively. The computation of these covariance estimates is performed using the SSI methods reviewed in Section 2.2.2.

Confidence intervals for natural frequency estimates are derived under the assumption that these estimates are approximately Gaussian. Such intervals provide a credible range around the computed estimates. For instance, a confidence level $\gamma = 0.9544$ corresponds to the $\pm 2\sigma$ bounds. Thus, for the ith natural frequency:

$$c_{f_i} = \left[f_i^{\min}, f_i^{\max}\right], \tag{2.25}$$

with

$$f_i^{\min} = \hat{f}_i - 2 \cdot \frac{1}{\sqrt{N}}\sigma_{f_i}, \quad f_i^{\max} = \hat{f}_i + 2 \cdot \frac{1}{\sqrt{N}}\sigma_{f_i}. \tag{2.26}$$

Here, $\hat{f}_i$ is the estimated frequency, σ_{f_i} is its standard deviation, and N is the data length. If the model-predicted frequency f_i^θ lies within c_{f_i}, then θ is statistically close to the true system parameter θ_*. Otherwise, f_i^θ lying outside c_{f_i} indicates a significant discrepancy. This concept is illustrated in Figure 2.13.

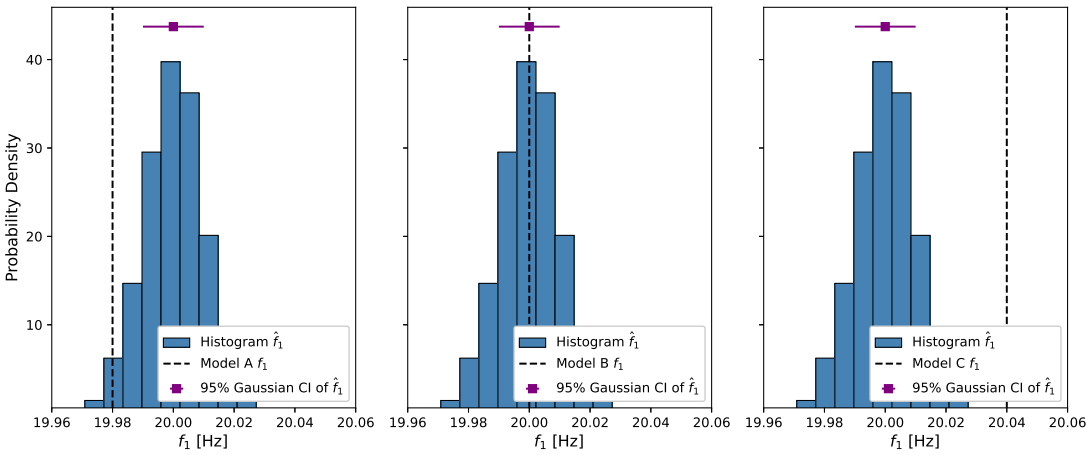

Figure 2.13: Confidence intervals for frequency estimates

In addition to frequency uncertainties, the study also incorporated MAC uncertainties into the stopping criteria of the objective function. This ensures that the optimisation process can terminate efficiently while still maintaining statistical rigor. Unlike frequencies, for which Gaussian confidence intervals are straightforward, MAC estimates are more complex due to their bounded nature and the possibility of non-Gaussian behaviour as MAC approaches unity.

When the MAC is not close to unity, first-order approximations and Gaussian-based UQ for MAC can be effectively applied (Mellinger et al., 2016; Reynders et al., 2008). However, in model updating problems where the goal is to achieve high consistency between measured and numerical mode shapes, $\mathrm{MAC}(\hat{\phi}_i, \psi_i^{\theta}) \to 1$ as $N \to \infty$. Under these idealised conditions, the MAC distribution no longer resembles a Gaussian form.

To address this challenge, higher-order approximations are required. Greś et al. (2021b) developed a framework that uses the quadratic form of the MAC function and propagates the covariance of mode shapes into the MAC distribution. By employing first-order and, when necessary, second-order Taylor expansions, the approach captures the asymptotic behaviour of MAC as it approaches unity.

The uncertainty in the mode shapes $(\hat{\phi} - \phi_*)_{\mathrm{Re}}$ can be expressed by Equation (2.24).

Since $\hat{\phi}$ and $\hat{\psi}$ represent mode shapes estimated from different datasets, their perturbations are independent. The MAC depends on these Gaussian variables, and the first-order delta method linearises the MAC around (ϕ_*, ψ_*) in Equation (2.27).

$$\mathrm{MAC}(\hat{\phi}, \hat{\psi}) \approx \mathrm{MAC}(\phi_*, \psi_*) + \mathcal{J}^{\mathrm{MAC}}_{\phi_*, \psi_*} \hat{X}, \tag{2.27}$$

where $\hat{X}$ combines the real and imaginary parts of $(\hat{\phi} - \phi_*)$ and $(\hat{\psi} - \psi_*)$.

When the MAC approaches unity, the linear approximation breaks down because $\mathcal{J}_{\phi_*}^{\mathrm{MAC}} \to 0$ as $\mathrm{MAC}(\phi_*, \psi_*) \to 1$. In this scenario, a second-order Taylor expansion is applied:

$$\begin{aligned} \mathrm{MAC}(\hat{\phi}, \psi_*) \approx \mathrm{MAC}(\phi_*, \psi_*) + \mathcal{J}_{\phi_*}^{\mathrm{MAC}}(\hat{\phi} - \phi_*)_{\mathrm{Re}} \\ + \tfrac{1}{2}(\hat{\phi} - \phi_*)_{\mathrm{Re}}^{\top} \mathbf{H}_{\phi_*}^{\mathrm{MAC}}(\hat{\phi} - \phi_*)_{\mathrm{Re}}, \end{aligned} \tag{2.28}$$

where $\mathbf{H}_{\phi_*}^{\mathrm{MAC}}$ is the Hessian matrix representing second derivatives and $\mathrm{MAC}(\phi_*, \psi_*)$, $\mathcal{J}_{\phi_*}^{\mathrm{MAC}}(\hat{\phi} - \phi_*)_{\mathrm{Re}}$ have values of 1 and 0 respectively. This second-order term accounts for the curvature of the MAC function near unity, yielding a more accurate statistical description of the MAC distribution in such regimes.

The methodology outlined in Section 4 builds upon the approaches presented in (Greś et al., 2021b; Greś et al., 2021d). These methodologies were adapted and tailored for SPI modelling, enabling the estimation of the studied parameters.

2.5 Limitations of the state of the art

The review in Chapter 2 highlights several key limitations that continue to hinder reliable simulation and monitoring of soil-pile systems. This thesis addresses these challenges by integrating physics-based modelling with data-driven system identification and optimisation frameworks. The most critical limitations are summarised below.

Static soil-property assumptions: Small-strain stiffness profiles obtained from field tests such as CPT or MASW are typically incorporated directly into Winkler-type formulations. However, soil properties, particularly stiffness, damping, and mobilised mass, evolve under the influence of loading history, cyclic degradation, ageing, and scour. Chapters 3 to 5 demonstrate that iterative calibration of a digital twin using measured vibration data can capture these effects in situ.

Dependency on known embedded length: Conventional physics-based models require the embedded pile length to be specified in advance, and any mis-specification introduces significant bias in the computed modal properties. Chapters 3 and 4 propose deterministic (FRF-based) and stochastic (CMA-ES-based) frameworks that estimate soil parameters and embedded length from either impact or ambient vibration data, eliminating the need for guided-wave testing or physical exposure.

Unknown input forces: Many pile length estimation techniques require knowledge of both input and output signals, which is unrealistic in most operational monitoring scenarios. Input forces are often unknown or cannot be measured directly in situ. Chapter 4 addresses this limitation by introducing an output-only model updating framework that estimates embedded length, soil stiffness, and soil mass profiles using stochastic system identification and evolutionary optimisation. This significantly enhances the practical applicability of model updating by removing the reliance on known excitations.

Limitations in uncertainty quantification: Most system identification applications provide limited treatment of uncertainty, often neglecting the variability in estimated modal parameters. Chapter 4 addresses this limitation by incorporating covariance information from subspace identification directly into both the objective function and the stopping criteria of the optimisation framework.

Ambiguity in scour detection: Natural-frequency-based alarms are widely used for scour detection but exhibit low specificity. Changes in soil stiffness and mass, or boundary conditions can also induce frequency shifts. Chapter 5 introduces three model updating frameworks (one deterministic and two stochastic) that incorporate mode shapes or FRFs to estimate scour depth with improved reliability.

Taken together, these limitations motivate the hybrid model updating approaches developed throughout this thesis.

Chapter 3

A two-stage method to estimate the embedded length of foundation piles using FRF-based model updating

Authors: Andreas Ioakim, Luke J. Prendergast
Paper Status: Published in Mechanical Systems and Signal Processing
(DOI: 10.1016/j.ymssp.2024.111603)

3.1 Introduction

Dynamic soil-structure interaction is an important field in civil engineering with applications in earthquake engineering, structural dynamics, and structural health monitoring (SHM). There is an ongoing need for the development of numerical methods that can accurately estimate soil-pile interaction (SPI) parameters to model these systems. In this work, a Frequency Response Function (FRF)-based model updating method is developed, which can estimate the embedded length of foundation piles, in addition to the mobilised soil mass and stiffness, when a lateral impact load is applied. Knowledge of the embedded length of piles is essential for modelling foundation behaviour, and may not be readily available from as-built construction information. For example, if developing reference damage models or digital twins of foundation structures, complete knowledge of the pile geometry is required. This study develops a two-stage iterative model updating method, which utilises FRF data obtained at the pile's head as a result of an applied lateral impact load. The method uses information from the 1st mode of vibration to estimate the mobilised soil mass and stiffness, and subsequently uses information from the 2nd mode of vibration to estimate the embedded length. To appraise the approach, impact tests are numerically simulated on a number of 'piles' (numerical spring-beam systems) with varying length/diameter (L/D) ratios to derive FRFs, whereby the models have known length and dynamic properties. These FRFs are then used as targets in the model updating approach, which iteratively varies the properties of a numerical model of a pile to obtain a match in the FRF data, and subsequently estimates the mobilised mass, stiffness, and embedded length. The results of the analyses illustrate that by minimising the difference in the first and second FRF peaks between the estimated target and numerical model FRF, the method can accurately estimate the mass, stiffness and embedded length properties of the test 'piles'. The performance of the approach against numerical case applications is assessed in this research work, as the properties of these systems are known in advance, facilitating quantification of the errors and performance. The developed method requires further validation through full-scale testing to confirm its effectiveness in real-world scenarios.

In the current chapter, a two-stage iterative model updating approach for estimating the embedded length of piles is presented. The study builds upon a method originally developed by Wu et al. (2018) which estimates the soil mass and stiffness of soil-pile systems using the first mode of vibration. The novel contribution of this work is the incorporation of both the first and second modes of vibration in the FRF, enabling simultaneous estimation of the embedded length, soil mass,

and soil stiffness. The proposed method is validated against numerically simulated pile models to assess its convergence behaviour and overall accuracy. The results indicate that the approach can reliably recover the SPI parameters with minimal instances of false convergence.

The remainder of the chapter is outlined as follows: Section 3.2 presents the numerical modelling used to simulate the piles and obtain dynamic responses; Section 3.3 presents the FRF-based model updating approach for estimating pile embedment lengths; and Section 3.4 demonstrates the approach against numerically generated example cases. Finally, Section 3.5 presents the conclusions of the study.

3.2 Numerical modelling

In this section, the numerical model used as the basis of the FRF-based model updating approach is described. A model of a linear Winkler-beam pile foundation is programmed in Python, and the general parameters are described in this section. Specific values are provided for the target (test case) models in Section 3.4.1, which are used in the analyses to appraise the performance at estimating the embedded lengths of a range of piles. The model is composed of 6 degree-of-freedom (DOF) Euler-Bernoulli beam elements to represent the pile, and a series of 2-DOF springs (and masses) to represent the soil, and therefore transforms the 3-D continuous problem of a pile foundation in soil into a simpler 1-D discrete problem.

For the embedded portion of the pile, the 2-DOF spring elements are attached to the lateral (x-direction) DOF of each embedded pile node, and the other end of each spring is fixed to represent the connection with the ground. The base of the pile is constrained in the vertical z-direction as axial deformations are not considered. A schematic of the pile model is shown in Figure 3.1.

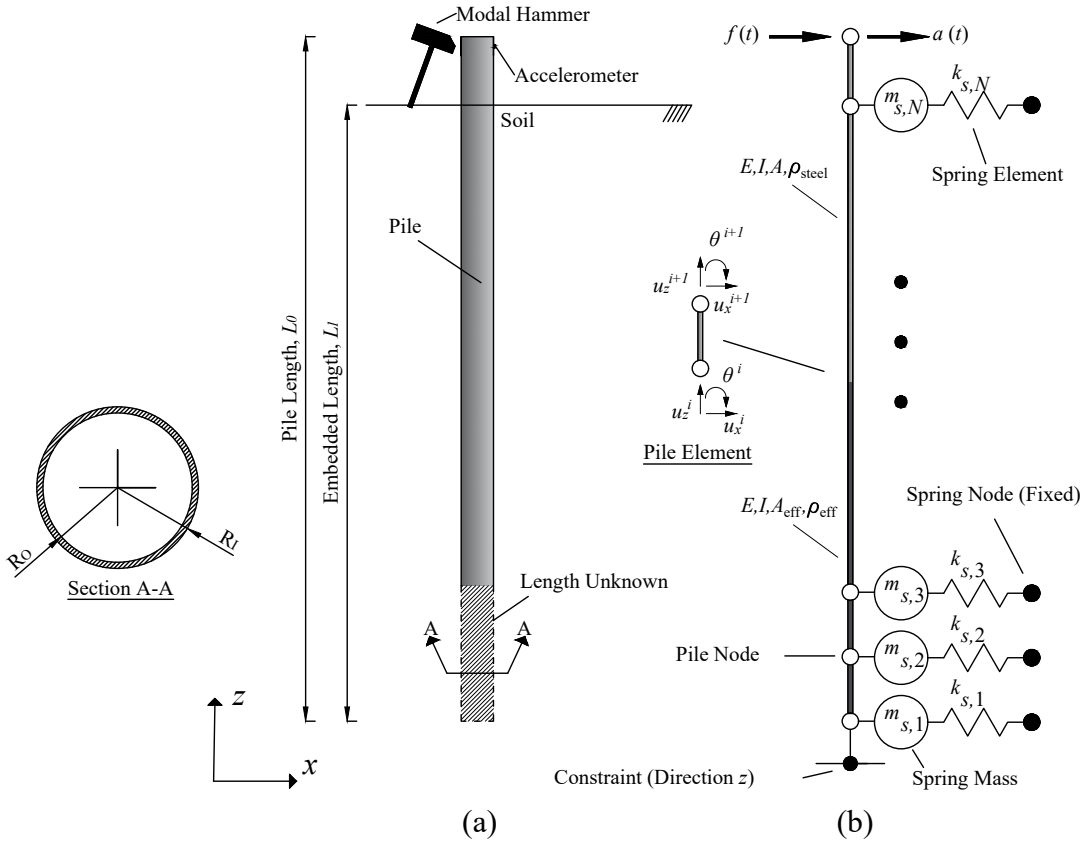

Figure 3.1: Schematic of pile model, (a) physical model, (b) numerical representation.

The pile model is assumed to be embedded into a single layer of cohesionless sand, and the groundwater table is assumed to be well below the tip of the pile (i.e. pore pressures are not simulated). To capture the flexural rigidity of the pile to which the springs are attached, Biot (1937), Okeagu and Abdel-Sayed Okeagu and Abdel-Sayed, 1984, and Vesić Vesić, 1961 (among others) provided relationships between the subgrade reaction modulus, and the material properties in the elastic problem, to calculate the coefficient of subgrade reaction $K_S(z)$. In this chapter, the relation provided by Vesić (1961) is used, which matches the maximum displacements of the infinite beam to compute the subgrade reaction $K_S(z)$ (Equation (2.3)).

$$K_S(z) = \frac{0.65 E_S(z)}{D(1-\nu_s^2)} \sqrt[12]{\frac{E_S(z) D^4}{EI}} \tag{2.3}$$

where $E_S(z)$ is the small-strain Young's modulus of the soil elements (N m^{-2}), ν_s is the soil's Poisson's ratio, D is the width of the pile (m), and E and I are the pile's Young's modulus (N m^{-2}) and moment of inertia (m^4), respectively. The small-strain Young's modulus of the soil is calculated in Equation (3.1).

$$E_S(z) = 2G_S(z)(1 + \nu_s) \tag{3.1}$$

where $G_S(z)$ is the shear modulus of the sand (N m^{-2}). Since $K_S(z)$ is in N m^{-3} and the springs allow stiffness in one dimension (N m^{-1}), the stiffness of the i^{th} spring element is given in Equation (3.2).

$$k_i = K_S(z)D_iL_i \tag{3.2}$$

where D_i and L_i are the i^{th} pile element's diameter and tributary length, and $K_S(z)$ is defined in Equation (2.3).

The pile nodes in the embedded portion are attached to the lateral springs while those above the ground level are free. The mass of soil contributing to the dynamic motion is simulated by adding lumped masses to the soil springs. The amount of mobilised soil mass is unknown and so is represented as the pile mass multiplied by a weighting factor and distributed among the active springs. The active springs are assumed to be those predominately contributing to the first mode of vibration and are assumed to be distributed along the upper quarter of the embedded length (Prendergast et al., 2019; Wu et al., 2018). This is because masses at lower depths have limited influence on the first mode shape and are therefore omitted (Wu et al., 2018). This is a result of laterally impacting the pile head whereby the mobilised soil mass at depth is assumed negligible and only near-surface soil is mobilised, which is a simplifying approximation. The i^{th} spring's mass is defined as a function of the pile's mass in Equation (3.3).

$$M_i = \frac{M_{\text{Pile}}}{Q} \tag{3.3}$$

where M_{Pile} is the pile's mass and Q is the number of springs in the top quarter of the pile.

The pile model used in the current application is assumed to be open-ended, and therefore the presence of soil inside the pile requires consideration. The contribution of the internal soil within the pile to the dynamic response is incorporated by changing the effective cross-sectional area of the pile elements up to the plug length to consider the influence of the internal soil density. This ensures that the internal soil adds mass to the system but does not affect the pile stiffness, in keeping with the physics of real piles. It should be noted that the method is equally applicable to closed-ended piles.

A dynamic impact load is simulated at the pile's head by applying a Dirac-delta type load to the lateral DOF at the pile head node, and the resulting acceleration

is derived. This is representative of an impact test from a modal hammer to excite the structure, and is undertaken to remain in keeping with the physics of testing real pile structures. Numerically, to obtain the acceleration data, the dynamic response of the pile (spring-beam system) can be obtained by solving Equation (3.4).

$$\mathcal{M}^{\theta}\ddot{\mathbf{q}}(t) + \mathcal{D}^{\theta}\dot{\mathbf{q}}(t) + \mathcal{K}^{\theta}\mathbf{q}(t) = \mathbf{u}(t) \tag{3.4}$$

where $\mathcal{M}^{\theta}$, $\mathcal{D}^{\theta}$, and $\mathcal{K}^{\theta} \in \mathbb{R}^{n_2 \times n_2}$ denote the mass, damping, and stiffness matrices of the system, respectively, and θ represents the system parameters. The vector $\mathbf{q}(t)$ describes the displacement profile at each timestep, while vectors $\mathbf{u}(t)$, $\dot{\mathbf{q}}(t)$, and $\ddot{\mathbf{q}}(t)$ represent the external loading, velocity, and acceleration profiles as functions of time (t). Such problems that evolve in time, with all their boundary conditions provided at $t_0 = 0$, are often posed as initial value problems. Therefore, predictions of a system's behaviour can be conducted if knowledge of the conditions at $t_0 = 0$ is available.

The computation of eigenvalues and eigenvectors for Equation (3.4) in the undamped case is discussed in Section B.1.1, while the derivation for Rayleigh damping is covered in Section B.1.2. For cases where the assumption of proportional damping is not valid, the eigenvalue problem requires a more generalised approach involving the reformulation of the governing equation into a first-order state-space system. A detailed derivation and discussion of this approach are provided in Section B.1.3.

A special case of proportional damping where the damping matrix $\mathcal{D}^{\theta}$ is defined using the two-term Rayleigh damping formulation (Clough & Penzien, 1975; Liu & Gorman, 1995), as a linear combination of the mass and stiffness matrices, where two damping coefficients are specified as shown in Equation (3.5).

$$\mathcal{D}^{\theta} = \alpha_0 \, \mathcal{M}^{\theta} + \alpha_1 \, \mathcal{K}^{\theta}, \tag{3.5}$$

where the coefficients α_0 and α_1 are the proportionality constants for the mass and stiffness, respectively, and are calculated in Equation (3.6):

$$\begin{bmatrix} \alpha_0 \\ \alpha_1 \end{bmatrix} = \frac{2\,\omega_0\,\omega_1}{\omega_1^2 - \omega_0^2} \begin{bmatrix} \omega_1 & -\omega_0 \\ 1/\omega_1 & 1/\omega_0 \end{bmatrix} \begin{bmatrix} \xi_0 \\ \xi_1 \end{bmatrix}, \tag{3.6}$$

where ξ_0 and ξ_1 are the Rayleigh damping ratios for the first and second modes, and ω_0 and ω_1 are the first and second circular frequencies ($\mathrm{rad\,s^{-1}}$). The implementation of a Rayleigh damping model may deviate in behaviour from that of

real pile systems, and is intended to represent a basic model for energy dissipation. This is deemed sufficiently accurate for small-strain soil-pile applications (Prendergast & Gavin, 2016), whereas for larger nonlinear SPI, hysteretic damping would also potentially be present.

To solve Equation (3.4), the Newmark-Beta method (Bathe, 2006; Newmark, 1959) is implemented, which is a direct solver for second-order differential equations. The Newmark-Beta method is capable of solving the dynamic ordinary differential equation in Equation (3.4) without the need to separate it into a coupled pair of first-order differential equations.

Equations (3.7) and (3.8) were derived for the acceleration, velocity, and displacement profiles:

$$\dot{\mathbf{q}}_{r+1} = \dot{\mathbf{q}}_r + \Delta t(1-\gamma)\ddot{\mathbf{q}}_r + \Delta t\gamma\ddot{\mathbf{q}}_{r+1} \tag{3.7}$$

$$\mathbf{q}_{r+1} = \mathbf{q}_r + \Delta t\dot{\mathbf{q}}_r + \frac{(1-2\beta)(\Delta t)^2}{2}\ddot{\mathbf{q}}_r + \beta(\Delta t)^2\ddot{\mathbf{q}}_{r+1} \tag{3.8}$$

The scalars γ and β represent the effect of the acceleration in calculating the velocity and displacement, respectively, and can be defined to gain integration accuracy and stability. When $\gamma = \frac{1}{2}$ and $\beta = \frac{1}{6}$, the linear acceleration method is implemented. Newmark originally proposed, as an unconditionally stable scheme, the constant-average-acceleration method or trapezoidal scheme, where $\gamma = \frac{1}{2}$ and $\beta = \frac{1}{4}$. For this particular problem, the unconditionally stable scheme is selected.

To optimise the performance of the solver, the SPD structural matrices were converted into the compressed sparse row (CSR) format. Because the $\mathcal{M}^\theta$, $\mathcal{D}^\theta$, and $\mathcal{K}^\theta$ matrices of Equation (3.4) are highly sparse, meaning that most of their elements are zero, it is beneficial to store them in a sparse format. Sparse techniques essentially store only the non-zero elements of such matrices along with the indices required to perform matrix operations efficiently (Tewarson & Tewarson, 1973). Although axial deformations are not considered in the final numerical implementation, the initial formulation includes axial degrees of freedom to allow future extensibility. These degrees of freedom are systematically excluded during the matrix assembly and conversion to CSR format, ensuring that only the lateral and rotational components relevant to this study are retained. Further details about the CSR format, along with an illustrative example, are presented in Section B.2.1.

The acceleration profile obtained from Equations (3.7) and (3.8) is analysed using a Fast Fourier Transform (FFT) to calculate the frequency content, and a

peak detection algorithm is used to detect the first n frequencies of the system, where n is the number of desired frequencies.

The FRF can then be calculated in Equation (3.9) directly, by taking the ratio for the FFT of the output acceleration to that of the input force, as would be required in tests on real structures.

$$FRF = \frac{\mathcal{F}(\ddot{\mathbf{q}}(t))}{\mathcal{F}(\mathbf{u}(t))} \tag{3.9}$$

3.3 FRF-based model updating to estimate embedded length

The formulation of an iterative model updating approach to ascertain the mobilised soil mass and stiffness profiles from an impact test on a pile using the FRF of the 1st mode of vibration was presented by Wu et al. (2018), for simulated numerical target models, and later expanded in an experimental application by Prendergast et al. (2019). The method works by updating the properties of a numerical model of a pile until the numerical model's FRF matches that of a target model (either a numerically simulated target model or a real experimental pile), using an iterative procedure based on linear projection. The target models developed in Wu et al. (2018) used numerically generated data, so it was known a priori what the stiffness and mass properties were, and this information was used to ascertain the model performance. For application on real piles, as per Prendergast et al. (2019), the only available data are the output acceleration and loading data of the piles, and certain pile geometry information, which are used to update the numerical model to estimate mobilised soil mass and stiffnesses through the generation of a target FRF. The properties are updated by means of estimating weighting factors to be applied to estimated soil mass and stiffness profiles acting on the piles. A hypothesised stiffness profile, estimated from geotechnical site data for example, is used as the initial estimate, and this is weighted by a factor w_k(stiffness weighting) in the updating process until the numerical model matches the response of the target system. Similarly, soil mass as a proportion of pile mass is assumed distributed along a certain length of the pile, which is weighted by a factor w_m (mass weighting) in the updating process. Note, the method estimates the weightings to be applied to profiles of stiffness and mass, w_k and w_m, rather than the stiffness and mass profiles directly. Readers are referred to Wu et al. (2018) for more information on the approach implementing stage one of the two-stage method. The two-stage method for estimating the pile length is described

in detail below.

The previously developed model (Wu et al., 2018) is capable of estimating the soil mass and stiffness for a linear mechanical system with linear material properties (small-strain criterion for Winkler springs). A pseudocode representation of the model updating approach developed to estimate the mobilised soil mass and stiffness acting along a pile is shown in Algorithm 5

Algorithm 5 Mass and Stiffness Weighting Calculation - Stage 1 of The Model Updating Method

Require: Initial numerical model $\text{model}_{0,1}$, target acceleration and loading data, convergence criteria e_m, e_k

Ensure: Optimised mass and stiffness weightings w_m, w_k

```
Initialise j = 0
Compute FRF for the target model
Compute FRF for the initial numerical model model_{0,1}
Calculate r_{m_j} and r_{k_j} using Equations (3.10)–(3.12)
while |r_{m_j} − 1| > e_m or |r_{k_j} − 1| > e_k do
    j = j + 1
    Compute FRF for the j-th numerical model model_{j,1}
    Calculate r_{m_j} and r_{k_j} using Equations (3.10)–(3.12)
    Update w_{m_{j+1}}, w_{k_{j+1}} using linear projection (Mode 1)
end while
return w_{m_j}, w_{k_j}
```

By enhancing the method originally proposed by Wu et al. (2018), and leveraging the first two modes of vibration, it is hypothesised that the pile embedded length can be estimated in addition to the mobilised mass and stiffness. The graphical representation of this enhanced methodology is depicted in Algorithm 6.

Algorithm 6 Pile Length Estimation - Stage 2 of The Model Updating Method

Require: Initial pile length L_0, convergence criteria e_F, e_f, initial numerical model $\text{model}_{0,2}$, and initial step size dL

Ensure: Optimised pile length L_i

```
Initialise i = 0
Calculate w_m and w_k for model_{0,2} using model updating (Stage 1)
Compute FRF for model_{i,2}
Calculate r_{F_i} and r_{f_i} using Equations (3.16)–(3.17)
while |r_{F_i} − 1| > e_F or |r_{f_i} − 1| > e_f do
    if i = 0 then
        L_{i+1} = L_0 + dL
    else
        L_{i+1} = ((L_i − L_{i−1})/(r_i − r_{i−1}))(1 − r_i) + L_i
    end if
    i = i + 1
    Calculate w_m and w_k for model_{i,2} using model updating (Stage 1)
    Calculate r_{F_i} and r_{f_i} using Equations (3.16)–(3.17)
end while
return L_i
```

The process works as follows. A target FRF is formulated from the target model's acceleration and load data in Equation (3.9), assumed to have been obtained from impact testing a target structure. For the cases in this chapter, this data is numerically generated so that the operational mass, stiffness, and length are known. The FRF data from the target model is used in the method to update the properties of a numerical model to estimate the target properties of interest (mass, stiffness, and length).

The model updating approach for estimating the embedded pile length operates in two stages. In Stage 1, the soil mass and stiffness profiles are estimated utilising the first mode of vibration in the FRF only. As elaborated above, it is the soil mass and stiffness weightings that are estimated, which are applied to initial guesses of soil mass and stiffness profiles, informed from geotechnical data such as Cone Penetration Tests (CPT).

Stage 2 subsequently employs the second mode of vibration from the FRF to refine the embedded pile length estimate. The process is iterated in several steps and is described herein. It is assumed that a user of the method would know certain physical and mechanical properties of the target pile, such as diameter and wall thickness, but the embedded length and mobilised soil mass and stiffness

are assumed unknown or uncertain.

An initial length guess L_0 is user-defined, and initial values for the springs' mass and stiffness are calculated using Equations (3.3) and (3.2). The initial stiffness profile guess should be informed by geotechnical estimates using sources such as CPT data, where the shape of the stiffness profile is known, but the actual magnitudes of stiffness might be incorrect due to testing and model transformation errors.

The initial mass profile guess is considered as some multiple of the pile mass acting as an added soil mass, as there are limited methods in the literature to propose soil mass that contributes to dynamic motion in SPI. This process results in an initial guess numerical model, denoted as $\text{model}_{0,1}$, where initial mass and stiffness weightings w_{m_0} and w_{k_0} are applied to the postulated soil stiffness and mass profiles. Subsequently, the initial FRF estimate, FRF_0, is obtained by solving the dynamic equation in Equation (3.4).

In the notation $\text{model}_{0,1}$, the first index (0) indicates that this is the initial model, while the second index (1) specifies whether this is part of Stage 1 or Stage 2 of the model updating approach.

For the initial guess model, $\text{model}_{0,1}$, the mass and stiffness profiles are initialised by selecting w_{m_0} from a uniform distribution ranging between 0 and 30 and multiplying it by the distributed pile mass as defined in Equation (3.3). w_{k_0} is set equal to 1 times the postulated stiffness profile, following the methodology of Wu et al. (2018), assumed to be available by correlation to site data such as CPTs or multi-channel analysis of surface waves (Vasconcelos et al., 2018). The range $[0, 30]$ for the mass weighting is arbitrary. The developed iterative model updating algorithm aims to minimise the difference between the FRF peak of the first mode of vibration for both the numerical and target models, by updating the mass and stiffness weightings, yielding the converged stiffness and mass profile estimates. Peak detection is automated using the SciPy library (Virtanen et al., 2020), which identifies numerical indices of local FRF peaks based on defined parameters and neighbouring values.

For the initial guess model, the relationships between mass ratio, frequency ratio, and stiffness ratio between the initial guess and target models are formalised in Equations (3.10), (3.11), and (3.12), respectively. The criteria for obtaining the converged mass and stiffness weighting estimates are specified in Equation (3.13).

$$r_{m_j} = \frac{F_{\text{target}_1}}{F_{\text{numerical}_{j,1}}} \tag{3.10}$$

$$r_{\omega_j} = \frac{f_{\text{numerical}_{j,1}}}{f_{\text{target}_1}} \tag{3.11}$$

$$r_{k_j} = r_{\omega_j}^2 \times r_{m_j} \tag{3.12}$$

$$|r_{m_j} - 1| < e_m \quad \text{and} \quad |r_{k_j} - 1| < e_k \tag{3.13}$$

The convergence criteria are established with tolerances e_m and e_k, both set to 0.001 for mass and stiffness, respectively. Should the initial guess ratios fail to meet these criteria, a subsequent model, referred to as $\text{model}_{1,1}$, is generated. This model retains the geometric and mechanical properties of the initial model ($\text{model}_{0,1}$) but incorporates new mass and stiffness weightings, w_{m_1} and w_{k_1}. These new weightings are selected from a predefined range and employed to recalculate the mass, frequency, and stiffness ratios using Equations (3.10), (3.11), and (3.12). Based on these recalculated ratios, and employing linear projection techniques, a new set of mass and stiffness weightings for the next iteration model, denoted as $\text{model}_{2,1}$, are calculated using Equations (3.14) and (3.15).

$$\text{w}_{m_{j+1}} = \frac{(\text{w}_{m_j} - \text{w}_{m_{j-1}})}{(r_{m_j} - r_{m_{j-1}})}(1 - r_{m_j}) + \text{w}_{m_j} \tag{3.14}$$

$$\text{w}_{k_{j+1}} = \frac{(\text{w}_{k_j} - \text{w}_{k_{j-1}})}{(r_{k_j} - r_{k_{j-1}})}(1 - r_{k_j}) + \text{w}_{k_j} \tag{3.15}$$

In the iterative process, j represents the current iteration number. The algorithm continues to iterate until the first numerical FRF peak (mode 1) aligns with the first target FRF peak, causing the mass and stiffness ratios (r_m and r_k) to fall within the predefined tolerances. Upon convergence, the algorithm yields a set of mass and stiffness weightings w_m and w_k that correspond to a model with the initially specified length (L_0). In this converged model, the numerical and target first FRF peaks essentially match.

It is important to note that while a matching FRF peak is an indicator of model convergence, it does not guarantee the accuracy of the embedded length guess. Consequently, the process advances to Stage 2, which involves examining the FRF peak of the second mode of vibration. Here, the goal is to align the second FRF peak between the numerical and target models (in addition to the first peak), following the algorithm detailed in Algorithm 6. For this stage, an initial guess model ($\text{model}_{0,2}$) is adopted, inheriting the properties of the converged model from Stage 1 (initial length L_0 and converged mass and stiffness weightings w_{m_j} and

w_{k_j}). The corresponding ratios for the second FRF peak are then calculated using Equations (3.16) and (3.17), as shown in Algorithm 6.

$$r_{F_i} = \frac{F_{\text{numerical}_{i,2}}}{F_{\text{target}_2}} \tag{3.16}$$

$$r_{f_i} = \frac{f_{\text{numerical}_{i,2}}}{f_{\text{target}_2}} \tag{3.17}$$

In this context, r_F and r_f represent the second FRF and frequency peak ratios between the numerical and target models, respectively. The variable i marks the current iteration in the updating process for the second mode of vibration. The terms $F_{\text{numerical}_{i,2}}$ and F_{target_2} refer to the amplitudes of the second mode's FRF peak for the numerical and target models, respectively. Similarly, $f_{\text{numerical}_{i,2}}$ and f_{target_2} indicate the corresponding peak frequencies.

Initially, the ratios r_{F_0} and r_{f_0} are computed for a given pile length L_0 and are compared against tolerances e_F and e_f. If these ratios do not meet the specified tolerances, it suggests that the initial length L_0 is incorrect. An arbitrary length L_1 is then considered for the first iteration, and the method goes back to Stage 1.

The mass and stiffness weightings w_{m_0} and w_{k_0}, originally calculated for the pile length L_0, are employed as the starting values for the $\text{model}_{1,2}$. A new set of weightings, w_{m_1} and w_{k_1}, is calculated using the first mode of vibration, following the procedure previously described for Stage 1. With these two models in place, linear projection is then implemented for the second mode of vibration in Stage 2, employing Equation (3.18) to compute the new length estimate L_{i+1}.

$$L_{i+1} = \frac{(L_i - L_{i-1})}{(r_i - r_{i-1})}(1 - r_i) + L_i \tag{3.18}$$

where

$$r = \max\left(|r_{F_i} - r_{F_{i-1}}|, |r_{f_i} - r_{f_{i-1}}|\right)$$

The process repeats iteratively between Stage 1 and 2, whereby the previously converged weightings $\mathrm{w}_{m_{i-1}}$ and $\mathrm{w}_{k_{i-1}}$ are applied to the new model, with $L_i = L_{i+1}$ and a new pair of weightings w_{m_i} and w_{k_i} is calculated by matching the 1st mode of vibration. This process is repeated until the ratios r_{F_i} and r_{f_i} fall within the tolerance defined for the 2nd mode of vibration, indicating that the correct length is estimated. By focusing on the maximum difference, the algorithm prioritises the correction of the largest error in each iteration. This approach tends to drive the solution more efficiently towards a state where both errors are minimised. Once both the first and second FRFs match, the method ceases and

the correct weightings for mass and stiffness, as well as the correct length, are assumed satisfied.

3.4 Numerical demonstration

The two-stage model updating method to estimate the embedded length of piles is appraised in this section. Firstly, an analysis is conducted to investigate the effect of the embedded length on the lateral dynamic response of piles, as well as the error introduced in the first-mode updating method proposed by Wu et al. (2018) when an assumed embedded length different from the actual length is used in the numerical model. Secondly, the two-stage approach is tested against a range of target pile models to ascertain its performance at successfully estimating the embedded length. It is important to note that in these synthetic tests, the updating model is identical to the target model, and only the soil mass, soil stiffness, and embedded length are treated as unknowns. This isolates the influence of those parameters and avoids complications related to uncertain boundary conditions, which would arise in real field applications. For efficient execution of the repeated length influence analysis, the code was parallelised using `joblib` (Varoquaux & Grisel, 2009), which is a thread-based parallelism library. This parallelised code was then executed on a High-Performance Computer (HPC).

3.4.1 Development of target models

The performance of the model updating method to estimate pile lengths is assessed by applying it to a number of numerically-generated target models. Specific values for the various parameters for generating the target models are provided herein. These target models are effectively pseudo-experimental datasets, whereby the operating mass and stiffness, and pile lengths, of these models are varied and an FRF is generated, which is used as the target in the model updating method to ascertain if convergence occurs. The target models are created using the procedure from Section 3.2 and have varied geometrical, physical, and mechanical properties. In order to investigate the application to both flexible and rigid piles, two pile diameters (D) are studied with annular cross-section and wall thickness (t_0) ($D = 1$ m, $t_0 = 0.025$ m, and $D = 4$ m, $t_0 = 0.1$ m) and three embedded lengths ($L_1 = 10$ m, $L_1 = 20$ m, and $L_1 = 30$ m). The models are generated by discretising the pile into a finite number of pile elements, each taken arbitrarily as a length of 0.1 m, and for all target models the pile length (L_0) is defined as the embedded length of the pile with a 1 m stick-up ($L_0 = L_1 + 1$ m). These properties were chosen to

model a range of foundation geometries encountered across various applications, including simulating monopiles commonly used as offshore wind turbine foundations. These types of foundations are a potentially significant area of application for the developed method, and therefore it is of interest to assess the relevance to such practical, real-world scenarios.

A total of 22 target models are created, and their FRFs are obtained for a given simulated impact load. A 10 kN impact is applied on the pile head in each model for an arbitrarily short time and the pile model is then left to oscillate freely for a period of 50 seconds, where the timestep (Δt) of the analysis is predefined as 0.005 seconds. The springs' stiffnesses in target models 1–12 (see Table 3.1) follow a constant profile with depth (analogous to an over-consolidated soil deposit) and models 12–16 follow a parabolic profile (analogous to normally-consolidated soil deposit). The soil's shear modulus for the constant stiffness profile is taken as 50 MPa, and for the parabolic stiffness profile, the bulk unit weight (γ) and the relative density (D_r) of the soil are taken to be 18 kN m^{-3} and 50% for a medium dense sand (see (Wu et al., 2018) for details). Figures 3.2(a) and (b) illustrate the shear modulus of two different target models: a constant profile and a parabolic profile. The Poisson's ratio is taken as 0.1 for small-strain applications (Prendergast et al., 2013), and the steel pile's Young Modulus and density are 200 GPa and 7850 kg m^{-3} respectively. The postulated stiffness profiles for each target model are weighted by multiplying by a pre-defined stiffness weighting, and soil masses are applied by weighting Equation (3.3) by different amounts. The damping ratios for the 1st and 2nd modes are taken as 3% and 5%, to reasonably model the energy dissipation from fully embedded piles. The 5% damping ratio for the 2nd mode of vibration is used as a simplification to suppress higher modes and is based on experimental and empirical observations from real piles (Wu et al., 2018). The target piles are assumed to be open-ended and fully coring (internal soil at same level as external ground level) and the internal sand's density is assumed as 2000 kg m^{-3}.

Noise is added to the acceleration data of target models 17 and 18 to simulate realistic conditions where sensors may encounter interference, simulating scenarios encountered in the field. In order to produce the signal with noise, the method developed by Lyons (1997) is used to incorporate noise using a signal-to-noise ratio (SNR). This incorporation of noise can be observed by the oscillations on the acceleration signal, and it allows the analysis to encompass the challenge of peak detection when those oscillations exist (Wu et al., 2018). In this work, signals with an SNR of 20 are used for target models 17 and 18.

In target models 19 to 22, uncertainty is introduced into the stiffness distribu-

tion, adopting a constant mean profile for models 19 and 21 and a parabolic mean profile for models 20 and 22, as depicted in Figures 3.2(c) to (f). The purpose of introducing uncertainty is to reflect the situation whereby there would be errors in estimating the stiffness distribution from a CPT profile in the real case, due to measurement and transformation errors (Reale et al., 2021). It is of interest to assess the influence of this error on the estimated embedded length. To introduce this uncertainty, random values are added from a Gaussian distribution to the shear modulus values at each depth. For models 19 and 20, random values with a standard deviation of the distribution equal to 5×10^5 Pa are added, and for models 21 and 22, random values with a standard deviation of the distribution equal to 20×10^5 Pa are added. This uncertainty then influences the stiffness profile at each spring's depth, which results in uncertainty in the spring stiffness value used in the model-updating method.

To help interpret the table structure, rows 1 and 2 are briefly explained. Model 1 represents a pile with radius $r = 0.5$ m and wall thickness $t_0 = 0.025$ m, embedded in a constant-stiffness soil profile with mass and stiffness weightings of 5 and 0.5, respectively, and an embedded length of 10 m. Model 2 is identical in geometry and soil profile but uses higher weightings (15 and 1.5), enabling comparison under controlled conditions. This structure is consistent across the table, supporting systematic evaluation of model performance under varied geometries, material properties, noise, and soil uncertainty. Table 3.1 presents information related to all 22 target models.

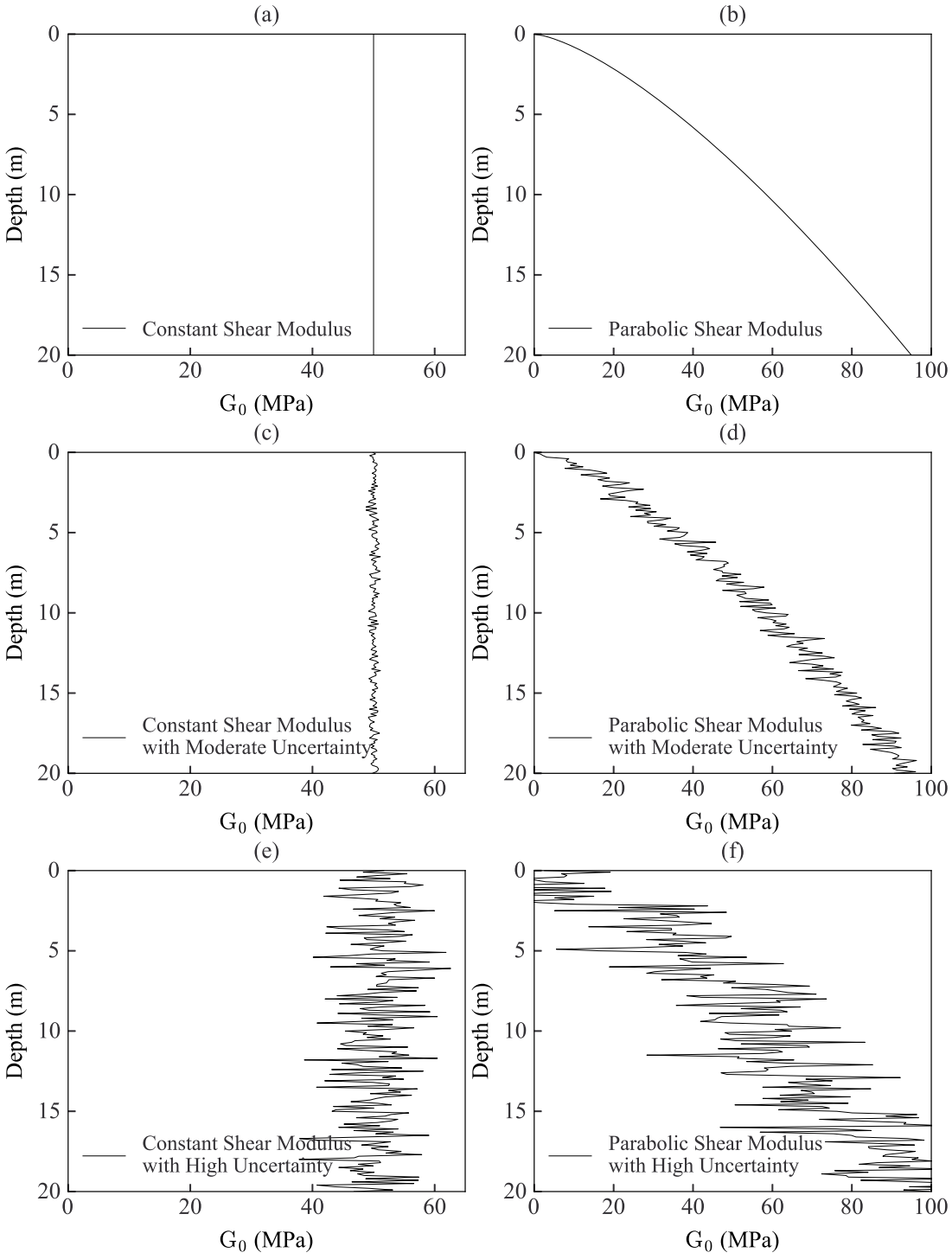

Figure 3.2: Shear modulus of soil profiles used in the analysis: (a) constant profile, (b) parabolic profile, (c) constant profile with moderate uncertainty, (d) parabolic profile with moderate uncertainty, (e) constant profile with high uncertainty, (f) parabolic profile with high uncertainty.

Table 3.1: Target models

Model	Profile	Mass Weighting	Stiffness Weighting	r (m)	t_0 (m)	L_1 (m)	L/D	SNR	Uncertainty (Y/N)
1	Const.	5	0.5	0.5	0.025	10	10	-	N
2	Const.	15	1.5	0.5	0.025	10	10	-	N
3	Const.	5	0.5	0.5	0.025	20	20	-	N
4	Const.	15	1.5	0.5	0.025	20	20	-	N
5	Const.	5	0.5	0.5	0.025	30	30	-	N
6	Const.	15	1.5	0.5	0.025	30	30	-	N
7	Const.	5	0.5	2	0.1	10	2.5	-	N
8	Const.	15	1.5	2	0.1	10	2.5	-	N
9	Const.	5	0.5	2	0.1	20	5	-	N
10	Const.	15	1.5	2	0.1	20	5	-	N
11	Const.	5	0.5	2	0.1	30	7.5	-	N
12	Const.	15	1.5	2	0.1	30	7.5	-	N
13	Parab.	5	0.5	0.5	0.025	10	10	-	N
14	Parab.	15	1.5	0.5	0.025	30	30	-	N
15	Parab.	5	0.5	2	0.1	10	2.5	-	N
16	Parab.	15	1.5	2	0.1	30	7.5	-	N
17	Const.	15	1.5	2	0.1	10	5	20	N
18	Const.	15	1.5	2	0.1	20	5	20	N
19	Const.	5	0.5	0.5	0.025	20	5	-	Y
20	Parab.	5	0.5	0.5	0.025	20	5	-	Y
21	Const.	5	0.5	0.5	0.025	20	5	-	Y
22	Parab.	5	0.5	0.5	0.025	20	5	-	Y

3.4.2 Influence of pile length on FRF

In this section, the influence of the pile length on the estimated mobilised stiffness and mass contribution of piles is assessed with a view to demonstrating how incorrect lengths can result in false predictions of soil mass and stiffness contributing to dynamic motion. The length of a pile, which generates significant soil reaction under lateral loading, is termed the active length L_a (Poulos & Davis, 1980). Piles with lengths greater than the active length do not experience significant changes in the lateral pile head displacements under applied loads, i.e., further increases of the length beyond the active length have limited to no further effects on the pile head lateral resistance properties. The active length is mostly affected by the pile-soil stiffness ratio and is typically 10 to 15 times larger than the diameter of the pile, but it also varies for static and dynamic loads (Randolph, 1981; Velez et al., 1983).

The active length influences the perceived dynamics of the soil-pile system. Figure 3.3 illustrates the magnitude of the first peak in the acceleration FRF for a 2 m diameter pile with varying embedded lengths. To construct these figures, a series of models were developed with embedded lengths ranging from 2 m to 100 m in increments of 0.1 m. Each model was subjected to a unit impulse load,

and the magnitude of the first peak in the acceleration FRF at the pile head was recorded. This procedure quantifies the sensitivity of the dynamic response to pile length and facilitates comparison with analytical predictions of active length.

Figure 3.3(a) corresponds to a pile exhibiting coring behaviour (internal soil fully present up to ground level) with an external soil mass applied over the top quarter of the pile, equal in magnitude to the pile mass. Figure 3.3(b) shows results for a pile with no internal soil and no external masses on the springs. These different assumptions significantly affect the dynamic response, which explains the difference in the vertical (Y-axis) scale between the two subfigures. Specifically, the Y-axis scale in (a) is smaller than in (b) due to the presence of additional external soil mass attached to the springs, which increases the overall inertia and therefore lowers the acceleration response under the same applied force.

It can be seen that the acceleration FRF peak stabilises for piles longer than approximately 25 m, indicating convergence towards the system's active length. This threshold aligns well with analytical expressions for active length found in the literature (Gazetas & Dobry, 1984; Pender, 1993; Poulos & Davis, 1980; Randolph, 1981). In contrast, the simplified case without internal soil or external mass reaches a plateau at a shorter length due to the reduced effective inertia and stiffness distribution.

Sample acceleration time signals, along with their corresponding FRFs, used to compute such peaks can be found later in Figures 3.9 and 3.10.

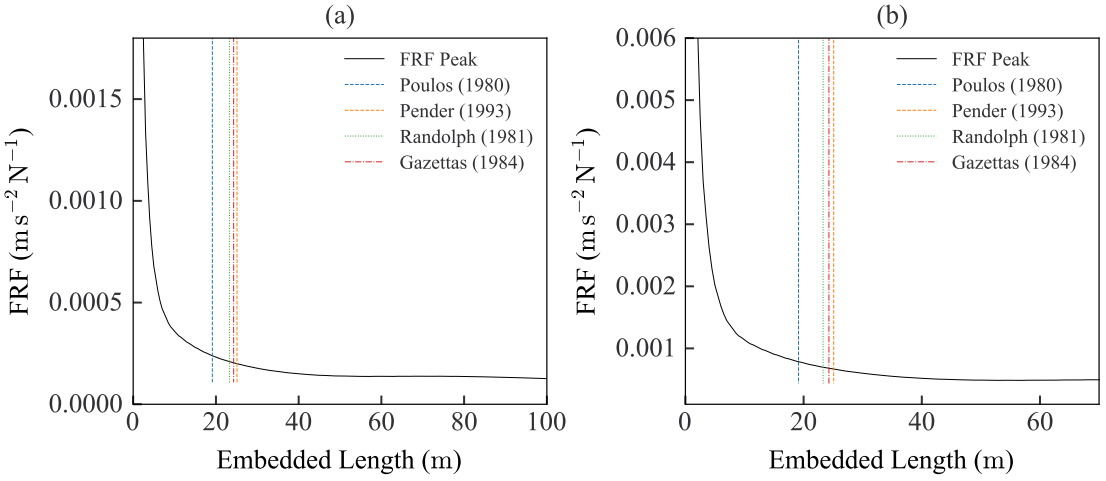

Figure 3.3: (a) Effect of pile length on the response of laterally loaded piles with masses distributed on the top quarter and with internal soil mass, (b) Effect of pile length on the response of laterally loaded piles without any soil mass distributed in the springs and without internal soil.

Figure 3.4(a) shows how the acceleration FRF peak varies with mass weighting and pile length, and Figure 3.4(b) shows how the acceleration FRF peak varies

with the stiffness weighting and pile length. To generate these plots, a stiffness weighting equal to 1 is considered in Figure 3.4(a), and a mass weighting equal to 1 in Figure 3.4(b). From Figures 3.4(a) and (b), it can be observed that a smaller length results in larger accelerations; for example, decreasing the pile length from 30 m to 10 m ($w_k = 1$, $w_m = 5.5$) results in a peak value increasing from 5.25×10^{-6} (ms^{-2} N^{-1}) to 1.54×10^{-5} (ms^{-2} N^{-1}) which as a percentage change is approximately 193%. Furthermore, the plots confirm the known theory that increased system mass (by higher applied weightings) results in lower acceleration FRF peaks, and that the acceleration FRF peaks are affected predominately by the mass weightings and the pile length, and less so from the stiffness weightings (which would affect the displacement FRF). As seen in Figure 3.4(b), increasing the stiffness weighting from 1 to 7 results in a slight increase in FRF peaks, 6.39×10^{-5} (ms^{-2} N^{-1}) to 7.48×10^{-5} (ms^{-2} N^{-1}), a change of 10% for a 17 m pile with $w_m = 1$. Conversely, for the same pile and with $w_k = 1$ in Figure 3.4(a), a significant decrease in FRF peak is observed when the mass weighting is increased from 1 to 7, from 2.87×10^{-5} (ms^{-2} N^{-1}) to 3.25×10^{-6} (ms^{-2} N^{-1}), a change of almost -89%.

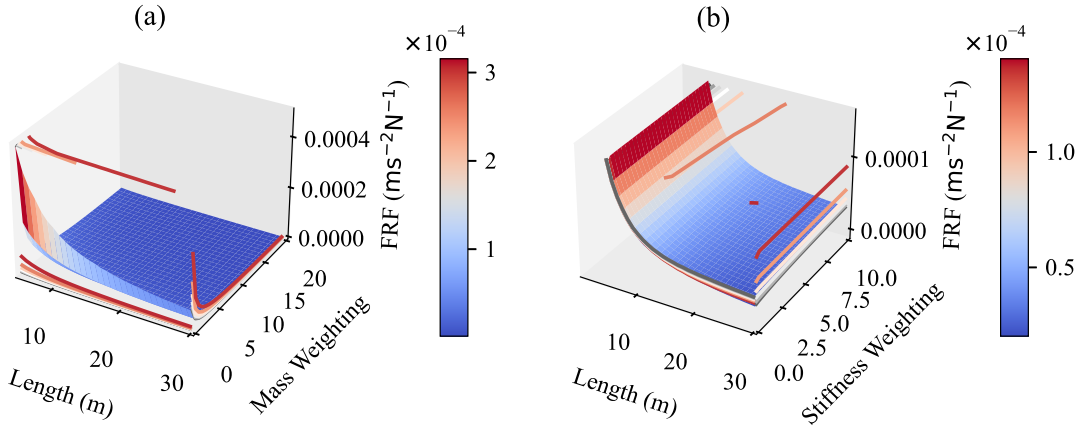

Figure 3.4: (a) Acceleration FRF peak as a function of the embedded length and mass weightings, (b) Acceleration FRF peak as a function of the embedded length and stiffness weightings.

The influence of an incorrect length on the converged mass and stiffness weightings relative to the target values is investigated in Figures 3.5–3.8. The numerical pile length is varied within a range of 60% to 140% of the original target length with a length step equal to 1% of the target length, and the converged mass and stiffness weightings (using the 1st mode model updating algorithm (Wu et al., 2018)) were compared against the target corresponding weightings for the target

models 1 - 12 (Table 3.1). For example, for Target 1, which is a 10 m pile, the lengths investigated vary from 6 m to 14 m with a step of 0.1 m. Each model is run 10 times using a HPC, and the mean value of the converged mass and stiffness weightings and their standard deviation is depicted against the relative percentage difference (DL %) of the length between the numerical and the target models. In general, Figures 3.5–3.8 demonstrate that when a numerical model has an embedded length that differs from the target model, it results in converged weightings that are associated with an error that is proportional to the error in pile length.

Figure 3.5 illustrates the mass and stiffness weighting errors for target models 1, 3, and 5, which have the same diameter (D = 1 m) and target weightings ($w_m = 5$, $w_k = 0.5$). The results show that in the shortest pile (Target 1), when modelled with a length smaller than the target pile's length, a larger error occurs as compared to longer piles (Targets 3 and 5). Furthermore, it is observed that the error is larger in the region where the pile is modelled with a smaller length than the target pile's length, compared to the region where the pile is modelled with longer lengths than the target length. This is not unexpected as longer piles approach the active length, and the errors tend towards a plateau. Additionally, by comparing the errors in mass and stiffness weightings of target models 1, 3, and 5 in the region where the numerical models are modelled with smaller lengths than the target model's length, it is observed that the error in the shorter piles is greater than the corresponding error in longer piles for the same DL %. However, when comparing the error in converged mass and stiffness weightings of the same models in the region where the numerical models have a greater length than the target model's length, a different error trend is observed in which the magnitude of the error cannot be associated with the pile length. This behaviour may be explained by the fact that the numerical models in Figure 3.5 (D = 1 m) have lengths greater than their active length, which is approximately 10 m long according to analytical equations (Gazetas & Dobry, 1984; Pender, 1993; Poulos & Davis, 1980; Randolph, 1981). Therefore, in such cases where the piles are modelled with lengths greater than their active length, the errors due to the internal soil or the distribution of the mass on the top quarter of springs could play a more significant role in the lateral behaviour than the length of the pile.

Figure 3.6 illustrates the error in mass and stiffness weightings for target models 2, 4, and 5, which have the same diameter (D = 1m) and target weightings ($w_m = 15$, $w_k = 1.5$). A similar behaviour is observed as in Figure 3.5, with the difference that greater mass and stiffness weightings ($w_m = 15$, $w_k = 1.5$) result in smaller errors compared to smaller mass and stiffness weightings ($w_m = 5$, $w_k = 0.5$).

Figures 3.7 and 3.8 present the results of the analysis performed on the remain-

ing target models, which consist of more rigid piles with a diameter of 4 m and L/D ratios of 2.5, 5, and 7.5. Compared to the flexible piles, the rigid piles exhibit greater errors, especially in the case of shorter piles. In both figures, the active length of the 4 m diameter pile is estimated at 40 m using analytical equations (Gazetas & Dobry, 1984; Pender, 1993; Poulos & Davis, 1980; Randolph, 1981), and the graphs demonstrate that the errors of the shorter piles are larger than those of the longer piles across the entire range.

In summary, Figures 3.5–3.8 demonstrate that, when the embedded length in the numerical model is shorter than that in the target model, larger errors result. This is because as the length of the pile increases, it approaches or exceeds the active length beyond which any further increase in length results in a minimal change in the lateral response of the pile. This brief study demonstrates that an incorrect length can result in a significantly inaccurate estimate of the mobilised soil mass and stiffness in an FRF-based model updating framework.

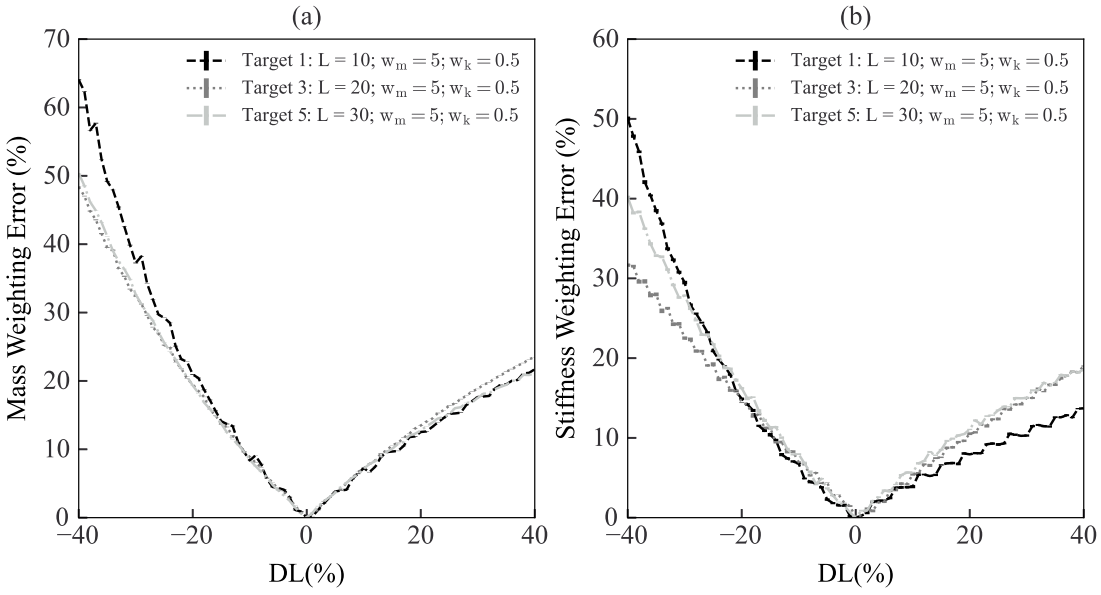

Figure 3.5: (a) Mass weighting error for target models 1, 3 and 5, (b) Stiffness weighting error for target models 1, 3 and 5 (DL = % difference in length between target and numerical model).

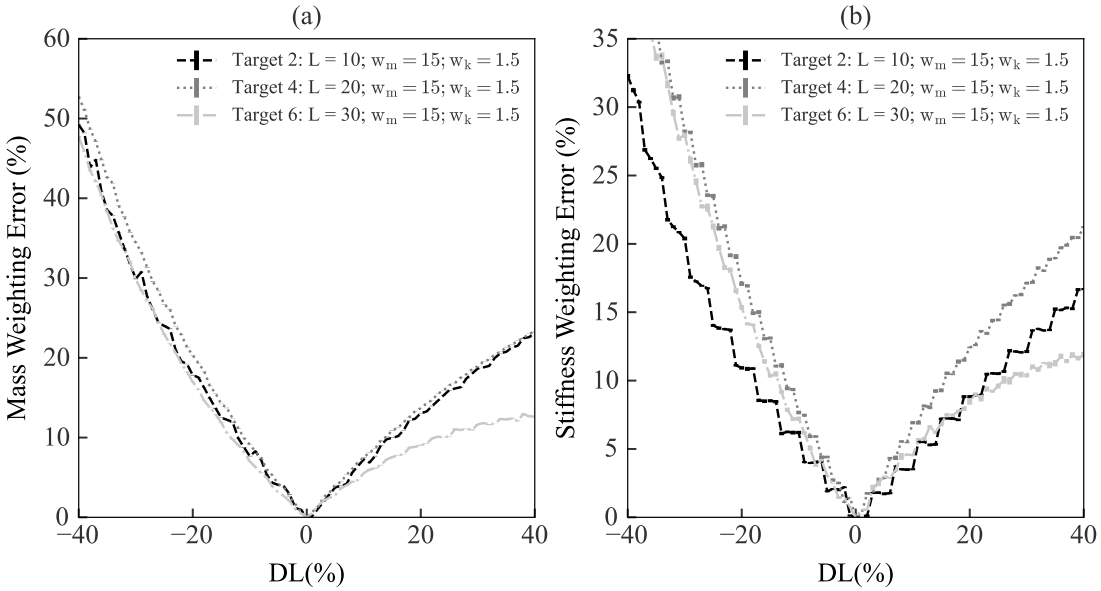

Figure 3.6: (a) Mass weighting error for target models 2, 4 and 6, (b) Stiffness weighting error for target models 2, 4 and 6 (DL = % difference in length between target and numerical model).

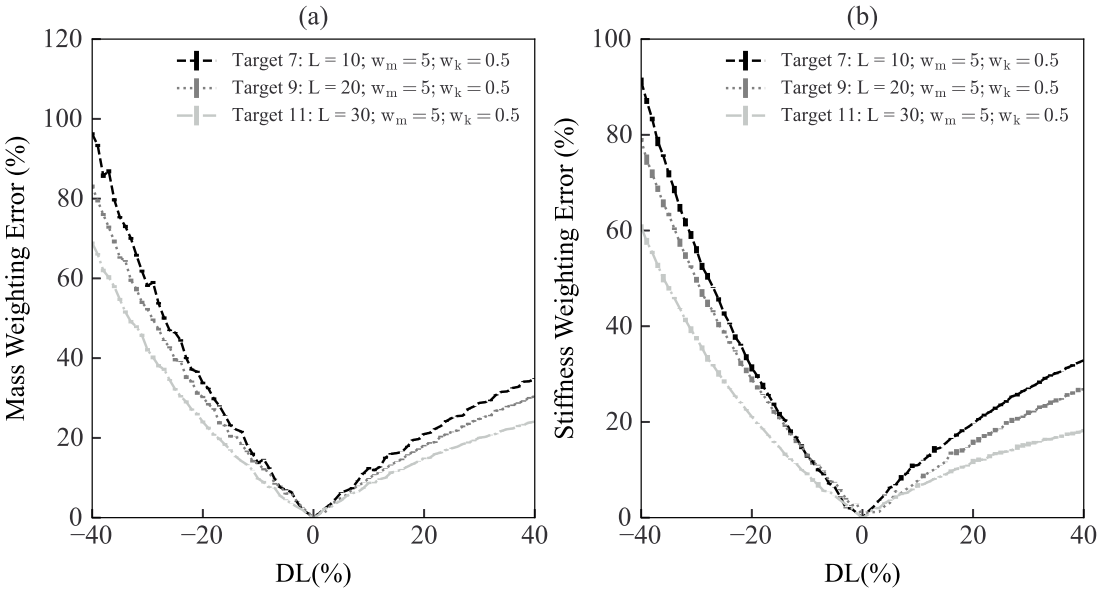

Figure 3.7: (a) Mass weighting error for target models 7, 9 and 11, (b) Stiffness weighting error for target models 7, 9 and 11 (DL = % difference in length between target and numerical model).

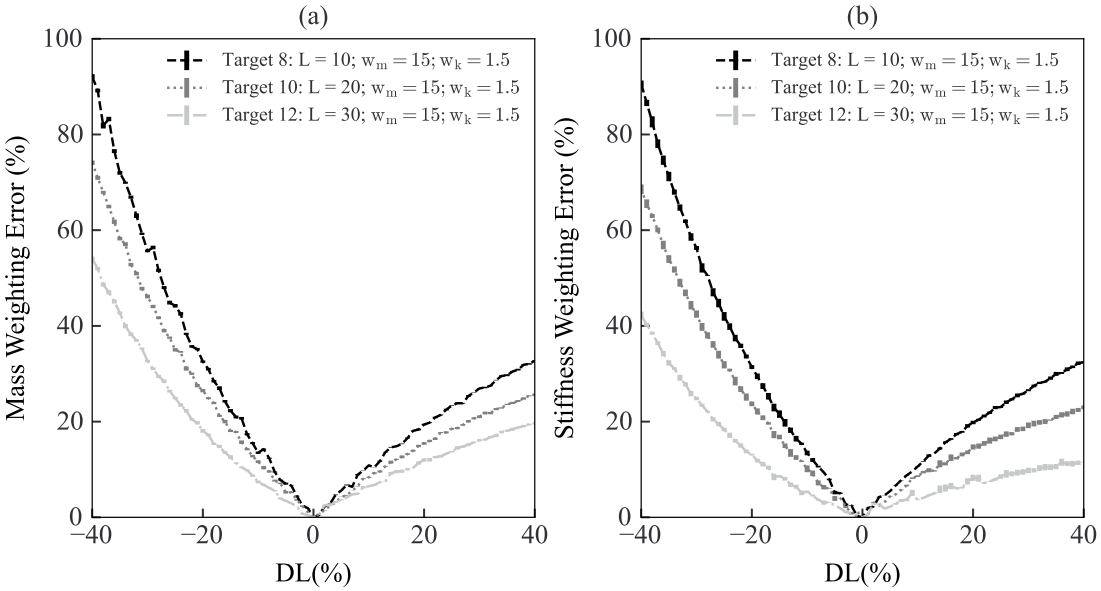

Figure 3.8: (a) Mass weighting error for target models 8, 10 and 12, (b) Stiffness weighting error for target models 8, 10 and 12 (DL = % difference in length between target and numerical model).

3.4.3 Estimation of length

The two-stage algorithm is used in this section to estimate the stiffness and mass of the target models, as well as the embedded lengths. Figure 3.9 illustrates a comparison of the acceleration profiles of target model 2 obtained after completing stage 1 of the updating process, i.e., to match the mass and stiffness weightings, but where the length may not be correct. The purpose of this analysis is to show that a match can be obtained to the first mode of vibration even when the lengths do not match, but the second mode of vibration will not match in this case. The figure compares two numerical models against the target model; the initial guess model with an embedded length of 20 m, and the converged model with an embedded length of 10.1 m. The model responses are evaluated against the monitored (calculated) acceleration profile of Target 2, which has an embedded length of 10 m. In order to compare the time-domain data for different modes, the acceleration signals are filtered using a low and band-pass Butterworth filter to separate the responses into modes 1 and 2. Specifically, Figure 3.9(a) presents the acceleration profiles for frequencies up to 6 Hz, with the first monitored frequency being 3.33 Hz, and Figure 3.9(b) displays the acceleration profiles after applying a filter for the frequency bands from 6 to 30 Hz, as the second natural frequency of the target model is 15.86 Hz. As expected, after completing stage 1 of the model updating, both models match the acceleration profiles of the target model in the first mode (3.33 Hz) in Figure 3.9(a). However, when examining the acceleration

for the second mode (15.86 Hz) in Figure 3.9(b), it is evident that the response of the initial guess model with a length of 20 m does not match that of the target model, whereas the response of the converged model with a length of 10.1 m closely matches the monitored acceleration of the target model.

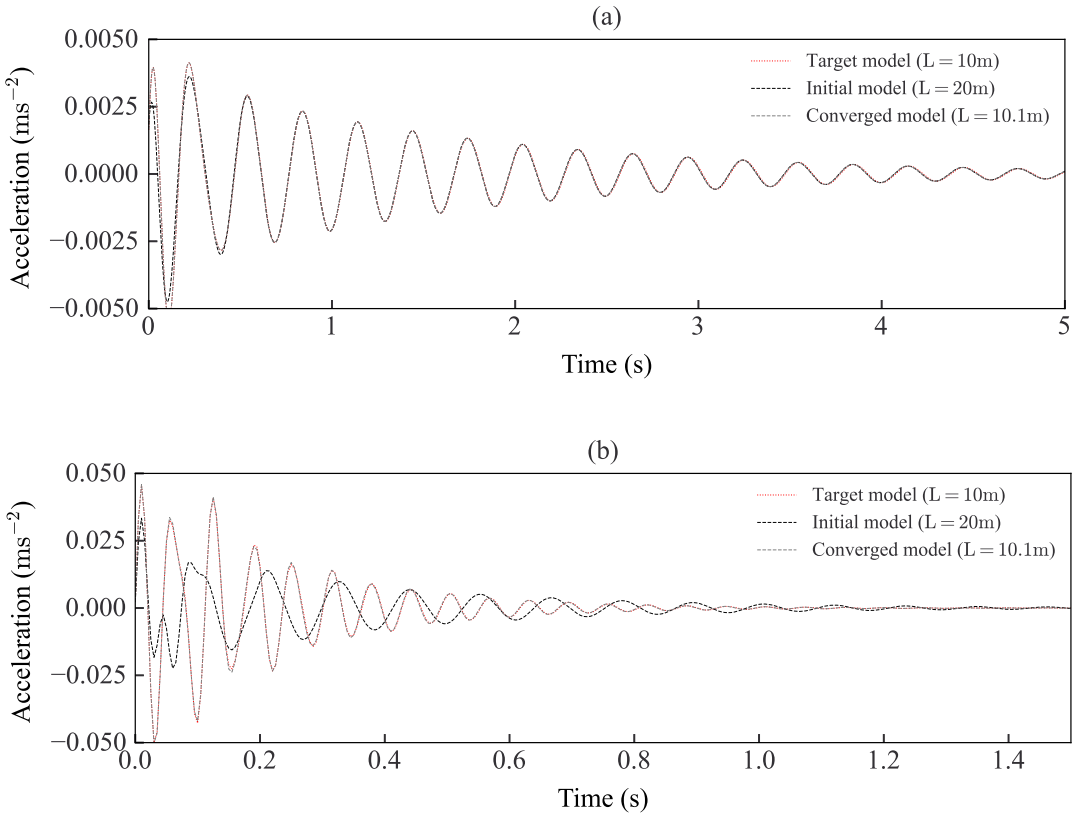

Figure 3.9: Comparison of acceleration profiles for initial (20 m) and converged (10.1 m) models against a target model (10 m). (a) First mode, (b) Second mode.

The use of the two-stage model updating approach is investigated herein against the target models in Table 3.1, whereby the first and second modes of vibration of the target model are used to estimate the pile length along with the mass and stiffness weightings of the pile. Figure 3.10 demonstrates the FRF after each iteration whereby the first mode is used to estimate the stiffness and mass weightings, and the second mode updates the pile length estimate. In this example, target model 2 is used, which has an embedded length of 10 m, and mass and stiffness weightings $w_m^{target} = 15$ and $w_k^{target} = 1.5$, respectively, while the guess model has an initial length of 20 m and randomly applied weightings. The model successfully converges to the correct length and weightings after 9 iterations (only 4 iterations are shown for clarity; 1, 3, 6, and 9), when both the first and second peaks of the converged models match the first and second peaks obtained in the target model. The figures show that the algorithm can only work efficiently in light to medium

damped structures for the peak algorithm to be able to identify the second peak. In the FRF-based updating algorithm described, the initial model's properties and a length step are defined. The length step is used only for the first iteration and is set to 1 m by default. Using the initial guess and the first model, the next length steps are updated using linear projection until the correct length is estimated.

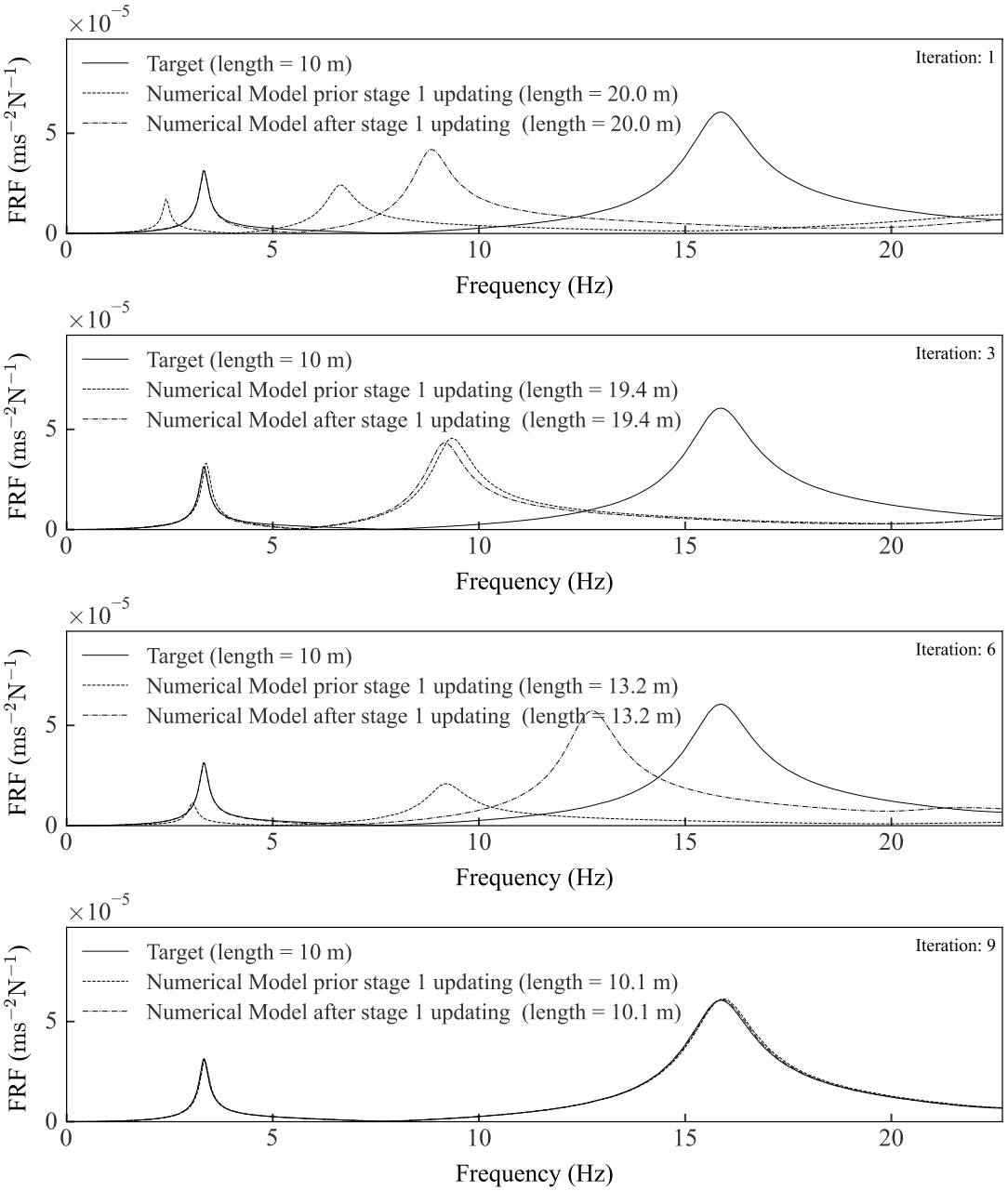

Figure 3.10: Estimation of the embedded length for target model 2 – Stage 2 Updating.

Figure 3.11 provides a visual representation of the iterative process used to optimise the length of the numerical model for the same analysis as in Figure 3.10. The graph shows that the algorithm converges to the correct length after

several iterations. The algorithm iterates until both the target and numerical models' peaks fall within the tolerance range. Eventually, the algorithm finds a solution that satisfies the tolerance criteria, resulting in a final length of 10.1 m. This demonstrates that the proposed approach is effective in optimising the length of the numerical model and achieving the desired level of accuracy. It is worth noting that the number of iterations required for convergence may vary depending on the parameters of the model and the desired level of accuracy. Nonetheless, the presented results show that the iterative optimisation approach can produce accurate numerical models that closely match the geometry of the target models.

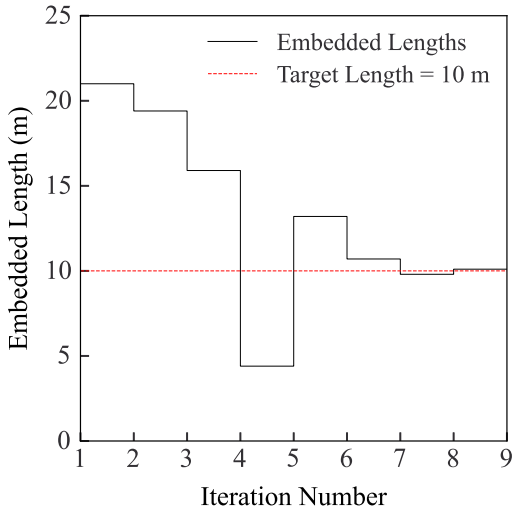

Figure 3.11: Length estimation after each iteration for target model 2.

Figure 3.12 illustrates the obtained mass and stiffness weightings after each iteration until the model reaches convergence. The figure shows that the algorithm adjusts the mass and stiffness weightings in each iteration until the first two peaks of the numerical and target models match. The convergence of the model indicates that the iterative procedure used for optimising the numerical model was successful. Ultimately, the final mass and stiffness weightings are shown to be very close to the target values, further demonstrating the effectiveness of the proposed approach.

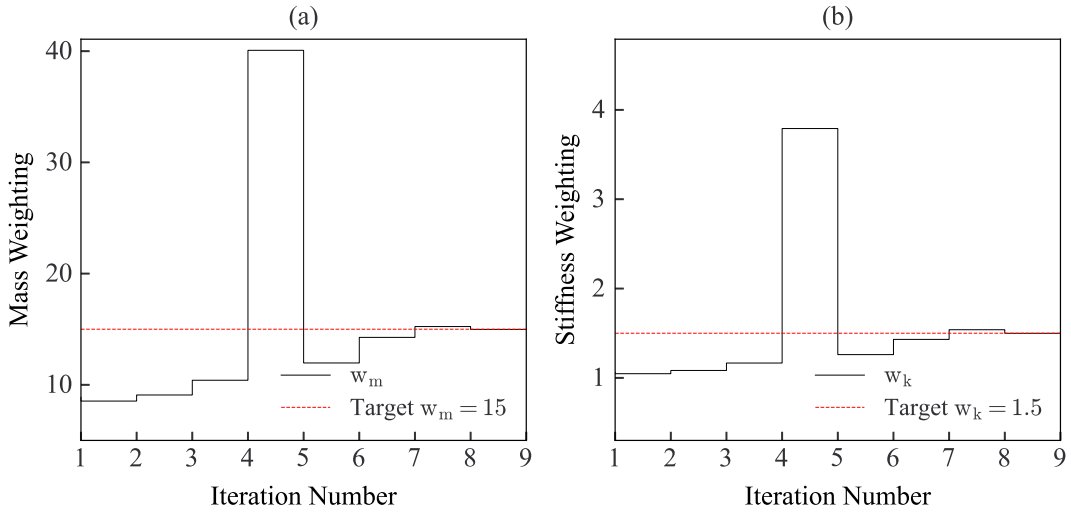

Figure 3.12: (a): Mass weighting after each iteration, (b) Stiffness weighting after each iteration, for target model 2.

Table 3.2 summarises the results from running all the target models one time. As can be seen, the percentage error in the calculated length is at most 3% (Target 18), which contained added noise. It is interesting to note that the models incorporating uncertainty in the derived stiffness profile (Targets 19 - 22) exhibited minimal errors regarding estimated length, indicating that the approach may not be overly sensitive to uncertainties in geotechnical characterisation for the scenarios evaluated in this study. However, in target models 21 and 22, slightly larger errors are observed in the model-updating approach, necessitating the use of a larger tolerance in the optimisation process to achieve convergence. For these simulations, the tolerance was increased from 0.1% to 3%. Additionally, target model 22, which features a parabolic mean stiffness profile with large added uncertainty, showed that while the optimisation accurately converged on the correct length and mobilised mass, there was a larger error in the converged stiffness weighting. This is sensible when one considers the error introduced to the model related to a mismatch in the stiffness profiles between the target and numerical model.

The high accuracy observed here is partly attributed to the fact that the target and updating models are identical in all aspects except for the three parameters being estimated. In practical applications involving experimental data, discrepancies are expected to be larger due to modelling assumptions, unknown boundary conditions, and additional sources of uncertainty.

Table 3.2: Updated parameters for all target models

Target	$\mathbf{L}_{\text{target}}$ **(m)**	$\mathbf{L}_{\text{num}}$ **(m)**	$\mathbf{L}_{\text{diff}}$ **(%)**	$\mathbf{w}_{\text{mnum}}$	$\mathbf{w}_{\text{knum}}$	$\mathbf{w}_{\text{mtarg}}$	$\mathbf{w}_{\text{ktarg}}$
1	10	10.0	0.00	5.000	0.497	5	0.5
2	10	10.1	1.00	14.982	1.497	15	1.5
3	20	20.1	0.50	4.961	0.500	5	0.5
4	20	19.7	1.50	15.116	1.522	15	1.5
5	30	30.4	1.33	4.947	0.498	5	0.5
6	30	29.9	0.33	15.0584	1.498	15	1.5
7	10	10.0	0.00	4.982	0.498	5	0.5
8	10	10.0	0.00	15.098	1.498	15	1.5
9	20	20.3	1.50	4.965	0.499	5	0.5
10	20	20.0	0.00	15.077	1.503	15	1.5
11	30	29.8	0.66	5.017	0.504	5	0.5
12	30	29.9	0.33	14.907	1.465	15	1.5
13	10	10.1	1.00	4.997	0.493	5	0.5
14	30	30.1	0.33	14.952	1.503	15	1.5
15	10	10.0	0.00	5.045	0.496	5	0.5
16	30	30.2	0.66	15.255	1.568	15	1.5
17	10	10.2	2.00	17.241	1.715	15	1.5
18	20	20.6	3.00	17.150	1.702	15	1.5
19	20	20.0	0.00	5.003	0.502	5	0.5
20	20	19.8	1.00	5.046	0.513	5	0.5
21	20	20.1	0.50	4.934	0.487	5	0.5
22	20	20.0	0.00	5.000	0.541	5	0.5

Figure 3.13 illustrates the repeatability of the application of the model updating method, in order to show how it can reliably calculate the properties when run a number of times. The method was run for target model 2 a total of 200 times, each model beginning with initial pile lengths sampled from a uniform distribution ranging from 5 m to 40 m. The purpose is to demonstrate that the approach works for a range of starting estimates of the initial pile length and weighting guesses. These bounds were selected to capture the range of realistic cases for pile lengths given the specific parameters defined for the properties of Target 2. As seen in Figure 3.13, the 200 runs converge to values of mass and stiffness weightings, and length values, that are close to the target values. The repeated procedure highlights the robustness of the method, and the results suggest that the initial guess of pile length does not impact the model's ability to converge accurately. This consistency underscores the reliability of the updating method, demonstrating its

effectiveness in adjusting the model to the target specifications irrespective of the starting values.

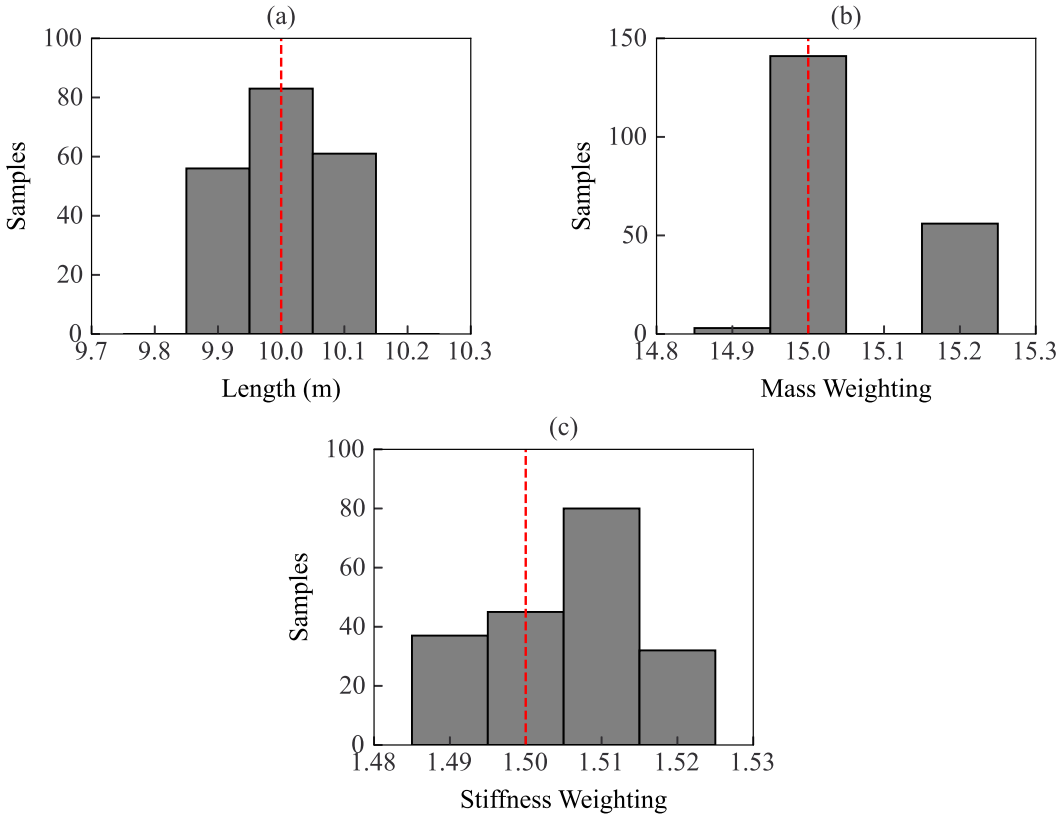

Figure 3.13: Histograms for parameters of target model 2 over 200 simulations. (a) Converged pile lengths, (b) converged mass weightings, and (c) converged Stiffness weightings. Red dashed lines show target values.

3.5 Conclusion

In this chapter, a two-stage model updating approach for estimating the embedded length, mobilised soil stiffness, and mass in laterally impacted foundation piles is presented. The approach is an enhancement of a previously developed method that uses simulated and experimental data to identify the mobilised mass and stiffness of the soil contributing to dynamic motion of laterally-impacted foundation piles. The method is extended in this study to estimate the embedded length by using the first two modes of vibration of the system, through a two-stage iterative approach. The embedded length is an important parameter, and estimating it correctly can improve the accuracy of damage detection models requiring accurate foundation data.

The previously developed updating method based on the 1st mode of vibration is initially used in this chapter to quantify the error when an incorrect pile length is

assumed in the reference numerical model. Simulated impact tests are performed on three piles with varying L/D ratios to derive FRFs, which are used as a target in an algorithm to estimate the updating parameters. The initial stiffness guess is informed using the subgrade reaction formulation, and the soil mass is assumed to be distributed in the upper quarter of the pile's embedded length. The results showed that the pile length has a critical role in the FRF, leading to changes in the obtained acceleration of the soil-pile system. When the assumed length of the pile does not match the length of the actual (target) pile, significant errors arise in the estimated soil mass and stiffness contributing to the dynamic motion. This signifies the need to develop a technique for estimating pile embedded length.

To address this need, an iterative two-stage model updating method is developed, which uses both the first and second mode of vibration peaks in the FRF to update the parameters of interest (mass, stiffness, and length). The method essentially tries to minimise the difference between the numerical and target model's FRF by matching both first and second frequency peaks. The updating method has been demonstrated in this chapter against numerically simulated data and has been shown to successfully converge on the correct pile length, as well as mobilised soil mass and stiffness, for each case application considered. It should be noted that for application to real piles, the mobilised soil stiffness and mass are not known beforehand, and only the FRF would be measured. It is also important to highlight that the approach requires a clear detection of both the first and second lateral vibration modes from embedded piles, and may not work well in heavily damped systems. While the numerical testing in this chapter shows promise, the method should be appraised against real experimental results before firm conclusions on its performance can be provided in this respect.

It should be noted that the method may only work effectively for cases where the pile length does not significantly exceed the active length of the system. This is because, as the pile length extends beyond a certain critical point, its impact on the lateral response becomes progressively less significant. Consequently, distinguishing changes in the pile's dynamic behaviour due to further length increases becomes more difficult, potentially affecting the accuracy of the estimation method in such scenarios.

Further enhancements to the approach include incorporating nonlinearity in the soil-pile interaction response, by enabling strain-related reductions in soil shear modulus to be estimated. Furthermore, the updating method holds strong potential to be modified for different mechanical systems and parameters beyond the application to pile foundations, as presented in this work.

Chapter 4

An indirect data-driven model-updating framework to estimate soil-pile interaction parameters using output-only data

Authors: Andreas Ioakim, Szymon Greś, Michael Döhler, Luke J. Prendergast, Eleni Chatzi

Paper Status: Published in Engineering Structures
DOI: 10.1016/j.engstruct.2025.119699

4.1 Introduction

This chapter presents a data-driven model updating framework to estimate the operational parameters of a laterally-impacted pile. The goal is to facilitate the estimation of soil-pile interaction (SPI) parameters such as the mobilised mass and stiffness, as well as geometrical data such as embedded pile length, using output-only information. Accurate knowledge of mass, stiffness, and pile embedded length is essential for understanding foundation behaviour when developing digital-twin models of structures for the purpose of damage detection. The method first employs subspace identification to determine modal parameters and quantifies their uncertainties using output-only data. The covariance matrix adaptation evolution strategy (CMA-ES), a stochastic evolutionary algorithm, is subsequently used to update the model. The effectiveness of the approach is demonstrated through its application to numerical models in this chapter, to quantify errors, and subsequently to data from a documented full-scale field test of a pile subjected to an impact load. The work underscores the potential of statistical updating in advancing the accuracy and reliability of soil-structure interaction parameter estimation for systems where only output data might exist.

In this study, the parameters of interest are the embedded length of the pile, as well as the distribution of soil stiffness and mass along its depth. As demonstrated in Chapter 3, deterministic model updating is feasible when both the input and output signals are known. However, in operational structures, input forces are often unknown or difficult to measure, making such methods inapplicable. The framework introduced in this chapter addresses this limitation by enabling parameter estimation using only output measurements, without requiring knowledge of the input force. This significantly broadens the applicability of model updating techniques to real-world structural monitoring scenarios.

The structure of the chapter is as follows: Section 4.2 provides an overview of the model updating framework. This section details the monopile system modelling using 1-D modelling, followed by the formulation of the objective function for model updating and the CMA-ES optimisation strategy. Section 4.3 presents a numerical application to test the framework. Section 4.4 evaluates the model updating procedure using data from a documented large-scale field test on a pile foundation. Final remarks on the effectiveness of the framework are discussed in Section 4.5.

4.2 Methodology

The objective of this work is to develop an approach that can estimate the physical properties of both the soil and the pile in a SPI problem, where the excitation applied is assumed unknown. The estimates of physical parameters are obtained through stochastic optimisation of an objective function that confronts the modal parameter estimates of the pile within their estimation uncertainties to the corresponding parameters of the pile model. This is based on the evolutionary optimisation strategy devised in Greś et al. (2021d).

The model updating framework proposed in this chapter is considered stochastic for two main reasons. Firstly, the system identification is performed using output-only Stochastic Subspace Identification (SSI), in contrast to the deterministic input-output identification via FRF peak picking used in Chapter 3. SSI accounts for noise in the data and does not require knowledge of the input excitation, making it particularly suitable for operational structures. Secondly, the model updating is carried out using a stochastic evolutionary optimisation algorithm (CMA-ES), which explores a population of models and incorporates randomness into the search process. This is fundamentally different from the deterministic updating method employed in Chapter 3, where a single model is iteratively adjusted using a linear projection-based approach. Therefore, the term stochastic in this context refers both to the nature of the system identification (noise-aware, output-only) and the optimisation method (population-based, randomised search), distinguishing it from the deterministic framework previously introduced.

Hereafter the parametric model of the pile foundation is described and the optimisation procedure is outlined.

4.2.1 Physics-based SPI modelling

The dynamics of the monitored parametric linear time-invariant system with d degrees of freedom (DOF) are described by the differential equation of motion. The governing differential equation (3.4) is linear in nature, as the system's response depends linearly on the external forces and state variables. The assumption of time-invariance is appropriate because the system matrices do not explicitly change with time during the analysis (Burd et al., 2020a; Doherty & Gavin, 2012a).

$$\mathcal{M}^{\theta}\ddot{\mathbf{q}}(t) + \mathcal{D}^{\theta}\dot{\mathbf{q}}(t) + \mathcal{K}^{\theta}\mathbf{q}(t) = \mathbf{u}(t) \tag{3.4}$$

where t denotes continuous time, $\mathcal{M}^{\theta}$, $\mathcal{D}^{\theta}$, and $\mathcal{K}^{\theta} \in \mathbb{R}^{d\times d}$ denote the mass,

damping, and stiffness matrices, respectively and θ is the system parameter. For the considered problem, the system parameter θ holds the embedded pile length L_1, which is the geometrical data of interest, and the mass and stiffness weightings (w_m) and (w_k) that scale the soil mass and stiffness profiles, respectively. These weightings are used to define the soil mobilised mass and stiffness profiles (Wu et al., 2018). The vectors $\mathbf{q}(t)$ and $\mathbf{u}(t) \in \mathbb{R}^d$ denote the continuous-time displacements and the unknown external forces, respectively.

The soil-pile system is modelled using a linear Winkler model, which utilises 6 DOF Euler-Bernoulli beam/pile elements to characterise the pile, paired with 2-DOF mass-spring elements to represent the soil behaviour. The model is capable of simulating the behaviour of SPI at low strains, whereby the response of the system can be assumed linear (Kallehave et al., 2012; Prendergast & Gavin, 2016). This is appropriate to systems oscillating with low-amplitude vibrations. The local mass and stiffness matrices for the pile elements can be calculated by simplifying the Timoshenko beam theory by ignoring the effects of shear deformation and rotatory inertia (Timoshenko, 1983). The 2-DOF soil springs are connected to the lateral DOF of each node within the embedded section of the pile. The pile's base is fixed in the vertical direction to exclude axial deformations from the system. This boundary condition effectively eliminates axial DOF contributions, while preserving the intended lateral behaviour of the system. Each pile element of the pile is associated with two corresponding mass-spring elements that simulates the lateral mass and stiffness provided by the soil, extending up to the N_sth spring, which represents the topmost spring element. Specifically, the pile is discretised into a finite number of pile elements, and each mth pile element has an associated nth and $(n+1)$th mass-spring element. A schematic of the system is illustrated in Figure 4.1, which illustrates the physical system and the numerical spring-beam model representation. This figure is identical to Figure 3.1 shown in Chapter 3, with the key distinction that here the input force is considered unknown, and no known lateral impact is simulated. This reflects the output-only nature of the system identification approach applied in this chapter.

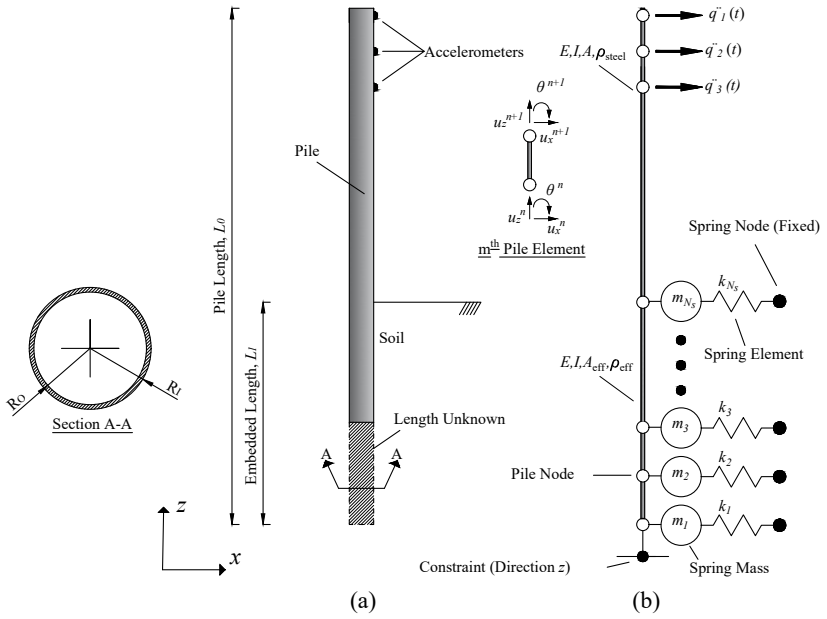

Figure 4.1: Schematic of the pile model. (a) Physical model, (b) Numerical representation.

The pile is assumed to be embedded in a single layer of cohesionless sand. The model captures the pile's flexural rigidity by incorporating the relationships between the subgrade reaction modulus and the pile material's elastic properties after Vesić (1961).

$$K_S(z) = \frac{0.65 E_S(z)}{D(1-\nu_S^2)} \sqrt{\frac{12(E_S(z)D^4)}{EI}}, \tag{4.1}$$

where, $E_S(z)$ represents the soil small-strain Young's modulus ($\mathrm{N\,m^{-2}}$) as a function of the depth z, ν_s is the soil's Poisson's ratio, D is the pile's width (m), and E and I denote the pile's Young's modulus ($\mathrm{N\,m^{-2}}$) and moment of inertia ($\mathrm{m^4}$), respectively. The small-strain Young's modulus of the soil is calculated as

$$E_S(z) = 2G_S(z)(1+\nu_S), \tag{4.2}$$

where $G_S(z)$ is the shear modulus of the soil ($\mathrm{N\,m^{-2}}$) as a function of z. Given that $K_S(z)$ has units of $\mathrm{N\,m^{-3}}$ and the springs provide one-dimensional stiffness ($\mathrm{N\,m^{-1}}$), the stiffness for each nth spring element is determined as

$$k_n = K_S(z) D L_m, \tag{4.3}$$

where L_m is the tributary length of the associated mth pile element, and $K_S(z)$ is defined in Equation (4.1). In the embedded layer, the pile nodes are attached to

lateral springs, while those above ground remain free. To simulate the dynamic influence of the mobilised mass of soil, lumped masses calculated as a fraction of the pile mass are distributed along the soil springs. Masses are added along the upper quarter of the embedded length, which is based on the premise that deeper masses exert a negligible effect on the first mode shape of a laterally-oscillating pile, leading to their exclusion (Wu et al., 2018). The mass for each nth spring is therefore a function of the pile's mass

$$M_n = \frac{M_{\text{Pile}}}{Q}, \tag{4.4}$$

where M_{Pile} is the pile's mass, and Q represents the number of springs in the top quarter of the pile.

4.2.2 Design of the objective function

The *true* modal parameters of system described in Equation (3.4) are obtained from the eigenvalues $\mu_i^\theta \in \mathbb{C}$ and eigenvectors $\Psi_i^\theta \in \mathbb{C}^d$, which are the solution of the eigenvalue problem

$$\left((\mu_i^\theta)^2 \mathcal{M}^\theta + \mu_i^\theta \mathcal{D}^\theta + \mathcal{K}^\theta\right) \Psi_i^\theta = 0 \ , \tag{4.5}$$

and yield the natural frequencies $f_i^\theta = \frac{|\mu_i^\theta|}{2\pi}$ and the mode shapes $\psi_i^\theta = L\Psi_i^\theta \in \mathbb{C}^r$ at the observed DOF for a given sensor type, where $L \in \mathbb{C}^{r\times d}$ maps the eigenvectors to the mode shapes that can be obtained from measurements at r sensors, respectively.

$\hat{f}_i$ and $\hat{\varphi}_i$ are denoted as the respective estimates of the i-th natural frequency and the i-th mode shape. The deployed system identification method is assumed consistent, i.e., $\hat{f}_i$ and $\hat{\varphi}_i$ converge to their true values $f_{i,*}$ and $\varphi_{i,*}$ when the data length N goes to infinity. This assumption is leveraged by multiple system identification methods, for example SSI methods (Döhler & Mevel, 2013; Döhler & Mevel, 2012; Peeters & De Roeck, 1999), where these parameters can be identified, e.g., from acceleration, velocity, displacement, or strain measurements. There is an inherent assumption that the system is subject to ambient white noise excitation. It should be noted that depending on the physical case considered, this assumption might not be fully valid. For example, this assumption might not be exactly true in the case of operating offshore wind turbines supported on monopiles. The modal parameter estimates have been proved to be asymptotically Gaussian for

SSI methods (Bauer et al., 1999; Mellinger et al., 2016), satisfying

$$\hat{f}_i \approx \mathcal{N}\left(f_{i,*},\ \tfrac{1}{N}\sigma_{f_i}^2\right),\ \text{and}\ \begin{bmatrix}\Re(\hat{\varphi}_i)\\ \Im(\hat{\varphi}_i)\end{bmatrix} \approx \mathcal{N}\left(\begin{bmatrix}\Re(\varphi_{i,*})\\ \Im(\varphi_{i,*})\end{bmatrix},\ \tfrac{1}{N}\Sigma_{\varphi_i}\right), \tag{4.6}$$

where $\Re(\cdot)$ and $\Im(\cdot)$ express the real and imaginary parts of a complex variable, $\mathcal{N}(\mu, \Sigma)$ denotes a Gaussian distributed variable with mean μ and covariance Σ, and $\sigma_{f_i}^2 \in \mathbb{R}$ and $\Sigma_{\varphi_i} \in \mathbb{R}^{2r\times 2r}$ are the asymptotic covariance of $\hat{f}_i$ and $\hat{\varphi}_i$, respectively. The computation of the respective covariance estimates $\hat{\sigma}_{f_i}^2$ and $\widehat{\Sigma}_{\varphi_i}$ from the same data set as the modal parameter estimates can be found, e.g., in Döhler and Mevel (2013), Mellinger et al. (2016), and Reynders et al. (2008). Since $\hat{f}_i$ is approximately Gaussian distributed, its confidence interval is symmetric and can be centred around the computed estimate. As such, it will cover a range of plausible values that include the true value of the parameter with some given confidence level γ, e.g., $\gamma = 0.9544$ for the $\pm 2\sigma$ bound. At this value, the corresponding confidence interval

$$c_{\hat{f}_i} = [\hat{f}_i^{\min}\ ,\ \hat{f}_i^{\max}] \tag{4.7}$$

encompasses the true value $f_{i,*}$, where $\hat{f}_i^{\min} = \hat{f}_i - 2\cdot\frac{1}{\sqrt{N}}\hat{\sigma}_{f_i}$ and $\hat{f}_i^{\max} = \hat{f}_i + 2\cdot\frac{1}{\sqrt{N}}\hat{\sigma}_{f_i}$ with 95.44% probability, which is hereafter denoted as the 95% confidence interval. If the natural frequency of the model f_i^θ is inside $c_{\hat{f}_i}$, then it can be inferred that both θ and θ_* are statistically close. Conversely, when θ is different from θ_*, the corresponding model frequency f_i^θ is likely to lie outside the confidence interval of the estimated frequency.

An objective function for the model optimisation is expressed by the difference between the modal parameter estimates and their model-based counterparts. It is hereafter assumed that the modal parameter pairing is accomplished with statistical criteria (Reynders, 2012). Denote $\Delta_{f_i}^\theta$ as the normalised difference between the estimated natural frequency $\hat{f}_i$ and the natural frequency f_i^θ from the model under parameter θ, with

$$\Delta_{f_i}^\theta = \begin{cases} 1 - \frac{f_i^\theta}{\hat{f}_i}, & \text{if } \hat{f}_i^{\min} \le f_i^\theta \le \hat{f}_i^{\max} \\ 1, & \text{otherwise}\ , \end{cases} \tag{4.8}$$

where a penalty of 1 is introduced when f_i^θ is outside the 95% confidence interval of $\hat{f}_i$. For the comparison of the mode shape estimate $\hat{\varphi}_i$ and model-based mode shape ψ_i^θ, the Modal Assurance Criteria (MAC) is used. If $\theta = \theta_*$, the MAC between both mode shapes is close to 1 and tends to 1 when the data length $N \to \infty$, since $\hat{\varphi}_i$ is a consistent estimate. Consequently, if the MAC between both mode shapes tends to 1, the parameter vector θ is a valid candidate for θ_*.

Let $\Delta^{\theta}_{\mathrm{MAC}_i}$ be the difference between 1 and the respective MAC, defined as

$$\Delta^{\theta}_{\mathrm{MAC}_i} = 1 - \mathrm{MAC}(\hat{\varphi}_i, \psi^{\theta}_i) \ , \tag{4.9}$$

where

$$\mathrm{MAC}(\hat{\varphi}_i, \psi^{\theta}_i) = \frac{|\hat{\varphi}_i^H \psi^{\theta}_i|^2}{\hat{\varphi}_i^H \hat{\varphi}_i \psi_i^{\theta\,H} \psi^{\theta}_i}.$$

The objective function $F(\theta)$ is expressed as the sum of the respective differences $\Delta^{\theta}_{f_i}$ and $\Delta^{\theta}_{\mathrm{MAC}_i}$ for all considered modes $i = 1, \ldots, n_{\mathrm{modes}}$, as

$$F(\theta) = \sum_{i=1}^{n_{\mathrm{modes}}} \left| \tilde{\Delta}^{\theta}_{f_i} \right| + \sum_{i=1}^{n_{\mathrm{modes}}} \Delta^{\theta}_{\mathrm{MAC}_i} \ . \tag{4.10}$$

Based on the confidence intervals (4.7), the acceptance region

$$\tilde{\Theta} = \{\theta : f^{\theta}_i \in c_{\hat{f}_i} \text{ for all } i = 1, \ldots, n_{\mathrm{modes}}\} \tag{4.11}$$

can be defined, which comprises all parameter vectors θ that yield model frequencies within the confidence intervals of their estimated counterparts. Thus, $\tilde{\Theta}$ comprises the statistically acceptable solutions for θ_* with regards to the considered frequencies, and a stopping criterion of the optimisation search can be formulated as $\theta \in \tilde{\Theta}$.

4.2.3 Model optimisation strategy

The solution θ^{sol} is obtained via minimisation of $F(\theta)$

$$\theta^{\mathrm{sol}} = \arg\min_{\theta} \ F(\theta), \tag{4.12}$$

which is achieved with an application of the CMA-ES (Hansen & Ostermeier, 2001). Starting with some initial value $\theta = \theta_{\mathrm{init}}$, the CMA-ES algorithm consists in generating λ model candidates θ^g_j, $j = 1, \ldots, \lambda$, in each population g, by sampling a multivariate Gaussian distribution. The sampling is carried out as

$$(\theta_j)^{g+1} = m^g + \varepsilon_j, \quad \varepsilon_j \sim \sigma^g \mathcal{N}\left(0, C^g\right), \tag{4.13}$$

where $j = 1, \ldots, \lambda$ and m^g is a weighted mean of the model candidates $(\theta_j)^g$ in the parent generation. Equation (4.13) represents a mutation and recombination into offspring, for which the CMA-ES algorithm adapts the parameters C^g and σ^g in each generation. The covariance matrix C^g denotes the covariance of the search distribution and σ^g denotes the scaling factor adapted (minimised) in the optimi-

sation procedure. Consequently, the optimisation continues and the best parent solutions replace the offspring until it converges to a solution. For CMA-ES, the covariance matrix C^g is incrementally updated with rank-one matrices representing the direction between the best parent solutions at two consecutive generations, such that the likelihood of previously successful search steps is increased (Hansen & Ostermeier, 2001). For the convergence to a solution, a stopping criterion is included in the algorithm that is adapted to the acceptance region (4.11), which is defined by the confidence intervals of the modal parameter estimates obtained from the sensor data. Once inside the acceptance region, there is no need to further minimise the objective function, avoiding unnecessary additional computations.

Figure 4.2 presents a flowchart of the model updating framework, demonstrating how the measurement data are linked with the SSI to obtain identified frequencies and mode shapes, coupled with their uncertainties. These identified modal properties are then combined with the computed modal properties from the numerical model to formulate the objective function used in the CMA-ES optimisation.

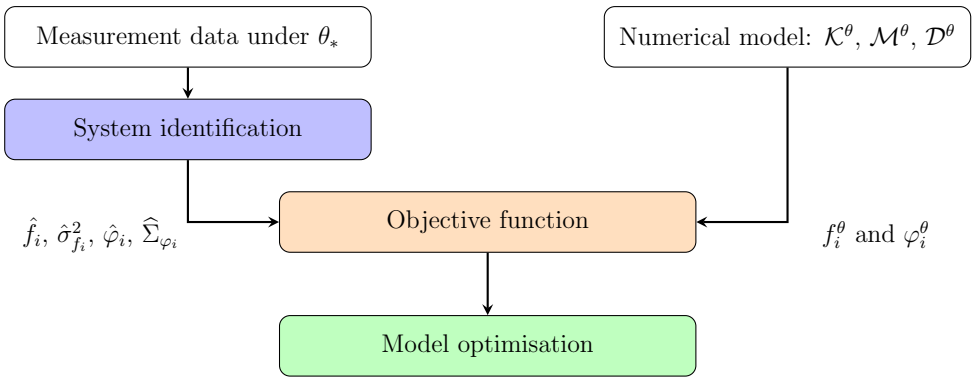

Figure 4.2: Model updating flowchart.

4.3 Numerical application

In this section, the efficacy of the proposed framework in estimating SPI parameters, including mobilised soil mass and stiffness, and embedded pile length, is evaluated. To undertake this demonstration, known values of soil mass and a profile of soil stiffness are altered by applying weightings w_m and w_k, and assessing how well the method can estimate these weightings, i.e. converge on the actual soil mass and stiffness profiles (see Wu et al. (2018) for more details on this approach). Weightings w_m and w_k are defined as scalars that adjust a given spring's mass and stiffness values. The optimisation methodology is applied to a set of target pile models (with varying geometries and soil profiles) to assess its accuracy in param-

eter estimation. For more information on the development of models for this type of application, see Ioakim and Prendergast (Ioakim & Prendergast, 2024).

Three target models (pseudo-experimental piles subjected to simulated impact tests) are developed to represent various types of piles, which are referred to as target models throughout this study. The schematic of the pile configuration is shown in Figure 4.3. As mentioned earlier, the mobilised mass of the soil is assumed as concentrated in the top quarter of the pile, in keeping with the mobilisation expected under vibration in the first mode. For simplicity, only some nodes are displayed in the schematic, with intervals of 1 meter. Table 4.1 provides specific parameter values used to create these models. To examine applications to both flexible and rigid piles, two diameters (D) with annular cross-sections and corresponding wall thicknesses (t_0) are explored: $D = 1$ m with $t_0 = 0.025$ m, and $D = 4$ m with $t_0 = 0.1$ m. Each model is constructed by discretising the pile into finite elements of 0.1 m in length. For all target models, the total pile length (L_0) is defined as the sum of the embedded length plus an additional 1 m stick-up ($L_0 = L_1 + 1$ m). These parameters are chosen to represent a range of foundation geometries typically found in various applications, including the simulation of monopiles used in offshore wind turbine foundations (Tott-Buswell et al., 2024). Additionally, to simulate real field scenarios where sensor data might be influenced by environmental factors, noise is introduced into the acceleration data.

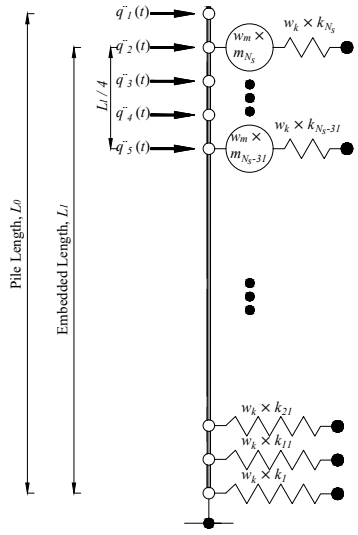

Figure 4.3: Pile configuration for numerical application.

The soil shear modulus profile is assumed as constant, analogous to an over-consolidated soil deposit, and is set at 50 MPa. Figure 4.4 illustrates the shear

modulus for target models 1 and 3, showing conditions for an exact constant profile, and a profile with some inherent variability, respectively. The Poisson's ratio is set to 0.1 for small-strain applications (Prendergast et al., 2013). For the steel piles, Young's modulus and density are specified as 200 GPa and 7850 kg m^{-3}, respectively. The stiffness profiles for each target model are adjusted by applying w_k, and soil masses are determined through w_m applied to Equation (4.4). A damping ratio of 1% is adopted to represent energy dissipation in the target piles. These piles are considered to be open-ended and fully coring, with the internal soil level matching the external ground level. Additionally, the internal sand's density is assumed to be 2000 kg m^{-3}.

In each model, a 10 kN impact load is applied to the pile for a short, arbitrary duration, following which the pile model is allowed to oscillate freely for 50 seconds. The time step (Δt) for this analysis is set at 0.005 seconds. Each target pile is equipped with five accelerometers positioned along its length (node points in numerical model), starting from the pile's head at 1 m intervals. Data from these five 'sensors' are subsequently utilised in the subspace identification process to determine four natural frequencies of the pile, along with their corresponding mode shapes. These identified parameters serve as the basis for formulating the objective function.

Table 4.1: Target models

Target Model	w_m	w_k	D (m)	t_0 (m)	L_1 (m)	L/D	Variability in G_0 (Y/N)
1	5	0.5	1	0.025	20	20	N
2	5	0.5	4	0.1	20	5	N
3	5	0.5	4	0.1	20	5	Y

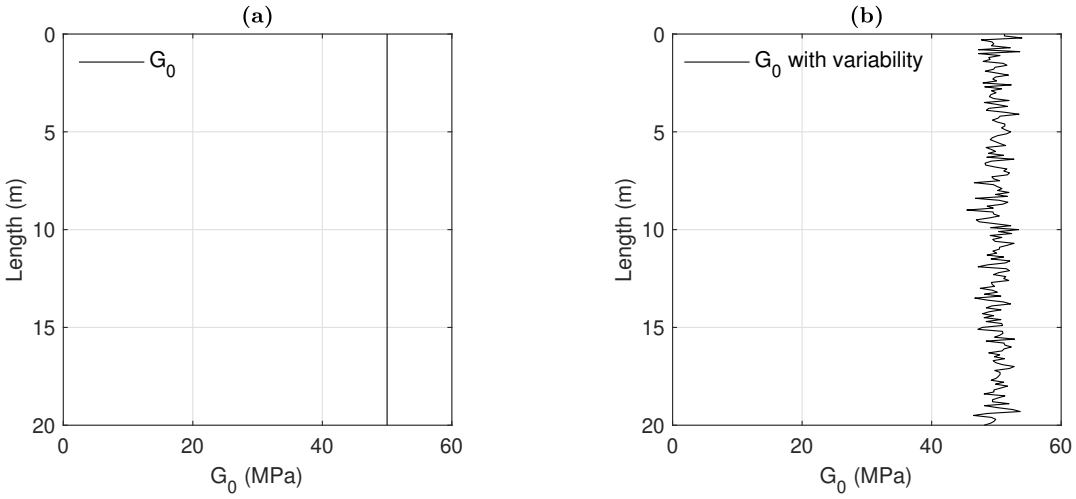

Figure 4.4: Shear modulus for (a) target 1 and (b) target 3. Target 1 represents a constant profile, where target 3 shows variability in the profile.

As an initial investigation, the objective function was plotted in Figure 4.5 for a number of parameter combinations to examine whether a global minimum existed. Specifically, w_k was set to 0.5 for target model 1, while L_1 and w_m were varied. As expected, the objective function, formulated based on the frequencies and mode shapes derived from the five sensors, was minimised for the target parameters, where $\mathrm{w}_m = 5$ and $L_1 = 20\,\mathrm{m}$.

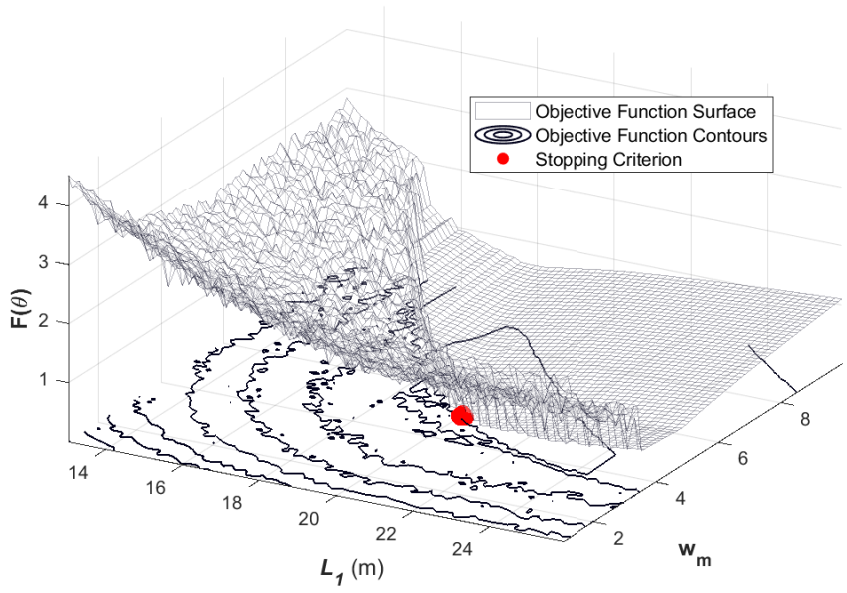

Figure 4.5: Objective function for the parameter pair L_1 and w_m in the numerical application for target model 1.

To assess the optimisation's performance to estimate w_m, w_k and L_1 effec-

tively, 100 Monte-Carlo simulations were conducted for each target model. The histograms illustrating the distributions of the estimated parameters are shown in Figures 4.6, 4.7, and 4.8 for target models 1, 2, and 3, respectively. These histograms represent the probability density functions (PDFs) of the estimated parameters, providing insight into how frequently certain parameter values occur across the simulations. A summary of the results, including the means and standard deviations of the estimated parameters, is presented in Table 4.2, providing a quantitative assessment of the optimisation's performance. From the results, it can be observed that the optimisation consistently converges to the expected values for all three parameters. It is noteworthy that in target model 3, where the stiffness has variability, the convergence results in a slightly increased stiffness. This can be explained by the fact that variability in the stiffness generates some bias, causing the actual w_k to shift slightly to the right.

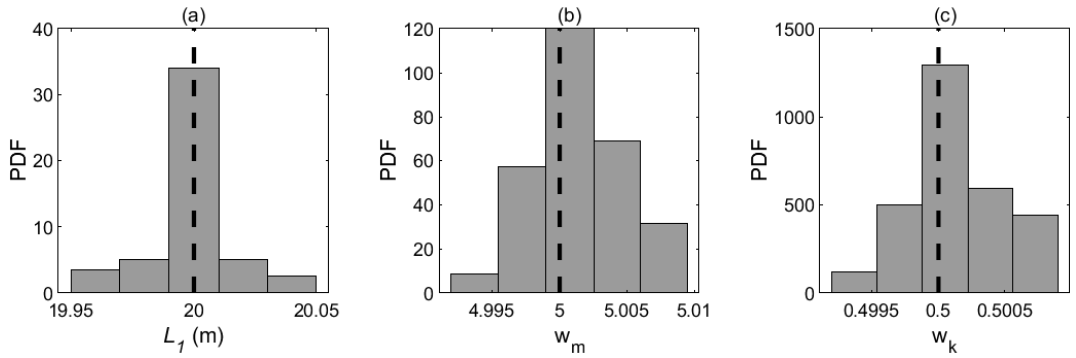

Figure 4.6: Histograms for target 1 showing the distribution of converged values for the three key parameters: (a) L_1, (b) w_m, and (c) w_k. The distributions are obtained from Monte-Carlo simulations and are plotted against the actual values of the corresponding parameters.

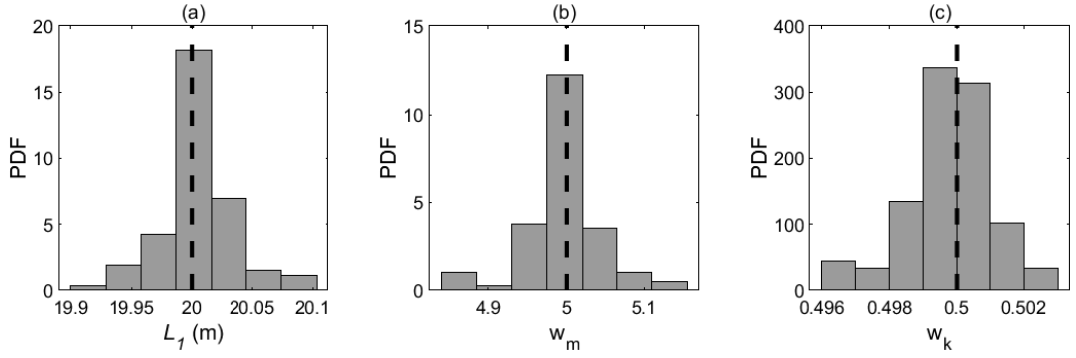

Figure 4.7: Histograms for target 2 showing the distribution of converged values for the three key parameters: (a) L_1, (b) w_m, and (c) w_k. The distributions are obtained from Monte-Carlo simulations and are plotted against the actual values of the corresponding parameters.

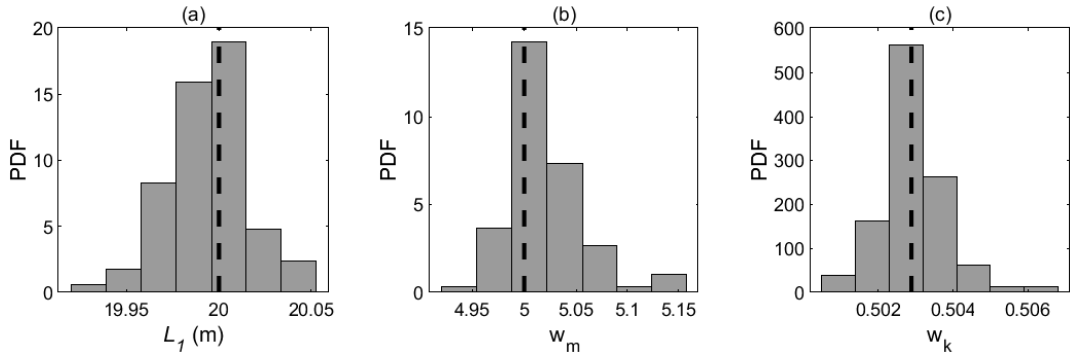

Figure 4.8: Histograms for target 3 showing the distribution of converged values for the three key parameters: (a) L_1, (b) w_m, and (c) w_k. The distributions are obtained from Monte-Carlo simulations and are plotted against the actual values of the corresponding parameters.

Table 4.2: Mean values and standard deviations of the parameters for target models 1, 2 and 3.

Target	Parameter	μ	σ	Actual Value
Target 1	L_1 (m)	20.0	0.017	20.0
	w_m	5.0	0.003	5.0
	w_k	0.5	0.0003	0.5
Target 2	L_1 (m)	20.0	0.029	20.0
	w_m	5.0	0.048	5.0
	w_k	0.5	0.001	0.5
Target 3	L_1 (m)	20.0	0.023	20.0
	w_m	5.0	0.037	5.0
	w_k	0.502	0.0009	0.502

4.4 Field application

Data from a field test reported by Prendergast and Gavin (2016) and Prendergast et al. (2019) are employed to assess the performance of the optimisation approach when applied to real data from impact tests conducted on piles. This assessment utilises small-strain soil stiffness data, including shear wave velocity measurements and the derived G_0 profile. The field test was executed at a quarry in Blessington, southwest of Dublin, Ireland and a general schematic of the pile and soil arrangement is shown in Figure 4.1. The experiment involved lateral impact testing of a 7.2 m open-ended steel pile with a diameter of 0.34 m and wall thickness of 0.014 m, embedded in dense, over-consolidated sand. Prior to testing, the soil was excavated leading to an embedment of 3.1m. In the experiment, the pile is impacted

laterally and accelerations are measured using three accelerometers placed near the top of the pile. For more information on the field testing, refer to Prendergast and Gavin (2016) and Prendergast et al. (2019).

The quarry at Blessington has undergone extensive characterisation in prior research (Doherty & Gavin, 2012b) and has been used to assess the performance of various model, prototype, and full-scale foundation installations, over a number of years. Comprehensive details on the geotechnical properties of the site can be found in several studies (Gavin et al., 2009; Gavin & Lehane, 2007; Prendergast et al., 2013). This field application relies on the site's small-strain stiffness properties, which were measured using Multi-Channel Analysis of Surface Waves (MASW) as detailed in Donohue et al. (2004). The shear wave velocity profile, depicted in Figure 4.9(a), is used to calculate the small-strain Young's modulus profile, shown in Figure 4.9(b). This calculation begins with the small-strain shear modulus (G_0) using the formula $G_0 = \rho v_s^2$, where v_s represents the shear wave velocity. Subsequently, the small-strain Young's modulus (E_0) is calculated using $E_0 = 2G_0(1+\nu_S)$, where ρ is the soil density ($\mathrm{kg\,m^{-3}}$) and ν_S is the small-strain Poisson ratio, assumed here to be 0.1. The site profile data begins at approximately 4.1 m below ground level due to the excavation process as described above, prior to dynamic testing (Prendergast & Gavin, 2016).

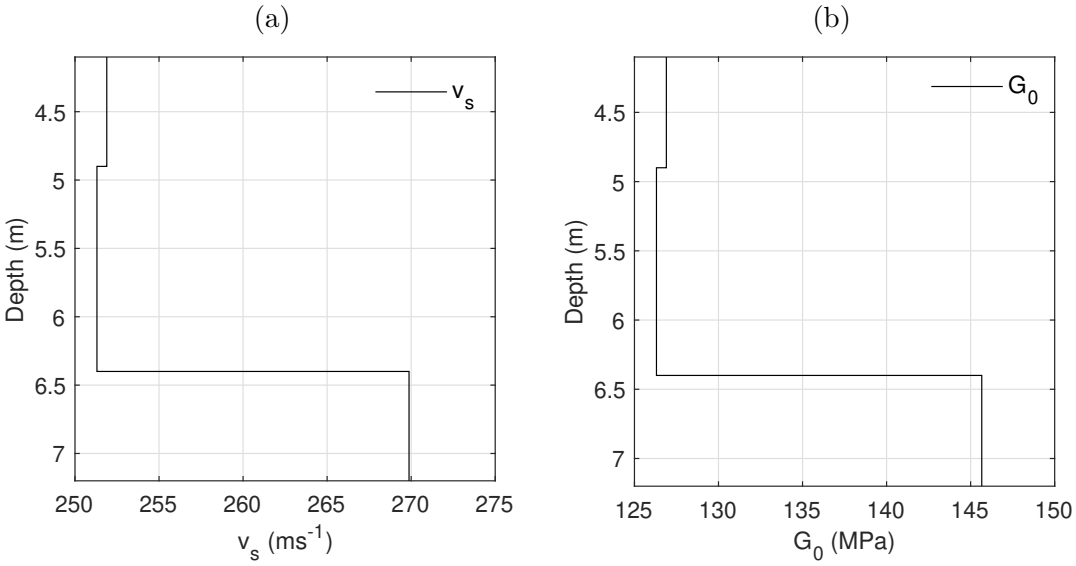

Figure 4.9: Small-strain MASW data. (a) Shear wave velocity profile. (b) Derived small-strain shear modulus profile.

The pile was equipped with three accelerometers along the exposed section of the pile, each set to record at a frequency of 1000 Hz. The testing protocol involved subjecting the pile to lateral impacts with a PCB Piezotronics 086D50 model sledgehammer-type modal hammer (PCB Piezotronics, 2018), which features a

tip mass of 5.5 kg and recording the resultant impact force time-history. Multiple impacts were performed to assess the repeatability of the results.

The procedure outlined in Section 4.2.1 is followed to construct the numerical model for the purpose of model-updating, and Equation (4.1) is applied to convert the G_0 profile into discrete spring stiffness values K_n. The response output data from two impact tests, 1 and 2, are presented in Figure 4.10, which shows the acceleration recorded by the three accelerometers located along the pile.

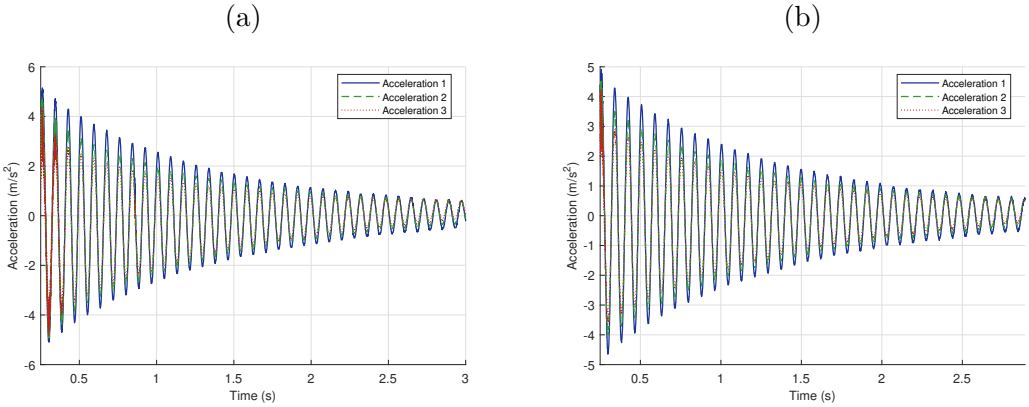

Figure 4.10: Acceleration profiles recorded at the three sensor locations. (a) Response following the first impact. (b) Response following the second impact.

The response output data under impact allows for application of different identification methods for modal parameter estimation. To this end, the modal parameters and their variances are identified using the output information-only with the covariance driven subspace identification method (Döhler & Mevel, 2013). The estimates are obtained for model orders ranging from 20 to 100, 25 time lags to compute the block Hankel matrix and 200 blocks to evaluate its sample covariance. The stabilisation diagram of the natural frequency estimates for impacts 1, 2 and 3 is depicted in Figure 4.11 alongside the singular value decomposition (SVD) plot, which displays the singular values of the cross power spectral density (CPSD) matrices derived from the acceleration data for impact 2. It can be viewed that among the spurious estimates, two modal alignments at around 12 Hz and 62 Hz can be distinguished, whose frequencies correspond the first and third bending modes for each pile.

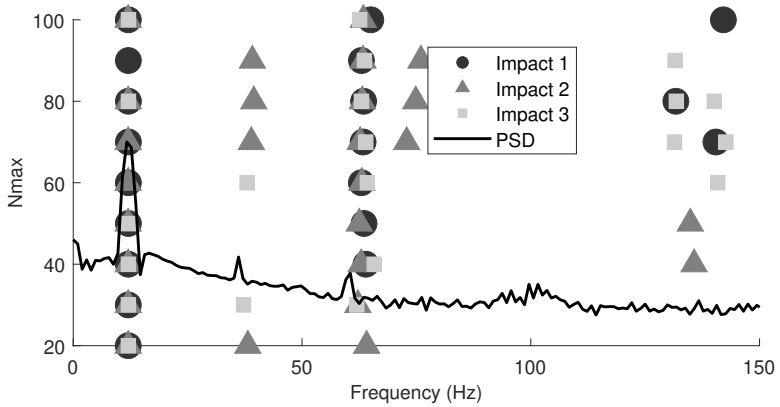

Figure 4.11: Stabilisation plot to identify excited modes from the field data across impacts 1 to 3 against a power spectral density (PSD) plot from the acceleration data of impact 2.

The function $F(\theta)$ is plotted for the parameter pair (w_m, L_0) within the intervals $\{0.5 - 30\}$ and $\{5 - 12\}$, respectively, and can be seen in Figure 4.12. The objective function is derived from the 1st and 3rd modes of vibration, with mode shapes based on the three accelerometers positioned on the pile. From the objective function, we observe a global minimum around the expected value for the total pile length, which is 7.2 m. This value corresponds to the full length of the pile, including both embedded and exposed segments. The embedded length, which is often the parameter of practical interest, can be directly obtained by subtracting the known exposed length of 4.1 m, yielding an embedded length of 3.1 m. In this analysis, the parameter w_k was set to the mean value obtained from the Monte Carlo simulations of Impact 1, as shown in Table 4.3. The resulting global minimum forms a ridge, rather than a well-defined minimum, likely due to the inclusion of only two modes and data from three sensors. This theory is reinforced by the objective function plot for target 1 in Figure 4.5, where four modes and data from five sensors are taken into account in the objective function, showing a clearly defined global minimum. This comparison highlights the impact of limited modal information on the optimisation landscape.

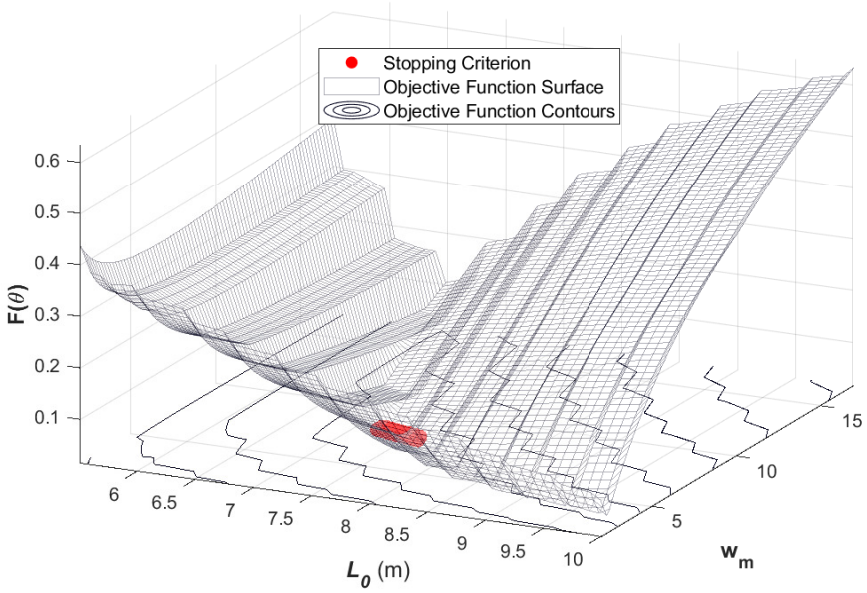

Figure 4.12: Objective function for the parameter pair L_0 and w_m in the field application.

To assess the performance of the optimisation to estimate w_m, w_k and L_0 with real data, Monte Carlo simulations were conducted, similar to the approach described in Section 4.3. The statistics for L_0, w_m, and w_k are summarised in Table 4.3. The analysis reveals that L_0 converges to approximately 7.8 m for Impact 1, 7.7 m for Impact 2, and 7.8 m for Impact 3, with standard deviations of 0.48 m, 0.56 m, and 0.55 m, respectively. Similarly, w_m has a mean value of 6.35 with a standard deviation of 2.32 for Impact 1, a mean value of 6.18 with a standard deviation of 3.17 for Impact 2, and a mean value of 6.4 with a standard deviation of 2.65 for Impact 3. For w_k, the mean value is 1.73 with a standard deviation of 0.48 for Impact 1, a mean value of 1.59 with a standard deviation of 0.28 for Impact 2, and a mean value of 1.68 with a standard deviation of 0.22 for Impact 3.

Table 4.3: Mean values and standard deviations of the parameters for Impact 1, 2 and 3.

Impact	Parameter	μ	σ	Actual Value
Impact 1	L_0 (m)	7.8	0.48	7.2
	w_m	6.35	2.32	-
	w_k	1.73	0.48	-
Impact 2	L_0 (m)	7.7	0.56	7.2
	w_m	6.18	3.17	-
	w_k	1.59	0.28	-
Impact 3	L_0 (m)	7.8	0.55	7.2
	w_m	6.4	2.65	-
	w_k	1.68	0.22	-

The parameter that can be validated is the pile's length, with the exact value being 7.2 m. Although the most likely length as predicted from the procedure is 7.8 m, this is still a good approximation given that the objective function is based on only two modes and three accelerometers positioned close to each other. If more accelerometers were placed along the shaft of the pile and more modes were excited, the objective function would be better defined. This would likely result in the solution converging more closely to the global minimum and the exact value.

Similarly, for w_m and w_k, it is observed that the mean values of the converged results are close for impacts 1, 2, and 3. The convergence of all three tests in the same region with similar mean values is significant, as it indicates that different load cases do not interfere with the subspace identification process. More specifically, the identified frequencies and mode shapes for modes 1 and 3 across all impacts yield similar optimisation values, reinforcing the robustness and validity of the proposed method.

4.5 Conclusions

This study successfully demonstrates the coupling of model updating, here effectuated via a stochastic evolutionary scheme, the CMA-ES, with a subspace identification method in a robust framework to determine operational mass, stiffness, and embedded length of a number of numerical and experimental piles. The framework adeptly addresses the challenge of estimating critical SPI parameters, such as pile length and the associated mobilised mass and stiffness, which are pivotal for accurate foundation behaviour modelling. The presented framework combines modal parameter determination through subspace identification with

the robustness of the CMA-ES for model updating. While the CMA-ES was chosen due to its practical ability to converge in rugged search landscapes, which may include discontinuities, sharp bends, ridges, noise, local optima, or outliers, any optimisation method featuring similar characteristics could be used. Additionally, CMA-ES features a covariance matrix, reflecting the algorithm's estimate of the variance in the search space. A larger covariance matrix indicates a broader exploration, while a smaller covariance matrix suggests the convergence toward a narrower region, typically near the minimum. Although this feature was not exploited in the current study, it presents a potential for the uncertainty quantification of the delivered estimates in the future work. The analysis was conducted in MATLAB on the High-Performance Computing (HPC) system of the University of Nottingham, specifically utilising a high-memory compute node equipped with 2 $\times$ 48-core AMD CPUs, 1536 GB of RAM . Under this configuration, the approximate convergence time for the optimisation of every target 1 model was around 12 minutes, with a variance of 1–2 minutes depending on the initial conditions. This approach effectively quantifies uncertainties using output-only data, enhancing the model's accuracy, especially for existing piles under operational loads. The framework's effectiveness has been validated through numerical model applications and via data reported from a real full-scale field test, demonstrating its practical applicability and potential to significantly improve soil-structure interaction parameter estimation. Ultimately, this research introduces a framework for estimating pile parameters using output-only data and highlights the significant potential of statistical updating techniques in advancing the accuracy and reliability of SHM systems in geotechnical and structural engineering. The approach might be useful for digital twin applications such as for offshore wind turbine structures.

Chapter 5

Monitoring pile scour using model-updating with deterministic and stochastic methods

Authors: Andreas Ioakim, Szymon Greś, Luke J. Prendergast
Paper Status: Work in Progress

5.1 Introduction

The rapid expansion of the offshore wind industry demands more reliable methods for assessing the integrity of monopile foundations, particularly under scour conditions that can significantly affect the dynamic behaviour and lateral capacity of the soil-pile system. To address this need, this chapter introduces and compares three distinct model updating frameworks for scour depth estimation in laterally loaded piles: a deterministic frequency response function (FRF)-based method, and two stochastic approaches.

The FRF-based method employs controlled lateral input-output data to extract vibration modes, enabling the estimation of scour depth, as well as the soil mass and soil stiffness interacting with the pile. In contrast, the two stochastic frameworks, based on Differential Evolution (DE) and Covariance Matrix Adaptation Evolution Strategy (CMA-ES) respectively, use output-only acceleration data and stochastic subspace identification (SSI) to derive modal properties, followed by evolutionary optimisation to estimate the SPI parameters. Furthermore, the CMA-ES framework incorporates uncertainty quantification (UQ), enhancing robustness in parameter estimation.

These three model updating frameworks are tested against a series of numerically generated datasets, which simulate various soil-pile properties and loading conditions. Two primary loading scenarios are considered: input-output data from impact testing and output-only data under ambient noise. This systematic evaluation explores the performance of the frameworks in terms of accuracy, robustness, and computational efficiency. By analysing the advantages and challenges associated with the frameworks, the study provides valuable insights into the applicability and limitations of each approach for real-world offshore wind turbine foundation monitoring.

The remainder of this chapter is structured as follows. Section 5.2 presents the methodology, beginning with the development of physics-based soil-pile interaction (SPI) modelling and simulation of scour conditions. This is followed by an explanation of the three model updating frameworks: the deterministic FRF-based approach, which uses controlled input-output data; the DE-based framework, which combines SSI and DE for parameter estimation from output-only data; and the CMA-ES-based framework, which enhances the output-only approach with UQ for robust parameter estimation. Results are presented in Section 5.3 for both impact testing and ambient noise scenarios, followed by a comparative evaluation of the methods. Section 5.4 concludes with key findings and practical recommendations for implementing these frameworks in monitoring offshore monopile foundations.

5.2 Methodology

5.2.1 Objective and problem description

The primary objective of this study is to develop and compare optimisation-based model updating frameworks for estimating the scour depth (D_s) of pile foundations using vibration-based structural health monitoring (SHM) techniques. Vibration-based SHM methods are particularly advantageous for D_s estimation due to their sensitivity to changes in the dynamic properties of the soil-pile system (Ioakim et al., 2025; Prendergast et al., 2018). Building on previously developed methods (Ioakim & Prendergast, 2024; Ioakim et al., 2025), this study refines both the FRF and CMA-ES-based frameworks for scour estimation, while also introducing a newly developed DE-based framework. Beyond quantifying scour depth, these frameworks estimate key parameters related to soil-pile interaction (SPI). To achieve this, measured vibration responses of the pile, obtained under either known (impact) or unknown (ambient) external excitations, are analysed to extract the governing system parameters. The main motivation is to compare a deterministic FRF-based approach with two stochastic optimisation methods, evaluating their accuracy, computational efficiency, and robustness against measurement uncertainty.

The system dynamics can be represented by the continuous-time equation of motion:

$$\mathcal{M}^{\theta}\ddot{\mathbf{q}}(t) + \mathcal{D}^{\theta}\dot{\mathbf{q}}(t) + \mathcal{K}^{\theta}\mathbf{q}(t) = \mathbf{u}(t) \tag{3.4}$$

where t denotes continuous time; $\mathcal{M}^{\theta}, \mathcal{D}^{\theta}$, and $\mathcal{K}^{\theta} \in \mathbb{R}^{d\times d}$ are the mass, damping, and stiffness matrices, respectively; and θ is a vector of system parameters. In this study, θ includes a mass weighting factor w_m, a stiffness weighting factor w_k, which scale the soil mass and stiffness profiles (Wu et al., 2018), in addition to D_s. The vector $\mathbf{q}(t) \in \mathbb{R}^d$ represents the system displacements, while $\mathbf{u}(t) \in \mathbb{R}^d$ denotes the unknown external forces acting on the pile.

5.2.2 Physics-based SPI modelling

To capture SPI dynamics at low strain levels, a linear Winkler foundation model is adopted due to its simplicity and effectiveness. In this approach, soil behaviour is approximated using lumped masses and linear springs at discrete points along the pile length. The SPI model follows the procedure described in Chapters 3 and 4, where the pile is treated as a 6-DOF Euler-Bernoulli beam element coupled with 2-DOF lateral soil elements (Prendergast & Gavin, 2016; Timoshenko, 1983).

The soil vertical profile is discretised into multiple layers, each associated with a spring-mass element pair attached to the pile nodes. By stacking these pairs along the embedded length of the pile, the model can represent the gradual stiffness and mass distribution of the soil. The topmost soil layer is represented by the N_s-th spring and mass element. Figure 5.1 illustrates the physical soil-pile system and its numerical representation using pile and spring elements.

Section 3.2 provides a detailed explanation of how specific SPI parameters are calculated. The model incorporates the small-strain Young's modulus of the soil ($E_S(z)$), the shear modulus ($G_S(z)$), and the subgrade reaction modulus ($K_S(z)$). For the pile, key parameters include the Young's modulus (E), the moment of inertia (I), and the stiffness (k_n) and mass (M_n) of individual n^{th} spring elements. The damping ratio for the i^{th} mode (ξ_i) is set to 2%. Unless explicitly stated otherwise, parameter values not specified in this section are consistent with those detailed in Section 3.2.

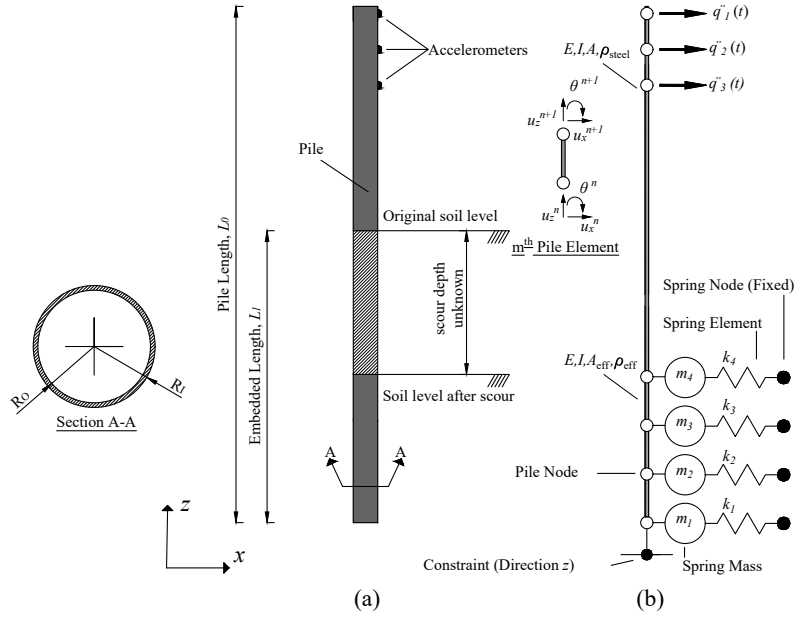

Figure 5.1: Schematic of the SPI model: (a) Physical system; (b) Numerical representation.

5.2.2.1 Modelling of scour

Scour around the pile reduces the effective embedded length of the pile within the supporting soil matrix. In the proposed model, the presence of scour is directly incorporated by removing the soil springs and lumped masses corresponding to the scoured region. This adjustment effectively shifts the boundary between the

supported and unsupported pile segments, altering the dynamic characteristics of the system. As scour depth increases, fewer soil elements remain attached, leading to reduced lateral stiffness and mass contribution from the soil. By systematically modifying the distribution of spring and mass elements, the model can simulate the effects of varying scour depths on the pile's dynamic response (Prendergast et al., 2018).

The pile is discretised into segments of length 0.1 m, and spring-mass elements above the specified scour depth are excluded to simulate the effects of scour on the pile's dynamic response. For all target models, an embedded pile length of $L_0 = 10$ m and a scour depth of $D_s = 2$ m are selected. The steel pile is modeled with a diameter of 4 m, a wall thickness of 0.1 m, and a Young's modulus of 200×10^9 Pa.

Different soil stiffness profiles are considered, including constant, parabolic, and those derived from in situ CPT data (Figure 5.2). To account for varying soil properties, the model scales spring stiffnesses and masses using user-defined parameters w_k and w_m.

The two loading scenarios reflect either an impact test, where a load is applied over the first 0.015 s followed by free vibrations, or a persistent ambient excitation, such as wind or wave loading. For the ambient case, only output-only methods are applicable, as no direct force measurements are available. Gaussian noise is added to the acceleration signals at varying signal-to-noise ratios (SNR) to assess the robustness of each method. Numerical target models are generated by systematically varying the soil profile type, w_m and w_k, and loading conditions.

This physics-based foundation model, combined with the appropriate representations of mass and stiffness system matrices, provides the underlying platform for the subsequent optimisation-based frameworks for scour depth estimation.

Table 5.1 summarises the key parameters used in the target models, including combinations of w_m, w_k, different stiffness profiles, SNR levels, and load types. These configurations ensure that the study covers a wide range of realistic scenarios and enables a thorough evaluation of the model updating frameworks.

Table 5.1: Target models

Target model	w_m	w_k	Stiffness profile	SNR (acceleration)	Load type
1	5	0.5	Constant	-	Impact
2	10	2	Constant (with perturbations)	-	Impact
3	10	2	Constant (with perturbations)	20	Impact
4	5	0.5	Parabolic	-	Impact
5	10	2	Parabolic (with perturbations)	-	Impact
6	10	2	Parabolic (with perturbations)	20	Impact
7	5	0.5	Real profile	-	Impact
8	10	2	Real profile	20	Impact
9	5	0.5	Constant	20	Ambient
10	5	0.5	Parabolic (with perturbations)	20	Ambient
11	5	0.5	Real profile	20	Ambient

Figures 5.2a–5.2e compare the stiffness profiles along the pile embedment for D_s of 2 m. The red dashed line in each figure marks the scour depth. Figure 5.2a and 5.2b depict a constant stiffness profile without and with variability around the mean, respectively, while figures 5.2c and 5.2d illustrate a parabolic stiffness distribution without and with variability around the mean. In all cases, the simulated variability involves random perturbations around the nominal profile to more realistically approximate potential heterogeneities in the soil. Finally, figure 5.2e shows a real cone penetration test (CPT) profile, featuring an irregular distribution of stiffness with depth. The shaded regions below the red dashed line in each plot correspond to the remaining soil elements after accounting for the 2 m scour. Overall, these visualisations illustrate the different $K_S(z)$, that characterise the target models.

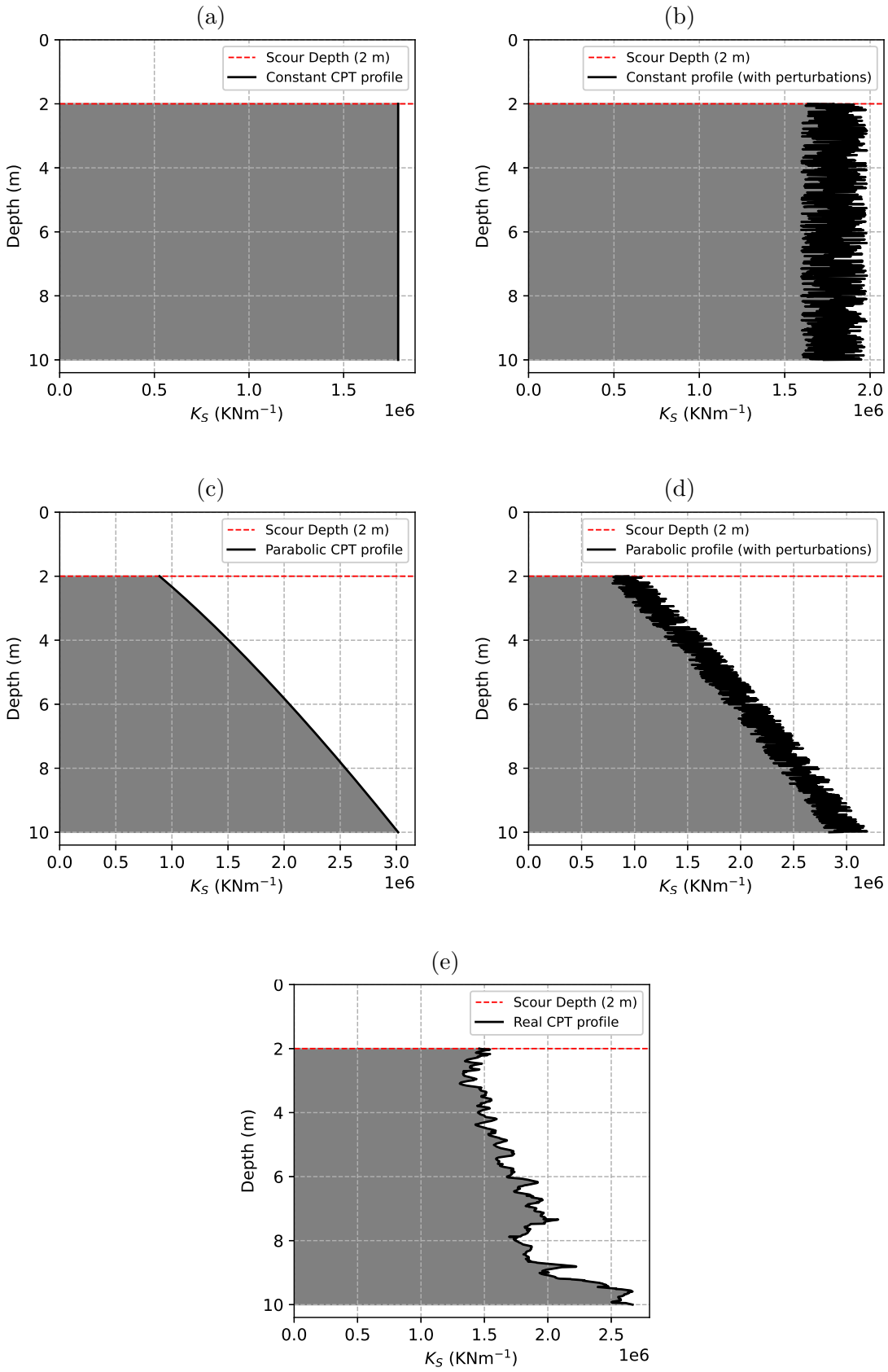

Figure 5.2: Comparison of $K_S(z)$ profiles for different scenarios: (a) and (b) constant profile without and with variability, (c) and (d) parabolic profile without and with variability, and (e) real CPT profile.

5.2.3 Application of deterministic FRF-based model updating framework for scour depth estimation

The FRF-based model updating framework builds upon a previously developed two-stage iterative approach intended to estimate the embedded length of pile foundations from measured vibration data (Ioakim & Prendergast, 2024). In the original methodology in Chapter 3, an impact load is applied laterally to the pile, and the resulting FRF, capturing the first and second vibration modes is employed to estimate the soil stiffness and mass profile, as well as the pile's embedment length. In the present work, this procedure is adapted to estimate scour depth, which effectively reduces the embedment length of the pile.

As described in Section 5.2.2.1, the removal of soil springs and masses in the scoured zone shifts the system's dynamic characteristics, which are reflected in its FRF. Controlled impact tests, capturing both acceleration and loading data at the pile head, provide the required information for constructing the FRF required to identify the modal properties. Figure 5.3 illustrates the effect of the scour depth on the FRF, and shows the framework's convergence to the actual FRF as the parameters D_s, w_m and w_k are iteratively refined.

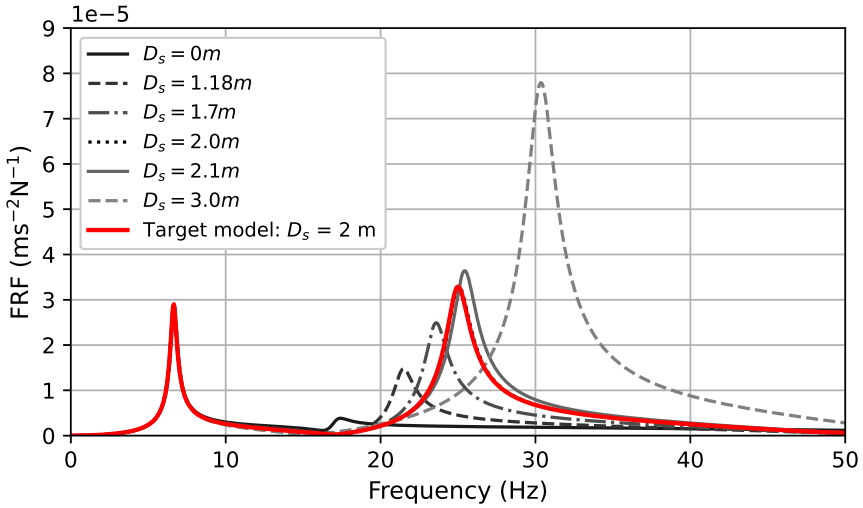

Figure 5.3: Comparison of the updated FRF with the actual FRF for target model 1, using the deterministic FRF-based framework.

5.2.3.1 Two-stage model updating procedure

Hereafter the procedure for the two-stage approach is outlined:

In the first stage, the first mode of vibration is used to determine the scaling weightings w_m and w_k. Starting with initial guess for D_s, w_m and w_k an iterative

procedure adjusts w_m and w_k until the numerical model's first-mode FRF peak closely matches that of the target (measured) FRF. This step ensures the correct calibration of the weightings based on the first mode of vibration. A detailed description of this procedure is provided in Chapter 3 and Algorithm 5.

Once the mass and stiffness parameters are satisfactorily matched using the first mode, the second mode of vibration is employed to estimate D_s. Similar to the embedded-length estimation process, the algorithm iteratively updates the assumed D_s while re-applying the first-stage mass and stiffness calibration at each step. By ensuring that the first and second mode FRF peaks of the numerical model align with those of the target model, the algorithm converges on the correct D_s (Ioakim & Prendergast, 2024). Using linear projection techniques, the second-mode FRF peak of the updated model is incrementally adjusted to align with the target FRF. The algorithm terminates when the difference in the second-mode peak falls below a predefined tolerance, yielding the estimated D_s. A similar procedure for estimating the embedded length is outlined in Chapter 3, with implementation details provided in Algorithm 6.

Similarly to Chapter 3, the Stage 2 objective function is defined via two residual terms:

$$r_0 = \frac{F_{\text{target}_2} - F_{\text{model}_2}}{F_{\text{target}_2}}, \tag{5.1}$$

$$r_1 = \frac{f_{\text{target}_2} - f_{\text{model}_2}}{f_{\text{target}_2}}, \tag{5.2}$$

where F_{target_2} and F_{model_2} denote the second peak FRF amplitudes, while f_{target_2} and f_{model_2} represent the corresponding frequencies of the target and physics-based model. The objective function is:

$$\mathcal{L} = \max\left(|r_0|, |r_1|\right), \tag{5.3}$$

which ensures the largest discrepancy between numerical and target FRFs is minimised.

5.2.3.2 Implementation and considerations

Algorithm 7 provides the pseudocode for the FRF-based scour depth estimation method. Peak picking isolates the peaks of interest from the FRF which are subsequently used for parameter calibration. In practice, success relies on accurately identifying these modal peaks, which can be challenging when damping is sig-

nificant or the peaks are closely spaced. Additionally, the method requires both input and output data, limiting its applicability to scenarios with well-controlled loading conditions. Nevertheless, numerical results demonstrate the robustness of the framework in estimating the soil mass and stiffness contributions and scour depth by iteratively matching the first and second vibration modes.

Algorithm 7 FRF-Based Framework for Scour Depth Estimation

Require: Initial parameters $\mathbf{x} = \{\mathrm{w}_m, \mathrm{w}_k, D_s\}$, measured target acceleration and loading data, convergence criterion ϵ

Ensure: Optimised parameters $\mathbf{x}^* = \{\mathrm{w}_m^*, \mathrm{w}_k^*, D_s^*\}$

Compute target FRF from acceleration and loading data

Construct the initial numerical model using the initial soil and pile properties (w_m, w_k and D_s).

Simulate the FRF of the initial model.

while Objective function ($\mathcal{L}$) $> \epsilon$ **and** maximum iterations not reached **do**

Stage 1: First Mode Matching

Identify the first-mode peak in the target FRF.

Iteratively adjust w_m and w_k to minimise the discrepancy between the numerical model's first-mode FRF peak and the target first-mode FRF peak.

Update the numerical model and recompute the FRF.

Stage 2: Second Mode Matching

Identify the second-mode peak in the target FRF.

Iteratively adjust the D_s and re-calibrate w_m and w_k (Stage 1) to minimise the discrepancy between the numerical model's second-mode FRF peak and the target second-mode FRF peak.

Update the numerical model and recompute the FRF.

end while

return $\mathbf{x}^* = \{\mathrm{w}_m^*, \mathrm{w}_k^*, D_s^*\}$

5.2.4 Application of stochastic optimisation frameworks for scour depth estimation

While the deterministic FRF-based approach described above relies on known input-output data from impact testing, many structural systems—especially in offshore environments—are subjected to operational or ambient excitations where the input force cannot be readily measured. To address such output-only scenarios, two stochastic optimisation frameworks are presented. Both methods estimate D_s along with w_m and w_k, but they differ in how the physics-based (interrogated) model's modal properties are obtained (via subspace identification or via eigen-

decomposition of the system matrices) and in the choice of evolutionary optimisation algorithm (DE or CMA-ES). These stochastic frameworks build on the authors' previous work in Ioakim et al. (2025), where a data-driven model updating framework for length estimation was proposed and tested against numerical and field test data.

5.2.4.1 DE-based framework

In the DE-based framework, the key model parameters (D_s, w_m and w_k) are optimised through a DE evolutionary algorithm. At each iteration, the soil-pile system is simulated in the time domain under impact or ambient excitation to generate synthetic acceleration responses. These responses are then analysed with the covariance-driven SSI method (SSI_COV) (Peeters, 2000) outlined in Algorithm 1 to extract the model's frequencies and mode shapes. To ensure a comprehensive capture of the system dynamics and mitigate the effects of noise or modelling inaccuracies, SSI_COV is applied with a larger number of modes, followed by mode stabilisation to identify and discard any spurious modes. Only the stable modes are retained for comparison with the target modal properties, which are also obtained via SSI_COV from the measured data. The mismatch between these modal features forms the objective function minimised by the DE. Although robust, this approach can be computationally demanding due to the need for full time-domain simulations and subsequent SSI at each iteration.

Convergence is achieved when the modal property discrepancies—such as frequency deviations and modal assurance criterion (MAC) values—fall below a specified threshold or when consecutive DE generations yield no further improvement. MAC values, which quantify the consistency between mode shapes, are used alongside frequency deviations to assess the accuracy of the model. This dual criterion ensures that both the natural frequency and mode shape alignment are accurately captured.

The MAC error is defined as:

$$\mathcal{L}_{\mathrm{mac}} = n_{\mathrm{modes}} - \sum_{i=1}^{n_{\mathrm{modes}}} \mathrm{MAC}_{ii}, \tag{5.4}$$

where n_{modes} is the number of modes considered, and MAC_{ii} is the diagonal entry of the MAC matrix comparing the i-th mode shapes of the target and physics-based model.

The frequency error is computed as:

$$\mathcal{L}_{\mathrm{f}} = \sum_{i=1}^{n_{\mathrm{modes}}} \left| \frac{f_{\mathrm{target}_i} - f_{\mathrm{model}_i}}{f_{\mathrm{target}_i}} \right|, \tag{5.5}$$

where f_{target_i} and f_{model_i} refer to the i-th mode frequencies of the target and physics-based model, respectively.

The combined objective function is:

$$\mathcal{L} = \mathcal{L}_{\mathrm{mac}} + \mathcal{L}_{\mathrm{f}}, \tag{5.6}$$

where $\mathcal{L}$ represents the combined error metric that DE seeks to minimise. This formulation ensures that both the frequency alignment and the mode shape similarity are optimised simultaneously, facilitating convergence towards an accurate representation of the target modal properties.

Algorithm 8 provides a high-level pseudocode description of the DE-based framework. Although computationally intensive due to repeated SSI analyses and stochastic optimisation, reduced order modelling (ROM), parallelisation and high-performance computing (HPC) can accelerate iterations.

For the physics-based model, a state-space formulation is adopted to accommodate the output-only scenario through the inclusion of stochastic noise terms: $\mathbf{w}_k$ and $\mathbf{v}_k$. As detailed in Section B.1.4, the equation of motion (3.4) is reformulated into a first-order discrete state-space representation. By incorporating process and measurement noise to account for unmeasured inputs and sensor inaccuracies, the stochastic state-space model is derived, as given in Equation (B.28):

$$\begin{aligned} \mathbf{x}_{k+1} &= \mathbf{A}\mathbf{x}_k + \mathbf{w}_k \\ \mathbf{y}_k &= \mathbf{C}\mathbf{x}_k + \mathbf{v}_k, \end{aligned} \tag{B.28}$$

Here, $\mathbf{x}_k \in \mathbb{R}^n$ is the state vector, and $\mathbf{y}_k \in \mathbb{R}^l$ is the output vector, with the remaining terms as defined in Section B.1.4.

Building on the ROM approach mentioned earlier, the process begins by extracting dominant modal parameters through eigen-value decomposition and merging these with the corresponding mode shapes. By mapping continuous-time poles to a discrete-time formulation, the system's principal dynamics are retained in a significantly smaller state-space. This reduced-order model enables more computationally efficient simulations. A pseudocode is provided in Algorithm 10.

Algorithm 8 DE-based Framework for Scour Depth Estimation

Require: Initial bounds for parameters $\mathbf{x} = \{\mathrm{w}_m, \mathrm{w}_k, D_s\}$, measured target acceleration data, convergence criterion ϵ

Ensure: Optimised parameters $\mathbf{x}^* = \{\mathrm{w}_m^*, \mathrm{w}_k^*, D_s^*\}$

Step 1: Initialise a population of candidate solutions $\mathbf{X}_0$ within prescribed bounds.

Step 2: Extract target modal properties $\{f_n^{\text{target}}, \Phi^{\text{target}}\}$ using `SSI_COV` coupled with mode stabilisation on the measured acceleration data.

while Objective function $(\mathcal{L}) > \epsilon$ and maximum iterations not reached **do**

for each candidate $\mathbf{x}_i$ in the population **do**

Simulate the reduced order time-domain response of the numerical model with $\mathbf{x}_i$.

Apply `SSI_COV` coupled with mode stabilisation to the simulated response to extract modal properties $\{f_n^i, \Phi^i\}$.

Compute the objective function $\mathcal{L}_i$ (5.6).

end for

Update population using DE operators (mutation, crossover).

end while

return Best candidate $\mathbf{x}^* = \{\mathrm{w}_m^*, \mathrm{w}_k^*, D_s^*\}$ with minimal $\mathcal{L}$

5.2.4.2 CMA-ES-based framework

The second stochastic optimisation framework leverages the CMA-ES evolutionary algorithm to estimate D_s and soil parameters w_m and w_k in an output-only setting. The CMA-ES-based framework compares the modal properties of the interrogated model with the target modal estimates obtained through SSI. The resulting discrepancies define the objective function to be minimised. Furthermore, the uncertainties associated with the identified modal parameters are quantified using the methodology described in Chapter 4, ensuring a robust assessment of the parameter estimates under measurement noise.

CMA-ES iteratively refines a multivariate Gaussian distribution over the parameter space, adjusting its mean vector and covariance matrix based on candidate solution performance. The algorithm terminates when the predicted frequencies fall within specified confidence intervals and the MAC values meet acceptable thresholds, or the search distribution becomes sufficiently narrow.

The main idea is to examine how small perturbations in the estimated subspace translate into variations in the identified modal parameters (i.e., frequencies, damping ratios, and mode shapes). First, the original dataset is divided into

resampled subsets. Each subset independently undergoes the covariance-driven SSI procedure (outlined in Algorithm 1), resulting in slightly different subspace estimates. Comparing these estimates reveals variations that capture the data-induced uncertainty.

These subspace variations are then mapped to the system matrices A and C using Jacobians, which quantify the sensitivity of A and C to changes in the subspace basis. Once A and C are perturbed, their eigenvalues and eigenvectors are recomputed to obtain updated estimates of frequencies, damping ratios, and mode shapes. Repeating this process across all subspace subsets generates a distribution of modal parameters whose spread serves as an indication of reliability.

Finally, statistical indices such as standard deviations or confidence intervals (e.g., $\pm 2\sigma$ bounds) are derived from these distributions to assess the robustness of the identified modal parameters. For MAC uncertainties, additional expansions (e.g., first-order or second-order Taylor series) can account for near-unity MAC values. This systematic UQ framework propagates data-level variability through to the final modal parameters, enhancing the reliability of subsequent model updating tasks (Greś et al., 2021b).

To guide the CMA-ES procedure, an objective function $\mathcal{L}$ is defined to quantify the discrepancy between the numerical model's modal predictions and those of the target system, as described in Section 4.2.2. This function penalises inaccuracies in both frequency estimates and mode shapes, evaluated using the Modal Assurance Criterion (MAC). The detailed formulation of $\mathcal{L}$ is presented in Equation (4.10).

Algorithm 9 provides a high-level overview of the CMA-ES-based workflow for D_s estimation.

Algorithm 9 CMA-ES-Based Framework for Scour Depth Estimation

Require: Initial parameters $\mathbf{x} = \{\mathrm{w}_m, \mathrm{w}_k, D_s\}$, measured target acceleration data, convergence criterion ϵ

Ensure: Optimised parameters $\mathbf{x}^* = \{\mathrm{w}_m^*, \mathrm{w}_k^*, D_s^*\}$

Step 1: Estimate reference modal properties $\{f_n^{\text{target}}, \Phi^{\text{target}}\}$ and uncertainties from measured target acceleration data using `SSI_COV` coupled with UQ of the estimates ($\hat{f}_n$, $\hat{\sigma}_{f_n}^2$, $\hat{\varphi}_n$, $\widehat{\Sigma}_{\varphi_n}$).

Step 2: Initialise CMA-ES (mean vector, covariance matrix) within parameter bounds.

while Objective function ($\mathcal{L}$) $> \epsilon$ **and** maximum iterations not reached **do**

  for each candidate $\mathbf{x}_i$ in the current CMA-ES population **do**

    Update the mass and stiffness matrices of the physics-based model with $\mathbf{x}_i$.

    Compute $\{f_n^i, \Phi^i\}$ for the interrogated model.

    Compute objective $\mathcal{L}_i$ (4.10).

  end for

  Update CMA-ES mean and covariance using the best $\mathcal{L}_i$ candidates.

end while

return Best parameters $\mathbf{x}^*$ that minimise $\mathcal{L}$

5.2.4.3 Summary of deterministic and stochastic frameworks

The main differences between the deterministic and stochastic approaches presented in this chapter lie in the system identification and optimisation strategies. The stochastic frameworks employ output-only SSI, which accounts for measurement noise and does not require input excitation signals, making them particularly suitable for operational conditions. In contrast, the deterministic framework relies on FRFs derived from known input-output data. Regarding optimisation, the deterministic approach applies an iterative update to a single model, whereas the stochastic frameworks use population-based algorithms that incorporate randomness, enabling broader exploration of the parameter space and improved robustness against local minima.

Both the DE-based and CMA-ES-based stochastic frameworks facilitate scour depth estimation without requiring direct input measurements, enhancing their practicality for in situ monitoring of offshore wind turbine foundations. The key distinctions between the two lie in the choice of evolutionary algorithm and the integration of UQ. By accounting for variability and uncertainty, both frameworks provide robust and realistic estimates of scour depth and soil properties under

operational offshore conditions.

Table 5.2 summarises the primary differences between the three approaches. The FRF-based method relies on input-output data to construct a deterministic update procedure, where the two stochastic methods (DE-based and CMA-ES-based) operate in an output-only setting and leverage evolutionary algorithms to optimise soil-pile parameters. Each framework extracts modal properties from the physics-based model differently, relies on varied optimisation strategies, and offers unique strengths and weaknesses in terms of computational cost, required data, and sensitivity to modelling assumptions.

Table 5.2: Comparison of deterministic (FRF-based) and stochastic optimisation frameworks (DE and CMA-ES) for scour depth estimation.

	FRF-based	**DE-based**	**CMA-ES-based**
Data Type	Input-output	Output-only	Output-only
Modal Extraction	Peak picking in FRF	SSI & stablilisation at each iteration	Eigen-decomposition of the system matrices.
Optimisation Method	Linear projection	DE	CMA-ES
Primary Advantage	Deterministic approach	Handles complex objective functions from time-domain data	Integrated UQ
Challenge	Input load knowledge and sensitivity to damping	Repeated time-domain simulations and sensitivity to stopping criteria	Potential sensitivity to model matrix construction

5.3 Comparative analysis

This section presents a comparative analysis of the deterministic FRF-based framework, the DE-based framework, and the CMA-ES-based framework. The comparison evaluates their performance in estimating key parameters, such as D_s and soil weightings (w_m and w_k), as well as their computational efficiency and robustness to noise and complex soil profiles. The analysis is supported by histograms and a table showing the distribution of converged parameter values across the target models. While a subset of the histograms is included in this chapter, the remain-

der is provided in Appendix C for convenience. Additionally, objective function convergence plots and computational runtime distributions are presented. The unique characteristics and trade-offs of each framework are discussed, including their handling of uncertainties, reliance on prior knowledge, and computational demands.

5.3.1 Convergence across independent simulations

Deterministic FRF-based framework

Figure 5.4 presents histograms of the converged parameter values for target model 1 using the deterministic FRF-based framework, based on 100 simulations. The estimated D_s, w_m, and w_k align reasonably well with the target values, although errors become more pronounced in scenarios with variable soil profiles. Histograms for target models 2–7 are provided in Appendix C for further reference.

In the target model 1, the estimated parameters w_m, and w_k appear to follow a normal distribution, with their mean values aligning closely with the actual parameter values, as expected. This indicates that the framework is able to reliably recover the true parameters. In particular, for the scour depth D_s, all simulations converge to a single discrete value. This is a consequence of the pile being discretised in increments of 0.1 m, limiting the resolution of the estimated depth. However, employing a finer discretisation is expected to yield a similar normal distribution pattern, with the estimated values converging to the actual scour depth.

Notably, the deterministic method failed to converge for target model 8, which incorporated a real CPT profile and noisy acceleration data (non-zero SNR). This highlights the method's sensitivity to input data quality. Furthermore, high variability in the data necessitated adjustments to the stopping criterion to achieve reliable convergence.

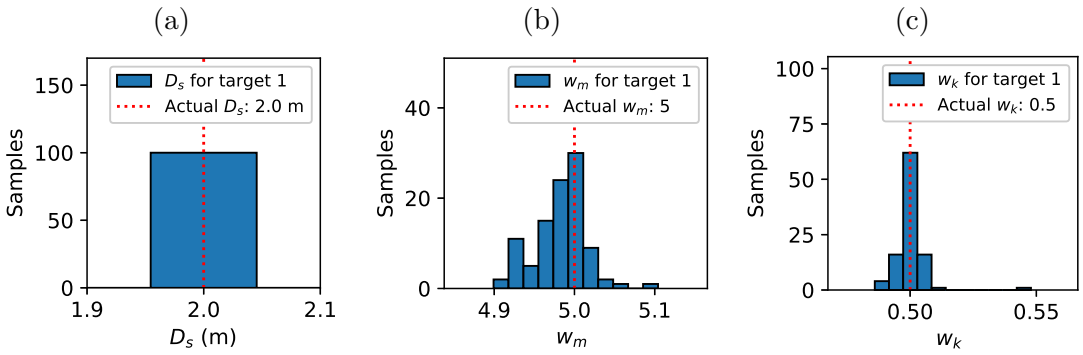

Figure 5.4: Histograms showing the distribution of the converged parameters for target 1 obtained using the FRF-based framework. (a), (b), and (c) correspond to D_s, w_m, and w_k, respectively. The actual parameter values are shown as red dashed lines.

Stochastic DE-based framework

Figure 5.5 and Figure 5.6 present histograms of the converged parameter values for target models 1 and 9, respectively, using the DE-based framework, each based on 100 independent runs. Target model 1 corresponds to an impact load scenario, while target model 9 is subjected to ambient noise. Unlike the deterministic FRF-based approach, the DE-based method employs SSI for both the target data and the interrogated model. As shown in the histograms, the DE-based strategy achieved robust convergence across both cases, with the estimated parameter values aligning closely with the actual parameters.

For further reference, histograms for target models 2–8 and 10–11 are provided in Appendix C. These results further illustrate the performance of the DE-based framework across a range of soil profile variations and loading conditions. The proximity of the converged distributions to the red dashed lines in the histograms indicates the strong agreement between the estimated and actual parameter values.

In target model 1, the estimated parameters w_m, and w_k exhibit a normal distribution, with their mean values closely matching the actual parameter values. Similar to the deterministic FRF-based method, the scour depth D_s consistently converges to a single discrete value due to the 0.1 m discretisation of the pile model. In contrast, for target model 9, where ambient excitation is considered, the estimated D_s shows increased variability, with deviations of up to 5% from the actual value. This variability stems from the inherent challenges of identifying modal parameters under unknown loading conditions, where lower excitation amplitudes can introduce greater uncertainty in the parameter estimation process.

Despite this success, several practical considerations warrant attention. Firstly,

UQ was not incorporated into the DE framework, necessitating fine-tuning of the convergence criteria on a case-by-case basis to ensure reliability. And secondly, the parameters of the SSI algorithm itself—such as model order and block size—required careful selection to ensure consistent mode extraction across varying numerical models. These constraints underscore the importance of expertise in managing the optimisation process and interpreting results effectively.

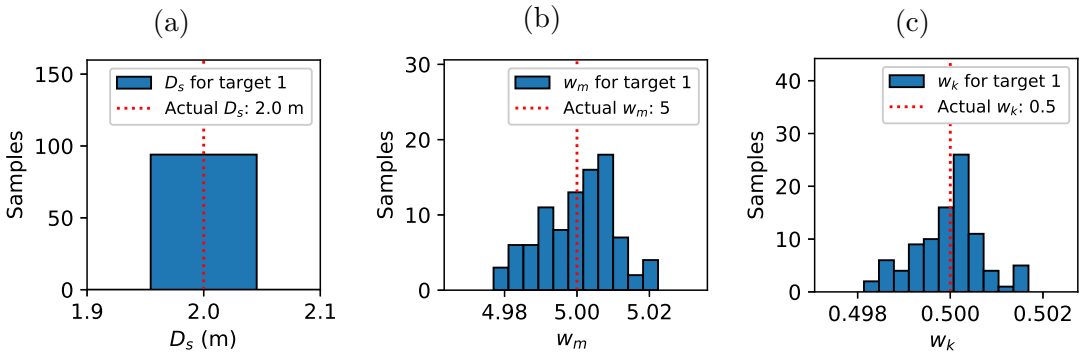

Figure 5.5: Histograms showing the distribution of the converged parameters for target 1 obtained using the DE-based framework. (a), (b), and (c) correspond to D_s, w_m, and w_k, respectively. The actual parameter values are shown as red dashed lines.

Notably, even for target models 9-11 (Figures 5.6, C.9, C.10), where ambient excitations resulted in less distinct modal peaks, the DE-based framework converged to the expected parameter values with minimal deviation from the true scour depth, mass weighting, and stiffness weighting. This robustness highlights the framework's applicability to operational monitoring scenarios where excitation measurements are unavailable.

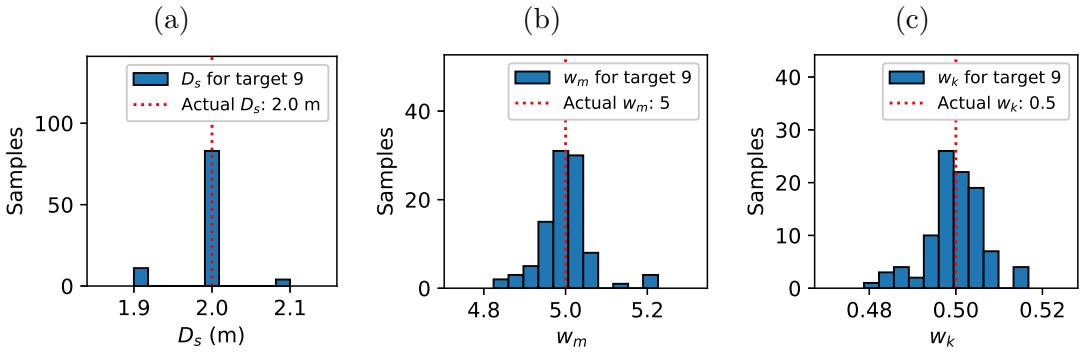

Figure 5.6: Histograms showing the distribution of the converged parameters for target 9 obtained using the DE-based framework. (a), (b), and (c) correspond to D_s, w_m, and w_k, respectively. The actual parameter values are shown as red dashed lines.

Stochastic CMA-ES-based framework

Figure 5.7 and Figure 5.8 display histograms of the estimated parameters for target models 1 and 9 using the CMA-ES-based framework, based on 100 independent runs. Target model 1 represents an impact load scenario, while target model 9 is characterised by ambient noise conditions. The CMA-ES framework integrates UQ for both identified frequencies and MAC estimates, eliminating the need for user-defined tolerance thresholds. This UQ strategy enhances convergence stability, ensuring reliable parameter estimation across different loading conditions.

For a broader assessment of performance, histograms for target models 2–8 and 10–11 are provided in Appendix C. Overall, the CMA-ES framework demonstrated robust performance for all tested configurations, including scenarios with noisy data or variable soil profiles. Although it remains a stochastic method and has a higher computational cost than deterministic schemes, it was notably faster than the DE-based alternative.

In target model 1 and 9, the estimated parameters D_s, w_m and w_k exhibit a normal distribution, with their mean values closely matching the actual parameter values. Compared to the previous frameworks, the CMA-ES-based approach demonstrates slightly larger standard deviations in the estimated parameters. This is attributed to the incorporation of UQ and the use of a robust objective function, which account for variability in frequency identification and MAC estimates.

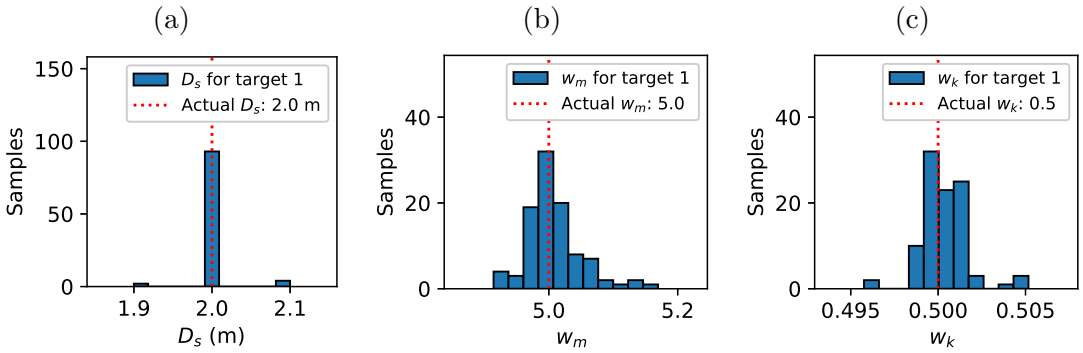

Figure 5.7: Histograms showing the distribution of the converged parameters for target 1 obtained using the CMA-ES-based framework. (a), (b), and (c) correspond to D_s, w_m, and w_k, respectively. The actual parameter values are shown as red dashed lines.

Furthermore, the CMA-ES framework achieved high accuracy in estimating D_s, w_m, and w_k for target models 9-11 (Figures 5.8, C.9, C.10), underscoring its potential as a robust and efficient tool for offshore foundation monitoring under ambient or operational loads.

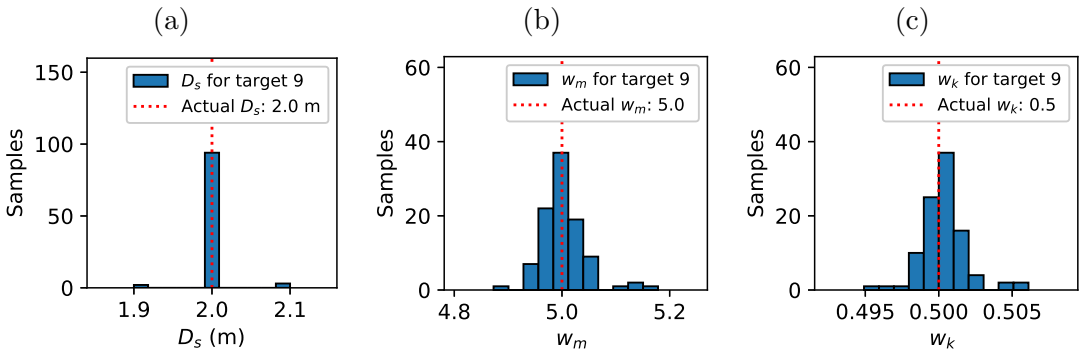

Figure 5.8: Histograms showing the distribution of the converged parameters for target 9 obtained using the CMA-ES-based framework. (a), (b), and (c) correspond to D_s, w_m, and w_k, respectively. The actual parameter values are shown as red dashed lines.

Quantitative comparison of frameworks

Table 5.3 provides a comprehensive comparison of the three frameworks in estimating key parameters (D_s, w_m, and w_k) across target models 1-11. The table reports the mean (μ) and standard deviation (σ) of parameter estimates over 100 independent simulations, highlighting the accuracy and consistency of each framework under varying soil heterogeneity and noise conditions.

Key observations for specific target models include:

For target 1, all three frameworks demonstrate high accuracy, with mean values for D_s, w_m, and w_k aligning closely with true values. The FRF-based method exhibits the lowest standard deviations, indicating consistent performance under noise-free conditions. The DE- and CMA-ES-based frameworks also show strong agreement but with slightly higher variability.

For target 5, which features a variable parabolic stiffness profile, the FRF-based framework accurately captures D_s and w_k, while the DE- and CMA-ES-based methods exhibit small deviations. This discrepancy arises from the output-only nature of the DE and CMA-ES methods and challenges posed by complex soil profiles.

For Target 7, which incorporates a real CPT profile the three frameworks again exhibit strong agreement with the true values for all parameters. The FRF-based method maintains low variability, while the DE-based and CMA-ES-based frameworks achieve comparable accuracy with slightly higher σ values for w_m.

Overall, The FRF-based framework demonstrates high accuracy and low variability in input-output scenarios, as indicated by consistently low σ values. However, it faces challenges in capturing FRF amplitude peaks when damping or input

forces are unknown.

In contrast, the DE- and CMA-ES-based frameworks are effective across all target models, including output-only scenarios with ambient noise. These stochastic methods exhibit slightly higher standard deviations, reflecting their exploration of the parameter space and robustness in handling uncertainties. The CMA-ES-based framework integrates UQ, which enhances exploration but introduces additional variability.

CMA-ES's ability to quantify uncertainties offers valuable insights into parameter reliability, making it especially useful for real-world scenarios with noise and complex models. This statistical understanding supports risk-informed decision-making and enhances robustness in practical engineering applications.

Table 5.3: Mean values (μ) and standard deviations (σ) of the parameter estimates for target models 1-11 using FRF-based, DE-based, and CMA-ES-based frameworks, with target values included.

Target	Parameter	Target Value	FRF-based		DE-based		CMA-ES-based	
			μ	σ	μ	σ	μ	σ
Target 1	D_s (m)	2.00	2.00	0.00	2.00	0.00	2.00	0.02
	w_m	5.00	4.98	0.03	5.00	0.01	5.01	0.04
	w_k	0.50	0.50	0.01	0.50	0.00	0.50	0.00
Target 2	D_s (m)	2.00	2.00	0.00	2.00	0.00	2.00	0.00
	w_m	10.00	9.95	0.02	9.97	0.03	9.95	0.04
	w_k	2.00	2.01	0.01	2.01	0.00	2.00	0.00
Target 3	D_s (m)	2.00	1.91	0.02	2.00	0.00	2.00	0.02
	w_m	10.00	10.86	0.22	9.96	0.03	9.95	0.04
	w_k	2.00	2.17	0.04	2.01	0.00	2.00	0.00
Target 4	D_s (m)	2.00	2.00	0.00	2.00	0.00	1.99	0.07
	w_m	5.00	4.99	0.02	5.00	0.01	4.99	0.13
	w_k	0.50	0.50	0.00	0.50	0.00	0.50	0.00
Target 5	D_s (m)	2.00	2.00	0.00	1.90	0.00	1.90	0.03
	w_m	10.00	10.00	0.02	9.31	0.03	9.24	0.16
	w_k	2.00	2.03	0.01	1.91	0.00	1.90	0.02
Target 6	D_s (m)	2.00	1.90	0.02	2.00	0.00	1.89	0.03
	w_m	10.00	11.12	0.25	9.34	0.06	9.24	0.16
	w_k	2.00	2.28	0.05	1.91	0.01	1.90	0.02
Target 7	D_s (m)	2.00	2.00	0.00	2.00	0.00	2.00	0.02
	w_m	5.00	5.04	0.03	5.00	0.01	5.00	0.04
	w_k	0.50	0.51	0.00	0.50	0.00	0.50	0.00
Target 8	D_s (m)	2.00	-	-	2.00	0.00	2.00	0.00
	w_m	10.00	-	-	10.01	0.04	10.00	0.05
	w_k	2.00	-	-	2.00	0.01	2.00	0.00
Target 9	D_s (m)	2.00	-	-	1.99	0.04	2.00	0.02
	w_m	5.00	-	-	5.00	0.06	5.00	0.04
	w_k	0.50	-	-	0.50	0.01	0.50	0.00
Target 10	D_s (m)	2.00	-	-	1.88	0.05	1.87	0.07
	w_m	5.00	-	-	4.79	0.09	4.75	0.12
	w_k	0.50	-	-	0.49	0.00	0.49	0.00
Target 11	D_s (m)	2.00	-	-	2.00	0.03	2.00	0.01
	w_m	5.00	-	-	5.00	0.06	5.01	0.04
	w_k	0.50	-	-	0.50	0.01	0.50	0.00

5.3.2 Convergence behaviour of frameworks

Figures 5.9–5.11 illustrate the progression of the objective function toward convergence for three representative target models, comparing the deterministic FRF-based, DE-based, and CMA-ES-based frameworks. This comparison highlights their respective strengths, weaknesses, and suitability for different types of scenarios.

Deterministic FRF-based framework

Figure 5.9 illustrates the convergence behaviour of the two-stage deterministic algorithm. Each run begins with an initial guess of $\{\mathrm{w}_m = 1, \mathrm{w}_k = 1, D_s = 0\}$. In Stage 2, D_s is updated, followed by a re-calibration of w_m and w_k in Stage 1.

The figure depicts five Stage 2 iterations for each target model, with each iteration involving multiple Stage 1 updates. The objective function (5.3) (denoted by r) decreases consistently and meets the convergence criterion (dashed line) within these iterations. For Models 1, 5, and 7, the deterministic method demonstrates rapid and predictable convergence, provided the input assumptions are accurate.

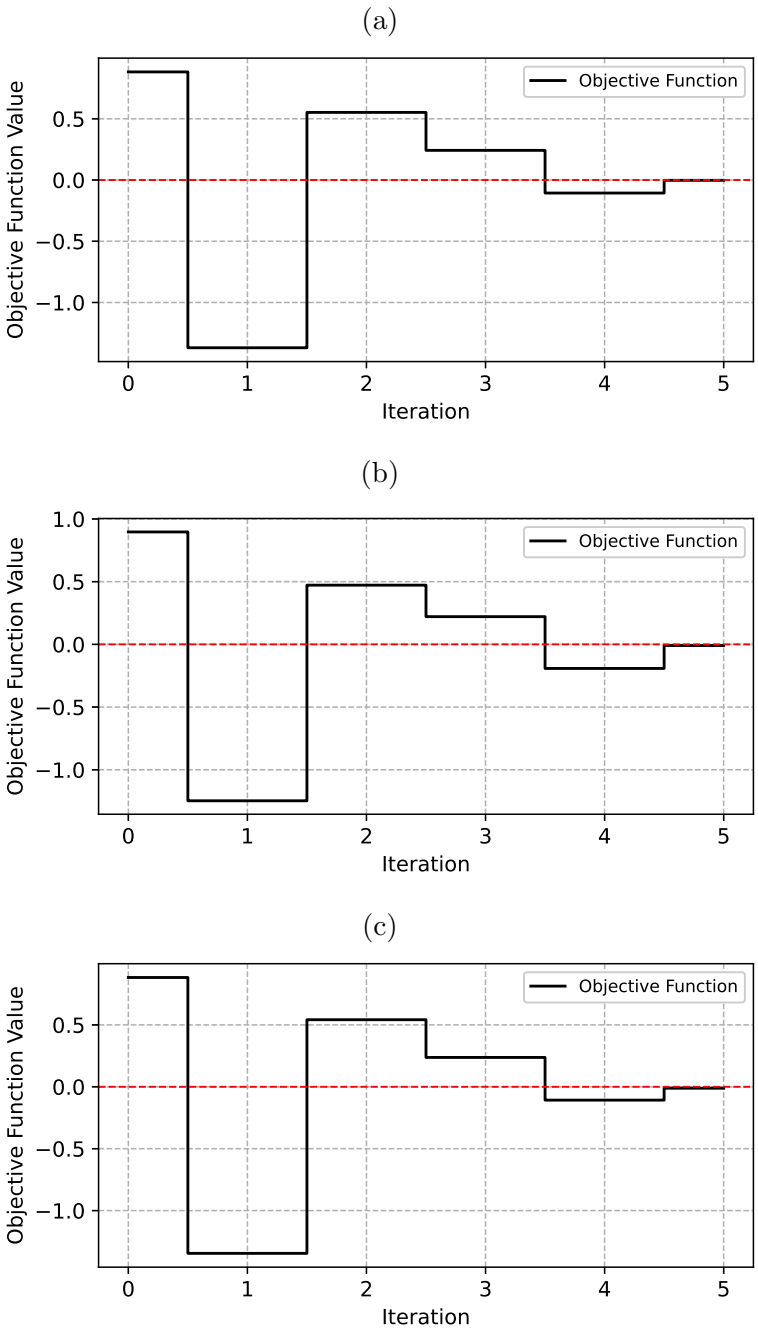

Figure 5.9: Objective value progression until convergence at each iteration of the deterministic FRF-based algorithm for (a) target model 1, (b) target model 5 and (c) target model 7.

Stochastic DE-based framework

Figure 5.10 shows the progression of the objective function for the DE-based framework. Unlike the deterministic approach, DE employs population-based mutation and crossover, leading to a more gradual and occasionally irregular convergence pattern. Models 1 and 7 converge within approximately 30 generations, reflecting

the relative simplicity of their soil profiles. In contrast, Model 5, which features parabolic stiffness with variability around the mean value, requires over 300 generations to converge due to the added noise in the data. However, in this case, convergence is achieved due to a larger threshold, allowing the algorithm to tolerate greater variations in the objective function.

The DE-based framework, while operating in an output-only setting, demonstrates robustness in handling noisy scenarios. However, this flexibility comes at the expense of computational efficiency, as repeated time-domain simulations and SSI computations within each DE generation significantly increase runtime. Furthermore, the lack of integrated UQ necessitates careful parameter tuning to ensure reliable convergence.

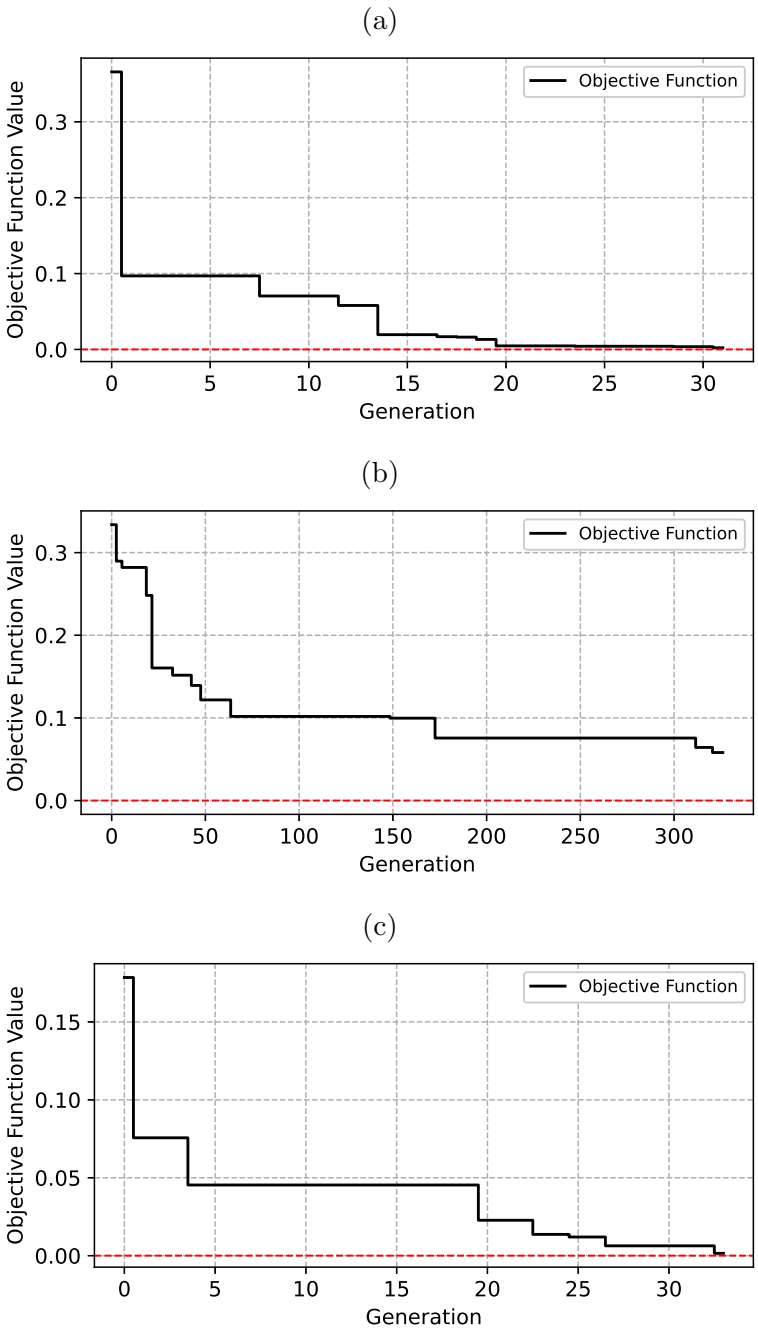

Figure 5.10: Objective value progression until convergence at each iteration of the stochastic DE algorithm for (a) target model 1, (b) target model 5 and (c) target model 7.

Stochastic CMA-ES-based framework

Figure 5.11 illustrates the convergence behaviour of the CMA-ES-based framework. This algorithm converges to the true parameter sets within approximately 13 generations for all three target models. Unlike the DE-based framework, CMA-ES incorporates UQ for both frequencies and MAC estimates, eliminating the need

for user-defined tolerance thresholds. Instead, uncertainties derived from modal properties directly inform the stopping condition, enhancing robustness and reducing manual intervention.

The CMA-ES-based approach achieves similar accuracy to the deterministic and DE-based method while requiring fewer iterations than DE. The UQ makes CMA-ES particularly effective in scenarios involving noisy data or complex parameter spaces, as evidenced by its performance on model 5. While CMA-ES remains computationally more expensive than deterministic methods, its integration of UQ and rapid convergence demonstrate its potential as a reliable and efficient framework for real-world offshore foundation monitoring.

(a)

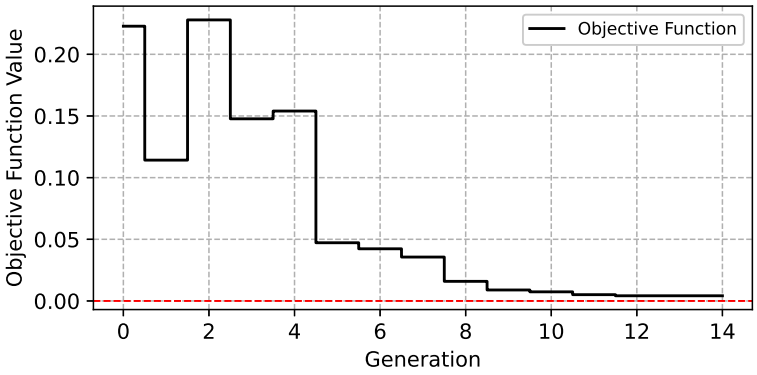

(b)

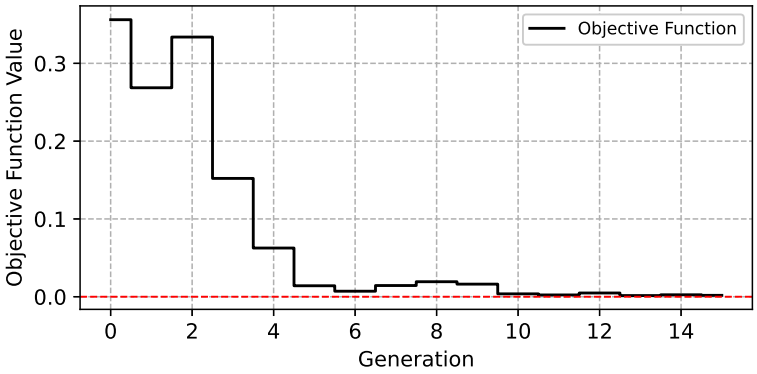

(c)

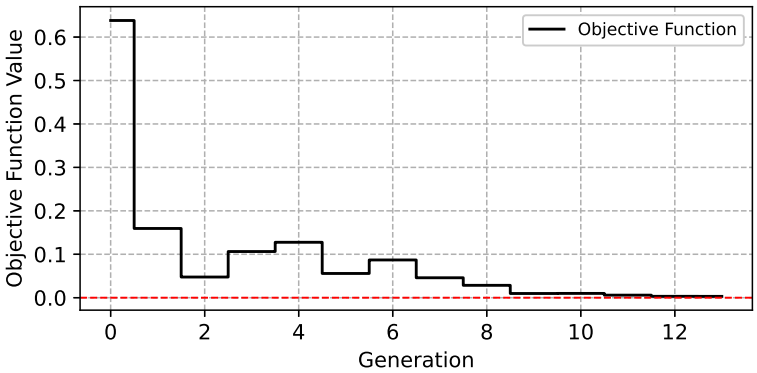

Figure 5.11: Objective value progression until convergence at each iteration of the stochastic CMA-ES algorithm for (a) target model 1, (b) target model 5 and (c) target model 7.

5.3.3 Runtime comparison of frameworks

Figures 5.12 and 5.13 show the distribution of convergence times for target models 1, 5, and 7, evaluated over 100 independent runs. As expected, the deterministic FRF-based framework converges more quickly, with most executions completing within approximately 70–140 s. In comparison, the CMA-ES method typically

requires 260–600 s, reflecting the additional computational overhead associated with stochastic evolutionary optimisation and UQ.

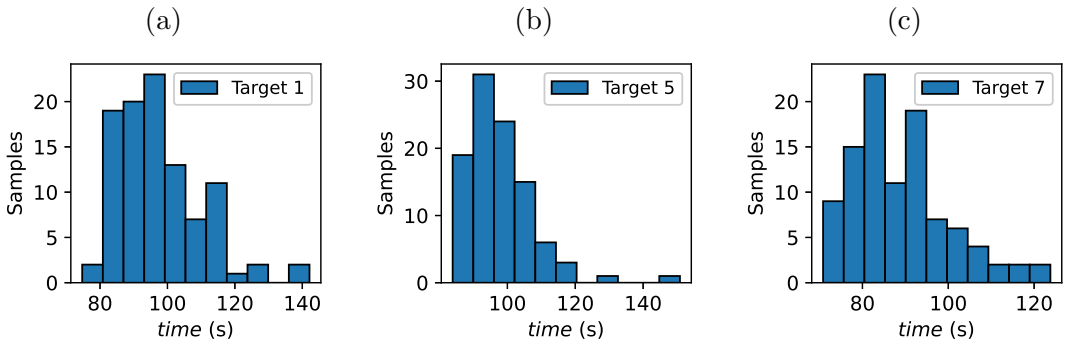

Figure 5.12: Histograms showing the distribution of the convergence time for target models (a) 1, (b) 2, and (c) 3 with the two-stage FRF-based algorithm.

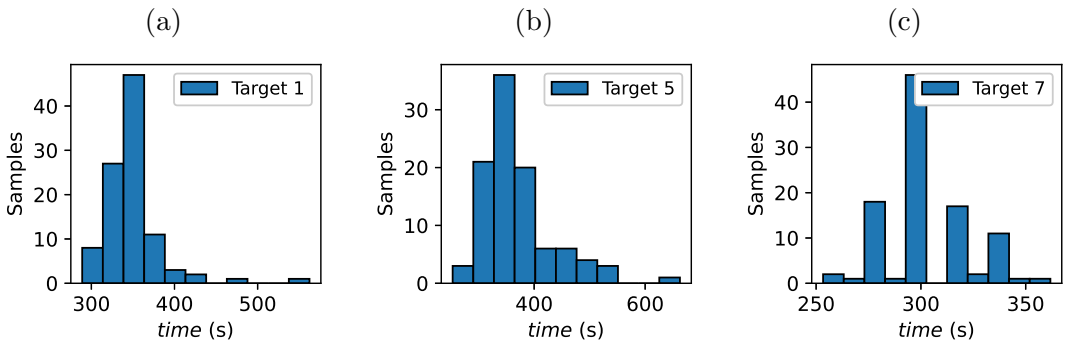

Figure 5.13: Histograms showing the distribution of the convergence time for target (a) model 1, (b) model 5, and (c) model 7 using the CMA-ES-based algorithm executed in serial.

The stochastic CMA-ES framework benefits significantly from parallel execution. Figure 5.14 shows the distribution of convergence times when the CMA-ES optimisation algorithm is executed in parallel using 50 threads. Compared to the serial implementation, parallelisation reduces runtime significantly, with most runs completing in 75-170 s, making the CMA-ES framework more competitive for near-real-time monitoring applications. This improvement is achieved by parallelising the evaluation of candidate solutions, significantly reducing the computational cost for each generation.

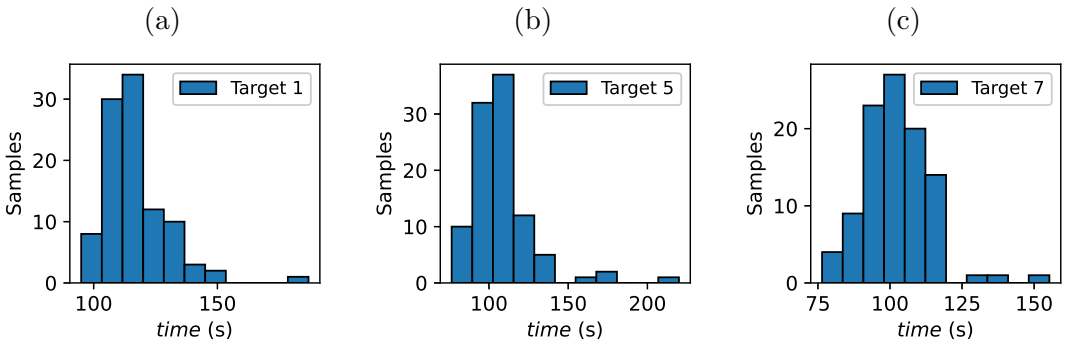

Figure 5.14: Histograms showing the distribution of the convergence time for target (a) model 1, (b) model 5, and (c) model 7 using the CMA-ES-based algorithm executed in parallel with multiple threads.

The DE-based framework, though not explicitly shown in Figures 5.12–5.14, requires significantly longer runtimes. This is due to its reliance on repeated time-domain simulations, SSI computations, and the intentional overestimation of system order to extract stable modes within each generation. For example, complex scenarios like target model 5 require hundreds of generations, substantially increasing computational time. While parallel execution could reduce these costs by distributing population evaluations, the framework's inherent overhead makes it less suitable for applications requiring rapid responses. As a reference, target model 1 typically requires 550–1900 s to converge.

All simulations were performed on the University of Nottingham's HPC cluster, specifically a high-memory node configured with 2 × 48-core AMD CPUs and 1.5 TB of RAM.

5.4 Conclusions

This study developed and compared three model updating frameworks for estimating the scour depth of pile foundations: a deterministic FRF-based method, and two stochastic approaches (DE-based and CMA-ES-based).

The deterministic FRF-based framework uses input-output data from impact testing to match first- and second-mode FRF peaks through a two-stage iterative algorithm. It demonstrated robust performance under noise and varying soil conditions, provided damping assumptions and load measurements were accurate. While it is computationally faster than the stochastic methods, significant variability in soil stiffness or noise required fine-tuning of the stopping criteria to ensure reliability.

In contrast, the DE-based approach operates in an output-only setting, relying

on repeated time-domain simulations and SSI to iteratively update key parameters in each generation. This approach demonstrated robustness to uncertainties in input loads and soil heterogeneity but demanded significant computational resources, especially for complex soil profiles. Its consistent performance across all target models, including those with ambient load conditions, underscores its applicability for in-service structures. However, the need to carefully configure SSI parameters and stopping criteria highlights the importance of user expertise.

The CMA-ES-based framework also operates in an output-only setting but avoids repeated time-domain simulations. By integrating UQ for frequencies and MAC estimates into the objective function, it eliminates the need for manual tolerance adjustments. This led to faster convergence than DE under noisy or variable conditions. Parallelisation further reduced runtime, enhancing its practicality. Incorporating a ROM for time-domain analyses could preserve these performance gains, although further studies are needed to confirm this.

Each framework can be selected based on load measurement availability, computational resources, and uncertainty in soil properties. While the study explored various SPI configurations and load scenarios, additional research involving field experiments could further validate these methods. Future work on integrating non-linear soil models and refining UQ schemes could enhance real-world applicability. Nonetheless, the three frameworks presented here offer viable solutions for scour monitoring in pile foundations.

Chapter 6

Conclusions and future work

6.1 Conclusions

This thesis has developed and demonstrated three model updating frameworks aimed at estimating critical parameters in soil-pile interaction (SPI) systems. Each framework was designed with specific constraints in mind, such as data availability and the practical realities of monitoring offshore foundations. Together, these approaches advance structural health monitoring (SHM) by integrating physical insight with data-driven methods, enhancing both interpretability and predictive accuracy.

The work is structured around three central contributions, each detailed in its respective chapter:

- A deterministic framework based on frequency response functions (FRFs) for estimating the embedded length and soil parameters of piles subject to controlled lateral impact (**Chapter 3**).
- A stochastic, output-only method that uses stochastic subspace identification (SSI) and Covariance Matrix Adaptation Evolution Strategy (CMA-ES) optimisation to estimate SPI parameters when input forces are unknown (**Chapter 4**).
- A comparative evaluation of three frameworks, namely FRF-based, Differential Evolution (DE)-based, and CMA-ES-based, for estimating scour depth in monopile foundations under various soil and loading conditions (**Chapter 5**).

The key findings of each chapter are summarised below, with a focus on their practical implications and performance under different conditions.

FRF-based estimation of embedded length (Chapter 3)

This chapter presents a two-stage FRF-based framework for estimating the embedded length and dynamic soil parameters of laterally loaded piles. Extending the method of Wu et al. (2018), the approach uses both the first and second vibration modes to improve accuracy. In Stage 1, soil mass and stiffness are iteratively adjusted to match the first-mode FRF peak. Stage 2 refines the embedded length by calling Stage 1 while aligning the second-mode peak. Numerical studies across different geometries and soil profiles show that ignoring the second mode leads to biased estimates, underscoring the need for both stages. The method is computationally efficient and converges reliably under moderate damping and known excitation, making it particularly suited to controlled loading environments.

Output-only model updating using SSI and CMA-ES (Chapter 4)

To address scenarios with unknown excitations, this chapter introduces a stochastic, output-only model-updating framework using SSI and CMA-ES. SSI extracts modal frequencies and mode shapes with associated uncertainty, which guides CMA-ES in refining SPI parameters by minimising the mismatch between modelled and measured modal properties. The framework incorporates uncertainty quantification (UQ) directly into the optimisation, improving robustness and eliminating the need for user-defined tolerance thresholds. Monte Carlo simulations and a full-scale field test confirm its accuracy and resilience to sensor limitations and noise, making it well suited for operational monitoring of pile foundations.

Scour depth estimation using deterministic and stochastic frameworks (Chapter 5)

This chapter compares three model updating frameworks for estimating scour depth: an FRF-based deterministic method, and two stochastic output-only approaches using DE and CMA-ES. The FRF-based method, effective under known impact loading, converges rapidly using a two-stage model updating framework. However, it is sensitive to damping and requires accurate force measurements. The DE-based and CMA-ES-based methods use time-domain identification (SSI)

to estimate modal properties, offering flexibility and noise tolerance at the cost of increased computational effort. A key distinction between the two stochastic methods lies in how they handle the physics-based model: the DE-based framework solves the model numerically during each optimisation iteration, allowing it to address problems where analytical solutions are unavailable, but incurring higher computational cost. In contrast, the CMA-ES-based framework derives modal properties directly from pre-assembled system matrices, enabling more efficient evaluations. The CMA-ES framework further improves performance by incorporating UQ into the optimisation loop, reducing manual tuning and enabling faster, more stable convergence. Numerical studies with various soil profiles and excitation types demonstrate that while all methods can estimate scour depth reliably, CMA-ES offers the best balance between robustness, efficiency, and practical applicability in output-only conditions.

6.2 Future work

In light of the results and methodologies presented throughout this thesis, several paths remain open for further investigation and development. While the foundations of data-driven and physics-based approaches have been established, their full potential in handling complex, real-time applications and uncertain environments has yet to be fully examined. The section below outlines prospective research directions that can broaden the impact and applicability of the current work.

A natural next step involves extending the underlying numerical formulations to better capture nonlinear soil-structure interactions. Although the Winkler-based assumptions are effective for small-strain or quasi-linear conditions, practical offshore wind turbine foundations often face varying degrees of nonlinearity due to large-amplitude excitations or changing soil properties (e.g., cyclic densification, scouring). Incorporating higher-fidelity soil models—possibly via nonlinear beam on Winkler models or advanced finite-element implementations—could improve the robustness and predictive accuracy of digital twins developed for pile foundations.

Machine learning models, such as neural networks and Gaussian processes, have demonstrated strong predictive capabilities but can struggle when extrapolating beyond their training domains. Embedding fundamental physics-based modelling into the learning architecture offers a means to regularise these models, thereby achieving better generalisation and interpretability. A promising extension of this approach is the use of Physics-Informed Neural Networks (PINNs), where an ODE similar to Equation (3.4) describing SPI informs the model structure. This inte-

gration would result in Physics-Enhanced Machine Learning (PEML) frameworks that maintain consistency with engineering principles while adapting to various operational and environmental conditions.

For sustained offshore monitoring, it is crucial that model updating and diagnostics are computationally efficient. Future research can capitalise on model reduction techniques to decrease the complexity of full-scale models without sacrificing accuracy. When combined with parallel computing or dedicated high-performance architectures, model reduction can provide near-real-time SHM capabilities. This would enable operators to promptly respond to structural differences, thereby enhancing the reliability and safety of offshore wind turbine foundations.

UQ proved invaluable for validating the reliability of model-updated predictions under noisy and incomplete measurements. Nonetheless, many additional UQ methods remain underexplored, ranging from Bayesian approaches to polynomial chaos expansions. Future studies could extend these strategies to incorporate multi-source data fusion by integrating measurements not only from accelerometers but also from strain gauges, hydrodynamic observations, and other sensor types. By merging diverse sensor data with robust UQ, the updated models would provide a more holistic and statistically justified view of the system's health.

Another promising direction involves further refining methods for minimal sensor placement. Future work could incorporate observability metrics—quantifying how effectively a certain sensor layout captures global modes and structural states—into the sensor configuration design process. Combining advanced optimisation algorithms with structural observability criteria might yield automated, cost-effective sensor deployment plans, especially relevant for large offshore wind farms.

Although advanced algorithms and numerical models are essential, the ultimate value of SHM lies in the decisions made by engineers, operators, and stakeholders. Future research can enhance transparency by integrating explainable artificial intelligence (AI) tools into the model updating workflow, ensuring that predictions, warnings, and recommendations are conveyed with interpretable rationales and confidence levels. Incorporating intuitive user interfaces and visual analytics can help non-experts understand and act upon the outputs of model updates in a timely and informed manner.

Finally, expanding the scope from monitoring individual foundations to entire wind farms represents a significant and achievable goal. Integrating comprehensive monitoring systems across multiple structures can enhance overall operational efficiency and structural integrity. This approach aligns with broader industry trends aimed at developing unified monitoring solutions for large-scale offshore energy assets, facilitating proactive maintenance, informed decision-making, and

sustained performance throughout the infrastructure's lifecycle.

Collectively, these directions illustrate how the methods, tools, and concepts presented in this thesis can evolve to tackle increasingly complex, data-rich, and operationally demanding applications. By merging detailed physics, advanced machine learning, UQ, and real-time capabilities, future research is well positioned to further enhance the reliability and efficiency of monitoring methods.

Appendix A

Preliminary analysis of an FRF-based depth-dependent stiffness estimation approach for lateral soil-pile interaction

Authors: Andreas Ioakim, Luke J. Prendergast
Paper Status: Published in ICCMSE proceedings
DOI: 10.1063/5.0247323

A.1 Introduction

Offshore wind turbines are complex structures subjected to significant dynamic forces, including wind and wave loads, which can substantially influence the structural response of supporting monopiles. Accurate modelling of soil-pile interaction (SPI) systems is essential, yet obtaining precise SPI parameters remains challenging, especially in inaccessible offshore environments. This study examines how variations in soil stiffness affect displacement and acceleration responses in example pile structures and quantifies the influence of key parameters. To address these challenges, an FRF-based model updating method is implemented to estimate the soil stiffness profile. In addition, the method is applied to identify a random soil stiffness distribution using acceleration data collected at multiple nodes along the pile. The findings provide valuable preliminary insights into characterising the behaviour of monopiles supporting offshore wind turbines, offering potential improvements for future designs and enhancing the safety and efficiency of offshore wind energy production.

This preliminary work presents an enhancement to an existing FRF-based model updating method, which updates the embedded length, soil mass, and stiffness by calculating a weighting factor based on the acceleration of the pile head. This weighting is applied to an initial stiffness guess when the profile is known (Ioakim & Prendergast, 2024; Wu et al., 2018). The enhanced method extends the approach to facilitate the estimation of depth-dependent stiffness profiles. It begins with a random initial profile and employs multiple nodes to iteratively compute the depth-dependent stiffness when the profile is unknown, assuming the soil mass is already known. The performance of a preliminary version of this model is presented in this appendix.

A.2 Numerical modelling of the soil-pile system

This section provides a description of the numerical model used in the analysis. A visual representation of the pile model is shown in Figure A.1.

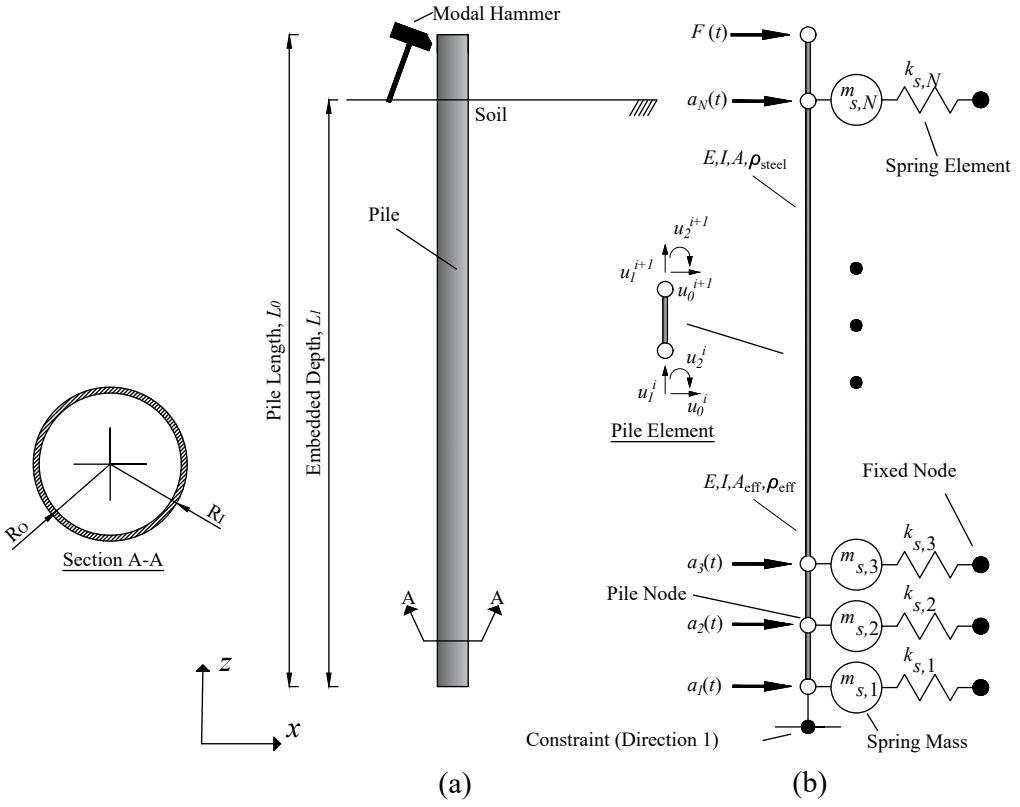

Figure A.1: (a) Schematic of the soil-pile system, and (b) Equivalent Winkler model

The soil mass is represented by attaching lumped masses to the pile nodes, which are connected to Winkler springs. The equation of motion for this dynamic system is given in Equation (3.4).

$$\mathcal{M}^\theta \ddot{\mathbf{q}}(t) + \mathcal{D}^\theta \dot{\mathbf{q}}(t) + \mathcal{K}^\theta \mathbf{q}(t) = \mathbf{u}(t) \tag{3.4}$$

At a specific time step in the numerical model, the vector $\mathbf{u}$ represents the external forces acting on each degree of freedom, while $\mathbf{q}$ denotes the displacement profile as a function of time t. The damping matrix $\mathcal{D}$ is constructed using a two-term Rayleigh damping approach, which expresses $\mathcal{D}$ as a linear combination of the mass matrix $\mathcal{M}$ and stiffness matrix $\mathcal{K}$, as described in Equation (3.5).

$$\mathcal{D}^\theta = \alpha_0 \, \mathcal{M}^\theta + \alpha_1 \, \mathcal{K}^\theta, \tag{3.5}$$

The example system in this appendix consists of a pile with a total length of 11 m, embedded 10 m into the soil. An impulse force of 10 000 N is applied for an arbitrary duration of 0.010 s in each case, simulating the impact of a modal hammer on the pile. Acceleration and velocity measurements are recorded at

multiple locations along the pile to facilitate depth-dependent stiffness updating.

The pile model is assumed to be embedded in a sand layer with depth-dependent stiffness variations. In this study, the equation provided by Vesic is utilised to calculate the coefficient of subgrade reaction $K_S(z)$, which varies with depth. This equation determines $K_S(z)$ by matching the maximum displacements of an infinite beam, as shown in Equation (2.3) (Vesić, 1961).

$$K_S(z) = \frac{0.65 E_S(z)}{D(1-\nu_s^2)} \sqrt[12]{\frac{E_S(z) D^4}{EI}} \tag{2.3}$$

The stiffness of the i^{th} spring is given by Equation (3.2)

$$k_i = K_S(z) D_i L_i \tag{3.2}$$

Figure A.2 presents a small-strain stiffness profile generated through numerical simulation to test the depth-dependent model updating approach.

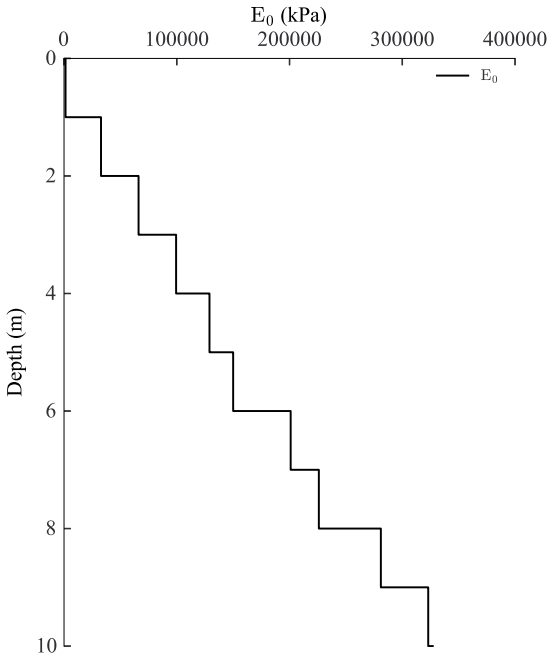

Figure A.2: Numerical generated E_0 profile

A.3 Effect of the soil stiffness on the lateral response of piles

This section evaluates the impact of soil stiffness on the lateral response characteristics of piles, illustrating how stiffness variations influence the displacement

and acceleration FRFs of monopiles subjected to dynamic lateral loading. Figure A.3(a) shows the amplitude of the first peak in the displacement frequency response function (FRF) for a 11 m long, 4 m diameter pile. These results were obtained by developing and analysing models with a mean stiffness (E_0) ranging from 110 000 kPa to 1 100 000 kPa, while applying an external soil mass equal to the pile's mass, distributed across the top quarter of the pile's length.

Similarly, Figure A.3(b) illustrates the magnitude of the first peak in the acceleration FRF for the same pile. The results align with the well-established principle that stiffness has a greater influence on the displacement FRF than on the acceleration FRF (Wu et al., 2018). It is important to note that these stiffness values are not intended to represent real soil conditions; rather, they serve to demonstrate their effect on the resulting FRF peaks.

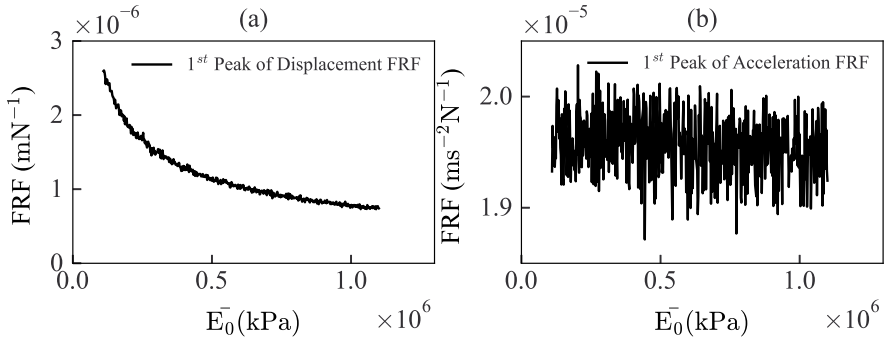

Figure A.3: (a) Effect of stiffness on the lateral displacement FRF of the top node in soil, (b) Effect of stiffness on the lateral acceleration FRF of the top node in soil

A.4 Depth-dependent stiffness updating

This section evaluates the performance of a preliminary iterative solution approach for estimating the depth-dependent stiffness of a beam-Winkler model using FRF data from multiple depths along the pile. This approach is a modified version of the method developed by Wu et al. (2018), which determined the weightings of operating mass and stiffness across an entire soil stiffness profile. In this enhanced method, accelerometers are assumed to be placed at various depths along the pile to independently compute the operating stiffness at each node.

Figure A.4 illustrates how the algorithm iteratively converges for three randomly selected degrees of freedom (DOFs) in the system: one near the top, one near the middle, and one near the bottom. Once the FRFs of all nodes converge to the target model, the extracted spring data are compared to the target values to assess convergence accuracy. Since the stiffness values of the target model

are unknown in real piles, this analysis relies on numerically simulated data to evaluate the effectiveness of the method.

Figure A.5 compares the initial guessed stiffness values and the converged stiffness values against the target model. The results presented in Figures A.4, A.5 demonstrate that the FRF-based model updating method successfully converges to stiffness values significantly closer to the target stiffness, highlighting its effectiveness in estimating the random stiffness profile of the soil.

However, further optimisation is required to improve convergence and accuracy, as discrepancies remain in the lower part of the stiffness profile. For instance, at a depth of 7 m, the target model indicates a spring stiffness of 48 000 kN m^{-1}, while the initial model has a stiffness of 30 600 kN m^{-1}. After convergence, the final model achieves a stiffness of 48 600 kN m^{-1}, corresponding to a relative error of 36.25 % for the initial model and 1.25 % for the converged model.

Similarly, at a depth of 4 m, the target stiffness is 26 100 kN m^{-1}, while the initial and converged models exhibit stiffness values of 16 000 kN m^{-1} and 25 700 kN m^{-1}, respectively, yielding relative errors of 38.70 % and 1.53 % for the initial and converged models, respectively.

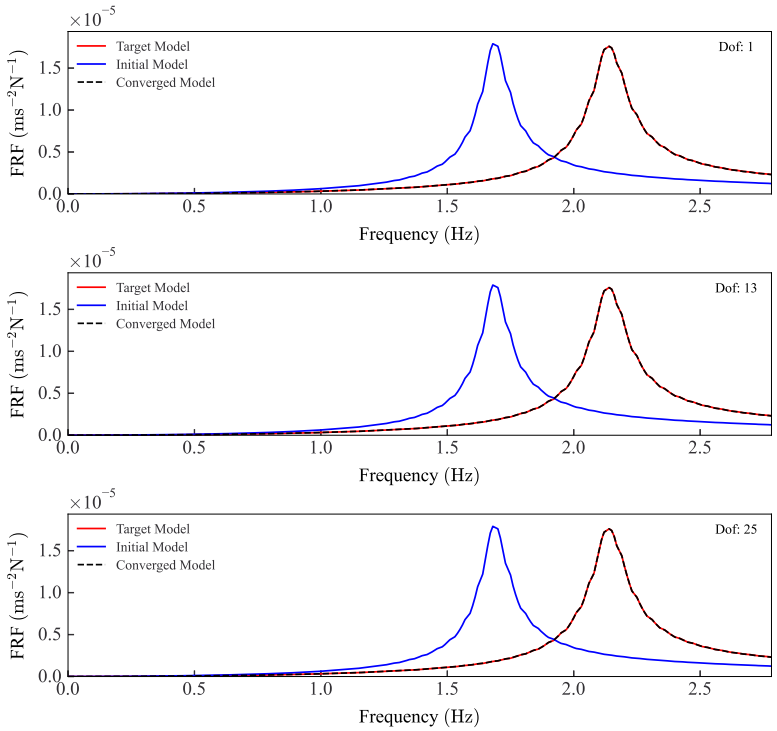

Figure A.4: Comparison of target, initial and converged model FRF

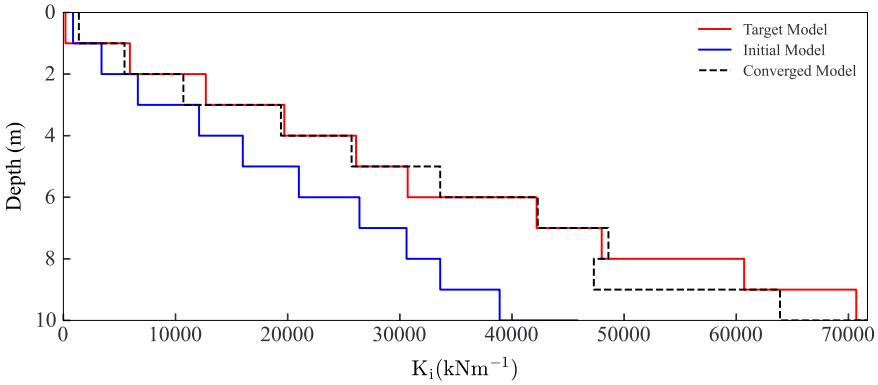

Figure A.5: Comparison of stiffness of converged numerical model to target model

A.5 Conclusion

In summary, this study investigated the influence of soil stiffness on the FRFs of laterally loaded piles. A preliminary version of a newly developed FRF-based model updating method was employed to estimate the depth-dependent soil stiffness profile and analyse its effect on the displacement and acceleration of an example SPI model. This enhanced FRF-based method-building on the approach by Wu et al. (2018), was used to identify the random stiffness profile of the soil based on acceleration measurements obtained at multiple nodes along the pile.

The findings of this study provide valuable insights and lay the groundwork for a finalised depth-dependent stiffness estimation method, which can be applied to real piles when acceleration data are available at multiple locations. Future work will incorporate real-world experimental conditions into the analysis to gain a comprehensive understanding of the applicability and performance of the updating approach in practical scenarios. Additionally, efforts will focus on extending the method to models with a higher number of degrees of freedom, further enhancing its accuracy and robustness.

Appendix B

Dynamic modelling of vibrating structures

This appendix provides a comprehensive examination of vibrational analysis techniques (Peeters & De Roeck, 1999) and the statistical evaluation of modal parameter variances (Greś, 2019). It begins with the analysis of undamped systems, followed by discussions on proportional and general viscous damping scenarios. The appendix further explores the state-space representation of system parameter identification and outlines model reduction strategies for developing efficient reduced-order models. Additionally, it delves into the assessment of modal parameter uncertainties using the Delta method and first-order perturbation theory. Together, these sections offer the theoretical and methodological foundations that support the main research presented in this thesis.

B.1 Vibrational analysis

B.1.1 Undamped case

The computation of eigenvalues and eigenvectors from Equation (3.4) is a standard approach commonly found in modal analysis textbooks. This derivation begins by considering the simplest case where damping is neglected. The solutions of the homogeneous model differential equations take the form shown in Equation (B.1):

$$\mathcal{M}^{\theta}\ddot{\mathbf{q}}(t) + \mathcal{K}^{\theta}\mathbf{q}(t) = 0 \tag{B.1}$$

Assuming a solution of the form $\mathbf{q}(t) = \phi_n \, e^{\lambda_n t}$, substituting into Equation (B.1) leads to a generalised eigenvalue problem described in Equation (2.5), which can be written as:

$$\mathcal{K}^\theta \phi_n = \mathcal{M}^\theta \phi_n \, (-\lambda_n^2) \tag{B.2}$$

where $\phi_n \in \mathbb{R}^{n_2}$ represents the eigenvectors, and $-\lambda_n^2$ is a real eigenvalue. These eigenvalues are often expressed as the square of an eigenfrequency ω_n^2, such that $\lambda_n = j\omega_n$ where j is the imaginary unit, defined by $j^2 = -1$. The generalised eigenvalue problem from Equation (B.2) can be reformulated into a matrix form as follows:

$$\mathcal{K}^\theta \mathbf{\Phi} = \mathcal{M}^\theta \mathbf{\Phi} \, \mathbf{\Omega}^2 \tag{B.3}$$

where $\mathbf{\Phi} \in \mathbb{R}^{n_2 \times n_2}$ is a matrix containing the eigenvectors also referred as mode shapes ϕ_n as its columns, and $\mathbf{\Omega} = \text{diag}([\omega_n]) \in \mathbb{R}^{n_2 \times n_2}$ is a diagonal matrix containing the eigenfrequencies ω_n in radians per second. The orthogonality properties of the eigenvectors can then be expressed as:

$$\mathbf{\Phi}^T \mathcal{M}^\theta \mathbf{\Phi} = \mathbf{M}_{\text{modal}}, \quad \mathbf{\Phi}^T \mathcal{K}^\theta \mathbf{\Phi} = \mathbf{K}_{\text{modal}}, \tag{B.4}$$

where $\mathbf{M}_{\text{modal}}$ and $\mathbf{K}_{\text{modal}}$ are diagonal matrices containing the modal masses m_n and modal stiffnesses k_n, respectively. Using this property, the eigenfrequencies ω_n can be related to the modal parameters as:

$$\omega_n^2 = \frac{k_n}{m_n}.$$

B.1.2 Proportional damping

$$\mathcal{M}^\theta \ddot{\mathbf{q}}(t) + \mathcal{D}^\theta \dot{\mathbf{q}}(t) + \mathcal{K}^\theta \mathbf{q}(t) = \mathcal{B}\mathbf{u}(t) \tag{B.5}$$

By multiplying Equation (B.5) (where $\mathcal{B} \in \mathbb{R}^{n_2 \times m}$, $\mathbf{u} \in \mathbb{R}^m$, and m represents the number of inputs) by $\mathbf{\Phi}^{\mathrm{T}}$, and introducing the coordinate transformation $\mathbf{q}(t) = \mathbf{\Phi} \, \mathbf{q}_m(t)$, the equation is reformulated in modal coordinates.

$$\mathbf{q}(t) = \mathbf{\Phi} \, \mathbf{q}_m(t),$$

the second-order finite element model equation, Equation (B.5), can be transformed into modal coordinates:

$$\mathbf{\Phi}^T \mathcal{M}^\theta \mathbf{\Phi}\, \ddot{\mathbf{q}}_m(t) \;+\; \mathbf{\Phi}^T \mathcal{D}^\theta \mathbf{\Phi}\, \dot{\mathbf{q}}_m(t) \;+\; \mathbf{\Phi}^T \mathcal{K}^\theta \mathbf{\Phi}\, \mathbf{q}_m(t) \;=\; \mathbf{\Phi}^T\, \mathcal{B}\, \mathbf{u}(t). \tag{B.6}$$

The vector $\mathbf{q}_m(t) \in \mathbb{R}^{n_2}$ contains the modal displacements. Using the orthogonality properties of the eigenvectors as defined in Equation (B.4), the first and third terms in the left-hand side of Equation (B.6) simplify. Additionally, under the assumption of proportional damping, the eigenvectors also diagonalise the damping matrix $\mathcal{D}^\theta$, leading to:

$$\mathbf{\Phi}^T \mathcal{D}^\theta \mathbf{\Phi} = \mathbf{\Gamma}\, \mathbf{M}_{\text{modal}}, \quad \mathbf{\Gamma} = \text{diag}\big([2\,\xi_n\,\omega_n]\big), \tag{B.7}$$

where ξ_n are the modal damping ratios, defined as $\xi_n = \frac{d_n}{2\,m_n\,\omega_n}$. Substituting these results into Equation (B.6) yields a fully decoupled set of modal equations, with diagonal left-hand-side matrices:

$$\mathbf{I}\, \ddot{\mathbf{q}}_m(t) \;+\; \mathbf{\Gamma}\, \dot{\mathbf{q}}_m(t) \;+\; \mathbf{\Omega}^2\, \mathbf{q}_m(t) \;=\; \mathbf{M}_{\text{modal}}^{-1}\, \mathbf{\Phi}^T\, \mathcal{B}\, \mathbf{u}(t). \tag{B.8}$$

The solutions of the homogeneous model differential equations with proportional damping retain the form $\mathbf{q}(t) = \phi_n\, e^{\lambda_n t}$.

It can be shown that the eigenvectors ϕ_n remain unchanged compared to the undamped case. From Equation (B.8), the eigenvalues λ_n are determined as solutions of the characteristic equation:

$$\lambda_n^2 \;+\; 2\,\xi_n\,\omega_n\,\lambda_n \;+\; \omega_n^2 \;=\; 0,$$

which yields the following solutions:

$$\lambda_n,\; \lambda_n^* \;=\; -\xi_n\,\omega_n \;\pm\; j\,\omega_n\,\sqrt{1-\xi_n^2},$$

where the superindex * denotes the complex conjugate. In cases where a damping description is required in physics-based modelling, modal damping ratios ξ_n are typically specified for the modes of interest. These ratios are often determined experimentally using system identification techniques applied to vibration data (reviewed in section 2.2). Using these modal damping ratios, a complete damping matrix $\mathcal{D}^\theta$ can be reconstructed as:

$$\mathcal{D}^\theta = \mathbf{\Phi}^{-T}\,\mathbf{M}_{\text{modal}}\,\mathbf{\Gamma}\,\mathbf{\Phi}^{-1} = \mathcal{M}^\theta\,\mathbf{\Phi}\,\mathbf{M}_{\text{modal}}^{-1}\,\text{diag}\big([2\,\xi_n\,\omega_n]\big)\,\mathbf{\Phi}^T\,\mathcal{M}^\theta, \tag{B.9}$$

B.1.3 General viscous damping

When the assumption of proportional damping is not valid, the eigenvalue problem becomes more complex. In such cases, the eigenvalues of the undamped system ($\mathcal{K}^\theta$ and $\mathcal{M}^\theta$) do not correspond to the eigenvalues of the damped system ($\mathcal{D}^\theta$). A reformulation of the governing equation is required to address general non-proportional damping. This reformulation involves expressing the second-order equation as a first-order state-space system.

Defining the state vector $\mathbf{x}(t) \in \mathbb{R}^s$ and:

$$\mathbf{x}(t) = \begin{pmatrix}\mathbf{q}(t)\\ \dot{\mathbf{q}}(t)\end{pmatrix}, \quad \mathbf{P} = \begin{pmatrix}\mathcal{D}^\theta & \mathcal{M}^\theta\\ \mathcal{M}^\theta & \mathbf{0}\end{pmatrix}, \quad \mathbf{Q} = \begin{pmatrix}\mathcal{K}^\theta & \mathbf{0}\\ \mathbf{0} & -\mathcal{M}^\theta\end{pmatrix}, \tag{B.10}$$

the original second-order system is transformed into a first-order system:

$$\mathbf{P}\dot{x}(t) + \mathbf{Q}x(t) = \begin{pmatrix}\mathcal{B}\\ 0\end{pmatrix} u(t) \tag{B.11}$$

The eigenvalue problem for this system can be written as:

$$\mathbf{P}\Psi\Lambda_\text{c} + \mathbf{Q}\Psi = \mathbf{0}. \tag{B.12}$$

Here, $\Psi \in \mathbb{C}^{s\times s}$ represents the $s = 2n_2$ complex eigenvectors, and $\Lambda_\text{c} \in \mathbb{C}^{s\times s}$ is the diagonal matrix containing the s complex eigenvalues λ_n. The eigenvalue matrix $\mathbf{\Lambda}_\text{c}$ and eigenvector matrix $\mathbf{\Psi}$ can be written as:

$$\Lambda_\text{c} = \begin{pmatrix}\Lambda & \mathbf{0}\\ \mathbf{0} & \Lambda^*\end{pmatrix}, \quad \Psi = \begin{pmatrix}\mathbf{\Theta} & \mathbf{\Theta}^*\\ \mathbf{\Theta\Lambda} & \mathbf{\Theta}^*\mathbf{\Lambda}^*\end{pmatrix}, \tag{B.13}$$

where $\mathbf{\Lambda}$ and $\mathbf{\Theta}$ are the eigenvalues and eigenvectors of the original second-order system. These eigenvalues satisfy the following equation:

$$\mathcal{M}^\theta\mathbf{\Theta\Lambda}^2 + \mathcal{D}^\theta\mathbf{\Theta\Lambda} + \mathcal{K}^\theta\mathbf{\Theta} = 0. \tag{B.14}$$

Unlike the case of proportional damping, where the eigenvectors diagonalise

$\mathcal{M}^\theta, \mathcal{D}^\theta, \mathcal{K}^\theta$, in non-proportional damping, the matrices are not fully diagonalizable. The eigenvalues for this case are given by:

$$\lambda_n, \lambda_n^* = -\xi_n \omega_n \pm j\omega_n \sqrt{1-\xi_n^2}, \tag{B.15}$$

where ξ_n and ω_n represent the modal damping ratios and natural frequencies, respectively.

To compute the modal matrices, orthogonality conditions are utilised:

$$\boldsymbol{\Psi}^\top \mathbf{P} \boldsymbol{\Psi} = \operatorname{diag}\big(a_n\big), \quad \boldsymbol{\Psi}^\top \mathbf{Q} \boldsymbol{\Psi} = \operatorname{diag}\big(b_n\big), \tag{B.16}$$

where $\operatorname{diag}\big(a_n\big)$ and $\operatorname{diag}\big(b_n\big)$ represent the modal mass and stiffness matrices. The eigenvalue matrix $\boldsymbol{\Lambda}_\mathrm{c}$ can be further expressed as:

$$\boldsymbol{\Lambda}_\mathrm{c} = \operatorname{diag}(\lambda_n) - \operatorname{diag}\left(\frac{1}{a_n} b_n\right). \tag{B.17}$$

B.1.4 State-space representation of SPI

The State Equation

Starting from the second-order equation of motion given in (B.5), one can recast these into a first-order system. By multiplying (B.11) by $\mathbf{P}^{-1}$, a normalised state-space representation is achieved. The normalisation itself involves the matrix

$$\mathbf{P}^{-1} = \begin{pmatrix} 0 & \mathcal{M}^{\theta^{-1}} \\ \mathcal{M}^{\theta^{-1}} & -\mathcal{M}^{\theta^{-1}} \mathcal{D}^\theta \mathcal{M}^{\theta^{-1}} \end{pmatrix}, \tag{B.18}$$

and applying it to (B.11) leads to the system in the form

$$\dot{\mathbf{x}}(t) = \mathbf{A}_c \, \mathbf{x}(t) + \mathbf{B}_c \, \mathbf{u}(t), \tag{B.19}$$

where $\mathbf{x}(t)$ is the state vector in first-order form, $A_c \in \mathbb{R}^{s \times s}$ is the continuous-time state matrix, and $\mathbf{B}_c \in \mathbb{R}^{s \times m}$ is the input matrix. In particular, (B.20) defines

$$\mathbf{A}_c = -\mathbf{P}^{-1}\mathbf{Q} = \begin{pmatrix} 0 & \mathcal{I} \\ -\mathcal{M}^{\theta^{-1}}\mathcal{K}^{\theta} & -\mathcal{M}^{\theta^{-1}}\mathcal{D}^{\theta} \end{pmatrix},$$
$$\mathbf{B}_c = P^{-1}\begin{pmatrix} \mathcal{B} \\ 0 \end{pmatrix}, = \begin{pmatrix} 0 \\ \mathcal{M}^{\theta^{-1}}\mathcal{B} \end{pmatrix}, \tag{B.20}$$

with the precise structure of these matrices governed by how $\mathbf{P}$ and $\mathbf{Q}$ are formed from the underlying mass, damping, and stiffness operators $(\mathcal{M}, \mathcal{D}, \mathcal{K})$.

One can show that $\mathbf{A}_c$ can be decomposed through a modal transformation (B.16) and property (B.17). Specifically, if $\mathbf{\Psi}$ is the matrix of eigenvectors and $\mathbf{\Lambda}_c$ is the diagonal matrix of eigenvalues, then (B.21) can be written as:

$$\mathbf{A}_c = \mathbf{\Psi}\,\mathbf{\Lambda}_c\,\mathbf{\Psi}^{-1}, \tag{B.21}$$

indicating that finding $\mathbf{\Lambda}_c$ and $\mathbf{\Psi}$ is essentially a standard eigenvalue problem. This diagonalisation highlights that $\mathbf{\Lambda}_c$ contains the system's eigenvalues, while Ψ contains the corresponding eigenvectors of $\mathbf{A}_c$.

The observation equation

In a practical experiment, not all degrees of freedom (DOFs) of the structure are directly measured. Instead, measurements may be taken at only a subset of DOFs at locations (l). Equation (B.22) introduces an output equation of the form

$$\mathbf{y}(t) = \mathbf{C}_a\,\ddot{\mathbf{q}}(t) + \mathbf{C}_v\,\dot{\mathbf{q}}(t) + \mathbf{C}_d\,\mathbf{q}(t), \tag{B.22}$$

where $\mathbf{y}(t) \in \mathbb{R}^l$ contains the measured outputs, and $\mathbf{C}_a$, $\mathbf{C}_v$, $\mathbf{C}_d \in \mathbb{R}^{l\times n_2}$ are output location matrices for acceleration, velocity, and displacement respectively. Equation (B.22) can be re-written using (B.5) and the definition of the state in (B.10), to express the outputs in terms of the state $\mathbf{x}(t)$. This yields (B.23),

$$\mathbf{y}(t) = \mathbf{C}_c\,\mathbf{x}(t) + \mathbf{D}_c\,\mathbf{u}(t), \tag{B.23}$$

where $\mathbf{C}_c \in \mathbb{R}^{l\times n}$ and $\mathbf{D}_c \in \mathbb{R}^{l\times m}$ are typically derived from the physics-based model matrices.

The state-space model

By combining the normalised first-order system (B.19) with the output equation (B.23), the classic continuous-time state-space system is obtained in Equation (B.24)

$$\begin{aligned} \dot{\mathbf{x}}(t) &= \mathbf{A}_c\,\mathbf{x}(t) + \mathbf{B}_c\,\mathbf{u}(t), \\ \mathbf{y}(t) &= \mathbf{C}_c\,\mathbf{x}(t) + \mathbf{D}_c\,\mathbf{u}(t) \end{aligned} \tag{B.24}$$

where in the discrete time-space it can be re-written as (B.25).

$$\begin{aligned} \mathbf{x}_{k+1} &= \mathbf{A}\mathbf{x}_k + \mathbf{B}\mathbf{u}_k, \\ \mathbf{y}_k &= \mathbf{C}\mathbf{x}_k + \mathbf{D}\mathbf{u}_k \end{aligned} \tag{B.25}$$

Finally when noise is added, then the stochastic components have to be included in the model in Equation (B.26)

$$\begin{aligned} \mathbf{x}_{k+1} &= \mathbf{A}\mathbf{x}_k + \mathbf{B}\mathbf{u}_k + \mathbf{w}_k, \\ \mathbf{y}_k &= \mathbf{C}\mathbf{x}_k + \mathbf{D}\mathbf{u}_k + \mathbf{v}_k \end{aligned} \tag{B.26}$$

Where $\mathbf{w}_k \in \mathbb{R}^n$ represents the process noise arising from disturbances and modelling errors, while $\mathbf{v}_k \in \mathbb{R}^l$ denotes the measurement noise resulting from sensor inaccuracies. Both $\mathbf{w}_k$ and $\mathbf{v}_k$ are unobservable vector signals, assumed to be zero-mean, white, and characterised by the following covariance matrices:

$$\mathbb{E}\left[\begin{bmatrix}\mathbf{w}_p \\ \mathbf{v}_p\end{bmatrix}\begin{pmatrix}\mathbf{w}_q^{\mathrm{T}} & \mathbf{v}_q^{\mathrm{T}}\end{pmatrix}\right] = \begin{pmatrix}\mathbf{Q} & \mathbf{S} \\ \mathbf{S}^{\mathrm{T}} & \mathbf{R}\end{pmatrix}\delta_{pq}, \tag{B.27}$$

where $\mathbb{E}$ is the expected value operator; δ_{pq} is the Kronecker delta ($p = q$ implies $\delta_{pq} = 1$, otherwise $\delta_{pq} = 0$); and p, q are two arbitrary time instants. $\mathbf{Q}$ and $\mathbf{R}$ represent the covariance of $\mathbf{w}_k$ and $\mathbf{v}_k$, respectively, while $\mathbf{S}$ represents the cross-covariance between $\mathbf{w}_k$ and $\mathbf{v}_k$.

In an output-only system, the available vibration information consists solely of the response of a structure subjected to unmeasurable inputs. Due to the absence of input data, it becomes impossible to distinguish between the input terms $\mathbf{u}_k$ and the noise terms $\mathbf{w}_k$ and $\mathbf{v}_k$ in Equation (B.26). Consequently, the

system is represented using the purely stochastic state-space model defined by Equation (B.28).

$$\begin{aligned} \mathbf{x}_{k+1} &= \mathbf{A}\mathbf{x}_k + \mathbf{w}_k, \\ \mathbf{y}_k &= \mathbf{C}\mathbf{x}_k + \mathbf{v}_k \end{aligned} \tag{B.28}$$

The input is implicitly represented by the noise terms. However, the assumption that these noise terms are white cannot be disregarded, as it is essential for validating the system identification methods discussed in the next chapter. If this white noise assumption is violated—such as when the input includes dominant frequency components alongside white noise—these frequency components cannot be distinguished from the system's eigenfrequencies. As a result, they may manifest as spurious poles in the state matrix $\mathbf{A}$.

B.2 Model optimisation

B.2.1 Compressed sparse row (CSR) matrices

When solving large-scale systems of equations arising from physics-based models, a significant fraction of the matrix elements are often zero. As a result, it is computationally inefficient and memory-intensive to store the entire matrix in a dense format. The CSR format addresses this challenge by storing only the non-zero elements and the indices required to locate them (Tewarson & Tewarson, 1973).

Overview of CSR Structure

The CSR format represents a sparse matrix $\mathbf{A} \in \mathbb{R}^{n \times n}$ with three arrays:

- `val`: Contains the non-zero values of the matrix, stored row-by-row.
- `col_ind`: Specifies the column indices corresponding to each non-zero element in `val`.
- `row_ptr`: Records the cumulative count of non-zero elements up to the beginning of each row. This array has a length of $(n + 1)$, where `row_ptr[i]` gives the index in `val` (and `col_ind`) where row i begins.

Matrix-vector multiplications, forward/backward substitutions, and other linear algebraic operations can then be carried out efficiently by traversing only the non-zero entries.

Illustrative 10×10 Example

In this section, we demonstrate CSR formatting using the 10×10 matrices $\mathcal{M}^\theta$, $\mathcal{D}^\theta$, and $\mathcal{K}^\theta$ from Equation (3.4). For compactness, we display three characteristic sparse matrices that might arise in structural dynamics.

A simple diagonal mass matrix is given by:

$$\mathcal{M}^{\theta} = \begin{bmatrix} 1 & 0 & 0 & 0 & 0 & 0 & 0 & 0 & 0 & 0 \\ 0 & 2 & 0 & 0 & 0 & 0 & 0 & 0 & 0 & 0 \\ 0 & 0 & 3 & 0 & 0 & 0 & 0 & 0 & 0 & 0 \\ 0 & 0 & 0 & 4 & 0 & 0 & 0 & 0 & 0 & 0 \\ 0 & 0 & 0 & 0 & 5 & 0 & 0 & 0 & 0 & 0 \\ 0 & 0 & 0 & 0 & 0 & 6 & 0 & 0 & 0 & 0 \\ 0 & 0 & 0 & 0 & 0 & 0 & 7 & 0 & 0 & 0 \\ 0 & 0 & 0 & 0 & 0 & 0 & 0 & 8 & 0 & 0 \\ 0 & 0 & 0 & 0 & 0 & 0 & 0 & 0 & 9 & 0 \\ 0 & 0 & 0 & 0 & 0 & 0 & 0 & 0 & 0 & 10 \end{bmatrix}.$$

Only the main diagonal has non-zero entries. Hence, to store this matrix in CSR:

- `val` = [1, 2, 3, 4, 5, 6, 7, 8, 9, 10],
- `col_ind` = [0, 1, 2, 3, 4, 5, 6, 7, 8, 9],
- `row_ptr` = $[0, 1, 2, 3, 4, 5, 6, 7, 8, 9, 10]$.

A banded damping matrix might look like:

$$\mathcal{D}^{\theta} = \begin{bmatrix} 0.1 & 0.05 & 0 & 0 & 0 & 0 & 0 & 0 & 0 & 0 \\ 0.05 & 0.1 & 0.05 & 0 & 0 & 0 & 0 & 0 & 0 & 0 \\ 0 & 0.05 & 0.1 & 0.05 & 0 & 0 & 0 & 0 & 0 & 0 \\ 0 & 0 & 0.05 & 0.1 & 0.05 & 0 & 0 & 0 & 0 & 0 \\ 0 & 0 & 0 & 0.05 & 0.1 & 0.05 & 0 & 0 & 0 & 0 \\ 0 & 0 & 0 & 0 & 0.05 & 0.1 & 0.05 & 0 & 0 & 0 \\ 0 & 0 & 0 & 0 & 0 & 0.05 & 0.1 & 0.05 & 0 & 0 \\ 0 & 0 & 0 & 0 & 0 & 0 & 0.05 & 0.1 & 0.05 & 0 \\ 0 & 0 & 0 & 0 & 0 & 0 & 0 & 0.05 & 0.1 & 0.05 \\ 0 & 0 & 0 & 0 & 0 & 0 & 0 & 0 & 0.05 & 0.1 \end{bmatrix}.$$

In this tridiagonal band structure, each row has at most three non-zero elements (the main diagonal and the off-diagonals at ± 1). Thus, the non-zero entries and their positions can be stored similarly in CSR arrays.

Finally, a tri-diagonal stiffness matrix is given by:

$$\mathcal{K}^{\theta} = \begin{bmatrix} 50 & -10 & 0 & 0 & 0 & 0 & 0 & 0 & 0 & 0 \\ -10 & 50 & -10 & 0 & 0 & 0 & 0 & 0 & 0 & 0 \\ 0 & -10 & 50 & -10 & 0 & 0 & 0 & 0 & 0 & 0 \\ 0 & 0 & -10 & 50 & -10 & 0 & 0 & 0 & 0 & 0 \\ 0 & 0 & 0 & -10 & 50 & -10 & 0 & 0 & 0 & 0 \\ 0 & 0 & 0 & 0 & -10 & 50 & -10 & 0 & 0 & 0 \\ 0 & 0 & 0 & 0 & 0 & -10 & 50 & -10 & 0 & 0 \\ 0 & 0 & 0 & 0 & 0 & 0 & -10 & 50 & -10 & 0 \\ 0 & 0 & 0 & 0 & 0 & 0 & 0 & -10 & 50 & -10 \\ 0 & 0 & 0 & 0 & 0 & 0 & 0 & 0 & -10 & 50 \end{bmatrix}.$$

This structure also lends itself to an efficient CSR representation, as each row has at most three non-zero entries.

By converting $\mathcal{M}^{\theta}$, $\mathcal{D}^{\theta}$, and $\mathcal{K}^{\theta}$ to CSR format, one can significantly reduce the memory footprint and accelerate numerical operations (e.g., factorisation, iterative solves) by accessing only the relevant, non-zero elements. This conversion is particularly advantageous in large finite element models where the structural matrices are often highly sparse.

B.2.2 Modal reduced order modelling (ROM)

Building an efficient ROM begins by extracting dominant modal parameters through eigen-value decomposition and merging these with the corresponding mode shapes. By mapping continuous-time poles to a discrete-time formulation, the system's principal dynamics are retained in a significantly smaller state-space. This reduced-order model enables more computationally efficient simulations. A pseudocode is provided in Algorithm 10

Algorithm 10 Modal Reduced-Order Model (ROM) Construction

Require: Natural frequencies $\{f_i\}$ and damping ratios $\{\xi_i\}$, $i \in [0, \ldots, n_{\text{mode}})$, mode shapes of interest ϕ (size: $n_{\text{DOF}} \times n_{\text{mode}}$), sampling time-step dt, sensor and input node indices (`sensors`, `inputs`)

Ensure: A reduced order discrete-time state-space model

Step 1: Compute Discrete Poles

For each mode:

$$\mu_i = -\xi_i(2\pi f_i) \; + \; i\,(2\pi f_i)\sqrt{1-\xi_i^2}, \quad \lambda_i = e^{\mu_i \cdot \mathtt{dt}}$$

Step 2: Partition Mode Shapes

$\phi_{\text{sens}} = \phi(\mathtt{sensors}, :)$ ▷ sensor rows

$\phi_{\text{inp}} = \phi(\mathtt{inputs}, :)$ ▷ input rows

Step 3: Assemble Real Matrices for Acceleration

In the acceleration case, construct C such that

$$\mathbf{C} \approx \phi_{\text{sens}} \cdot \text{diag}(\mu_i^2)$$

Construct **D** based on input locations

Step 4: Form Discrete-Time State-Space

Convert λ_i to real-valued **A**-matrix (real-imag form)

Compute **B**-matrix using transform of input shape ϕ_{inp}

`state-space`(**A**, **B**, **C**, **D**, `dt`)

return `Return Reduced-Order State-Space Model`

B.3 Variance of modal parameters

During the process of determining system matrices and their associated modal parameters from experimental measurements, two primary types of statistical errors are commonly encountered: variance and bias. Variance errors arise due to inherent statistical fluctuations caused by limited data samples and the presence of measurement noise. Conversely, bias errors are introduced by modelling decisions, such as the selection of the system order, and can result in the emergence of spurious modes. These erroneous modes are often mitigated through the use of stabilisation diagrams or other model validation techniques.

To evaluate the variance of the estimated modal parameters, a statistical framework can be employed that provides explicit formulations for quantifying their uncertainties. When the distribution of an estimator is sufficiently characterised, confidence intervals serve as an effective tool for representing the associated uncertainty. For instance, Figure B.1 schematically depicts a 95% confidence interval surrounding a parameter estimate assumed to follow a Gaussian distribution.

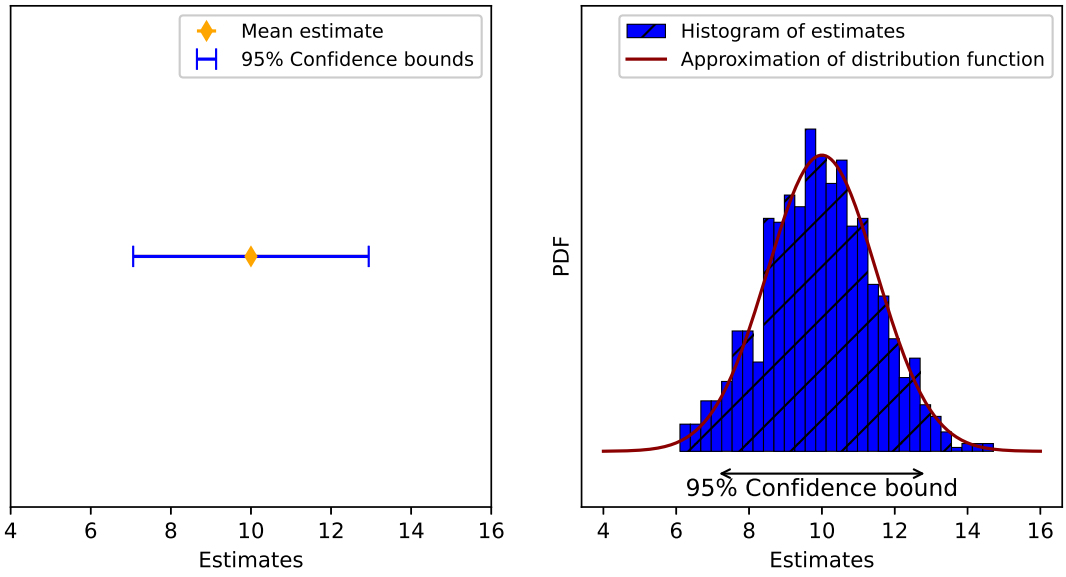

Figure B.1: Conceptual depiction of confidence intervals for a Gaussian estimate.

B.3.1 The delta method and first-order perturbation theory

A widely adopted technique for propagating measurement uncertainties to the estimated modal parameters involves the integration of the Delta method with

first-order perturbation theory. This methodology essentially linearises the relationship between the observed data and the parameter estimates by expanding the target functions (such as the modal parameters) around a nominal operating point. These linear approximations facilitate the examination of how minor variations in the measured data influence the resulting modal parameter estimates.

This approach enables the derivation of analytical expressions for the variances of the parameters of interest. Provided that certain regularity conditions are met, the propagation of variance can be directly calculated using the covariance matrix of the original estimates in conjunction with the Jacobian matrix of the pertinent transformation. Figure B.2 schematically represents this variance propagation process.

By implementing this procedure, a systematic linkage is established between measurement uncertainties and the variability inherent in the identified model. This connection offers a more transparent understanding of the reliability and robustness of the estimated modal parameters, thereby enhancing the credibility of the modal identification process.

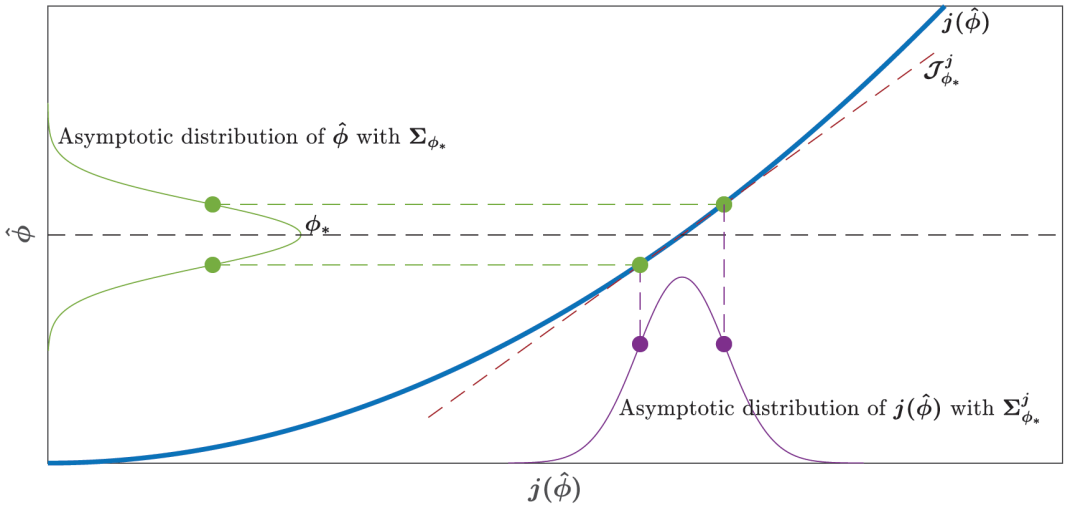

Figure B.2: Illustration of uncertainty propagation based on the Delta method and first-order perturbation theory (Greś, 2019).

Appendix C

Supplementary material

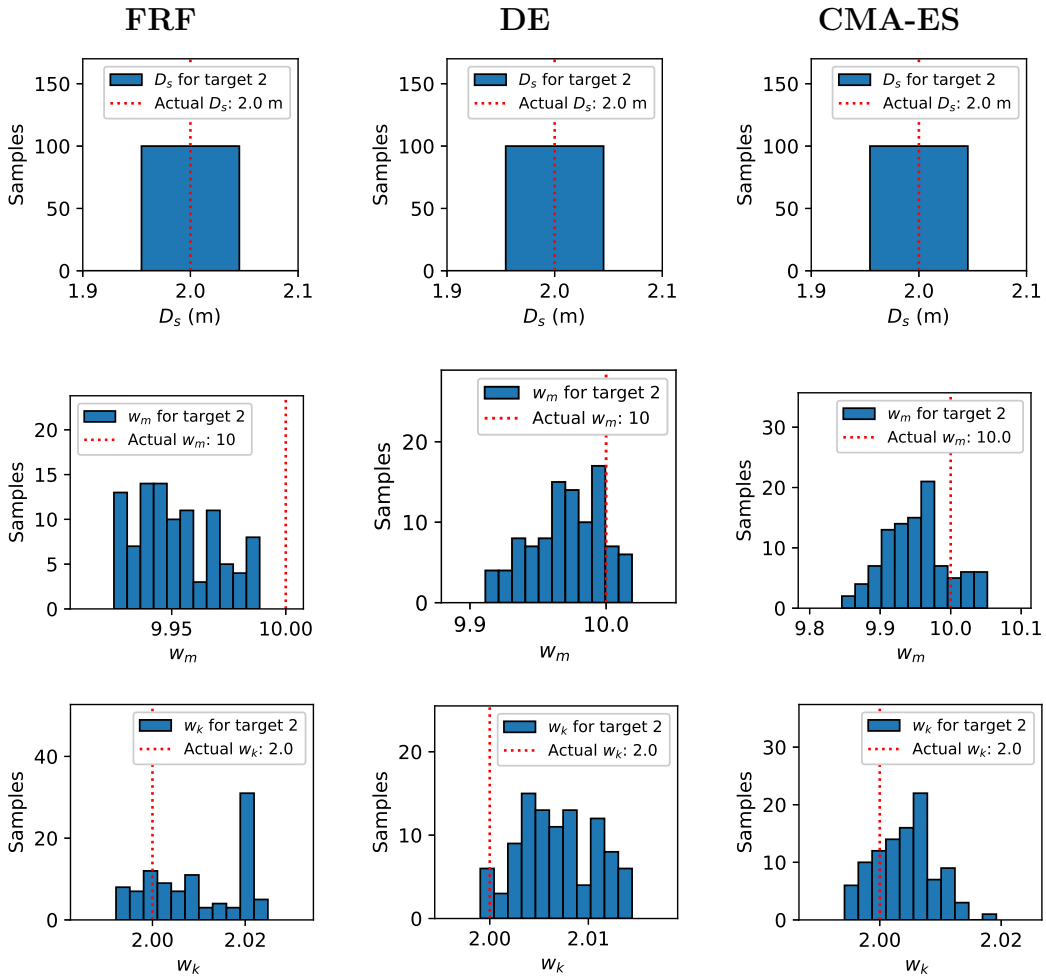

Figure C.1: Comparison of converged parameter distributions for target 2 across FRF-based (left), DE-based (middle), and CMA-ES-based (right) frameworks. Each row corresponds to a parameter: (top) D_s, (middle) w_m, and (bottom) w_k.

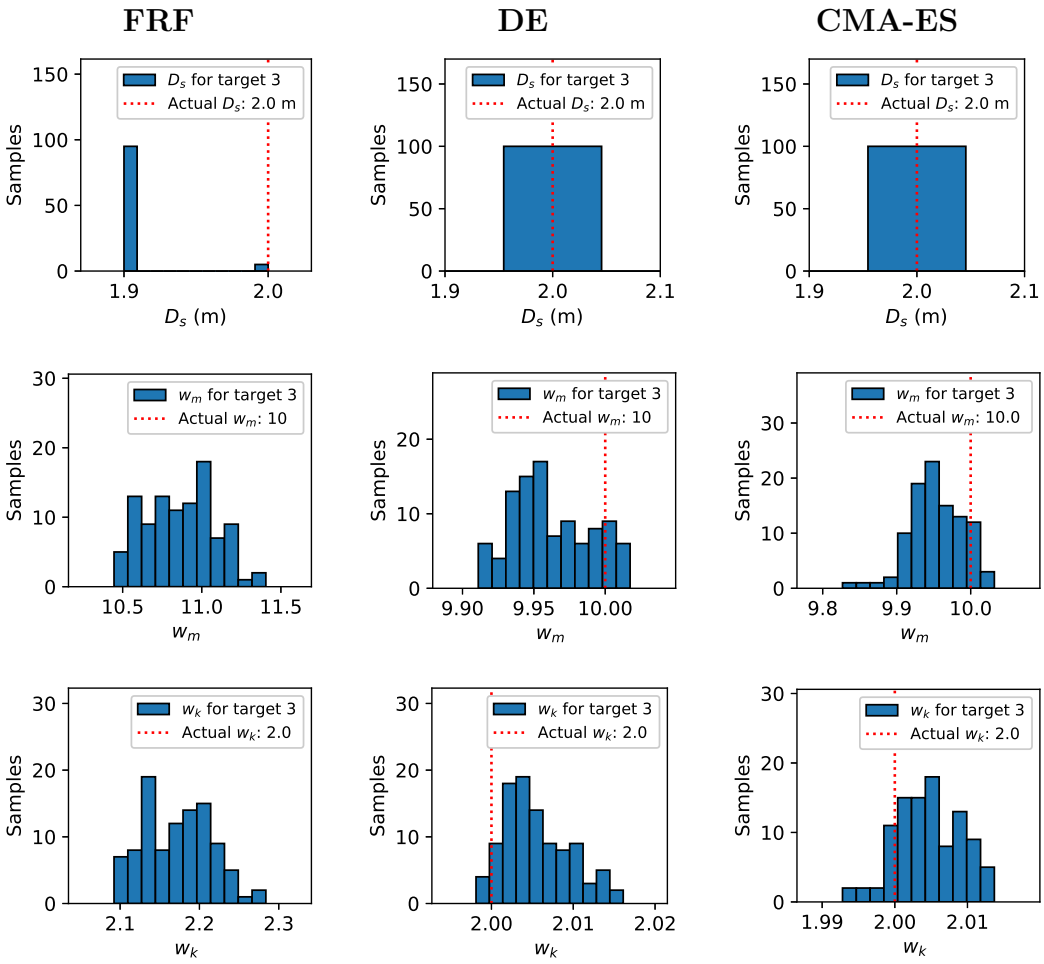

Figure C.2: Comparison of converged parameter distributions for target 3 across FRF-based (left), DE-based (middle), and CMA-ES-based (right) frameworks. Each row corresponds to a parameter: (top) D_s, (middle) w_m, and (bottom) w_k.

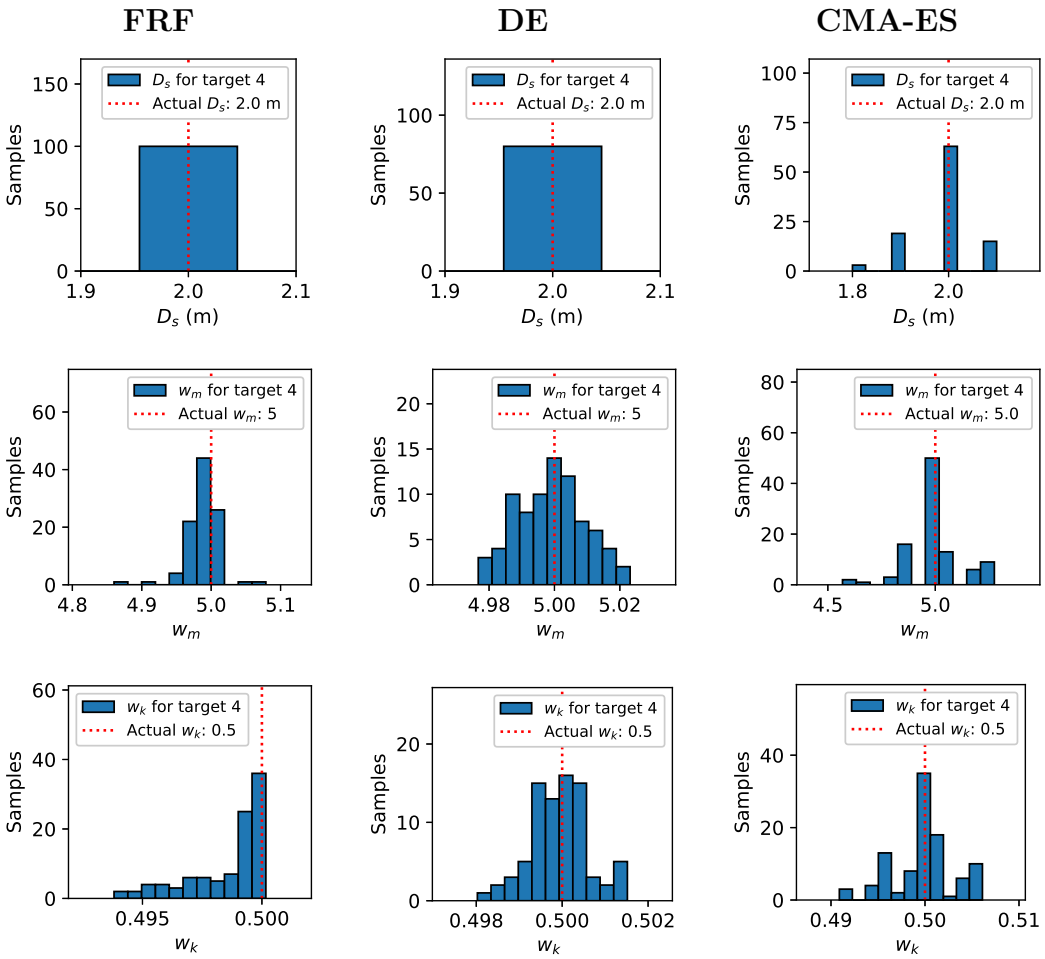

Figure C.3: Comparison of converged parameter distributions for target 4 across FRF-based (left), DE-based (middle), and CMA-ES-based (right) frameworks. Each row corresponds to a parameter: (top) D_s, (middle) w_m, and (bottom) w_k.

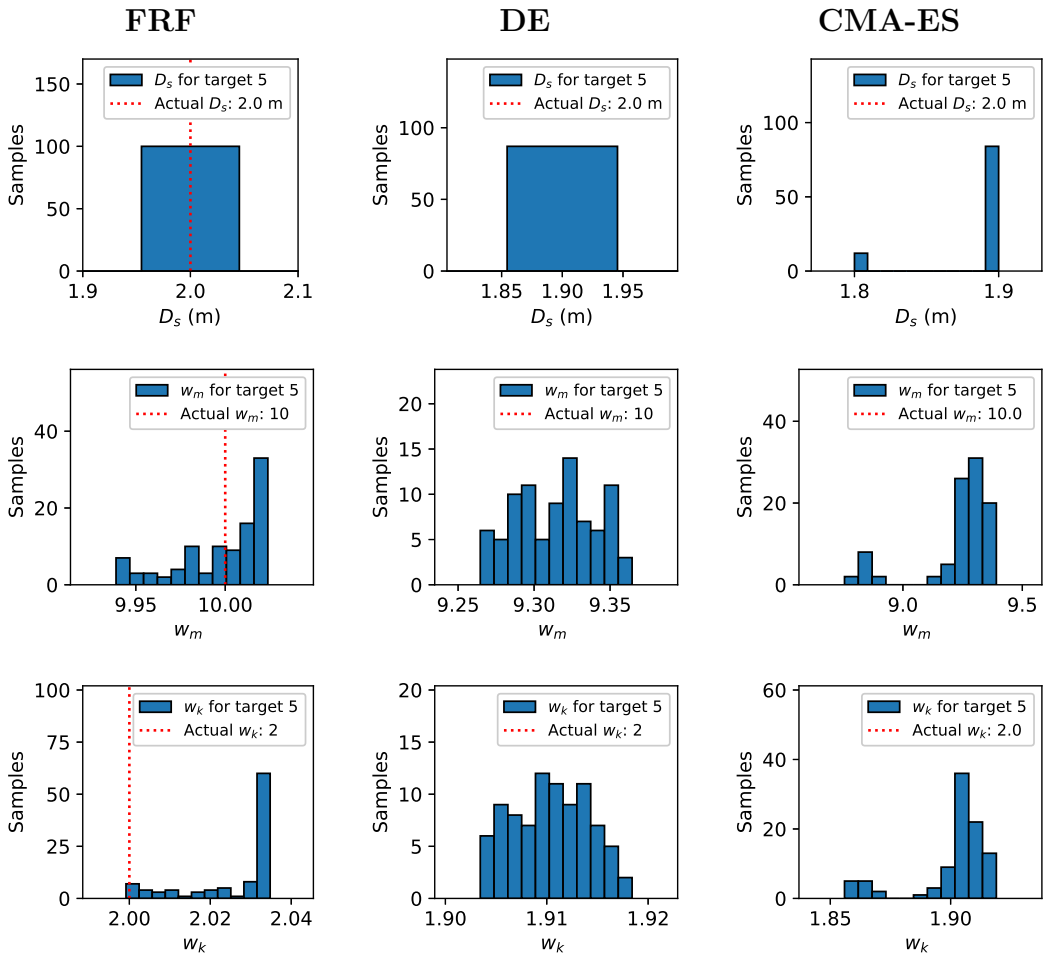

Figure C.4: Comparison of converged parameter distributions for target 5 across FRF-based (left), DE-based (middle), and CMA-ES-based (right) frameworks. Each row corresponds to a parameter: (top) D_s, (middle) w_m, and (bottom) w_k.

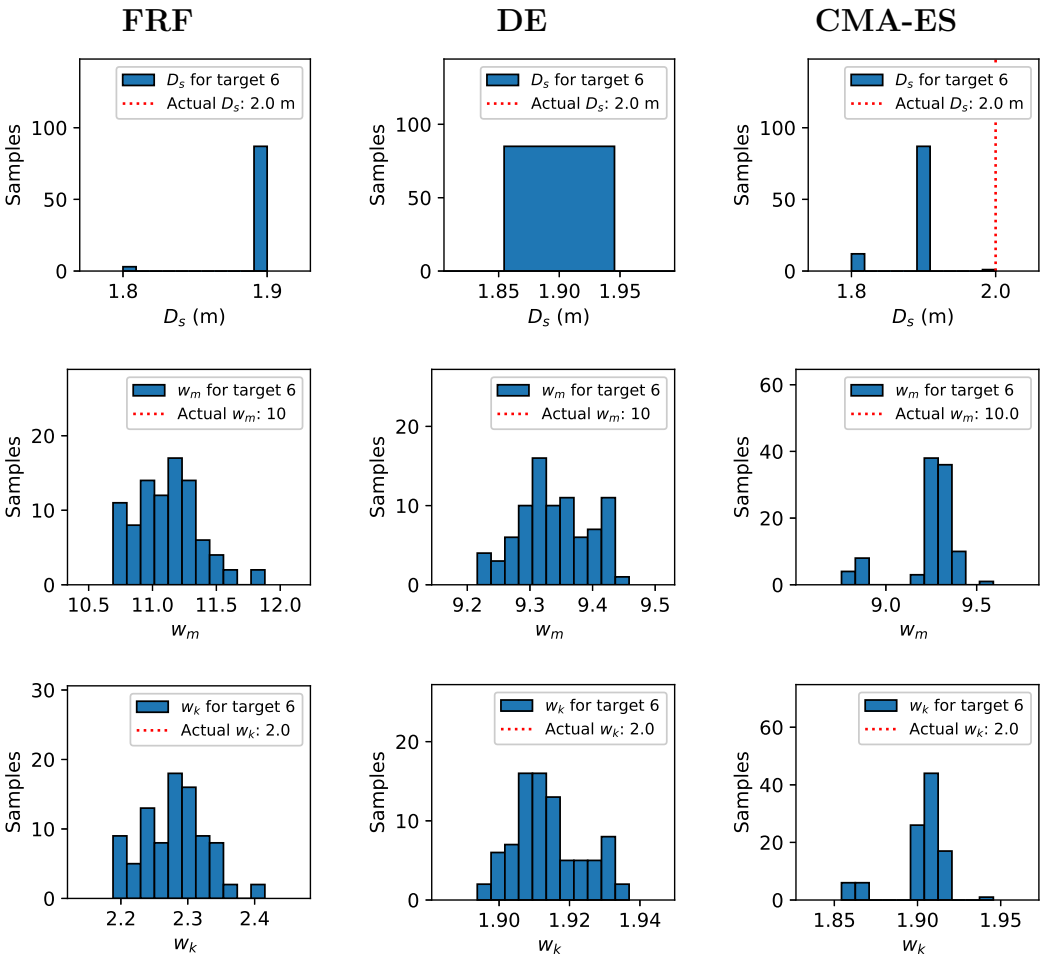

Figure C.5: Comparison of converged parameter distributions for target 6 across FRF-based (left), DE-based (middle), and CMA-ES-based (right) frameworks. Each row corresponds to a parameter: (top) D_s, (middle) w_m, and (bottom) w_k.

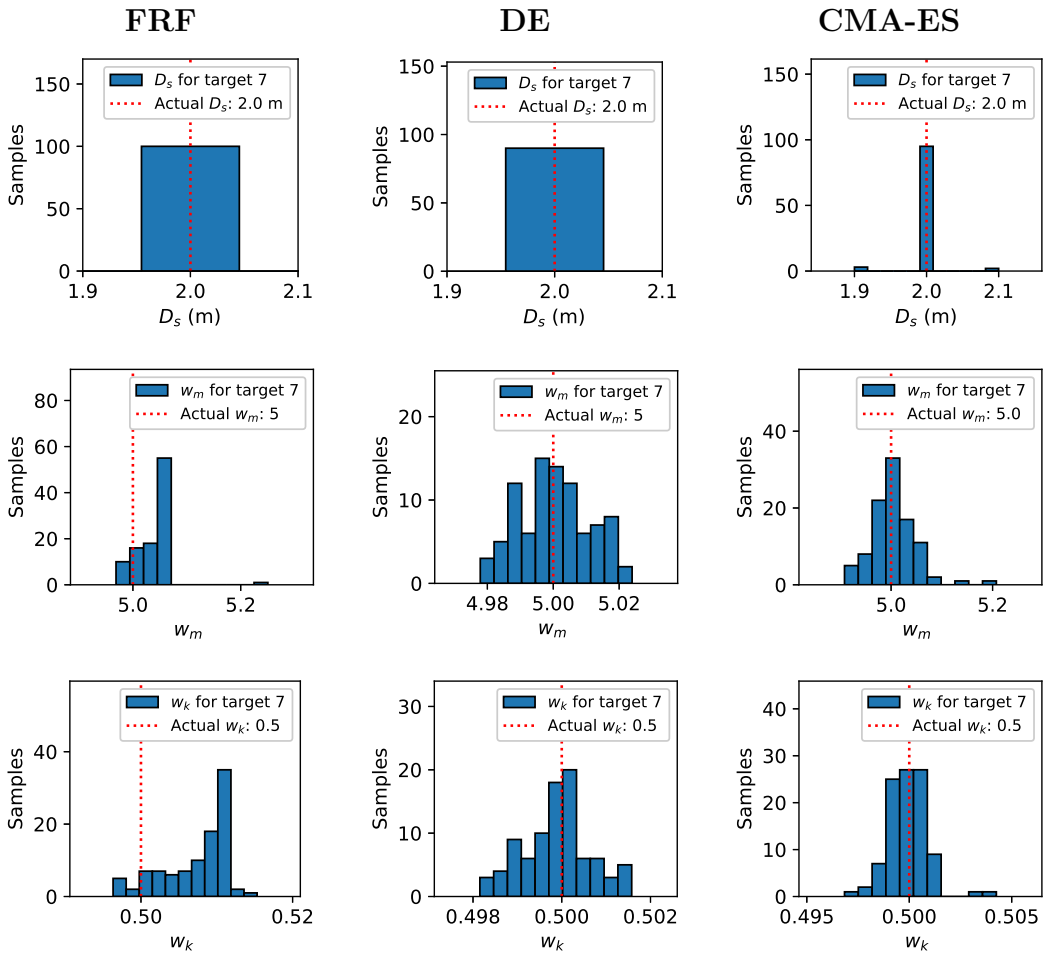

Figure C.6: Comparison of converged parameter distributions for target 7 across FRF-based (left), DE-based (middle), and CMA-ES-based (right) frameworks. Each row corresponds to a parameter: (top) D_s, (middle) w_m, and (bottom) w_k.

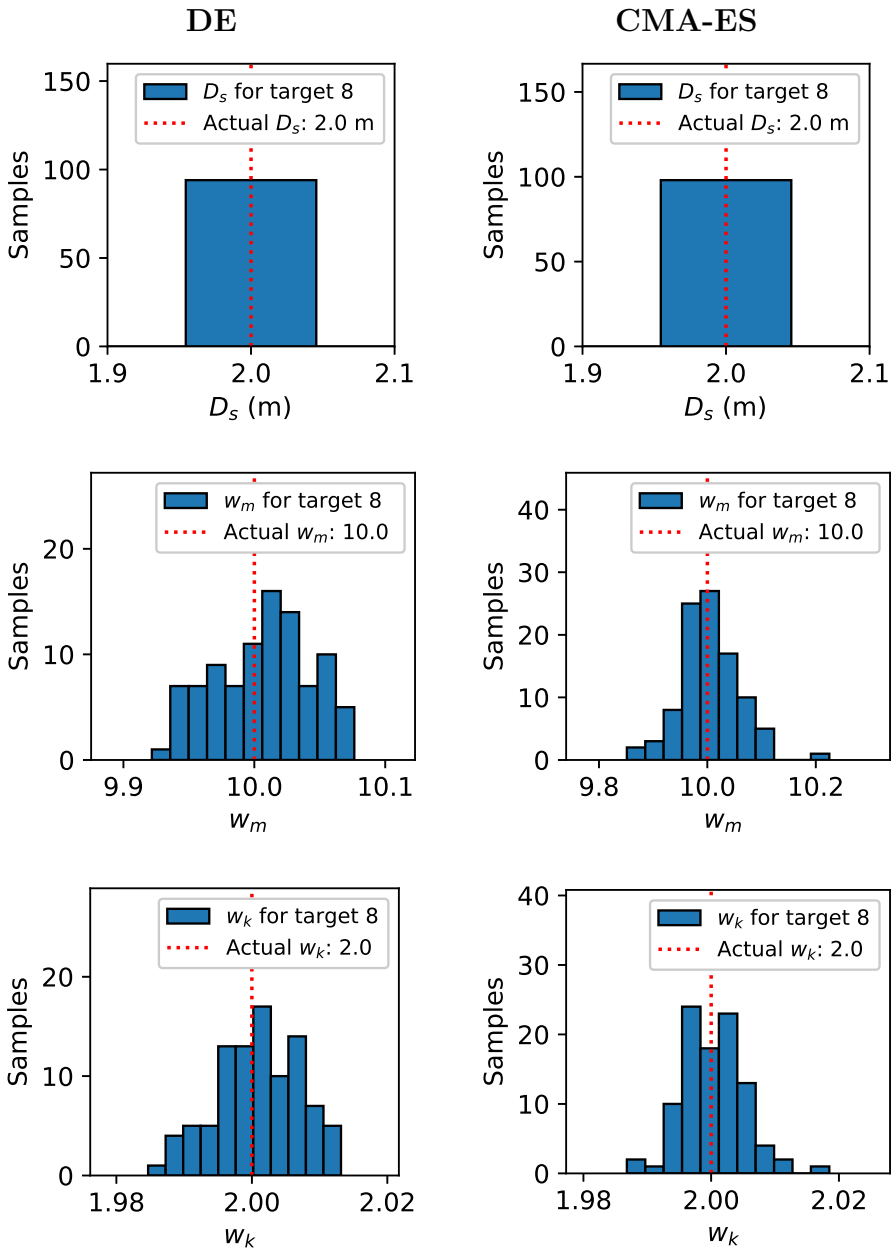

Figure C.7: Comparison of converged parameter distributions for target 8 across DE-based (left) and CMA-ES-based (right) frameworks. Each row corresponds to a parameter: (top) D_s, (middle) w_m, and (bottom) w_k.

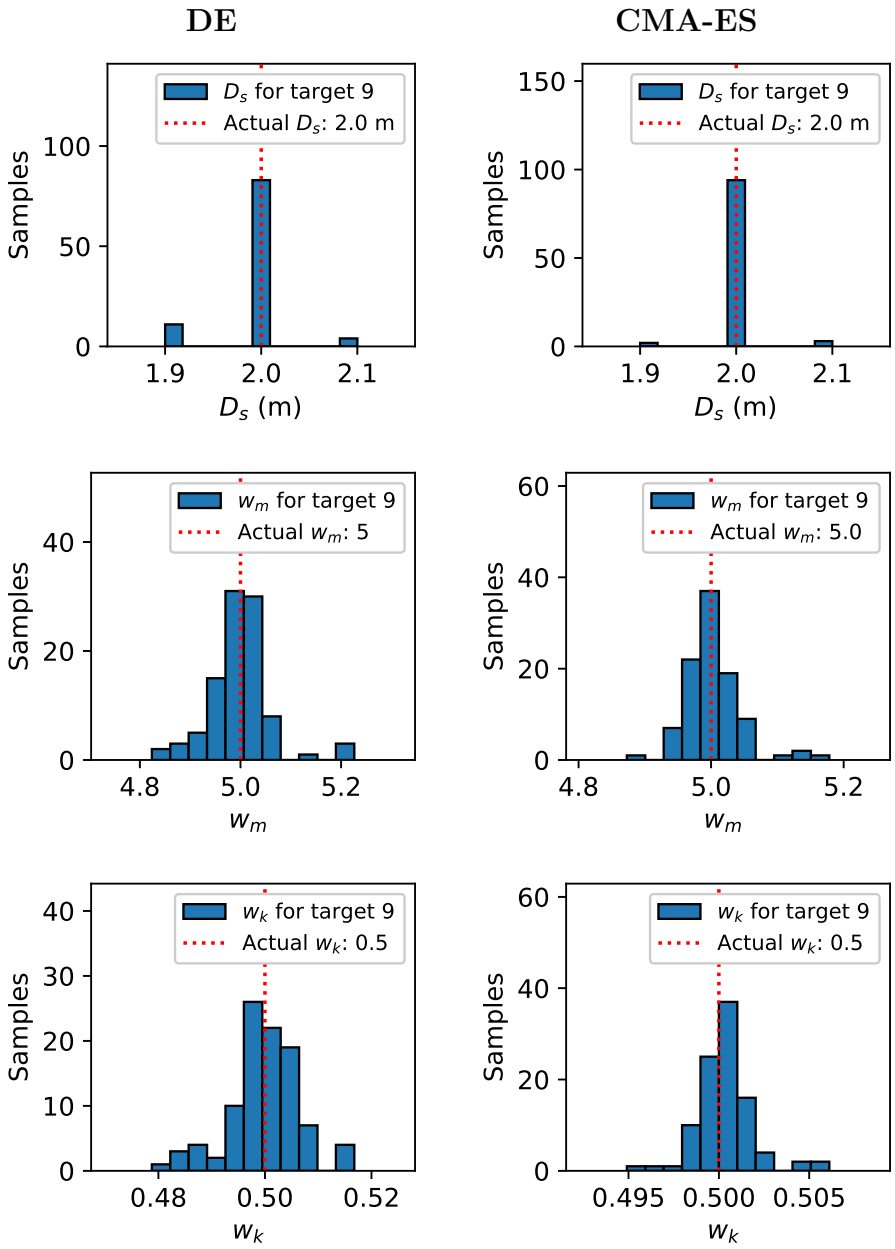

Figure C.8: Comparison of converged parameter distributions for target 9 across DE-based (left) and CMA-ES-based (right) frameworks. Each row corresponds to a parameter: (top) D_s, (middle) w_m, and (bottom) w_k.

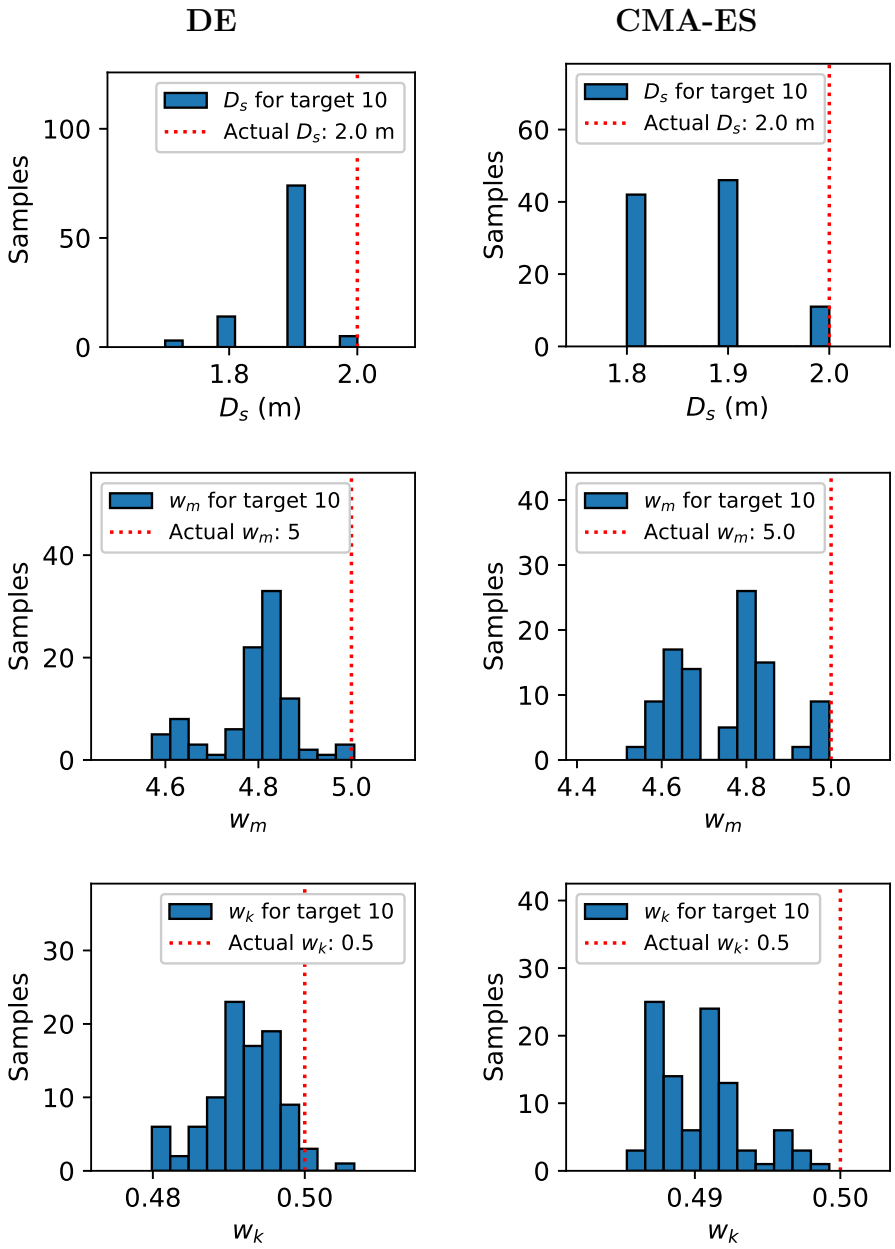

Figure C.9: Comparison of converged parameter distributions for target 10 across DE-based (left) and CMA-ES-based (right) frameworks. Each row corresponds to a parameter: (top) D_s, (middle) w_m, and (bottom) w_k.

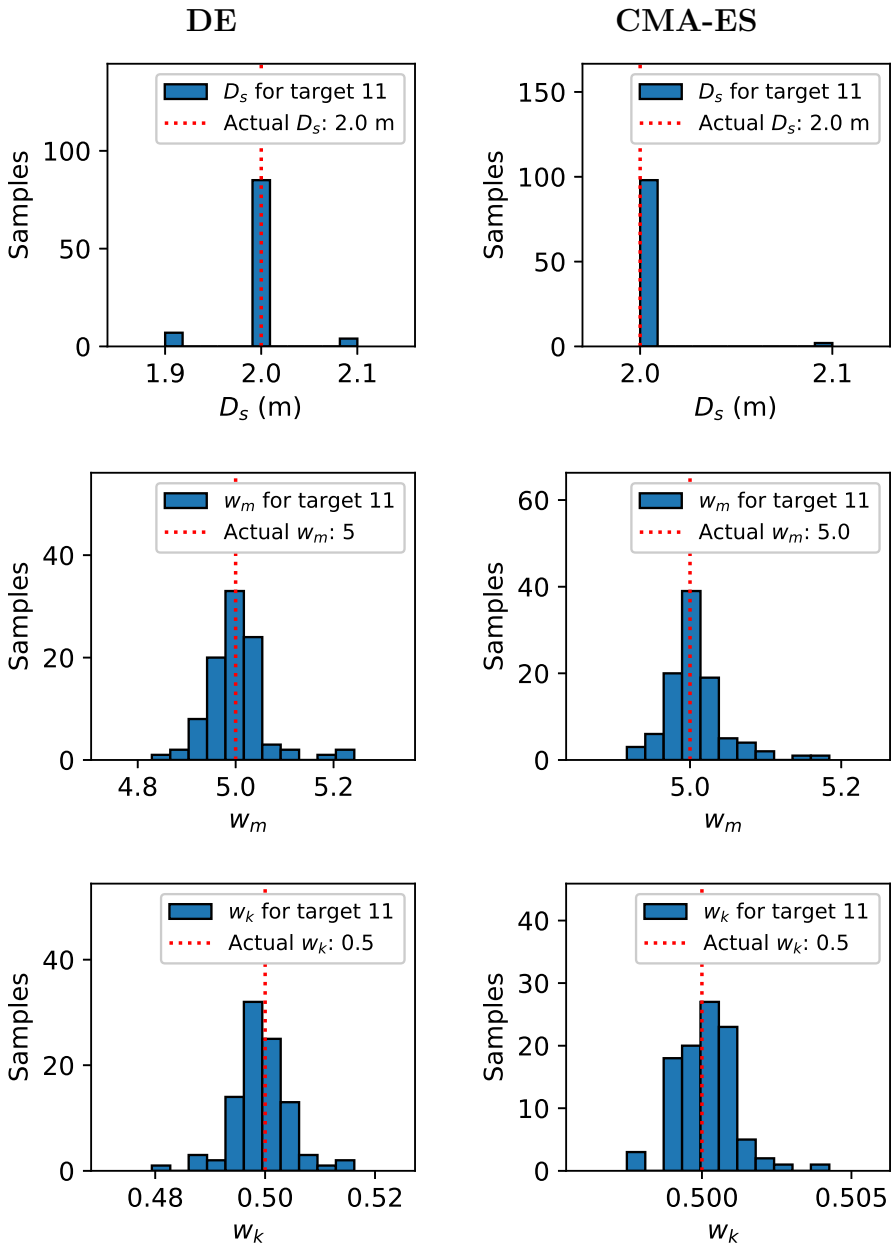

Figure C.10: Comparison of converged parameter distributions for target 11 across DE-based (left) and CMA-ES-based (right) frameworks. Each row corresponds to a parameter: (top) D_s, (middle) w_m, and (bottom) w_k.

Bibliography

Abdallah, I., Dertimanis, V., Mylonas, H., Tatsis, K., Chatzi, E., Dervili, N., Worden, K., & Maguire, E. (2018). Fault diagnosis of wind turbine structures using decision tree learning algorithms with big data. In *Safety and reliability–safe societies in a changing world* (pp. 3053–3061). CRC Press.

Abdel-Rahman, K., & Achmus, M. (2005). Finite element modelling of horizontally loaded monopile foundations for offshore wind energy converters in Germany. *Proceedings of the international symposium on frontiers in offshore geotechnics. Taylor and Francis, Perth*, 391–396.

Abhinav, K., & Saha, N. (2017). Effect of scouring in sand on monopile-supported offshore wind turbines. *Marine Georesources & Geotechnology*, *35*(6), 817–828.

Achmus, M., Kuo, Y.-S., & Abdel-Rahman, K. (2009). Behavior of monopile foundations under cyclic lateral load. *Computers and Geotechnics*, *36*(5), 725–735.

Aghmasheh, R., Rashtchi, V., & Rahimpour, E. (2017). Gray box modeling of power transformer windings for transient studies. *IEEE Transactions on Power Delivery*, *32*(5), 2350–2359.

Aktan, A. E., Farhey, D. N., Helmicki, A. J., Brown, D. L., Hunt, V. J., Lee, K.-L., & Levi, A. (1997). Structural identification for condition assessment: Experimental arts. *Journal of Structural Engineering*, *123*(12), 1674–1684.

Alkayem, N. H., Bakir, P. G., Friswell, M. I., & Ozer, H. (2018). Inverse finite element model updating using hybrid optimization technique for damage identification in beam-like structures. *Mechanical Systems and Signal Processing*, *105*, 143–160.

Allemang, R. J. (2003). The modal assurance criterion: Twenty years of use and abuse. *Sound and vibration*, *37*(8), 14–23.

Amador, S. D., & Brincker, R. (2021). Robust multi-dataset identification with frequency domain decomposition. *Journal of Sound and Vibration*, *508*, 116207.

An, Y., Chatzi, E., Sim, S.-H., Laflamme, S., Blachowski, B., & Ou, J. (2019). Recent progress and future trends on damage identification methods for bridge structures. *Structural Control and Health Monitoring*, *26*(10), e2416.

Anastasia, S., García-Macías, E., Ubertini, F., Gattulli, V., & Ivorra, S. (2023). Damage identification of railway bridges through temporal autoregressive modeling. *Sensors*, *23*(21), 8830.

Antoniadou, I., Dervilis, N., Papatheou, E., Maguire, A., & Worden, K. (2015). Aspects of structural health and condition monitoring of offshore wind turbines. *Philosophical Transactions of the Royal Society A: Mathematical, Physical and Engineering Sciences*, *373*(2035), 20140075.

Arany, L., Bhattacharya, S., Macdonald, J., & Hogan, S. (2017). Design of monopiles for offshore wind turbines in 10 steps. *Soil Dynamics and Earthquake Engineering*, *92*, 126–152. https://doi.org/https://doi.org/10.1016/j.soildyn.2016.09.024

Åström, K. J., & Bohlin, T. (1965). Numerical identification of linear dynamic systems from normal operating records. *IFAC Conference on Self-Adaptive Systems*.

Åström, K. J., & Eykhoff, P. (1971). System identification: A survey. *Automatica*, *7*(2), 123–162.

Augustyn, D., Smolka, U., Tygesen, U. T., Ulriksen, M. D., & Sørensen, J. D. (2020). Data-driven model updating of an offshore wind jacket substructure. *Applied Ocean Research*, *104*, 102366.

Avendano-Valencia, L. D., Chatzi, E. N., & Tcherniak, D. (2020). Gaussian process models for mitigation of operational variability in the structural health monitoring of wind turbines. *Mechanical Systems and Signal Processing*, *142*, 106686.

Azam, S. E., Chatzi, E., & Papadimitriou, C. (2015). A dual kalman filter approach for state estimation via output-only acceleration measurements. *Mechanical Systems and Signal Processing*, *60*, 866–886.

Bailey, H., Brookes, K. L., & Thompson, P. M. (2014). Assessing environmental impacts of offshore wind farms: Lessons learned and recommendations for the future. *Aquatic Biosystems*, *10*, 1–13.

Baruch, M., & Itzhack, I. Y. (1978). Optimal weighted orthogonalization of measured modes. *AIAA Journal*, *16*(4), 346–351. https://doi.org/10.2514/3.60896

Basu, D., Salgado, R., & Prezzi, M. (2009). A continuum-based model for analysis of laterally loaded piles in layered soils. *Geotechnique*, *59*(2), 127–140.

Bathe, K.-J. (2006). *Finite Element Procedures*. Klaus-Jurgen Bathe.

Bauer, D., & Jansson, M. (2000). Analysis of the asymptotic properties of the MOESP type of subspace algorithms. *Automatica*, *36*(4), 497–509.

Bauer, D. (2005). Asymptotic properties of subspace estimators. *Automatica*, *41*(3), 359–376.

Bauer, D., Deistler, M., & Scherrer, W. (1999). Consistency and asymptotic normality of some subspace algorithms for systems without observed inputs. *Automatica*, *35*(7), 1243–1254.

Beattie, C., & Smith, S. (1992). Optimal matrix approximants in structural identification. *Journal of Optimization Theory and Applications*, *74*(1), 23–56.

Been, K., & Jefferies, M. G. (1985). A state parameter for sands. *Géotechnique*, *35*(2), 99–112.

Bendat, J. S., & Piersol, A. G. (1993). *Engineering Applications of Correlation and Spectral Analysis* (2nd). John Wiley & Sons.

Benveniste, A., & Mevel, L. (2007). Nonstationary consistency of subspace methods. *IEEE Transactions on Automatic Control*, *52*(6), 974–984.

Berman, A., & Nagy, E. (1983). Improvement of a large analytical model using test data. *AIAA Journal*, *21*(8), 1168–1173.

Berman, A. (1979). Mass matrix correction using an incomplete set of measured modes. *AIAA Journal*, *17*(10), 1147–1148. https://doi.org/10.2514/3.61290

Bhattacharya, S. (2019, April). *Design of Foundations for Offshore Wind Turbines*. Wiley. https://doi.org/10.1002/9781119128137

Bi, S., Beer, M., Cogan, S., & Mottershead, J. (2023). Stochastic model updating with uncertainty quantification: An overview and tutorial. *Mechanical Systems and Signal Processing*, *204*, 110784.

Biot, M. A. (1937). Bending of an infinite beam on an elastic foundation. *Journal of Applied Mechanics*, *4*(1), A1–A7. https://doi.org/10.1115/1.4008739

Bishop, R. E. D., & Gladwell, G. M. L. (1963). An investigation into the theory of resonance testing. *Philosophical Transactions of the Royal Society of London. Series A, Mathematical and Physical Sciences*, *255*(1055), 241–280.

Bolton, M. (1986). The strength and dilatancy of sands. *Geotechnique*, *36*(1), 65–78.

Boulanger, R. W., Curras, C. J., Kutter, B. L., Wilson, D. W., & Abghari, A. (1999). Seismic soil–pile–structure interaction experiments and analyses. *Journal of Geotechnical and Geoenvironmental Engineering*, *125*(9), 750–759. https://doi.org/10.1061/(ASCE)1090-0241(1999)125:9(750)

Briaud, J.-L., Chen, H.-C., Li, Y., Nurtjahyo, P., & Wang, J. (2005). SRICOS-EFA method for contraction scour in fine-grained soils. *Journal of Geotechnical and Geoenvironmental Engineering*, *131*(10), 1283–1294.

Brincker, R., Ventura, C. E., & Andersen, P. (2001a). Damping estimation by frequency domain decomposition. *Proceedings of IMAC 19: A Conference on Structural Dynamics*, 698–703.

Brincker, R., Zhang, L., & Andersen, P. (2000). Output-only modal analysis by frequency domain decomposition. *Proceedings of ISMA25: 2000 international conference on noise and vibration engineering*, 717–723.

Brincker, R., Zhang, L., & Andersen, P. (2001b). Modal identification of output-only systems using frequency domain decomposition. *Smart materials and structures*, *10*(3), 441.

Broms, B. B. (1964). Lateral resistance of piles in cohesionless soils. *Journal of the Soil Mechanics and Foundations Division*, *90*(3), 123–156.

Brown, D. A., & Shie, C.-F. (1990). Three dimensional finite element model of laterally loaded piles. *Computers and Geotechnics*, *10*(1), 59–79.

Burd, H. J., Abadie, C. N., Byrne, B. W., Houlsby, G. T., Martin, C. M., McAdam, R. A., Jardine, R. J., Pedro, A. M. G., Potts, D. M., Taborda, D. M. G., Zdravković, L., & Andrade, M. P. (2020a). Application of the PISA design model to monopiles embedded in layered soils. *Géotechnique*, *70*, 1067–1082. https://doi.org/10.1680/jgeot.20.PISA.009

Burd, H. J., Taborda, D. M., Zdravković, L., Abadie, C. N., Byrne, B. W., Houlsby, G. T., Gavin, K. G., Igoe, D. J., Jardine, R. J., Martin, C. M., et al. (2020b). PISA design model for monopiles for offshore wind turbines: Application to a marine sand. *Géotechnique*, *70*(11), 1048–1066.

Byrne, B. W., Burd, H. J., Zdravković, L., McAdam, R. A., Taborda, D. M., Houlsby, G. T., Jardine, R. J., Martin, C. M., Potts, D. M., & Gavin, K. G. (2019). PISA: New design methods for offshore wind turbine monopiles. *Revue Française de Géotechnique*, (158), 3.

Byrne, B. W., & Houlsby, G. T. (2003). Foundations for offshore wind turbines. *Philosophical Transactions of the Royal Society of London. Series A: Mathematical, Physical and Engineering Sciences*, *361*(1813), 2909–2930.

Capecchi, D., Ciambella, J., Pau, A., & Vestroni, F. (2016). Damage identification in a parabolic arch by means of natural frequencies, modal shapes and curvatures. *Meccanica*, *51*, 2847–2859.

Chao, H. (2002). *An Experimental Model for Non-Destructive Evaluation on Pile Foundations Using Guided Wave Approach* [Doctoral dissertation, Northwestern University].

Chatzi, E. N., & Papadimitriou, C. (2016). *Identification Methods for Structural Health Monitoring* (Vol. 567). Springer.

Chen, J. C., & Garba, J. A. (1980). Analytical model improvement using modal test results. *AIAA Journal*, *18*(6), 684–690. https://doi.org/10.2514/3.50805

Chiuso, A., & Picci, G. (2004). The asymptotic variance of subspace estimates. *Journal of Econometrics*, *118*(1), 257–291.

Chortis, G., Askarinejad, A., Prendergast, L., Li, Q., & Gavin, K. (2020). Influence of scour depth and type on p–y curves for monopiles in sand under monotonic lateral loading in a geotechnical centrifuge. *Ocean Engineering*, *197*, 106838.

Ciang, C. C., Lee, J.-R., & Bang, H.-J. (2008). Structural health monitoring for a wind turbine system: A review of damage detection methods. *Measurement Science and Technology*, *19*(12), 122001.

Cicirello, A. (2024). Physics-enhanced machine learning: A position paper for dynamical systems investigations. *arXiv:2405.05987*.

Clough, R. W., & Penzien, J. (1975). *Dynamics of Structures*. McGraw-Hill.

Cole, H., JR. (1968). On-the-line analysis of random vibrations. *9th structural dynamics and materials conference*, 288.

Collins, J. D., Hart, G. C., Hasselman, T. K., & Kennedy, B. (1974). Statistical identification of structures. *AIAA Journal*, *12*(2), 185–190. https://doi.org/10.2514/3.49190

Costanzo, G., Brindley, G., Willems, G., Ramirez, L., Cole, P., & Klonari, V. (2023). *Wind energy in Europe 2023: Statistics and the outlook for 2024–2030* (R. O'Sullivan, Ed.; tech. rep.) (Prepared with contributions from WindEurope members and national associations.). WindEurope. Brussels, Belgium.

Cui, S., Liu, H., & Maghoul, P. (2022). Pile length estimation based on guided wave theory for unknown foundations. *The 75th Annual Canadian Geotechnical Society Conference (GeoCalgary 2022)*, 1–6.

D'Ambrogio, W., & Zobel, P. (1994). Damage detection in truss structures using a direct updating technique. *Proc. 19th Int. Seminar for Modal Analysis on Tools for Noise and Vibration Analysis*, 657–667.

Darvishi-Alamouti, S., Bahaari, M. R., & Moradi, M. (2017). Natural frequency of offshore wind turbines on rigid and flexible monopiles in cohesionless soils with linear stiffness distribution. *Applied Ocean Research*, *68*, 91–102. https://doi.org/https://doi.org/10.1016/j.apor.2017.07.009

Das, S., & Suganthan, P. N. (2010). Differential evolution: A survey of the state-of-the-art. *IEEE transactions on evolutionary computation*, *15*(1), 4–31.

De Munck, M., Moens, D., Desmet, W., & Vandepitte, D. (2008). A response surface based optimisation algorithm for the calculation of fuzzy envelope FRFs of models with uncertain properties. *Computers & Structures*, *86*(10), 1080–1092.

DeCastro, M., Salvador, S., Gómez-Gesteira, M., Costoya, X., Carvalho, D., Sanz-Larruga, F. J., & Gimeno, L. (2019). Europe, China and the United States: Three different approaches to the development of offshore wind energy. *Renewable and Sustainable Energy Reviews*, *109*, 55–70.

Devriendt, C., De Sitter, G., & Guillaume, P. (2010). An operational modal analysis approach based on parametrically identified multivariable transmissibilities. *Mechanical Systems and Signal Processing*, *24*(5), 1250–1259.

Dezi, F., Gara, F., & Roia, D. (2012). Dynamic response of a near-shore pile to lateral impact load. *Soil Dynamics and Earthquake Engineering*, *40*, 34–47.

Dhandole, S. D., & Modak, S. V. (2010). A comparative study of methodologies for vibro-acoustic FE model updating of cavities using simulated data. *International Journal of Mechanics and Materials in Design*, *6*, 27–43. https://doi.org/10.1007/s10999-010-9116-4

Díaz, H., & Soares, C. G. (2020). Review of the current status, technology and future trends of offshore wind farms. *Ocean Engineering*, *209*, 107381.

Doherty, P., & Gavin, K. (2012a). Laterally loaded monopile design for offshore wind farms. *Proceedings of the Institution of Civil Engineers - Energy*, *165*(1), 7–17.

Doherty, P., & Gavin, K. (2012b). Laterally loaded monopole design for offshore wind farms. *Proceedings of Institution of Civil Engineers: Energy*, *165*, 7–17. https://doi.org/10.1680/ener.11.00003

Döhler, M., & Mevel, L. (2013). Efficient multi-order uncertainty computation for stochastic subspace identification. *Mechanical Systems and Signal Processing*, *38*(2), 346–366.

Döhler, M. (2011). *Subspace-based System Identification and Fault Detection: Algorithms for Large Systems and Application to Structural Vibration Analysis* [Doctoral dissertation, Université Rennes 1].

Döhler, M., & Mevel, L. (2012). Fast multi-order computation of system matrices in subspace-based system identification. *Control Engineering Practice*, *20*(9), 882–894.

Domaneschi, M., Limongelli, M. P., Martinelli, L., et al. (2013). Vibration based damage localization using MEMS on a suspension bridge model. *Smart Struct. Syst*, *12*(6), 679–694.

Donohue, S., Long, M., Gavin, K., & O'Connor, P. (2004). Shear wave stiffness of irish glacial till. *Proceedings of the 2nd International Conference on Site Characterization*, 459–466.

Dührkop, J. (2009). *Zum Einfluss von Aufweitungen und Zyklischen Lasten auf das Verformungsverhalten lateral beanspruchter Pfähle in Sand*. TUHH.

Ebrahimian, H., Astroza, R., Conte, J. P., & Papadimitriou, C. (2018). Bayesian optimal estimation for output-only nonlinear system and damage identification of civil structures. *Structural Control and Health Monitoring*, *25*(4), e2128.

Elachachi, S. M., Breysse, D., & Houy, L. (2004). Longitudinal variability of soils and structural response of sewer networks. *Computers and Geotechnics*, *31*, 625–641.

Ereiz, S., Duvnjak, I., & Jiménez-Alonso, J. F. (2022). Review of finite element model updating methods for structural applications. *Structures*, *41*, 684–723.

Faes, M., & Moens, D. (2020). Recent trends in the modeling and quantification of non-probabilistic uncertainty. *Archives of Computational Methods in Engineering*, *27*, 633–671.

Fathi, A., Esfandiari, A., Fadavie, M., & Mojtahedi, A. (2020). Damage detection in an offshore platform using incomplete noisy FRF data by a novel Bayesian model updating method. *Ocean Engineering*, *217*, 108023.

Felber, A. J. (1994). *Development of a Hybrid Bridge Evaluation System* [Doctoral dissertation, University of British Columbia].

Feng, W.-H., Wu, C.-Y., Fu, J.-Y., Ng, C.-T., & He, Y.-C. (2023). Automatic modal identification via eigensystem realization algorithm with improved stabilization diagram technique. *Engineering Structures*, *291*, 116449.

Ferrari, R., Froio, D., Rizzi, E., Gentile, C., & Chatzi, E. N. (2019). Model updating of a historic concrete bridge by sensitivity-and global optimization-based Latin hypercube sampling. *Engineering Structures*, *179*, 139–160.

Fitzgerald, P. C., Malekjafarian, A., Bhowmik, B., Prendergast, L. J., Cahill, P., Kim, C.-W., Hazra, B., Pakrashi, V., & OBrien, E. J. (2019). Scour damage detection and structural health monitoring of a laboratory-scaled bridge using a vibration energy harvesting device. *Sensors*, *19*(11), 2572.

Foti, S., & Sabia, D. (2011). Influence of foundation scour on the dynamic response of an existing bridge. *Journal of bridge engineering*, *16*(2), 295–304.

Friswell, M. I., Inman, D. J., & Pilkey, D. F. (1998). Direct updating of damping and stiffness matrices. *AIAA Journal*, *36*, 491–493. https://doi.org/10.2514/2.396

Friswell, M., & Mottershead, J. E. (1995). *Finite Element Model Updating in Structural Dynamics* (Vol. 38). Springer Science & Business Media.

Gattulli, V. (2016). Implementation of identification methodologies on large-scale structures. In *Identification methods for structural health monitoring* (pp. 1–34). Springer.

Gavin, K., Adekunte, A., & O'Kelly, B. (2009). A field investigation of vertical footing response on sand. *Proceedings of the Institution of Civil Engineers - Geotechnical Engineering*, *162*, 257–267. https://doi.org/10.1680/geng.2009.162.5.257

Gavin, K., & Lehane, B. (2007). Base load – displacement response of piles in sand. *Canadian Geotechnical Journal*, *44*, 1053–1063. https://doi.org/10.1139/T07-048

Gazetas, G., & Dobry, R. (1984). Horizontal response of piles in layered soils. *Journal of Geotechnical Engineering*, *110*(1), 20–40. https://doi.org/10.1061/(ASCE)0733-9410(1984)110:1(20)

Ghanem, R., & Shinozuka, M. (1995). Structural-system identification. I: Theory. *Journal of Engineering Mechanics*, *121*(2), 255–264.

Giagopoulos, D., Arailopoulos, A., Dertimanis, V., Papadimitriou, C., Chatzi, E., & Grompanopoulos, K. (2019). Structural health monitoring and fatigue damage estimation using vibration measurements and finite element model updating. *Structural Health Monitoring*, *18*(4), 1189–1206.

Giordano, P. F., Prendergast, L. J., & Limongelli, M. P. (2020). A framework for assessing the value of information for health monitoring of scoured bridges. *Journal of Civil Structural Health Monitoring*, *10*, 485–496.

Goethals, I. (2005). *Subspace Identification for Linear, Hammerstein and Hammerstein-Wiener Systems* [Doctoral dissertation, Katholieke Universiteit Leuven].

Goethals, I., Van Gestel, T., Suykens, J., Van Dooren, P., & De Moor, B. (2003). Identification of positive real models in subspace identification by using regularization. *IEEE Transactions on Automatic Control*, *48*(10), 1843–1847.

Goulet, J.-A., Kripakaran, P., & Smith, I. F. (2010). Multimodel structural performance monitoring. *Journal of Structural Engineering*, *136*(10), 1309–1318.

Greś, S., Döhler, M., Andersen, P., & Mevel, L. (2021a). Uncertainty quantification for the modal phase collinearity of complex mode shapes. *Mechanical Systems and Signal Processing*, *152*, 107436.

Greś, S., Döhler, M., & Mevel, L. (2021b). Uncertainty quantification of the modal assurance criterion in operational modal analysis. *Mechanical Systems and Signal Processing*, *152*, 107457.

Greś, S. (2019). *Vibration-based Monitoring of Structures: Algorithms for Fault Detection and Uncertainty Quantification of Modal Indicators* [Doctoral dissertation, Aalborg University].

Greś, S., Döhler, M., Andersen, P., & Mevel, L. (2021c). Kalman filter-based subspace identification for operational modal analysis under unmeasured periodic excitation. *Mechanical Systems and Signal Processing*, *146*, 106996.

Greś, S., Döhler, M., Jacobsen, N.-J., & Mevel, L. (2022a). Uncertainty quantification of input matrices and transfer function in input/output subspace system identification. *Mechanical Systems and Signal Processing*, *167*, 108581.

Greś, S., Döhler, M., & Mevel, L. (2021d). Statistical model-based optimization for damage extent quantification. *Mechanical Systems and Signal Processing*, *160*, 107894.

Greś, S., Riva, R., Süleyman, C. Y., Andersen, P., & Łuczak, M. (2022b). Uncertainty quantification of modal parameter estimates obtained from subspace identification: An experimental validation on a laboratory test of a large-scale wind turbine blade. *Engineering Structures*, *256*, 114001.

Greś, S., Tatsis, K. E., Dertimanis, V., & Chatzi, E. (2023). Low-rank approximation of Hankel matrices in denoising applications for statistical damage diagnosis of wind turbine blades. *Mechanical Systems and Signal Processing*, *197*, 110391.

Gui, G., Pan, H., Lin, Z., Li, Y., & Yuan, Z. (2017). Data-driven support vector machine with optimization techniques for structural health monitoring and damage detection. *KSCE Journal of Civil Engineering*, *21*, 523–534.

Guillaume, P., Verboven, P., & Vanlanduit, S. (1998). Frequency-domain maximum likelihood identification of modal parameters with confidence intervals. *Proceedings of the international seminar on modal analysis*, *1*, 359–366.

Guillaume, P., Verboven, P., Vanlanduit, S., Van Der Auweraer, H., & Peeters, B. (2003). A poly-reference implementation of the least-squares complex frequency-domain estimator. *Proceedings of IMAC*, *21*(01).

Haiderali, A., & Madabhushi, G. (2016). Improving the lateral capacity of monopiles in submarine clay. *Proceedings of the Institution of Civil Engineers-Ground Improvement*, *169*(4), 239–252.

Hanifah, A. A. (1999). *A Theoretical Evaluation of Guided Waves in Deep Foundations* [Doctoral dissertation, Northwestern University].

Hansen, J. B., Brincker, R., López-Aenlle, M., Overgaard, C. F., & Kloborg, K. (2017). A new scenario-based approach to damage detection using operational modal parameter estimates. *Mechanical Systems and Signal Processing*, *94*, 359–373.

Hansen, N., & Ostermeier, A. (2001). Completely derandomized self-adaptation in evolution strategies. *Evolutionary Computation*, *9*(2), 159–195.

Hao, H., & Xia, Y. (2002). Vibration-based damage detection of structures by genetic algorithm. *Journal of Computing in Civil Engineering*, *16*(3), 222–229. https://doi.org/10.1061/(asce)0887-3801(2002)16:3(222)

Holt, J. D., Chen, S., & Douglas, R. A. (1994). Determining lengths of installed timber piles by dispersive wave propagation. *Transportation research record*.

Hu, S.-L. J., Li, H., & Wang, S. (2007). Cross-model cross-mode method for model updating. *Mechanical Systems and Signal Processing*, *21*(4), 1690–1703. https://doi.org/10.1016/j.ymssp.2006.07.012

Huang, Y., Dimitriadis, G., Kielb, R. E., & Li, J. (2017). System eigenvalue identification of mistuned bladed disks using least-squares complex frequency-domain method. *Turbo Expo: Power for Land, Sea, and Air*, *50930*, V07BT36A001.

Ibata-Arens, K., Monticelli, L., Geelan, T., & Chen, K. K. (2018). Opportunities and challenges for a sustainable energy future. *30th Annual Meeting*.

Ibrahim, S., Mikulcik, E., et al. (1976). The experimental determination of vibration parameters from time responses. *The Shock and Vibration Bulletin*, *46*(5), 187–196.

Igel, C., Hansen, N., & Roth, S. (2007). Covariance matrix adaptation for multi-objective optimization. *Evolutionary computation*, *15*(1), 1–28.

Imregun, M., Visser, W. J., & Ewins, D. J. (1995). Finite element model updating using frequency response function data. *Mechanical Systems and Signal Processing*, *9*(2), 187–202. https://doi.org/10.1006/mssp.1995.0015

Ioakim, A., & Prendergast, L. (2024). A two-stage method to estimate the embedded length of foundation piles using frf-based model updating. *Mechanical Systems and Signal Processing*, *219*, 111603. https://doi.org/10.1016/j.ymssp.2024.111603

Ioakim, A., Greś, S., Döhler, M., Prendergast, L. J., & Chatzi, E. (2025). An indirect data-driven model-updating framework to estimate soil–pile interaction parameters using output-only data. *Engineering Structures*, *328*, 119699.

James, G., Carne, T., & Laufer, J. (1995). The natural excitation technique (NExT) for modal parameter extraction from operating structures. *Journal of Analytical and Experimental Modal Analysis*, *10*.

Juang, J.-N., Cooper, J. E., & Wright, J. (1988). An eigensystem realisation algorithm using data correlations (ERA/DC) for modal parameter identification. *Control-Theory and Advanced Technology*, *4*(1), 5–14.

Juang, J.-N., & Pappa, R. S. (1985). An eigensystem realization algorithm for modal parameter identification and model reduction. *Journal of Guidance, Control, and Dynamics*, *8*(5), 620–627.

Juirnarongrit, T., & Ashford, S. A. (2006). Soil-pile response to blast-induced lateral spreading. II: Analysis and assessment of the p–y method. *Journal of Geotechnical and Geoenvironmental Engineering*, *132*(2), 163–172.

Jung, S., Kim, S.-R., Patil, A., et al. (2015). Effect of monopile foundation modeling on the structural response of a 5-MW offshore wind turbine tower. *Ocean Engineering*, *109*, 479–488.

Kabe, A. M. (1985). Stiffness matrix adjustment using mode data. *AIAA Journal*, *23*(9), 1431–1436. https://doi.org/10.2514/3.9103

Kallehave, D., Thilsted, C. L., & Liingaard, M. (2012). Modification of the API py formulation of initial stiffness of sand. *SUT Offshore Site Investigation and Geotechnics*, SUT–OSIG.

Kallehave, D., Byrne, B. W., LeBlanc Thilsted, C., & Mikkelsen, K. K. (2015). Optimization of monopiles for offshore wind turbines. *Philosophical Transactions of the Royal Society A: Mathematical, Physical and Engineering Sciences*, *373*(2035), 20140100.

Kamariotis, A., Chatzi, E., & Straub, D. (2023). A framework for quantifying the value of vibration-based structural health monitoring. *Mechanical Systems and Signal Processing*, *184*, 109708.

Kampitsis, A., Sapountzakis, E., Giannakos, S., & Gerolymos, N. (2013). Seismic soil–pile–structure kinematic and inertial interaction—a new beam approach. *Soil Dynamics and Earthquake Engineering*, *55*, 211–224. https://doi.org/https://doi.org/10.1016/j.soildyn.2013.09.023

Kennedy, J., & Eberhart, R. (1995). Particle swarm optimization. *Proceedings of ICNN'95 - International Conference on Neural Networks*, *4*, 1942–1948. https://doi.org/10.1109/ICNN.1995.488968

Kim, K.-O., Anderson, W. J., & Sandstrom, R. E. (1983). Nonlinear inverse perturbation method in dynamic analysis. *AIAA Journal*, *21*(9), 1310–1316. https://doi.org/10.2514/3.8245

Klinga, J. V., & Alipour, A. (2015). Assessment of structural integrity of bridges under extreme scour conditions. *Engineering Structures*, *82*, 55–71.

Komusanac, I., Brindley, G., Fraile, D., & Ramirez, L. (2021). *Offshore Wind in Europe: Key Trends and Statistics 2020* (R. O'Sullivan, Ed.; tech. rep.) (Prepared with cooperation from national associations across Europe). WindEurope Business Intelligence. Brussels, Belgium.

Krämer, C., De Smet, C., & De Roeck, G. (1999). Z24 bridge damage detection tests. *IMAC 17, the International Modal Analysis Conference*, *3727*, 1023–1029.

Kurata, M., Lynch, J. P., Law, K. H., & Salvino, L. W. (2012). Bayesian model updating approach for systematic damage detection of plate-type structures. *Topics in Model Validation and Uncertainty Quantification, Volume 4: Proceedings of the 30th IMAC, A Conference on Structural Dynamics, 2012*, 85–94.

Lee, U., & Shin, J. (2002). A frequency response function-based structural damage identification method. *Computers & Structures*, *80*(2), 117–132.

Levin, R. I., & Lieven, N. A. J. (1998). Dynamic finite element model updating using simulated annealing and genetic algorithms. *Mechanical Systems and Signal Processing*, *12*(1), 91–120. https://doi.org/10.1006/mssp.1996.0136

Li, Q., Gavin, K., Askarinejad, A., & Prendergast, L. J. (2022). Experimental and numerical investigation of the effect of vertical loading on the lateral behaviour of monopiles in sand. *Canadian Geotechnical Journal*, *59*(5), 652–666.

Li, Q., Prendergast, L., Askarinejad, A., Chortis, G., & Gavin, K. (2020). Centrifuge modeling of the impact of local and global scour erosion on the monotonic lateral response of a monopile in sand. *Geotechnical Testing Journal*, *43*(5), 1084–1100.

Lin, R. M., Lim, M. K., & Du, H. (1995). Improved inverse eigensensitivity method for structural analytical model updating. *Journal of Vibration and Acoustics*, *117*(2), 192–198. https://doi.org/10.1115/1.2873889

Lin, R., & Ewins, D. (1990). Model updating using FRF data. *Proceedings of the 15th international seminar on modal analysis*, 141–162.

Lin, R., & Zhu, J. (2006). Model updating of damped structures using FRF data. *Mechanical Systems and Signal Processing*, *20*(8), 2200–2218.

Lin, R., & Zhu, J. (2007). Finite element model updating using vibration test data under base excitation. *Journal of Sound and Vibration*, *303*(3-5), 596–613.

Liu, G., & Mao, Z. (2017). Structural damage diagnosis with uncertainties quantified using interval analysis. *Structural Control and Health Monitoring*, *24*(10), e1989.

Liu, J., Liu, J., Li, Z., Hou, X., & Dai, G. (2021a). Estimating CPT parameters at unsampled locations based on kriging interpolation method. *Applied Sciences*, *11*(23), 11264.

Liu, M., & Gorman, D. G. (1995). Formulation of Rayleigh damping and its extensions. *Computers & Structures*, *57*(2), 277–285. https://doi.org/10.1016/0045-7949(94)00611-6

Liu, Q., Wang, F., Li, J., & Xiao, W. (2021b). A hybrid support vector regression with multi-domain features for low-velocity impact localization on composite plate structure. *Mechanical Systems and Signal Processing*, *154*, 107547.

Ljung, L. (1999). *System Identification (2nd ed.): Theory for the User*. Prentice Hall PTR.

Lye, A., Cicirello, A., & Patelli, E. (2021). Sampling methods for solving Bayesian model updating problems: A tutorial. *Mechanical Systems and Signal Processing*, *159*, 107760.

Lynch Jr, J. J. (2007). *Experimental Verification of Flexural Guided Waves in Concrete Cylindrical Piles* [Doctoral dissertation, Northwestern University].

Lyons, R. G. (1997). *Understanding Digital Signal Processing, 3/E*. Pearson Education India.

Lysmer, J., Ostadan, F., & Chin, C. (1999). *SASSI2000: A System for Analysis of Soil–Structure Interaction* (Technical Report) (Department of Civil and Environmental Engineering). University of California, Berkeley. Berkeley, California.

MacKay, D. J. (2016). *Sustainable Energy–Without the Hot Air*. Bloomsbury Publishing.

Maes, K., Van Meerbeeck, L., Reynders, E., & Lombaert, G. (2022). Validation of vibration-based structural health monitoring on retrofitted railway bridge kw51. *Mechanical Systems and Signal Processing*, *165*, 108380.

Maia, N., & Silva, J. (2001). Modal analysis identification techniques. *Philosophical Transactions of the Royal Society of London. Series A: Mathematical, Physical and Engineering Sciences*, *359*(1778), 29–40.

Mao, Y., Xu, C., Chen, J., Pu, Y., & Hu, Q. (2022). Auxiliary model-based iterative estimation algorithms for nonlinear systems using the covariance matrix adaptation strategy. *Circuits, Systems, and Signal Processing*, *41*(12), 6750–6773.

Marwala, T. (2002). Finite element model updating using wavelet data and genetic algorithm. *Journal of Aircraft*, *39*(4), 709–711. https://doi.org/10.2514/2.2985

Marwala, T. (2010). *Finite Element Model Updating Using Computational Intelligence Techniques: Applications to Structural Dynamics*. Springer Science & Business Media.

Matutano, C., Negro, V., López-Gutiérrez, J.-S., & Esteban, M. D. (2013). Scour prediction and scour protections in offshore wind farms. *Renewable Energy*, *57*, 358–365.

Mayall, R., Byrne, B. W., Burd, H. J., Mcadam, R., Cassie, P., & Whitehouse, R. (2018). Modelling of foundation response to scour and scour protection

for offshore wind turbine structures. *Scour and Erosion IX: Proceedings of the 9th International Conference on Scour and Erosion (ICSE 2018), November 5-8, 2018, Taipei, Taiwan*, 405.

Mehrjoo, A., Song, M., Moaveni, B., Papadimitriou, C., & Hines, E. (2022). Optimal sensor placement for parameter estimation and virtual sensing of strains on an offshore wind turbine considering sensor installation cost. *Mechanical Systems and Signal Processing*, *169*, 108787.

Mellinger, P., Döhler, M., & Mevel, L. (2016). Variance estimation of modal parameters from output-only and input/output subspace-based system identification. *Journal of Sound and Vibration*, *379*, 1–27.

Meyerhof, G., & Baikie, L. (1963). Strength of steel culvert sheets bearing against compacted sand backfill. *Highway Research Record*, (30).

Modak, S. V. (2014). Direct matrix updating of vibroacoustic finite element models using modal test data. *AIAA Journal*, *52*, 1386–1392. https://doi.org/10.2514/1.J052558

Mottershead, J. E., & Friswell, M. (1993). Model updating in structural dynamics: A survey. *Journal of Sound and Vibration*, *167*(2), 347–375.

Mottershead, J. E., Link, M., & Friswell, M. I. (2011). The sensitivity method in finite element model updating: A tutorial. *Mechanical Systems and Signal Processing*, *25*(7), 2275–2296.

Negro, V., López-Gutiérrez, J.-S., Esteban, M. D., & Matutano, C. (2014). Uncertainties in the design of support structures and foundations for offshore wind turbines. *Renewable Energy*, *63*, 125–132.

Nehete, D., Modak, S., & Gupta, K. (2015). Structural FE model updating of cavity systems incorporating vibro–acoustic coupling. *Mechanical Systems and Signal Processing*, *50-51*, 362–379. https://doi.org/10.1016/j.ymssp.2014.05.028

Newmark, N. M. (1959). A method of computation for structural dynamics. *Journal of the Engineering Mechanics Division*, *85*(3), 67–94. https://doi.org/10.1061/JMCEA3.0000098

OBrien, E. J., & Malekjafarian, A. (2016). A mode shape-based damage detection approach using laser measurement from a vehicle crossing a simply supported bridge. *Structural Control and Health Monitoring*, *23*(10), 1273–1286.

Okeagu, B., & Abdel-Sayed, G. (1984). Coefficients of soil reaction for buried flexible conduits. *Journal of Geotechnical Engineering*, *110*(7), 908–922. https://doi.org/10.1061/(ASCE)0733-9410(1984)110:7(908)

Oliveira, G., Magalhaes, F., Cunha, A., & Caetano, E. (2021). Modal decomposition of the dynamic response of wind turbine during one year of continuous monitoring. *Structural Control and Health Monitoring*, *28*(8), e2754.

Oliveira, G., Magalhães, F., Cunha, Á., & Caetano, E. (2018). Vibration-based damage detection in a wind turbine using 1 year of data. *Structural Control and Health Monitoring*, *25*(11), e2238.

O'Neill, M. W., & Murchison, J. M. (1983). *An Evaluation of p-y Relationships in Sands* (tech. rep.) (Report to the American Petroleum Institute). University of Houston.

Osman, A. I., Chen, L., Yang, M., Msigwa, G., Farghali, M., Fawzy, S., Rooney, D. W., & Yap, P.-S. (2023). Cost, environmental impact, and resilience of renewable energy under a changing climate: A review. *Environmental Chemistry Letters*, *21*(2), 741–764.

Ou, Y., Chatzi, E. N., Dertimanis, V. K., & Spiridonakos, M. D. (2017). Vibration-based experimental damage detection of a small-scale wind turbine blade. *Structural Health Monitoring*, *16*(1), 79–96.

Papadimitriou, C., Beck, J. L., & Au, S.-K. (2000). Entropy-based optimal sensor location for structural model updating. *Journal of Vibration and Control*, *6*(5), 781–800.

PCB Piezotronics. (2018). Impulse Hammer 086d50: Model 086d50 Product Specification.

Peeters, B., & De Roeck, G. (2001). Stochastic system identification for operational modal analysis: A review. *Journal of Dynamic Systems, Measurement, and Control*, *123*(4), 659–667.

Peeters, B. (2000). *System Identification and Damage Detection in Civil Engineering* [Doctoral dissertation, Katholieke Universiteit Leuven].

Peeters, B., & De Roeck, G. (1999). Reference-based stochastic subspace identification for output-only modal analysis. *Mechanical Systems and Signal Processing*, *13*(6), 855–878.

Peeters, B., Van der Auweraer, H., Guillaume, P., & Leuridan, J. (2004). The PolyMAX frequency-domain method: A new standard for modal parameter estimation? *Shock and Vibration*, *11*(3-4), 395–409.

Peeters, B., & Ventura, C. (2003). Comparative study of modal analysis techniques for bridge dynamic characteristics. *Mechanical Systems and Signal Processing*, *17*(5), 965–988.

Pender, M. J. (1993). Aseismic pile foundation design analysis. *Bulletin of the New Zealand Society for Earthquake Engineering*, *26*(1), 49–160. https://doi.org/10.5459/bnzsee.26.1.49-160

Pintelon, R., Guillaume, P., & Schoukens, J. (2007). Uncertainty calculation in (operational) modal analysis. *Mechanical Systems and Signal Processing*, *21*(6), 2359–2373.

Pintelon, R., Guillaume, P., Rolain, Y., Schoukens, J., & Van Hamme, H. (1994). Parametric identification of transfer functions in the frequency domain-a survey. *IEEE Transactions on Automatic Control*, *39*(11), 2245–2260.

Pintelon, R., & Schoukens, J. (2012). *System Identification: A Frequency Domain Approach*. John Wiley & Sons.

Poulos, H. G., & Davis, E. H. (1980). *Pile Foundation Analysis and Design*. John Wiley & Sons.

Pradhan, S., & Modak, S. (2012). A method for damping matrix identification using frequency response data. *Mechanical Systems and Signal Processing*, *33*, 69–82. https://doi.org/10.1016/j.ymssp.2012.07.002

Prendergast, L. J., & Gavin, K. (2016). A comparison of initial stiffness formulations for small-strain soil–pile dynamic Winkler modelling. *Soil Dynamics and Earthquake Engineering*, *81*, 27–41.

Prendergast, L. J., Gavin, K., & Doherty, P. (2015). An investigation into the effect of scour on the natural frequency of an offshore wind turbine. *Ocean Engineering*, *101*, 1–11. https://doi.org/https://doi.org/10.1016/j.oceaneng.2015.04.017

Prendergast, L. J., Hester, D., Gavin, K., & O'Sullivan, J. J. (2013). An investigation of the changes in the natural frequency of a pile affected by scour. *Journal of Sound and Vibration*, *332*, 6685–6702. https://doi.org/10.1016/j.jsv.2013.08.020

Prendergast, L., Wu, W., & Gavin, K. (2019). Experimental application of FRF-based model updating approach to estimate soil mass and stiffness mobilised under pile impact tests. *Soil Dynamics and Earthquake Engineering*, *123*, 1–15.

Prendergast, L. J., & Gavin, K. (2014). A review of bridge scour monitoring techniques. *Journal of Rock Mechanics and Geotechnical Engineering*, *6*(2), 138–149.

Prendergast, L. J., Limongelli, M. P., Ademovic, N., Anžlin, A., Gavin, K., & Zanini, M. (2018). Structural health monitoring for performance assessment of bridges under flooding and seismic actions. *Structural Engineering International*, *28*(3), 296–307.

Prevosto, M. (1982). *Algorithmes d'identification des caractéristiques vibratoires de structures mécaniques complexes* [Doctoral dissertation, INSA de Lyon].

Radzieński, M., Krawczuk, M., & Palacz, M. (2011). Improvement of damage detection methods based on experimental modal parameters. *Mechanical Systems and Signal Processing*, *25*(6), 2169–2190.

Randolph, M. F. (1981). The response of flexible piles to lateral loading. *Géotechnique*, *31*(2), 247–259. https://doi.org/10.1680/geot.1981.31.2.247

Reale, C., Tott-Buswell, J., & Prendergast, L. J. (2021). Impact of geotechnical uncertainty on the preliminary design of monopiles supporting offshore wind turbines. *ASCE-ASME Journal of Risk and Uncertainty in Engineering Systems, Part B: Mechanical Engineering*, *7*(4). https://doi.org/10.1115/1.4051418

Ren, W., & Chen, H. (2010). Finite element model updating in structural dynamics by using the response surface method. *Engineering Structures*, *32*(8), 2455–2465. https://doi.org/10.1016/j.engstruct.2010.04.019

Reynders, E. (2012). System identification methods for (operational) modal analysis: Review and comparison. *Archives of Computational Methods in Engineering*, *19*(1), 51–124.

Reynders, E. (2021). Uncertainty quantification in data-driven stochastic subspace identification. *Mechanical Systems and Signal Processing*, *151*, 107338.

Reynders, E., Pintelon, R., & De Roeck, G. (2008). Uncertainty bounds on modal parameters obtained from stochastic subspace identification. *Mechanical Systems and Signal Processing*, *22*(4), 948–969.

Rosquoet, F., Thorel, L., Garnier, J., & Canepa, Y. (2007). Lateral cyclic loading of sand-installed piles. *Soils and foundations*, *47*(5), 821–832.

Sadrekarimi, J., & Akbarzad, M. (2009). Comparative study of methods of determination of coefficient of subgrade reaction. *Electronic Journal of Geotechnical Engineering*, *14*, 1–14.

Saidou Sanda, M., Gauron, O., Turcotte, N., Lamarche, C.-P., Paultre, P., Talbot, M., & Laflamme, J.-F. (2018). Efficient finite elements model updating for damage detection in bridges. *Experimental Vibration Analysis for Civil Structures: Testing, Sensing, Monitoring, and Control 7*, 293–305.

Samu, V., & Guddati, M. (2020). Nondestructive length estimation of an embedded pile through combined analysis of transverse and longitudinal waves. *NDT & E International*, *110*, 102203. https://doi.org/10.1016/j.ndteint.2019.102203

Samu, V., & Guddati, M. (2019). Nondestructive method for length estimation of pile foundations through effective dispersion analysis of reflections. *Journal of Nondestructive Evaluation*, *38*(2), 45.

Sarvi, F., Shojaee, S., Torkzadeh, P., et al. (2014). Damage identification of trusses by finite element model updating using an enhanced levenberg-marquardt algorithm. *Int. J. Optim. Civil Eng*, *4*(2), 207–231.

Schommer, S., Nguyen, V. H., Maas, S., & Zürbes, A. (2017). Model updating for structural health monitoring using static and dynamic measurements. *Procedia engineering*, *199*, 2146–2153.

Sehgal, S., & Kumar, H. (2016). Structural dynamic model updating techniques: A state of the art review. *Archives of Computational Methods in Engineering*, *23*, 515–533. https://doi.org/10.1007/s11831-015-9150-3

Shadan, F., Khoshnoudian, F., & Esfandiari, A. (2016). A frequency response-based structural damage identification using model updating method. *Structural Control and Health Monitoring*, *23*(2), 286–302.

Shadan, F., Khoshnoudian, F., Inman, D. J., & Esfandiari, A. (2018). Experimental validation of a FRF-based model updating method. *Journal of Vibration and Control*, *24*(8), 1570–1583.

Shih, C., Tsuei, Y., Allemang, R., & Brown, D. (1988). Complex mode indication function and its applications to spatial domain parameter estimation. *Mechanical Systems and Signal Processing*, *2*(4), 367–377.

Simoen, E., De Roeck, G., & Lombaert, G. (2015). Dealing with uncertainty in model updating for damage assessment: A review. *Mechanical Systems and Signal Processing*, *56*, 123–149.

Simoen, E., & Lombaert, G. (2016). Bayesian parameter estimation. In *Identification methods for structural health monitoring* (pp. 89–115). Springer.

Söderström, T., & Stoica, P. (1981). Comparison of some instrumental variable methods—consistency and accuracy aspects. *Automatica*, *17*(1), 101–115.

Sohn, H., & Law, K. H. (1997). A Bayesian probabilistic approach for structure damage detection. *Earthquake Engineering & Structural Dynamics*, *26*(12), 1259–1281.

Sohn, H., & Law, K. H. (2000). Bayesian probabilistic damage detection of a reinforced-concrete bridge column. *Earthquake Engineering & Structural Dynamics*, *29*(8), 1131–1152.

Sørensen, S. P. H., & Ibsen, L. B. (2013). Assessment of foundation design for offshore monopiles unprotected against scour. *Ocean Engineering*, *63*, 17–25.

Sørensen, S. P. H., Ibsen, L. B., & Frigaard, P. (2010). Experimental evaluation of backfill in scour holes around offshore monopiles. *Frontiers in Offshore Geotechnics II. London: Taylor & Francis Group*, 635–640.

Steenackers, G., & Guillaume, P. (2006). Finite element model updating taking into account the uncertainty on the modal parameters estimates. *Journal of Sound and Vibration*, *296*(4), 919–934.

Stewart, J., Crouse, C. B., Hutchinson, T., Lizundia, B., Naeim, F., & Ostadan, F. (2012). *Soil-Structure Interaction for Building Structures* (tech. rep.). National Institute of Standards and Technology, Gaithersburg, MD.

Stone, K., Arshi, H., & Zdravkovic, L. (2018). Use of a bearing plate to enhance the lateral capacity of monopiles in sand. *Journal of Geotechnical and Geoenvironmental Engineering*, *144*(8), 04018051.

Sumer, B. M., Fredsøe, J., & Christiansen, N. (1992). Scour around vertical pile in waves. *Journal of waterway, port, coastal, and ocean engineering*, *118*(1), 15–31.

Suryasentana, S. K., & Lehane, B. M. (2016). Updated CPT-based p–y formulation for laterally loaded piles in cohesionless soil under static loading. *Géotechnique*, *66*(6), 445–453.

Tedesco, J. W., Stallings, J. M., & El-Mihilmy, M. (1999). Finite element method analysis of a concrete bridge repaired with fiber reinforced plastic laminates. *Computers & Structures*, *72*(1-3), 379–407.

Tewarson, R. P., & Tewarson, R. P. (1973). *Sparse Matrices* (Vol. 69). Academic press New York.

Timoshenko, S. (1983). *History of Strength of Materials: With a Brief Account of the History of Theory of Elasticity and Theory of Structures*. Courier Corporation.

Tott-Buswell, J., Prendergast, L. J., & Gavin, K. (2024). A CPT-based multi-spring model for lateral monopile analysis under SLS conditions in sand. *Ocean Engineering*, *293*, 116642.

United Nations Framework Convention on Climate Change (UNFCCC). (1997). Kyoto Protocol to the United Nations framework convention on climate change.

United Nations Framework Convention on Climate Change (UNFCCC). (2015, November). Paris Agreement [Adopted at the 21st Conference of the Parties (COP21), Paris].

Van der Auweraer, H., Guillaume, P., Verboven, P., & Vanlanduit, S. (2001). Application of a fast-stabilizing frequency domain parameter estimation method. *Journal of Dynamic Systems, Measurement, and Control*, *123*(4), 651–658. https://doi.org/10.1115/1.1410369

Van Overschee, P., & De Moor, B. (1996). *Subspace Identification for Linear Systems*. Springer.

Varoquaux, G., & Grisel, O. (2009). Joblib: Running Python Functions as Pipeline Jobs.

Vasconcelos, J. O., O'Donovan, J., Doherty, P., & Donohue, S. (2018). Development of numerical method for pile design to ec7 using CPT results. *Cone Penetration Testing 2018*, 657–662.

Velez, A., Gazetas, G., & Krishnan, R. (1983). Lateral dynamic response of constrained-head piles. *Journal of Geotechnical Engineering*, *109*(8), 1063–1081. https://doi.org/10.1061/(ASCE)0733-9410(1983)109:8(1063)

Verahegen, M., & Dewilde, P. (1992). Subspace model identification. part i: The output-error state-space model identification class of algorithm. *Int. J. Control*, *56*, 1187–1210.

Verhaegen, M. (1993). Subspace model identification part 3. analysis of the ordinary output-error state-space model identification algorithm. *International Journal of control*, *58*(3), 555–586.

Verhaegen, M., & Dewilde, P. (1992). Subspace model identification part 2. analysis of the elementary output-error state-space model identification algorithm. *International journal of control*, *56*(5), 1211–1241.

Vesić, A. B. (1961). Bending of beams resting on isotropic elastic solid. *Journal of the Engineering Mechanics Division*, *87*, 35–53. https://doi.org/10.1061/JMCEA3.0000212

Viberg, M., Wahlberg, B., & Ottersten, B. (1997). Analysis of state space system identification methods based on instrumental variables and subspace fitting. *Automatica*, *33*(9), 1603–1616.

Viberg, M. (1995). Subspace-based methods for the identification of linear time-invariant systems. *Automatica*, *31*(12), 1835–1851.

Virtanen, P., Gommers, R., Oliphant, T. E., et al. (2020). Scipy 1.0: Fundamental algorithms for scientific computing in python. *Nature Methods*, *17*(3), 261–272. https://doi.org/10.1038/s41592-019-0686-2

Wahab, M. A., & De Roeck, G. (1999). Damage detection in bridges using modal curvatures: Application to a real damage scenario. *Journal of Sound and Vibration*, *226*(2), 217–235.

Wang, H. (2004). *Theoretical Evaluation of Embedded Plate-like and Solid Cylindrical Concrete Structures With Guided Waves* [Doctoral dissertation, Northwestern University].

Wang, Z., Hu, R., Leng, H., Liu, H., Bai, Y., & Lu, W. (2020). Deformation analysis of large diameter monopiles of offshore wind turbines under scour. *Applied Sciences*, *10*(21), 7579.

Winkler, E. (1867). *Die Lehre von Elastizitat und Festigkeit (on Elasticity and Fixity)*. Dominicus.

Wolf, J. (1985). *Dynamic Soil–Structure Interaction*. Prentice Hall, Inc.

Wu, W. H., Prendergast, L. J., & Gavin, K. (2018). An iterative method to infer distributed mass and stiffness profiles for use in reference dynamic beam-Winkler models of foundation piles from frequency response functions. *Journal of Sound and Vibration*, *431*, 1–19. https://doi.org/10.1016/j.jsv.2018.05.049

Wu, X., Hu, Y., Li, Y., Yang, J., Duan, L., Wang, T., Adcock, T., Jiang, Z., Gao, Z., Lin, Z., et al. (2019). Foundations of offshore wind turbines: A review. *Renewable and Sustainable Energy Reviews*, *104*, 379–393.

Wu, Y., Zhu, R., Cao, Z., Liu, Y., & Jiang, D. (2020). Model updating using frequency response functions based on Sherman–Morrison formula. *Applied Sciences*, *10*(14), 4985.

Yang, Z., & Jeremić, B. (2002). Numerical analysis of pile behaviour under lateral loads in layered elastic–plastic soils. *International Journal for Numerical and Analytical Methods in Geomechanics*, *26*(14), 1385–1406.

Zappa, W., Junginger, M., & Van Den Broek, M. (2019). Is a 100% renewable European power system feasible by 2050? *Applied Energy*, *233*, 1027–1050.

Zdravković, L., Jardine, R. J., Taborda, D. M., Abadias, D., Burd, H. J., Byrne, B. W., Gavin, K. G., Houlsby, G. T., Igoe, D. J., Liu, T., et al. (2020). Ground characterisation for PISA pile testing and analysis. *Géotechnique*, *70*(11), 945–960.

Zhao, J. H., & Zhang, L. (2012). Structural damage identification based on the modal data change. *International Journal of Engineering Management*, *4*, 59–66.

Ziegler, L., Voormeeren, S., Schafhirt, S., & Muskulus, M. (2015). Sensitivity of wave fatigue loads on offshore wind turbines under varying site conditions. *Energy Procedia*, *80*, 193–200.